Characterisation of polar (0001) and non-polar (11-20) Ultraviolet nitride semiconductors

Rio Tse-Yang Chang

Downing College

A thesis submitted for the degree of Doctor of Philosophy at the University of Cambridge

January 2012

Abstract

Characterisation of polar (0001) and non-polar (11-20) ultraviolet nitride semiconductors

Rio Tse-Yang Chang

UV and deep-UV emitters based on AlGaN/AlN heterostructures are very inefficient due to the high lattice mismatch of these films with sapphire substrates, leading to high dislocation densities. This thesis describes the characterisation of the nanostructures of a range of UV structures, including *c*-plane (polar) AlGaN epilayers grown on AlN template, and nonpolar GaN/AlGaN MQWs grown on *a*-plane GaN template. The results are based primarily on transmission electron microscopy (TEM), cathodoluminescence in the scanning electron microscope (SEM-CL), high-resolution X-ray diffraction (HRXRD) and atomic force microscopy (AFM) measurements.

The structural and optical properties of various types of defect were examined in the *c*-plane AlGaN epilayers. Strain analysis based on in-situ wafer curvature measurements was employed to describe the strain relief mechanisms for different AlGaN compositions and to correlate the strain to each type of defect observed in the epilayers. This is followed by the investigation of AlN template growth optimisation, based on the TMA pre-dose on sapphire method to enhance the quality and the surface morphology of the template further. The initial growth conditions were shown to be critical for the final AlN film morphology. A higher TMA pre-dose has been shown to enable a better Al coverage leading to a fully coalesced AlN film at 1 μm thickness. An atomically smooth surface of the template was achieved over a large 10 x 10 μm AFM scale. Finally, the investigation of UV emitters based on nonpolar crystal orientations is presented. The SiN_x interlayer was able to reduce the threading dislocation density but was also found to generate voids with longer SiN_x growth time. The relationship between voids, threading dislocations, inversion domain boundaries and their associated V-defects and the variation in MQW growth rate has been discussed in detail.

Preface

This thesis is submitted to the University of Cambridge for the degree of Doctor of Philosophy. It is an account of the research that I have undertaken under the supervision of Professor C. J. Humphreys and Dr. M. A. Moram in the Department of Materials Science and Metallurgy, at the University of Cambridge. It is my own work and contains nothing which is the outcome of work done in collaboration with others, except where specified in the text and acknowledgements. This dissertation does not exceed 60,000 words in length and has not been submitted to any other institution for a degree.

Rio Tse-Yang Chang

January 2012

Acknowledgements

I feel tremendously lucky to have had the opportunity to work in the GaN group. This work would not have been possible without the help of various people, who I would like to acknowledge here.

I would like to express my sincere gratitude to my supervisor, Professor Sir Colin Humphreys, for giving me the opportunity to work in this wonderful group and his helpful advices throughout the course of my study. I am extremely grateful to my mentor, Dr. Michelle Moram, for her patience, motivation, enthusiasm, and immense knowledge. Her guidance helped me in all the time of research and writing of this thesis. I could not have imagined having a better advisor and mentor for my Ph.D study.

I am also grateful to many people who have provided help and support in completing this thesis, specific thanks go to (in no particular order): Dr. Menno Kappers for growing the samples in this thesis, and for corrections to this work and various papers and posters. Dr. Fabrice Oehler for growing the AlN samples for chapter 5 and his helpful discussions. Dr. Rachel Oliver for AFM training and her help and guidance on my first year report and viva. Dr. Jonathan Barnard, Dr. Carol Johnston, Dr. Stanley Zhang, Dr. TongTong Zhu, Rui Hao and Dr. Lewis Liu for electron microscopy related training and discussions; to Dr. Ron Broom, Dr. Suman-Lata Sahonta, Dr. Ted Thrush and Dr. Tom Sadler for corrections and suggestions to the thesis chapters. I also wish to thank all the members of the GaN group who have made it an enjoyable place to work. I acknowledge EPSRC and Cambridge Overseas Trust for financial support, Downing College for the travel grants and the Department of Materials Science & Metallurgy for use of their facilities.

Finally, I would like to thank my family, my future wife, Eve Ko, and my pet for their love and support. They have made countless sacrifices for me, and have provided me with steady guidance and on-going encouragement.

Publications and presentations

The following is a list of publications and presentations during the course of the PhD project.

Publications

T.Y. Chang, M.A. Moram, C. McAleese, M.J. Kappers, and C.J. Humphreys, "Inclined dislocation arrays in AlGaN/AlGaN quantum well structures emitting at 290 nm." *J. Appl. Phys.* **108**, 123522 (2010).

R. Hao, T. Zhu, M. Haeberien, T.Y. Chang, M.J. Kappers, R.A. Oliver, C.J. Humphreys, and M.A. Moram, "The effects of annealing on non-polar (11-20) a-plane GaN films." *J. Cryst. Growth* **312**, 3536 (2010).

Presentations

Oral contributions at the UK Nitride Consortium (Cork, Ireland, 2010), the International Workshop on Nitride semiconductors (IWN-9, Tampa, USA, 2010) and the 4th Oxbridge Taiwan Science and Technology Symposium (Oxford, 2011).

Poster contributions at the UK Nitride Consortium (Oxford, 2009) and the International Conference of Nitride Semiconductors (ICNS-9, Glasgow, 2011).

Contents

1

Literature Review

1.1 Introduction

High power lighting devices based on InGaN/GaN heterostructures for emission in the green and blue regions of the electromagnetic (EM) spectrum already have surprisingly high efficiencies. However, UV and deep-UV emitters based on AlGaN/AlN heterostructures are very inefficient due to the high lattice mismatch of these films with sapphire substrates, leading to high dislocation densities. This must be overcome to realise the full potential of these devices.

This thesis investigates the structural and optical properties of growth defects and their impact on device performance in UV structures grown by metal organic chemical vapour deposition (MOCVD). Electron microscopy techniques such as transmission electron microscopy (TEM) and scanning transmission electron microscopy with high angle annular dark field (STEM-HAADF) enable the microstructural study of the defects originating from plastic deformation of the heterostructures. The results obtained are compared to those from other characterisation techniques such as cathodoluminescence in the scanning electron microscope (SEM-CL), atomic force microscopy (AFM) and X-ray diffraction (XRD) to interpret the data.

Chapter 1 provides comprehensive background knowledge of the basic materials properties, growth and applications of III-nitrides. Problems currently encountered for nitride devices grown on the *c*-plane of sapphire substrates, and for other possible crystal orientations, will be defined and discussed, with particular focus on the use of Al-containing alloys for UV emitters. Chapter 2 introduces the main characterisation techniques that were used in this work. The basic principles, their importance for the analysis of III-nitrides and their limitations are described. As the majority of the results obtained are TEM-related, TEM sample preparation techniques are also described in detail.

Chapters 3 and 4 are results chapters describing the study of a series of c-plane deep-UV emitting structures: AlGaN epilayers with different aluminium contents grown on thick high quality AlN templates. Several types of defect were found in the AlGaN materials. The structural and optical properties of the defects were investigated. In order to understand the effect of the defects on the quality of the heterostructures, strain analysis based on in-situ wafer curvature measurements was employed to describe the strain relief mechanisms for different AlGaN compositions and to correlate the strain to each type of defect observed in the epilayers.

An atomically smooth template surface is essential for subsequent high quality epilayer and multiple quantum wells (MQW) growth. Chapter 5 presents an improved growth method based on a trimethylaluminium (TMA) predose to enhance the quality and the surface morphology of an Al-polar c-plane AlN template even further. The role that nitrogen plays in the initial growth stage before the TMA predose is examined.

Chapters 6 and 7 describe the investigation of UV emitters based on nonpolar crystal orientations. A series of UV quantum well heterostructures with different GaN multiple quantum well thicknesses and AlGaN barrier compositions were grown on nonpolar GaN templates of low dislocation density using a SiN_x interlayer. The SiN_x interlayer was able to reduce the threading dislocation density but was also found to generate voids with longer SiN_x growth time. The relationship between voids, threading dislocations, inversion domain boundaries and their associated V-defects

and the variation in MQW growth rate is described in this chapter. Cathodoluminescence (CL) and photoluminescence (PL) spectra showed the influence of thickness fluctuations on the optical properties of the MQWs. Spatially resolved monochromatic CL images with corresponding TEM images were used to identify the defect-related luminescence, suggesting that there was a correlation between the yellow band emissions and the density of partial dislocations.

Chapter 8 reviews the work carried out in this thesis and general conclusions are drawn. Suggestions are also made for future work in this field.

1.2 Overview of Solid-State-Lighting

Artificial lighting is one of the most significant inventions in human history. It has become completely integrated into modern civilization and the world could not function properly without it. However, we pay a colossal price to use this resource: 19 % of total global electricity consumption is used for general illumination [1] and unfortunately the conversion of electricity to light is also very inefficient. For incandescent light bulbs, only 5 % of the electricity supplied is converted into visible light and only 20 % is converted to light by energy-saving compact fluorescent lamps [2]. The rising awareness of climate change and our rapidly growing energy consumption demand that we research into more efficient ways of producing light.

Solid-state lighting (SSL) is a technology which uses direct bandgap semiconductors to directly convert electricity into light. It has already shown enormous potential as a more efficient alternative to current artificial lighting and indeed a solid-state device emitting infrared light has been achieved with an electrical-to-optical conversion of 76% external quantum efficiency (EQE) [3]. Current SSL technology consists of three broad categories: (i) inorganic light emitting materials such as group III nitrides, (II) organic materials that are carbon based compounds and (iii) hybrid organic-inorganic materials. All the systems have limits to efficiency for many complex reasons. The research projects at the Cambridge Centre for Gallium Nitride are currently focused

on producing efficient and robust nitride device materials technology that can be employed in areas such as high power lighting and water purification. This requires the use of inorganic materials that have higher tolerance to water and heat damage than the organic materials. Current research in inorganic materials, in particular the group III nitrides (*e.g.* gallium-, aluminium-, and indium nitride and their ternary alloys), has been successfully developed and commercialised for illumination purposes.

Light emitting diodes (LEDs) were discovered decades ago when Holonyak and Bevacqua demonstrated the first infrared GaAs LED in 1962 [4] and Maruska demonstrated the first GaN LED in 1972 [5]. The fabrication of blue LEDs involves the use of wide band gap semiconductor materials. There are three candidates: silicon carbide (SiC, group IV), zinc selenide (ZnSem group II-VI) and gallium nitride (GaN, group III-V). Their energy gaps and lattice constants are shown in figure 1.1.

Silicon carbide has superior thermal conductivity and n-type/p-type doping is relatively simple, so it became the first material to be used in commercialised blue LEDs. However its indirect bandgap leads to low internal quantum efficiency hindering device development.
Zinc selenide is a material with direct band gap of 2.67 eV [6] under ambient conditions. It emits blue light and lattice-matching substrates are available. However, the electrical properties of ZnSe are strongly influenced by the presence of impurities, native defects and extended defects. These result in a high resistivity when the crystal is grown at high temperature, which leads to a low internal quantum efficiency and a short device lifetime.

III-nitrides require a high crystal growth temperature of about 1050 °C, much higher than the 400 °C used for ZnSe materials. They have a high tolerance to high temperatures and their device performance is relatively insensitive to the presence of high densities of crystal defects, so a robust device can be produced. Most importantly, with its direct band gap of 3.4 eV, GaN is considered the most suitable material for developing blue LEDs. Also, as shown in figure 1.1, related nitride materials, aluminium nitride (AlN) and indium nitride (InN) have band gap of 6.2 eV

and 0.6 eV respectively. By varying the ternary alloying ratio, a complete coverage of band gap energy from 0.6 eV to 6.2 eV can be achieved, allowing emissions from red, yellow, green, blue and UV light. Therefore group III-V nitrides are excellent candidate materials for fabricating LEDs emitting at visible wavelengths.

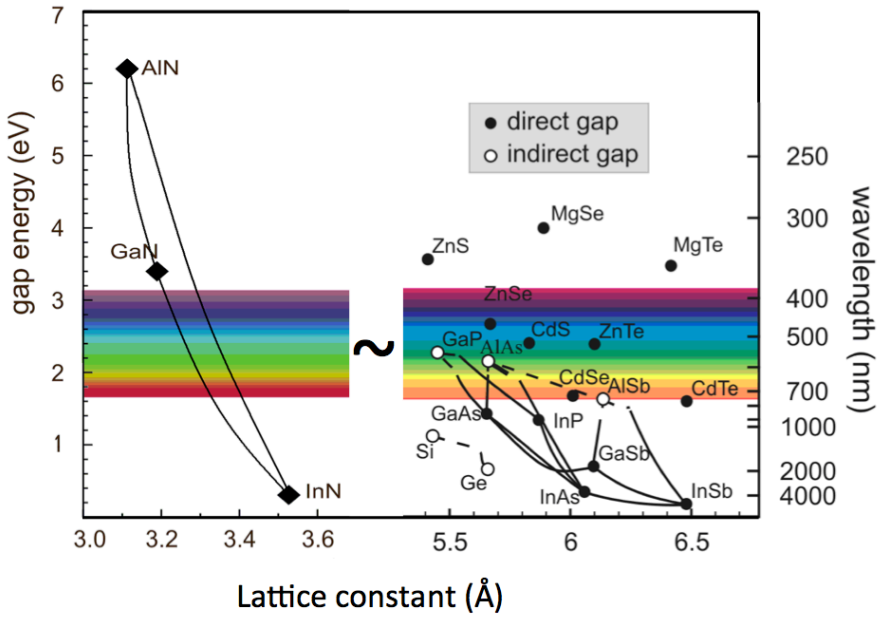

Figure 1.1: Variation of band gap with lattice parameters for various semiconductors. Modified from [1]

However, p-type doped GaN was considered very difficult to produce in the early days [7] and the lack of a substrate with appropriate lattice constants hindered the development of this semiconductor material. The research based on group III-nitride remained slow until 1992 when Akasaki [8] announced the first successful p-n homojunction GaN LED grown on sapphire. Soon after, Nakamura revealed the first blue LED in 1993 [9]. These advances focused more attention into GaN research.

Almost all white LEDs sold today are based on blue GaN/InGaN LEDs coated with a yellow phosphor. The mixture of blue and yellow light creates a cool white light, however, a warm white light is required for office and home illumination purposes. Near-UV LEDs are more efficient than blue LEDs at exciting some phosphors, in particular the red phosphors, which are vital for creating the required warm white light. For the past five to seven years, these UV emitters have advanced from less than

0.1 % external quantum efficiency (EQE) to between 1 % and 10 % depending on the emission wavelength [10]. However, the EQE must be higher before UV LEDs can be employed successfully as a universal lighting resource or for water purification purposes.

1.3 Basics of III-nitride semiconductors

1.3.1 Crystallography

Gallium nitride is a direct bandgap semiconductor. Its large bandgap of 3.4 eV allows it to be widely used in optoelectronic, high power and high frequency devices. GaN can be deposited onto sapphire, silicon or silicon carbide substrates in thin film form. It can be n-doped with silicon (Si) or p-doped with magnesium (Mg). It crystallises into the wurtzite (hexagonal) or the zinc blende (cubic) crystal structure, as shown in figure 1.2. The wurtzite form is stable under ambient conditions and is easier to grow, hence it has been extensively focused on by researchers.

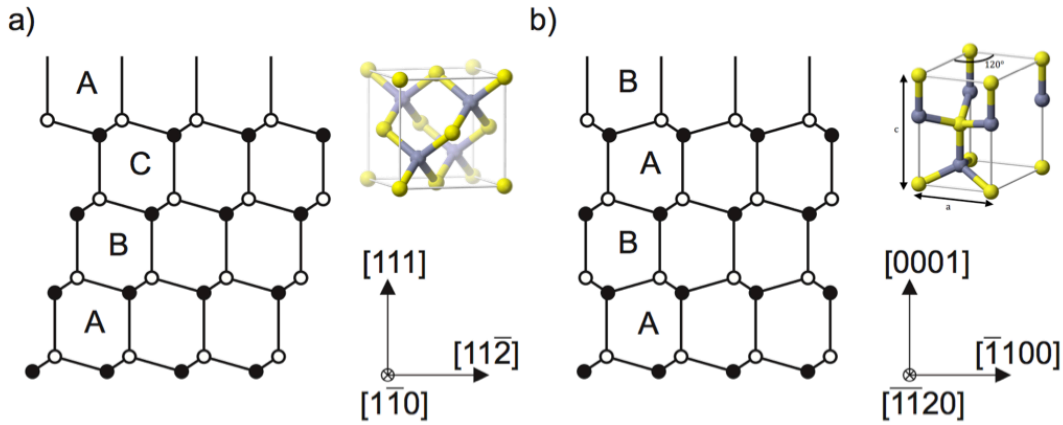

Figure 1.2: Atomic arrangement of a: (a) cubic zinc blende and (b) hexagonal wurtzite lattice (insets showing a unit cell of the structures). Modified from [11]

Atoms in III-nitrides are arranged as two interpenetrating hexagonal lattices in the wurtzite structure. The stacking sequence is …ABABAB… in the [0001] direction,

where one layer (either yellow or grey dots) represents gallium or other group III atoms (Al or In) and the other layer represents nitrogen atoms. The zinc blende structure follows a sequence of …ABCABC… in the [111] direction Bonding in III-nitrides is partly covalent and partly ionic, due to differences in electronegativities between the group III atoms and nitrogen atoms.

The wurtzite unit cell can be described by three lattice vectors a_1, a_2 and c. The former two vectors are the same in length and are separated by an angle of 120°. c is perpendicular to the plane generated by a_1 and a_2. The values of these lattice parameters are summarised for all binary nitrides in Table 1.1.

Table 1.1: Lattice parameters of AlN, GaN and InN. [12]

type	a / nm	c / nm	c/a
AlN	0.31106 ± 0.00003	0.49795 ± 0.00002	1.6008 ± 0.0002
GaN	0.31896 ± 0.00003	0.51855 ± 0.00002	1.6258 ± 0.0002
InN	0.35378 ± 0.00001	0.57033 ± 0.00001	1.6121 ± 0.0001

1.3.2 Polarization

Gallium and nitrogen in the wurtzite crystal structure have different electronegativities, resulting in a dipole parallel to the bond between the atoms along the c-axis. The partially ionic nature of the bonding within the asymmetric wurtzite structure results in a spontaneous polarization (P_{sp}). Thus the c-axis is often termed the polar axis; in other words, the [0001] and [000-1] directions are not equivalent (figure 1.3). The distinction between the two polarities is important because the (0001) and (000-1) surfaces have quite different chemical and physical properties. For instance, the N-polar face decomposes more rapidly in hydrogen at high temperature than Ga-polar face. This strongly affects the surface morphology of AlN films (see chapter 5).

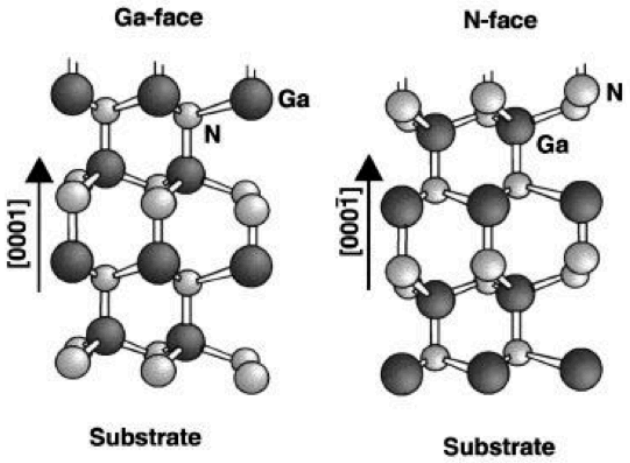

Figure 1.3: Illustration of Ga-polar (left) and N-polar (right) wurtzite GaN [13]

In addition to this spontaneous polarization, there is also a piezoelectric polarization (P_{pz}) arising from the strained crystalline wurtzite films (due to lattice mismatch and thermal mismatch with the substrate). The magnitude and direction of this piezoelectric polarization are directly related to the magnitude and direction of the stress in the layers. This polarization has been calculated to be often larger than the spontaneous polarization. The combination of these two polarizations can lead to detrimental effects on nitride semiconductors as discussed later in section 1.6.

1.3.3 Substrates

The degree of mismatch between substrate and thin film determines the number of defects present in the device. These defects are believed to act as non-radiative recombination centres and limit device performance. Therefore, choosing a suitable substrate is usually the first step in epitaxial growth. The best substrate for GaN-based LED should have the same lattice constant as GaN, and hence, is GaN itself. However high-quality bulk single crystal GaN substrates (larger than 2” diameter wafer) are not cost-effective. This is due to the extremely high vapour pressure of nitrogen (~ 150 kbar) at the GaN melting point (~ 2400 °C) required in order to prevent decomposition and allow bulk crystal growth methods to be used. For this reason alternative substrates have to be used: sapphire (Al_2O_3), silicon carbide (6H-SiC) and more recently silicon (Si). Aluminium nitride (AlN) substrates have also lately

become more popular for UV emitters. Further detail on UV LEDs will be discussed in section 1.5.

Silicon carbide

Silicon carbide possesses certain advantages. It has a comparable lattice constant and thermal expansion coefficient to GaN. It can be doped to achieve electrical conductivity to allow back-contacting and thus to simplify the overall device structure. However, it is expensive and has yet to be proven cost-effective. Furthermore, silicon carbide substrates absorb light at wavelengths below 427 nm and therefore have not been widely used in UV LEDs.

Silicon

The use of silicon substrates has recently gained much attention because large high-quality silicon wafers are readily available. They are cheap and electrically conductive. Silicon processing is already a mature technology which may be integrated with III-nitride device processing. However, cracking and bowing can be caused due to the large lattice mismatch and the large differences in thermal expansion coefficients between GaN on silicon [14]. GaN grown on Si typically has very high defect densities and the small band gap of Si absorbs UV and visible light. Nevertheless, silicon is a promising alternative substrate material.

Sapphire

Sapphire is the most commonly used substrate despite its electrically insulating nature and the large lattice mismatch (~ 16.3 %). This mismatch is relieved by the formation of high densities of threading dislocations (typically 10^9 to 10^{11} cm^{-2}), which is one of the main factors that decrease device performance (see section 1.3.4). However, sapphire substrates are dominating the current LED market owing to several advantages: large high quality sapphire substrates are relatively cheap and readily available on the market. Sapphire wafers are chemically and thermally stable at high growth temperatures and are also transparent to green, blue and UV wavelengths. In addition, nucleation layers can be grown on the sapphire substrate acting as a buffer layer that reduces the density of threading dislocations in the epilayers (see section

1.3.5 for defect reduction techniques). Buffer layers are also used in SiC and Si wafers.

Aluminium nitride substrates

Today, the performance of UV LEDs is fundamentally limited by the high density of dislocations caused by the large lattice mismatch between the nitride heterostructures, and the non-native substrates such as those discussed earlier. Therefore bulk aluminium nitride (AlN) substrates have attracted much attention owing to its close matching of lattice parameter and thermal expansion coefficient with AlGaN heterostructures typical of UV emitters. With these advantages, AlN is believed to be the substrate platform for the next generation of high performance UV optoelectronic devices. Several demonstrations of III-nitride devices grown on AlN substrates have been reported [15][16][17] and have already shown promising results. However the current issues that hinder the large volume production of AlN substrates are the relatively high fabrication cost and the difficulty of producing large high-quality bulk AlN substrates. In addition, current bulk AlN substrates still exhibit significant UV absorption. Nevertheless, high quality AlN substrates are expected to be relatively low-cost and readily available for the market in the next three to five years [18].

1.3.4 Growth

The growth methods for GaN and related materials can be categorised into three different types. These include molecular beam epitaxy (MBE), metal-organic chemical vapour deposition (MOCVD) and halide vapour phase epitaxy (HVPE). Each growth method represents a wide and interesting research focus.

The MBE technique is able to produce high purity thin films but the growth rate is low and the process is expensive due to the use of ultra-high vacuum (UHV). The metal sources are thermally evaporated and reactive nitrogen is (usually) generated by a plasma source, producing molecular beams, which then condense on the substrate where they may react with each other and the reaction product is then deposited as a thin film.

MOCVD and HVPE are both chemical vapour deposition methods for epitaxial growth. Films are grown in the reactor on a heated substrate by introducing vapour phase precursors. The formation of the epitaxial layers is done by final pyrolysis of the chemicals on the substrate surface. MOCVD and HVPE differ in the choices of precursors: MOCVD uses metal-organic compounds (trimethylgallium (TMG), trimethylaluminium (TMA), or trimethlyindium (TMI) as the Ga, Al and In sources) whereas HVPE uses metal-halide precursors (such as $GaCl_3$). In contrast to MBE, this growth takes place in the gas phase at moderate pressures (2 to 100 kPa) instead of a vacuum, producing a relatively high growth rate ~ 1 μm/h and therefore has become a well-established production technology for manufacturing LDs and LEDs. MOCVD growth of nitrides is complex, and many different reactions may occur during the process. However, the basic reaction to obtain GaN is given as follows:

$$Ga(CH_3)_3(g) + NH_3(g) \rightarrow GaN(s) + 3CH_4(g)$$

Although the design of MOCVD reactors can vary extensively, they all share some common features and the major components can be categorised into four subsystems; (a) reactants, carrier gas (b) gas handling system (c) reaction chamber and (d) exhaust. All the samples studied in this work were grown by Dr Menno Kappers or Dr Clifford McAleese in a 6 x 2 inch (capable of growth up to six 2” diameter wafers in a single run) Thomas Swan close-coupled showerhead reactor as shown in figure 1.4. The key advantage of this setup is that the group III and V precursors are injected via separate chambers. Separation of the NH_3 from the metal-organic sources ensures that undesired gas phase reactions are prevented until the chamber itself.

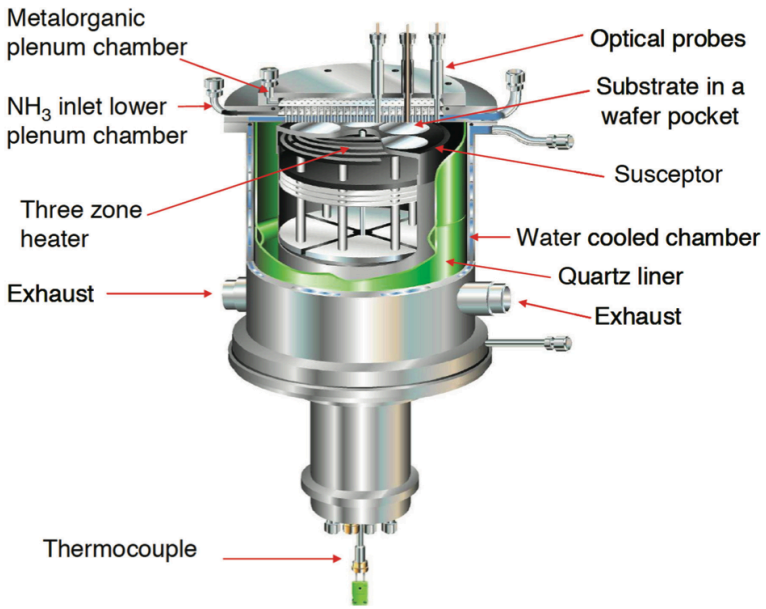

Figure 1.4: Schematic illustration of close-coupled showerhead reactor (courtesy of M.Kappers)

Once the species reactions take place at the growing crystal surface (*e.g.* sapphire, which consists of atomically flat terrace regions separated by steps, figure 1.5), the adatoms diffuse to more energetically favourable kink sites and are incorporated within the crystal lattice. The crystal growth therefore consists of the propagation of steps, and the formation of two- and three-dimensional islands.

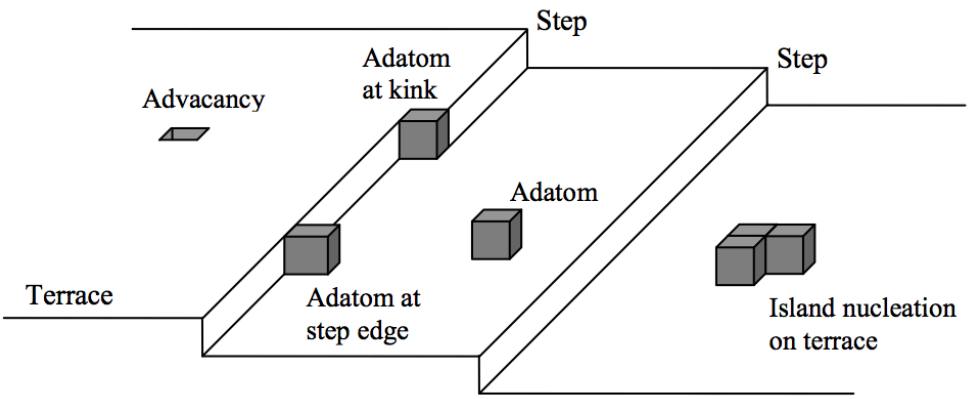

Figure 1.5: Schematic diagram of the growing surface. Adapted from [150].

The thin film growth may be monitored in-situ by a reflectometer, a pyrometric temperature measurement apparatus and by measuring the wafer curvature.

Reflectivity is used to assess whether the film is fully coalesced and the period of oscillation can be used to calculate the growth rate. A typical reflectivity trace is shown in figure 1.6. A lower reflected intensity at the beginning of the growth indicates that the film surface is rough and light reflected from the surface is scattered in all directions. Once the layer thickens and a smoother surface is obtained, the reflectivity intensity becomes higher. Oscillations arise, from the interference between the beam reflected from the film-substrate interface and the film surface, as the film thickens. The film thickness per period of oscillation, D, is given by $D=\lambda/2n$, where n is the refractive index of GaN and λ is the incident wavelength. Constructive interference corresponds to the peaks when film thickness is an integer number of wavelengths. Thus growth rate can be determined from this reflectivity trace.

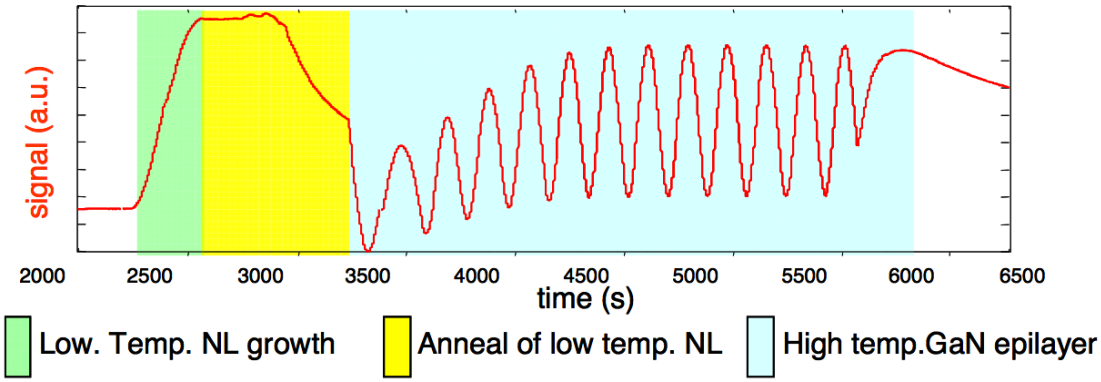

Figure 1.6: Schematic reflectivity trace for a c-plane GaN film showing the different phases of film growth (courtesy of E.J. Thrush)

Thermal and lattice mismatch usually lead to stress in the layers, which can cause cracking (*e.g.* for thick GaN on large Si substrates during cooling down of the wafer) [19]. Stress management is therefore one of the key factors in obtaining high-quality structures. This can be done by in-situ wafer curvature measurements (the EpiCurve TT sensor by Laytec is used for this work), which allows tailoring of the growth parameters. Strain engineering [20] and subsequent strain analysis can be carried out to obtain for additional information by observing defects in nitride heterostructures [21] (see chapter 3 for more details).

In III-nitride MOCVD growth, there are three important parameters used to control the morphology of the film: temperature, pressure and V/III ratio (molar ratio of the

nitrogen containing precursor to the Ga-containing precursor). For instance, three-dimensional (3D) to 2D growth method [22] is often employed for the growth of low defect density templates, where 3D growth (island growth) is promoted initially and these three parameters are altered to then encourage 2D growth for subsequent film coalescence. Throughout this thesis, polar (0001) *c*-plane AlN templates were grown on (0001) *c*-plane sapphire, and nonpolar (11-20) *a*-plane GaN films were grown on (1-102) r-plane sapphire. The growth conditions and additional growth steps (*e.g.* interlayers and nucleation layers) for each sample will be described in the experimental details of the relevant chapter.

1.3.5 Defects

Dislocations:

It is well known that III-nitride devices grown on highly lattice-mismatched substrates have high dislocation densities. These dislocations are termed 'threading dislocations (TDs)' and can be categorised into three different types: for *c*-plane GaN, they are '*a*-type or edge type' (Burgers vector **b** = ⅓<11-20>), '*c*-type or screw type' (**b** = ⅓<0001>), and '*a*+*c* type or mixed type' (**b** = ⅓<11-23>) [23]. If dislocations with line directions parallel to [0001] are considered, then a, c and a+c type dislocations are edge, screw and mixed-type respectively (figure 1.7). If a dislocations line is in the (0001) plane, the a-type dislocations with **b** = ⅓[-1-120] can be pure-screw (dislocation line lies parallel to [-1-120]) or pure-edge (dislocation line lies parallel to [1-100]) in the two alternative orientations also shown in figure 1.7. This is important when analysing the weak beam dark field TEM images as interfacial mismatch strain (discussed in detail in chapter 3) can only be relieved when a dislocation line lying in the (0001) plane has an edge component, in order to accomodate an extra half plane of material.

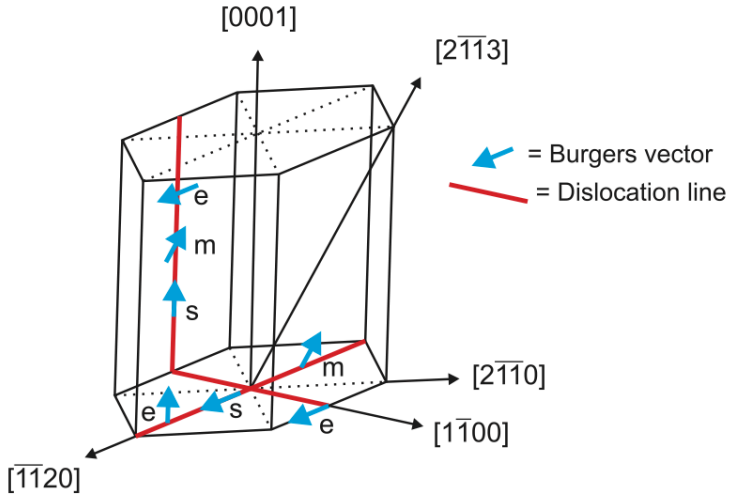

Figure 1.7: Schematic showing different dislocation types in the wurtzite structure. For each line direction, Burgers vectors for the edge (e), mixed (m) and screw (s) dislocation types are indicated. Adapted from [24]

The models that describe the formation of TDs are controversial. Ning *et al*. have suggested that TDs are formed when GaN islands coalesce during growth [25]. If islands coalesced with some degree of tilting (*i.e.* relative misorientations along [0001]), edge dislocations can be created, and similarly coalescence with twisting (*i.e.* relative misorientations in the *c*-plane) giving rise to screw dislocations, and mixed dislocations are created by the combination of tilt and twist. Wu *et al.* [26] supported this island coalescence model with further transmission electron microscopy (TEM) studies. However, Narayanan *et al.* [27] presented evidence against this model, as they have shown that edge and mixed TDs were already present in the islands before they were fully coalesced. Instead, Narayanan suggested that the TDs were created from the defects occurring near the layer/substrate interface. The dissociation of a Shockley partial (**b** = ⅓[-1100]) to another Shockley partial (**b** = ⅓[0-110]) with a basal plane dislocation that is parallel to the substrate interface can thread to the surface leading to edge dislocations. On the other hand, the formation of two Frank faults (½[0001]) can lead to screw dislocations. This model where TDs do not form at coalescence boundaries was also supported by Oliver *et al.* [28] where AFM was used to examine the dislocations on partially coalesced silane treated films [29] and the dislocation density at the coalescence boundaries was found to be unchanged relative to overall surface dislocation density.

Although there are contradictory views on the origin of threading dislocations, it is also worth mentioning that the further studies by Narayanan [30] suggested that TD generation by island coalescence is still possible under certain growth conditions. This model is also supported by Moram *et. al.* [175] where SEM-CL and AFM studies showed that the lateral length scales of the island network, at any stage of film coalescence, do not match with the lateral length scales of TD-free regions, suggesting that the dislocations in the MOCVD grown GaN on sapphire films are generated primarily in the nucleation layer and not by island coalescence.

In addition to Narayanan's theory, misfit dislocations are also believed to generate threading dislocations in III-nitride materials. The lattice mismatch created between the substrate and layer interfaces is initially accommodated by elastic strain. Once a critical film thickness is reached, more energetically favourable misfit dislocations [31] are created to compensate for the differences in the lattice constants. These dislocations are categorised as 'edge-type' dislocations (*i.e.* dislocation line is perpendicular to its Burgers vector). The Frank and van der Merwe formula [32] was proposed in 1962 and attempted to predict the critical thickness. It was done by equating the energy contained in the misfit dislocation network with the elastic energy contained in a strained layer of a particular thickness. Later in 1974, Matthews and Blakeslee [31] reconsidered the theory and obtained a similar formula as van der Merwe but allowed consideration of the kinetics of the process. However a recent literature survey performed by Holec *et al.* [33] showed that most of the current models for critical thickness predictions were based on isotropic cubic materials (*e.g.* GaAs) and therefore much effort has since been put into developing a theoretical model specifically for wurtzite III-nitride materials [34][35][36].

Stacking faults:

As discussed earlier, perfect dislocations may split into two partial dislocations (with **b** = ⅓<1-100>, **b** = ½[0001] or **b** = <2-203>) as this lowers the total energy. They must border a two-dimensional defect, typically a stacking fault [37]. For this reason, they are generally found terminating stacking faults.

There are three types of basal plane stacking faults (BSF) that can separate partial dislocations. Stacking faults produced by vacancy agglomeration are termed 'intrinsic I_1, I_2 and I_3 type' and interstitial agglomeration is termed 'extrinsic E type'. Prismatic stacking faults (PSF) can also be found on {11-20} prismatic planes [38].

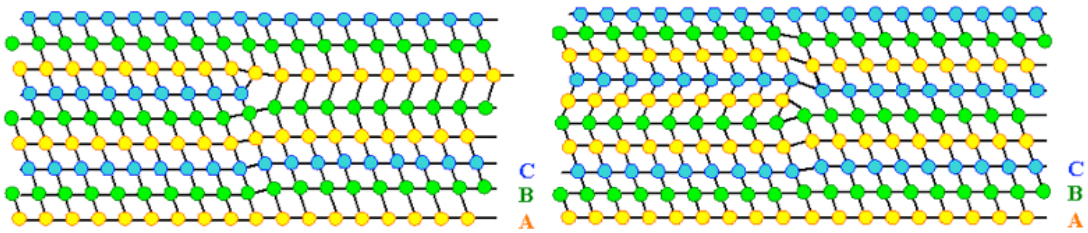

Figure 1.8: Schematic (left) shows an intrinsic stacking fault, where a C-bilayer is removed (stacking sequence changed from …ABCABC… to …ABCABABC…). (right) shows an extrinsic stacking fault, where an extra A-bilayer is inserted (stacking sequence changed to …ABCABACABC…). Modified from [37].

I_1 type fault occur with one rotation of the stacking sequence, and are created when inserting or removing a basal plane, followed by shear along ⅓<10-10>. I_2 type faults are created when a perfect dislocation is split into partial dislocations (the occurrence of this reaction is determined by the balance of stacking fault energy and the repulsive forces between the partial dislocations). I_3 type faults also occur, but these are essentially a double I_1 fault, which subsequently returns the material to its original stacking configuration, so they are not bound by any type of dislocation. E type faults are created when an extra basal plane is inserted (as shown in figure 1.8).

For nonpolar and semipolar III-nitride films, it has been observed that stacking faults and their associated partial dislocations are present in high densities [39]. BSFs may act like quantum wells, changing the band structure and affecting the light emission [40] (see Chapter 6 for further details).

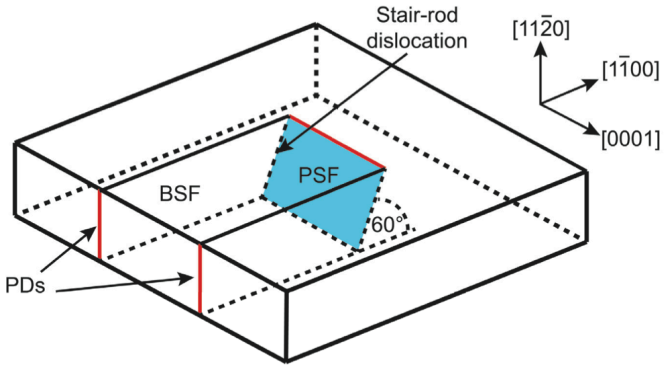

Figure 1.9: Schematic of stacking faults in a-plane GaN grown on r-plane sapphire. Adapted from [38].

Effect of defects

It is well known that defects are very detrimental to the performance of most semiconductor devices [41]. In general, it has been proven that the higher the dislocation densities, the poorer the optoelectronic performance. For instance, a green LED made from GaP has a greatly reduced efficiency when the TD density is above ~ 10^5 cm^{-2}, and when TD density is above ~ 10^6 cm^{-2} there is no light emission at all [41]. However for GaN-based LEDs that contain more than 10^{10} cm^{-2} TD density, high external quantum efficiency (EQE) can still be achieved. Therefore, the effect of dislocations in GaN has undergone much debate.

For light emitting diodes, on applying a forward bias, electrons and holes travel through the materials and recombine with each other to emit photons. This process is called radiative recombination in the LED devices. However, there is also non-radiative recombination that releases heat energy instead of photons. It decreases the internal quantum efficiency of the devices and in addition increases the operating temperature via Joule heating which has a deleterious effect for the device.

Rosner *et al.* [42] and Sugahara *et al.* [43] suggested that these dislocations were non-radiative recombination centres by showing lack of light emission from the same TD in cathodoluminescence (CL) in conjunction with AFM images and plan-view TEM images. The presence of TDs was confirmed in AFM and TEM and they appeared as

dark spots in CL measurements, which indicated that they do not luminesce. Further studies by Katona *et al.* [44] have also agreed on the findings by studying CL in epitaxial lateral overgrown (ELOG) materials. However, these results do not necessarily confirm that dark spots are indeed caused by non-radiative recombination, as they could be due to charged dislocations [176].

Lester *et al.* suggest that dislocations do not act as non-radiative recombination centres [45] because the non-radiative recombination model does not explain the high external quantum efficiency only observed in GaN but not in other materials such as GaAs. The high EQE was thought to be the result of carrier localisation in quantum wells, which was due to the indium clusters observed in TEM. However, this explanation was later greatly disputed, as indium clustering is now considered to be an artefact produced by beam damage in the TEM [46]. A more recent explanation of carrier localisation is the fluctuation in quantum well width, which is also discussed in chapter 6. Nevertheless, determining the properties of defects and their effects in GaN-based devices is still an on-going investigation and this must first be understood in order to develop techniques to eliminate these dislocations efficiently.

1.3.6 Defect reduction methods

Several research groups have developed defect reduction techniques that are beneficial for improving III-nitride device performance. This section aims to review these techniques, which can be classified into two categories: in-situ and ex-situ defect reduction methods, and which have mainly been used for GaN so far. For the in-situ methods, defect reduction is accomplished within the growth chamber. This involves the nitridation of sapphire substrates, the use of buffer layers and interlayers, and the variation of growth conditions. For the ex-situ methods, defect reduction requires additional treatments outside the growth chamber, for instance, epitaxial lateral overgrowth (ELOG) and pendeoepitaxy (PE).

In-situ defect reduction methods:

- **Nitridation of the sapphire substrates**

Nitridation involves the exposure of the substrate to NH_3 at 1050 °C before epitaxial growth. This creates several AlN layers on top of the substrate, which provide a closer lattice match to the GaN layer which is subsequently grown, and hence lower the dislocation density of that layer [47].

- **Use of buffer layers**

The buffer layer is mostly used to improve the substrate wetting and also to provide nucleation sites for the subsequent main growth layers (also known as two-step growth). There are two commonly used buffer layers in MOCVD growth: (i) Low temperature GaN nucleation layers are grown between 450 °C and 600 °C, typically with a thickness between 25 and 35 nm [39]. This layer permits growth of a subsequent high quality film, possibly due to the evaporation and re-deposition of GaN at higher temperatures, which promotes step flow growth for the high temperature layer [30]. (ii) AlN is another successful buffer layer that is grown at ~600 °C with an optimum thickness between 50 and 100 nm [48]. AlN buffer layers also provide nucleation sites for the subsequent GaN layer growth and are able to produce lower TD density films. These 'two-step' growth methods have now become a standard for the growth of GaN on highly mismatched substrates.

- **Use of interlayer**

The in-situ deposition of a sub-monolayer quantity of SiN_x using silane and ammonia has been shown to be effective at dislocation reduction for c-plane GaN [49]. The SiN_x interlayer does not wet the underlying III-nitride films and acts as a nano-mask and blocks the dislocations. Some dislocations that propagate through the gaps between SiN_x islands in the mask may be bent (see chapter 6) and annihilate with one another or terminate at voids (figure 1.10). TD density reduction by two orders of magnitude to ~10^7 cm^{-2} has been achieved by the use of a relatively thick single SiN_x interlayer [38] (see also chapter 6). A ScN interlayer has also been shown successfully to reduce the TD density down to ~10^7 cm^{-2} in c-plane material [38]. The Sc metal layer is deposited ex-situ and then annealed in ammonia to form a ScN interlayer. The dislocation reduction mechanism is believed to be similar for both types of interlayers.

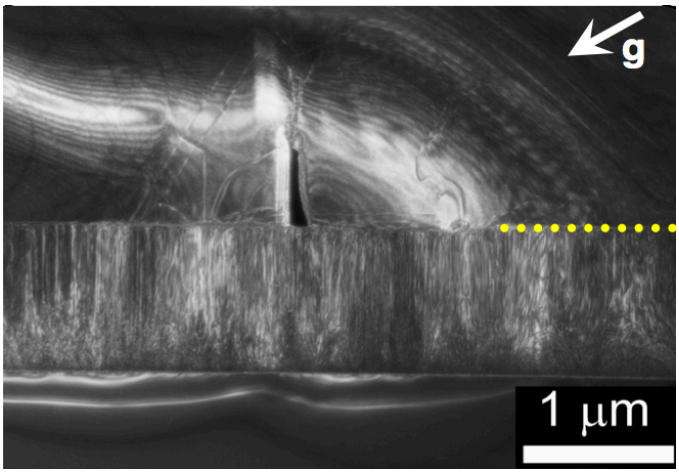

Figure 1.10: Cross-sectional TEM image of a sample with SiN interlayer (indicated by yellow dotted line) showing a significant reduction in TD density. [38]

- **Variation in growth conditions**

It is possible to grow the initial GaN layer with either '2D' or '3D' growth methods. 2D growth forms flat GaN layer surfaces, which involves using a low temperature GaN buffer layer, as mentioned in the previous section. 3D growth involves the formation of an islanded morphology. It is worth mentioning that a 3D growth method can be considered as an in-situ method of ELOG as GaN grows laterally from the island nucleation sites and coalescences to form films with lower TD densities. This is due to the dislocations bending at the island facets [50]. The dislocation then either meets and annihilates with another one or is terminated by the voids in between the coalescence boundaries resulting in dislocation-free regions in the upper part of the film. It is also worth mentioning that delayed coalescence time and control of island sizes may also influence the TD density. For instance, a lower V/III ratio delayed the island coalescence process, permitting more lateral growth of GaN layers and further reducing the TD density [51]. Also, larger islands were shown by AFM [28] and TEM to have lower TD density.

Ex-situ defect reduction methods

- **Epitaxial lateral overgrowth (ELOG)**

A reduction in the dislocation density from 10^{10} to 10^{8} cm^{-2} may improve the optical and electrical properties of the device [1]. A major leap forward came at the end of 1997 when the epitaxial lateral overgrowth technique (ELOG) was developed, which greatly reduces the dislocation density. The ELOG template can be patterned with SiO_2 or SiN_x masks on top of previously grown GaN layers. These masks are etched into stripes by photolithography, where the stripes are separated by a certain distance, allowing the GaN layers to grow through the gaps (termed 'window' regions) and then grow laterally over the SiO_2 or SiN_x stripes (termed 'wing' regions) until they coalesce and form a continuous film (figure 1.11). The dislocations in the preceding GaN layer either progress through the window regions or stop beneath the masks. Therefore the lateral growth on top of the wing regions can contain very few TDs in these areas (2 x 10^{7} cm^{-2}) [177]. The ELOG structure contains regions of both high and low densities of dislocations, but has a lower overall dislocation density.

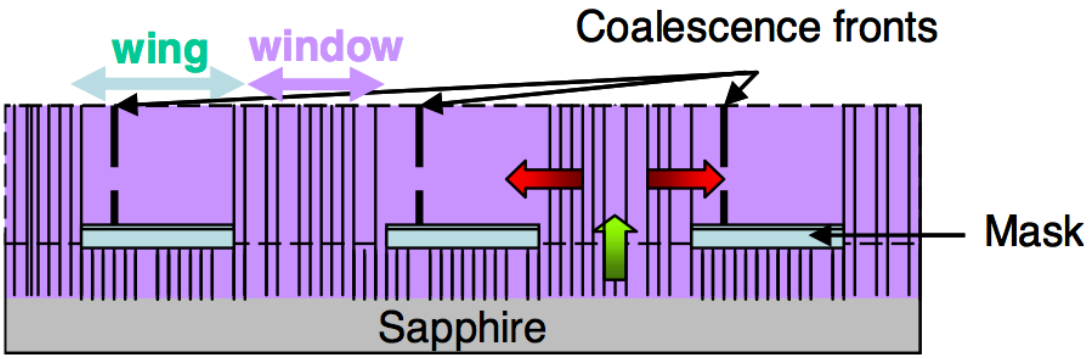

Figure 1.11: Schematic of the ELOG process for a nonpolar layer. Adapted from [38].

The quality of the ELOG material is determined by several factors including reactor temperature and pressure, the V/III ratio and the carrier gas composition. Controlling these variables is a further interesting research topic [52].

The general ELOG technique is known as 1-step ELOG where constant growth conditions are used. Another technique known as 2-step ELOG can further decrease the dislocation density. This is achieved by altering the growth conditions so that vertical growth is favoured over lateral growth, which leads to the formation of pyramidal stripes. The facets of the pyramid promote the bending of TDs as discussed earlier in 3D growth and produce a smaller 'window' region, which results in even

lower overall dislocation density (5 x 10^6 cm^{-2} TD density has been reported at the coalescence boundary regions) [50]. Likewise, more reduction steps are possible (termed 'multi-step' ELOG) and a dislocation density as low as 7 x 10^5 cm^{-2} has been demonstrated [53]. However, the photolithography step for masking is time-consuming and expensive and hence the fabrication becomes complicated as more steps are involved.

Pendeoepitaxy (PE) is another type of ELOG involving etching down to the substrate prior to applying masks on top of the GaN stripes. Voids are produced below the coalescence regions, which provide the laterally grown layers with lower dislocation densities. This method is able to achieve low dislocation densities similar to 2-step ELOG but only one photolithography step is required.

1.4 Light emitting diodes

Light emitting diodes are based on p-n junctions; charge carriers (electron and holes) are injected from the electrodes by application of a forward bias. These carriers then recombine across the band gap and produce photons. For the QW LEDs, charge carriers flow into the active regions from electrodes and are confined to the quantum wells (which are made of a lower band gap material), increasing the overlapping of electron-hole wavefunctions and leading to more efficient radiative recombination. The emission wavelength is dependent on the energy band gap of the material used in the active region of the device and the desired wavelength can be obtained by varying the thickness or composition of the quantum wells.

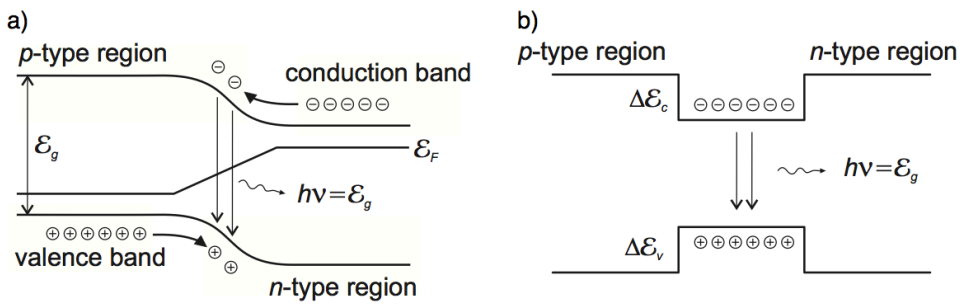

Figure 1.12: Schematic of operating principles of two basic kinds of LEDs: (a) a p-n junction based LED and (b) a quantum well based LED. [33]

A typical LED structure (Figure 1.13) has a p-type surface layer that is highly doped for an ohmic contact. Below this lies the active region often containing quantum wells, and an n-type layer. A buffer layer of GaN or AlN is used to accommodate the lattice mismatch with the sapphire substrate. In between QWs are barrier layers, which provide energy barriers on either side of the wells to prevent charge carriers escaping from the QWs.

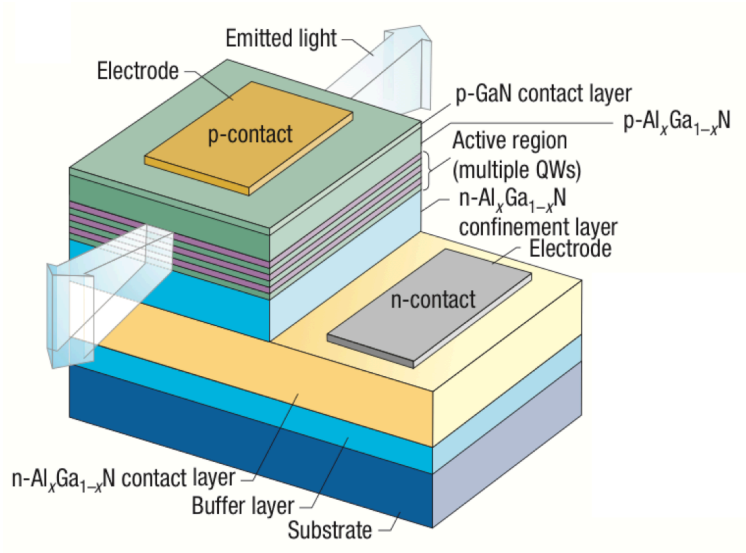

Figure 1.13: Schematic of a near-UV (using AlGaN buffer layers) LED structure [10].

The performance of an LED device is referred to as the external quantum efficiency (EQE), which is the product of the internal quantum efficiency (the proportion of all electron-hole recombination in the active region that are radiative and produce photons), the current injection efficiency and the extraction efficiency (the number of photons emitted from the LED per photon generated in the active region). Figure 1.14 shows the current best external quantum efficiencies achieved in GaN based UV LEDs by research groups across the world. Many challenges still remain to be solved to achieve UV LEDs with EQE values comparable to those of visible LEDs. The reason for decreasing efficiencies at shorter wavelengths is mainly due to the lattice mismatch of substrates with high aluminium content alloys, which will be discussed in more detail in section 1.5.

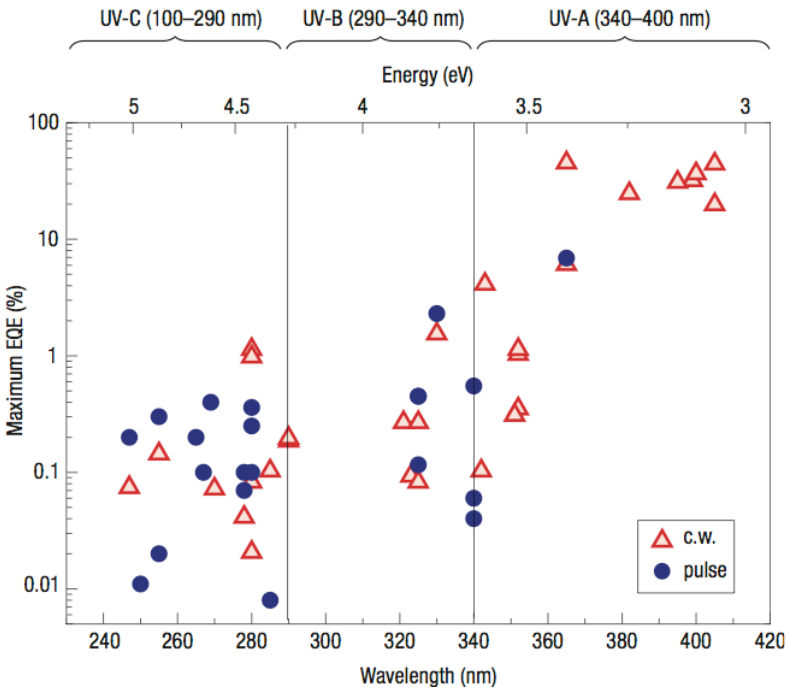

Figure 1.14: Summarised plot of the maximum EQE reported for c.w (triangles) and pulsed (circles) operation of UV LEDs by different research groups [10].

1.4.1 General problems with III-nitride LEDs

- **Quantum-Confined Stark Effect (QCSE)**

The performance of light-emitting devices based on conventional polar (c-plane) GaN film suffers from a phenomenon termed the 'quantum-confined Stark effect' (QCSE) [54] due to a spontaneous polarisation and a piezoelectric polarisation in the materials (see section 1.3.2). Spontaneous polarisation occurs because of the non-centrosymmetric orientation of gallium and nitrogen atoms along the [0001] direction in the wurtzite GaN structure. Piezoelectric polarisation occurs when the thin film is strained, such as for lattice-mismatch induced strains between the quantum wells and barriers.

For c-plane InGaN/GaN devices, the QWs are under compression due to InGaN having a larger lattice parameter than GaN resulting in much larger piezoelectric polarisation and a net polarisation is created along the [0001] c-axis direction. On the other hand, AlGaN/GaN devices may have relaxed QWs but the spontaneous polarisation is high and again, a net polarisation along [000-1] is created.

This net polarisation creates an internal electric field across the wells [55][56], resulting in band bending, which decreases the electron-hole wavefunction overlap and increases the radiative recombination time (*i.e.* lower radiative recombination rates). This consequently decreases the quantum efficiency of the device and also red shifts the emitted wavelength, due to the smaller bandgap (see figure 1.15 a). The QCSE can be potentially reduced or eliminated with alternative growth directions such as nonpolar or semipolar planes (figure 1.15 b), more details in section 1.6.

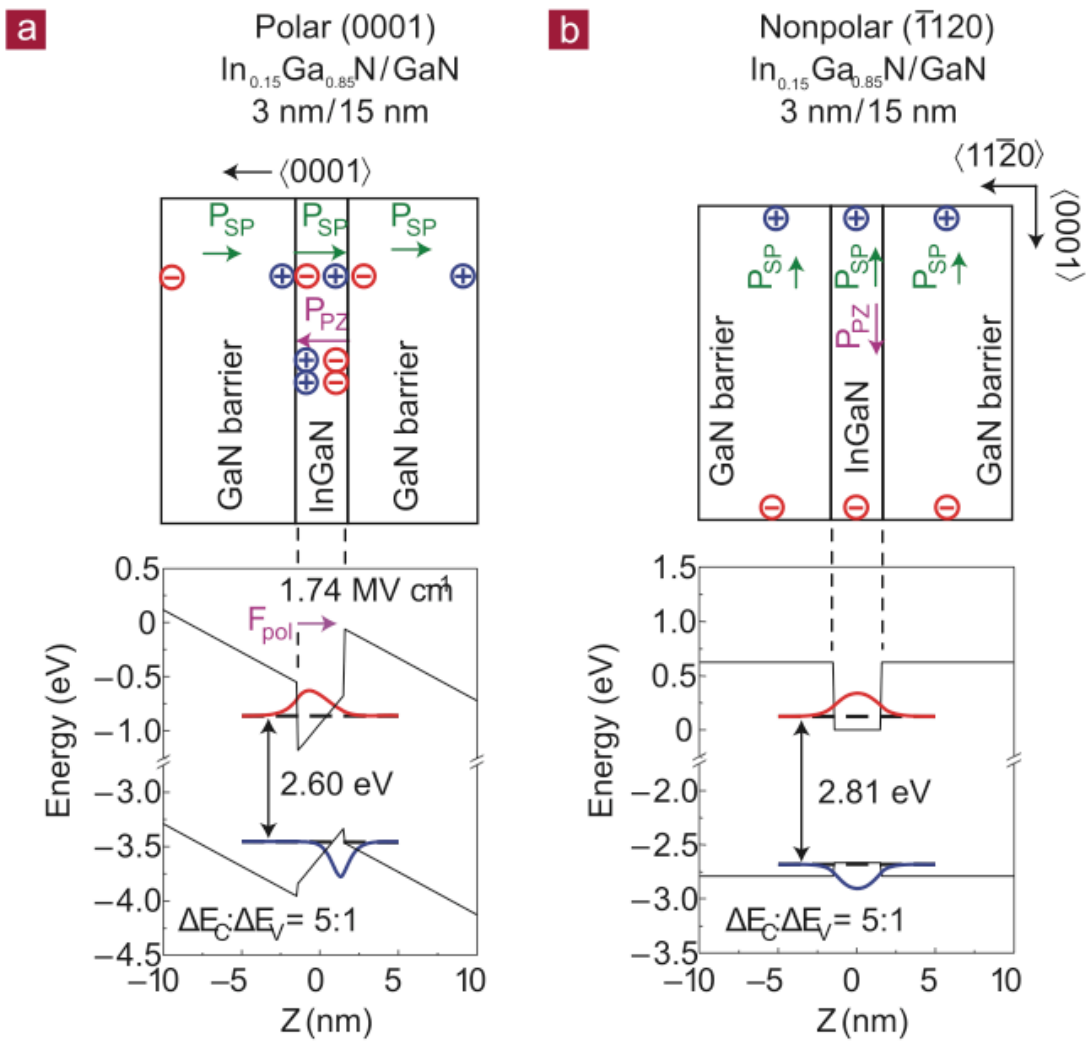

Figure 1.15: Schematic demonstrating the quantum confined Stark effect (QCSE). (a) Net polarisation in Ga-face (0001) material causes an electric field across a 3 nm InGaN QW. (b) No net polarisation in the growth direction for nonpolar material. Reproduced from [24].

Although the emission wavelength is initially red shifted, there is a subsequent blue shift as the drive current increases, which is due to screening of the internal electric fields by the increasing charge carrier density. This variation in emission wavelength is detrimental to devices such as white LEDs.

- **Current crowding**

Most LEDs are fabricated on insulating substrates such as sapphire or AlN (for deep-UV emitters). Therefore the electrical contacts have to be attached on one side of the device (figure 1.13). The attainment of high doping levels in n-type (Si-doped) and p-type (Mg-doped) AlGaN is more difficult than in GaN due to the higher dopant ionization energies, a consequence of the larger band gap. This low doping level makes the AlGaN layers less electrically conductive. This leads to a problem of uneven current injection into the active region caused by the higher resistivity of the electrode contacts to the AlGaN layer. This phenomenon is termed 'current crowding' (*i.e.* some regions have very high current densities) [57]. In addition, higher resistivity also leads to Joule heating when using higher operating voltages. Therefore, additional thermal management efforts have to be employed to cool the device. However, a promising solution to this problem has been proposed in the literature. For example, a micro-pixel design was demonstrated, which provided a more uniform current injection distribution [58].

1.5 Ultraviolet light emitting diodes

Today, 'visible' light emitting device technology is approaching its maturity and GaN-based white LEDs can already be found in many applications such as stadium television displays, traffic lights, flashlights and vehicle lighting. Many research groups are shifting their focus towards shorter wavelength UV GaN-based devices that can be employed in 'non-visual' applications, such as Blue-ray™ Discs, sterilization of water and other substances, and biomedical instruments [59]. These applications for UV LEDs together with the potential of producing warm white lights with red phosphors will create a promising new market that will be worth billions of dollars [18].

The UV region (10-400 nm) in the electromagnetic spectrum is categorised into four sub-regions: UV-A, UV-B, UV-C and vacuum UV (figure 1.16).

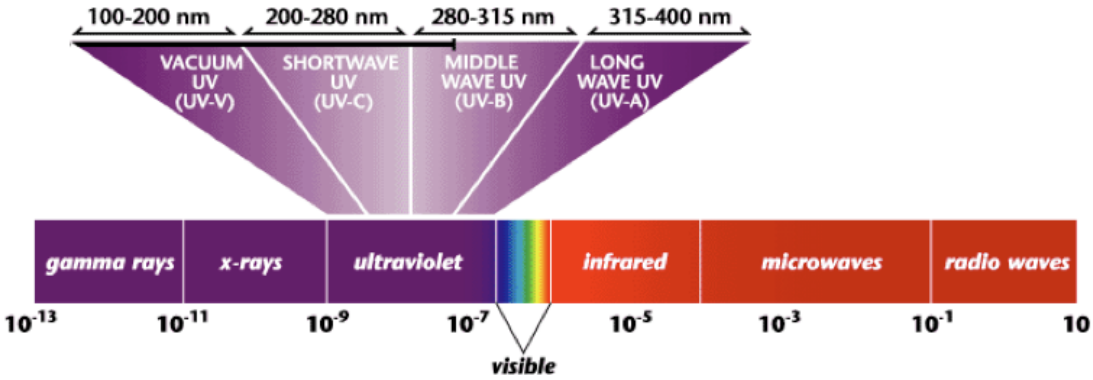

Figure 1.16: An EM spectrum showing the UV sub-regions. Modified from [1].

According to the band energy diagram shown in figure 1.1, the wavelength of III-nitride materials spans the entire UV-A, UV-B and UV-C regions from about 200 nm for AlN to 400 nm for InGaN. Thus, in theory III-nitrides can be excellent candidate materials for fabricating these UV devices. Their existing and potential future applications are briefly summarised in Table 1.2.

Table 1.2: Existing and potential future applications for UV LEDs [10].

UV-A	UV-B and UV-C
• Counterfeit currency detection • Industrial curing • Photocatalytic deodorizing • Pump sources for phosphors for white light LEDs	• Purification of air or water microbiological contaminants. • Biological weapon detection • Treatment for skin disorders

UV-A devices are relatively easy to manufacture owing to the similarity with growth technology for existing visible LEDs. These devices have already found a wide range of applications, especially in the industrial curing sector [60]. A UV LED with an output power of over 5 W at 365 nm has already been commercialised [61].

The Earth's ozone layer is a strong absorber for deep UV (UV-C and below), so very little can penetrate through the atmosphere and arrive at the Earth's surface.

Biological species therefore do not develop any resistance towards deep UV, and hence deep UV is commonly used to inactivate microbiological contaminants in air and water. It is possible to produce UV-B and UV-C wavelengths artificially, but the existing UV mercury lamps are expensive, fragile and inefficient [60]. For this reason, UV LEDs are soon expected to replace these lamps and will also find many other applications, especially in portable products. It is predicted that UV-C LEDs will contribute to half of all UV-LED sales by 2015 [18] owing to the crucial air and water disinfection market and by 2017 they will account for over two-thirds of the total UV LED market [18].

Although several LED manufacturers are strongly targeting the UV devices market, significant improvements over technical and economic challenges such as lifetime, efficiency and cost (UV-C LEDs are currently at least 50 times more expensive than UV-A LEDs [18]) are required before they become truly cost-effective.

1.5.1 Specific problems with UV LEDs

- **Long-wave (UV-A)**

In the UV-A (long-wave) region, the devices can be sub-divided into the AlGaN system and the InGaN system. For a UV emission wavelength that is longer than 365 nm, InGaN quantum wells are normally used, whereas AlGaN and GaN can be used for wavelengths between 365 nm and 330 nm.

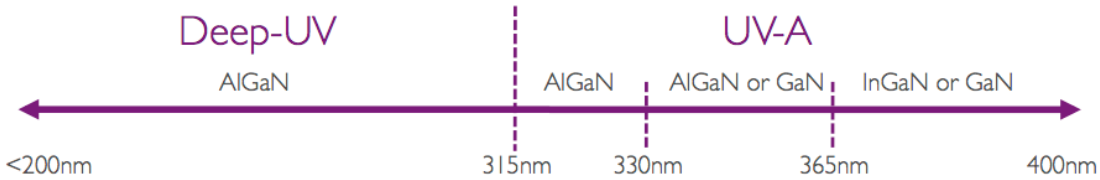

Figure 1.17: Typical quantum well materials used in the UV region.

InGaN UV-A devices with >365 nm emission wavelength have a mature device technology due to their similarity with blue LED technology. 330-365 nm UV devices can also be obtained with narrow GaN quantum wells with AlGaN barriers but the large lattice-mismatch between the different materials can impinge on the device performance. In the case of 315-330 nm emission ranges, AlGaN quantum wells are

required and several issues start to arise. Although several groups have been using other approaches, such as $Al_xGa_{1-x}N/Al_yGa_{1-y}N$ multiple quantum wells [62] or double-heterostructure active layers [63] in an attempt to achieve similar efficiencies to InGaN devices, the emission efficiency is still lower for AlGaN devices.

The origin of the relatively high efficiency of InGaN QWs compared to AlGaN is controversial. High dislocation densities are believed to cause low device performance. However, as mentioned earlier, III-nitride LEDs based on In-related alloys still emit intense light despite the high dislocation densities occurring in the material. The original explanation was based on the formation of indium-rich clusters in the InGaN quantum wells. These clusters have a smaller bandgap than GaN, which localises electron and hole carriers so that they are not able to diffuse to the surrounding dislocations, resulting in lower non-radiative recombination rates. The evidence was supported by electron microscopy [64][65] and thermodynamic calculations [66]. However, this hypothesis has been questioned. It has been observed that the indium-rich clusters were formed by electron beam damage inside the electron microscope, and a clear correlation between electron beam dosage and the amount of clustering was observed [46]. This indicates the possibility of clustering being just an artefact of the observation techniques.
More recent work suggests that the intense light emission in InGaN-based devices might be due to monolayer-height interface steps on the InGaN quantum wells [67] and a recent 3-D atom probe study has confirmed that this phenomenon occurs [68]. 3-D atom probe also confirms that the InGaN is a random alloy with no gross In-rich clusters. These interface steps are believed to produce sufficient carrier confinement at room temperature. An additional carrier localisation mechanism is due to statistical fluctuations in the In content of the random InGaN alloy. Nevertheless, more studies are required in order to understand the fundamental physics in the active regions of both visible and UV LEDs.

- **Mid- and short-wave (UV-B and UV-C)**

Mid- and short-wave UV devices are sometimes termed ‘deep-UV’ devices. As mentioned earlier, these deep UV devices are of great interest in many applications but have yet to be proven cost-effective due to several key challenges that are

currently the subject of intense research: (i) metal contacts absorb light emitted by QWs. (ii) It is difficult to p-dope AlGaN due to the much higher dopant ionisation energies. Therefore p-GaN has to be used instead but it has a smaller band gap than the active region, which means that it absorbs the light emitted from the quantum wells and causes low light extraction efficiency. Several groups [69][70] have demonstrated that by decreasing the defect densities in devices with p-GaN layers, the devices are able to output reasonable powers despite the absorbing nature of the substrates. (iii) UV-transparent and low defect density AlN and AlGaN materials are essential to produce high quality UV LEDs with emission wavelengths below 365 nm. AlGaN films with high Al contents are necessary to achieve the required bandgap for deep UV wavelengths (see figure 1.17). However high Al content AlGaN is considerably more difficult to grow than GaN, because aluminium adatoms have a significantly lower surface mobility than Ga adatoms at the growth temperature. During growth, these Al adatoms would not be able to diffuse toward the energetically favourable lattice steps or kinks to create a smooth layer-by-layer growth front [61] (see figure 1.5). Consequently, a rougher initial growth surface is created with higher dislocation densities (~ 10^{10} – 10^{11} cm^{-2}) as the islands coalesce.

There have been several attempts to overcome this high-Al content issue: Pulsed atomic layer epitaxy (PALE) is a technique in which the flow rate of precursors is modulated during growth [71]. This could improve the mobility of aluminium adatoms to achieve a more uniform surface. A similar approach was used for the samples studied in chapter 3 and chapter 5, where a TMA pre-dose step was involved prior to the thin film growth to create an Al-polar growth surface, resulting in a much smoother template surface and lower TD density compared to the conventional (mixed polarity) AlN growth. Another approach in the literature involves the use of much higher temperatures (~ 1500 °C) during growth. A lower dislocation density of ~ 10^{6} cm^{-2} has been reported for AlN layers grown on 6H-SiC [72].

Strain is also an important factor that should be addressed when fabricating these high-Al content III-nitrides. The large lattice mismatch and thermal expansion coefficient mismatch with GaN template and sapphire substrate easily results in cracking of the layers, especially for the thick n-type AlGaN layer. One approach is

the use of AlN/AlGaN superlattices (SLs) as buffer layers [73]. This has shown promising results in reducing the cracking of thick AlGaN layers on top of sapphire substrates. In fact, the use of these buffer layers together with the PALE growth technique and other packaging improvements (*e.g.* flip-chip design) facilitated the development of the first high quality UV-C LEDs with an external quantum efficiency (EQE) higher than 1% [74].

1.6 Alternative crystal orientations

Most of the III-nitride research and device development so far has been based on the growth along hexagonal wurtzite (0001) c-plane. As mentioned previously, this leads to the quantum-confined Stark effect, which ultimately decreases the internal quantum efficiency and causes a red shift.
One solution is to grow the cubic zinc blende form of the material, where the centrosymmetric crystal structure eliminates any possible polarisation. However, this method is not widely accepted due to cubic III-nitrides being metastable phases, requiring MBE growth.

A potential solution to the QCSE problem is growth on III-nitride films orientated along crystallographic directions where the piezoelectric field is small or zero, such as the nonpolar (11-20) or semipolar (11-22) planes. Much research has now been focused on films oriented in these directions, since the publication of the first report of successful nonpolar GaN growth in 2000 [75] and the development of the first nonpolar and semipolar LEDs in 2004 by Chakraborty *et al*. [76].

- **Nonpolar**

Nonpolar GaN grown on (11-20) or {1-100} can theoretically lead to shorter radiative recombination times and thus higher device emission efficiency. Since nonpolar GaN is in a stable structure (hexagonal wurtzite), its growth is not limited to MBE and therefore higher growth rate MOCVD and HVPE growth methods can be used, which provide the ability to fabricate more complex and thicker films.

Nonpolar GaN can either be grown with 'a-plane' {11-20} or 'm-plane' {1-100} orientations. Both directions are perpendicular to the polar c-axis, which in this case lies in the growth plane, so films grown in these orientations are free from internal electric fields. This can be particularly beneficial for the device performance as electron-hole wavefunctions can remain overlapped resulting in high recombination efficiencies and there is no screening effect as the driving current increases, ensuring no shift in the emitted wavelength. This phenomenon has been confirmed in the literature [38] and also demonstrated in the photoluminescence data obtained in this work (see chapter 6).

'*a*-plane' GaN can be grown on substrates such as r-plane (1-102) sapphire, *a*-plane SiC or (001) $LaAlO_3$ and 'm-plane' GaN can be grown on m-plane SiC, (100) $LiAlO_2$ or bulk m-plane GaN. Both have been demonstrated successfully [38].

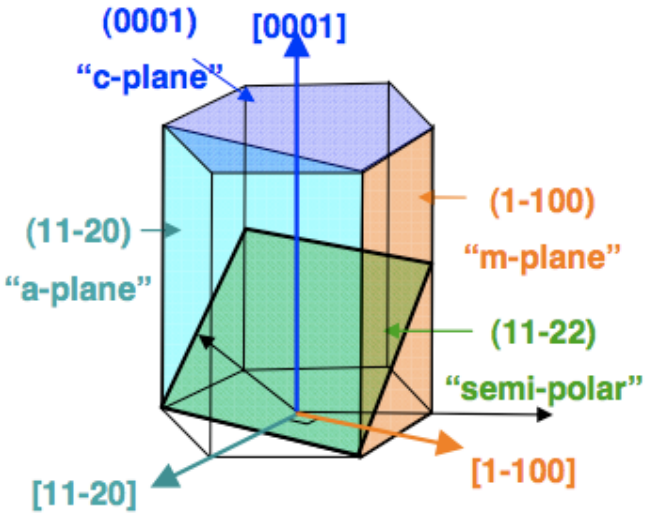

Figure 1.18: Schematic of nonpolar and semipolar planes relevant for experimental growth. Reproduced from [38].

The idea of nonpolar growth was reported more than thirty years ago [160], but unfortunately initial films had surfaces too rough for device growth. A breakthrough regarding these nonpolar films was finally achieved in 2000 when Waltereit *et al.* [75] reported the growth of m-GaN grown on a (100) $LiAlO_2$ substrate using MBE. They obtained a film surface almost as smooth as c-plane GaN films. This at last enabled the growth of nonpolar III-nitrides device heterostructures. Since then research into

nonpolar III-nitride has spread rapidly and significant progress has been achieved in only a few years. For example in 2002 a-plane GaN grown on r-plane sapphire by MOCVD was reported by Craven *et al.* [77] and a year later, a-plane GaN grown by HVPE was successfully demonstrated by Haskell *et al.* [78].

- **Semipolar**

Although the progress in nonpolar devices has already shown some promising results, the performance is not yet fully optimised due to many challenges (which will be addressed in the next section). Therefore significant interests have been focused on alternative inclined surfaces such as (10-1-3), (10-1-1) and (11-22) [160]. These orientations have lower polarisation, as theoretical calculations show that the total polarisation discontinuity varies with these growth orientations (figure 1.19). These planes are commonly termed 'semipolar' planes.

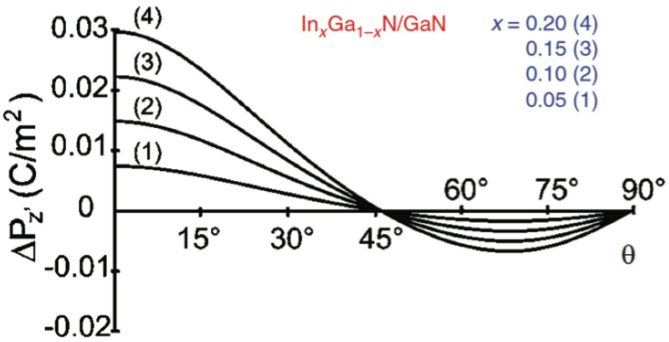

Figure 1.19: Calculated polarisation charge density in InGaN/GaN QWs as a function of growth orientations, in which θ = 0° corresponds to the c-plane. The internal electric field is zero around θ = 45°. (after [79])

The first (10-1-1) semipolar GaN film was fabricated on (100) $MgAl_2O_2$ by MOCVD [80], and the first (10-1-3) film on (110) $MgAl_2O_2$ by HVPE [81]. A smooth surface morphology was obtained for these films by a 3-degree substrate miscut in the [001] direction. (11-22) semipolar GaN/InGaN MQWs were first produced with a stripe patterned GaN template [82]. These devices have already shown a reduction in the red-shift of emission wavelength, as predicted by the theory.

1.6.1 Problems with nonpolar and semipolar orientations

Despite progress and development of both nonpolar and semipolar nitride materials, there are many challenges yet to be solved and several microstructural defects such as dislocations will have to be fully analysed and understood in order to optimise the devices.

Nitride heterostructures are known to have high dislocation densities, which are highly detrimental to device performance. Although dislocation density reduction is not as crucial as for group II-IV devices, for other III-Vs, reduction of dislocation densities will improve device performance. Nonpolar and semipolar nitrides are known to have high stacking fault (SF) densities [38] in addition to high threading dislocation (TDs) densities. Stacking faults have typical densities of ~10^5 cm^{-1} in nonpolar films grown on r-plane sapphire [38] and the dominating type of stacking fault is the basal plane stacking fault (BSF), which is bounded by two partial dislocations (see section 1.3.4). A detailed study [83] of BSFs present in a-plane GaN grown on r-plane sapphire suggested that they are type I_1, which constitutes as a very thin zinc-blende quantum well embedded in a wurtzite matrix (figure 1.20). Charge carriers can be confined in these zinc-blende quantum wells and they are responsible for a 365 nm emission peak in photoluminescence (PL). Liquid helium temperature cathodoluminescence (CL) spectra also suggested that the spectra from nonpolar GaN films are generally dominated by strong 362-363.4 nm emissions. The variation in the wavelength is dependent on film thickness [80].

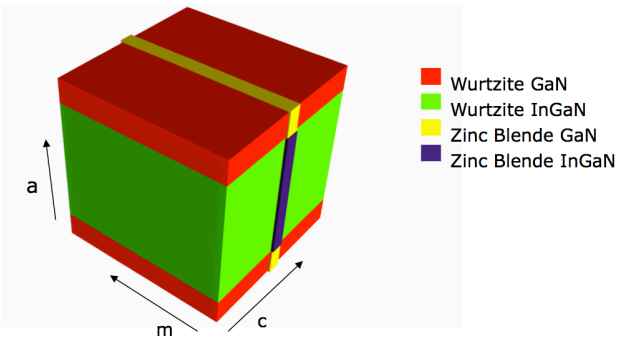

Figure 1.20: Schematic of nonpolar GaN/InGaN SQW showing the intersection between zinc-blende BSF and SQW. [84]

Other observed emission bands such as the yellow emission band represent the same defects, *i.e.* impurities, as in polar materials. Semipolar orientations are less studied with respect to the origin and behaviour of luminescence features. However they are expected to be comparable with those observed in nonpolar GaN due to the similar crystalline defects present in the microstructure. Other important defects such as the commonly observed threading dislocations and partial dislocations also appear in these off c-axis orientations and may act as non-radiative recombination centres. It is crucial to reduce defect densities in order to realise the potential of these off c-axis optoelectronic devices.

Another key challenge with nonpolar and semipolar orientations is that the surface morphology is much rougher than for c-plane films due to anisotropic in-plane biaxial lattice constants leading to different strain states at different planes. For instance, the lattice mismatch is larger in the [1-100] direction compared to [0001] directions in a-plane GaN grown on r-plane sapphire, causing large surface striations (with several hundreds of nanometres difference in heights) along the [0001] direction (figure 1.21).

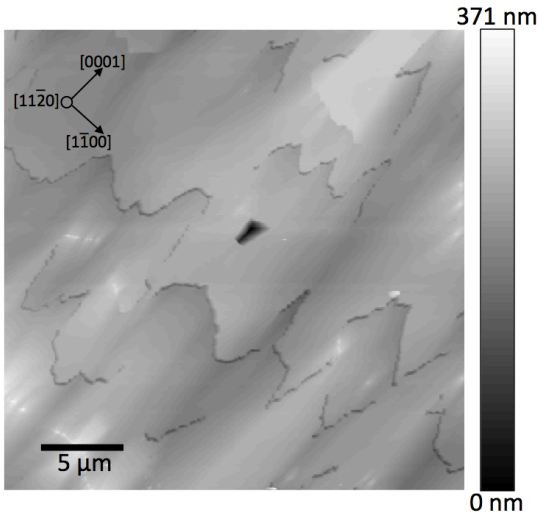

Figure 1.21: AFM image of a nonpolar *a*-plane GaN surface showing large fluctuation in surface height and domain boundaries (further details in chapter 6).

This surface roughness is detrimental to the quality of subsequent layer growth, especially for the active region where planar film growth is essential to ensure that carriers do not get trapped at interfacial defects caused by surface undulations.

1.7 Summary and challenges

The development of conventional c-plane near-UV LEDs is approaching a mature stage. However, deep-UV c-plane LEDs, with high Al-content alloys, still have very low internal and external quantum efficiencies and much attention is required to address issues such as the high dislocation densities present in the film. Growth of nonpolar and semipolar crystal orientations has made rapid progress over the last 10 years, and off c-axis growth may be beneficial for UV devices owing to the potential for achieving a reduced or eliminated QCSE. So far, the application of ELOG has enabled a reduction in defect densities in both polar and nonpolar films, but this does not prove to be effective on AlGaN films as AlGaN nucleates on the mask itself. Alternative approaches such as 'hetero-ELO' [86] where AlGaN is grown on a grooved GaN substrate using an AlN interlayer has been reported to give low dislocation densities (2×10^7 cm^{-2}). Despite these advances, the efficiency of UV emitters is around ~5 % of that of InGaN/GaN blue/green emitters [85]. This indicates that there are many challenges and more detailed work is necessary before the full potential of these UV emitters can be exploited. On-going development includes further optimisation of growth quality and better understanding of the effects and properties of the defects.

2

Experimental techniques

2.1 Aim

It has been discussed in chapter 1 that the performance of III-nitride optoelectronic devices is closely related to their microstructures, in particular the effects of defects. These microstructural features are typically on a nanometre scale. Characterisation techniques with the capabilities of extracting structural, compositional and optical information from the sample within this sub-micron to nanometre scale ranges can be extremely important. The use of a combination of several experimental techniques is required in order to fully characterise these III-nitride films. Destructive techniques such as transmission electron microscopy (TEM) and cathodoluminescence scanning electron microscopy (SEM-CL) can be used to investigate the internal microstructure, chemical composition and optical properties of the films, while non-destructive techniques such as atomic force microscopy (AFM), X-ray diffraction (XRD) and optical microscopy can be used to determine the surface morphology and crystallinity of the films.

2.2 Atomic force microscopy (AFM)

Many types of scanning probe microscopy (SPM) were established soon after the invention of SPM in the early 1980s [87]. Atomic force microscopy (AFM) is a very high vertical resolution type of SPM and has become one of the foremost tools for

imaging, measuring and manipulating matter at the nanoscale. In this work, AFM is used to obtain surface topographical information regarding III-nitride materials non-destructively. An atomic force microscope includes a small tip attached to the end of a flexible cantilever. This cantilever is rastered over the sample surface and experiences attractive forces when the tip/surface distance is large, due to Van der Waals forces, and repulsive forces when tip/surface distance is small, due to electron clouds of both surface and the tip. These forces cause deflection of the cantilever hence creating a variation in its vertical and lateral position. A laser and a photodiode detector are used to measure this change in position precisely (see figure 2.1) and a feedback loop is used to restore the tip to its original position at each measurement point, producing a map containing vertical and lateral information.

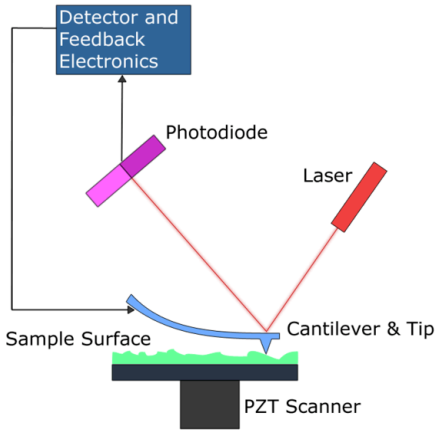

Figure 2.1: Schematic of AFM setup.

There are two primary operating modes in AFM: contact mode and tapping mode. Contact mode is the most common method of operation of the AFM. The tip and sample remain in close contact as the scanning proceeds. “Contact” occurs when the tip is in the repulsive regime of the intermolecular force curve (see figure 2.2) and large lateral forces are exerted on both the sample and the tip as the tip is ‘dragged’ over the specimen. The lateral frictional forces are eliminated in the case of TappingMode mode to reduce tip wear: the cantilever vibrates near its resonant frequency close to the sample surface so that the tip ‘taps’ the surface at the bottom of its swing. Changes in the tip-to-surface distance caused by the surface morphology lead to changes in the resonant frequency of the cantilever and the damping of the oscillation. An electron feedback loop monitors these changes in oscillation amplitude

and moves the tip higher or lower to keep a constant oscillation amplitude and hence a distance from the surface. These vertical tip movements are recorded to produce a map of surface topography.

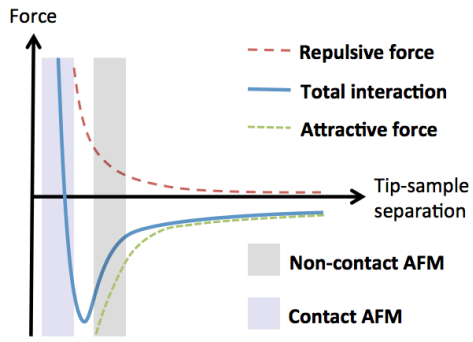

Figure 2.2: An intermolecular force curve

The X, Y and Z direction movement of the sample stage is controlled by three piezoelectric motors, which have extremely small step sizes and hence the vertical resolution is extremely high, as good as 0.25 Å [88]. However, the lateral resolution is poorer and is dependent on the size of the tip, *i.e.* a typical silicon tip has a radius of 5-15 nm and this is the theoretical lateral resolution. The resolution can be worse if the tip becomes blunt or acquires debris during the scanning [89] (figure 2.3), the breadth of a tip may prevent it reaching the bottom of narrow pits or feature (figure 2.3b): the image may also become distorted during scanning or may show the tip geometry itself in the case of a damaged tip [90]. Therefore care should be taken when interpreting the features on the image that are smaller than the tip.

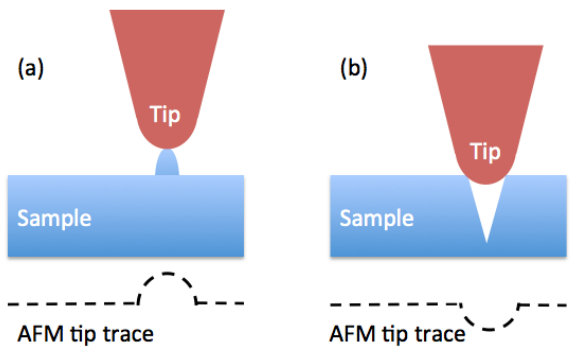

Figure 2.3: Schematic showing the lateral resolution of a protuberance is dependent on the tip size. (a) AFM trace width increase due to the tip size is larger than the

surface feature. (b) AFM trace depth is under-estimated as the tip is larger than the trench.

AFM was performed on a Veeco Dimension 3100 AFM. Most of the nonpolar samples studied in chapter 6 exhibited some directionality in surface morphology along [0001] direction in GaN and therefore a [1-100] scan direction was used perpendicular to the surface features to minimise artefacts and ensure an accurate representation of the sample surface. A slow scan rate and low amplitude set-point (distance between the tip and surface) was also used for these nonpolar samples with rough surfaces to minimise tip damage and obtain good feedback.

The AFM has several advantages over the scanning electron microscope (SEM). Scanning electron microscopy can only provide a two-dimensional projection of a sample surface while AFM is able to provide a true three-dimensional surface profile. Furthermore, in contrast to electron microscopy, AFM is a non-destructive technique and the sample does not require any special treatment. Most AFM modes work perfectly well in air or even liquid environments without the need for a vacuum environment. These key benefits make AFM an incredibly versatile technique.

2.3 Scattering from crystals

The characterisation techniques that are described in the rest of this chapter (X-ray diffraction and electron microscopy) are all related to the interactions of X-rays or electrons passing through a specimen and therefore the theory of scattering from crystals will be briefly reviewed.

The periodic array of atoms in a crystal can act as a diffraction grating, where high-energy electrons (*e.g.* 200-300 keV electrons in the TEM) and X-ray waves can be scattered from each atom and interfere with each other either constructively or destructively (overlapping waves either add together to produce stronger peaks or subtract from each other to remove peaks), producing a diffraction pattern on a

detector. The resulting wave interference pattern is described by the Bragg Law and can be analysed using the crystals reciprocal lattice.

Bragg diffraction describes the intense peaks of reflected patterns of radiation at certain specific wavelength and incident angles, during diffraction through crystalline materials:

$$n\lambda = 2d_{hkl}\sin\theta_B$$

Where n is an integer, λ is the wavelength of incident wave, d_{hkl} is the spacing between the planes in the atomic lattice, and θ_B, the Bragg angle, is the angle between the incident ray and the scattering planes (figure 2.4).

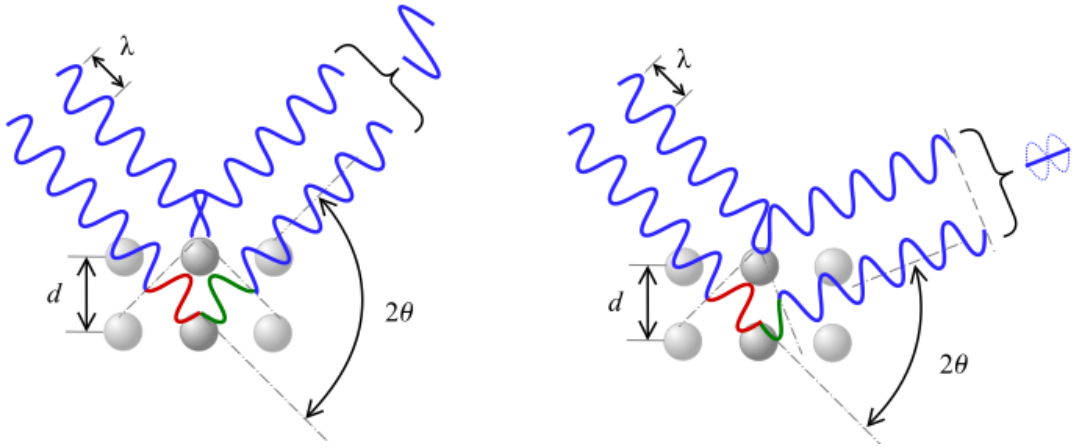

Figure 2.4: Schematic of constructive interference (left) and destructive interference (right) of an electron or X-ray incident beam diffracted from parallel planes in the crystal separated by a distance d_{hkl}. Modified from [92].

The diffraction pattern is related to the crystal's reciprocal lattice. Each set of planes (hkl) in a crystal corresponds to a reciprocal lattice point, the distance between each point is described by a lattice vector |**g**| (= h$\mathbf{g_1}$ + k$\mathbf{g_2}$ + l$\mathbf{g_3}$) which is equal to the reciprocal of the plane spacing d_{hkl}, and is related to the real lattice vectors of the crystal, where:

$$g_1 = \frac{a \times b}{a \cdot b \times c}, \; g_2 = \frac{b \times c}{a \cdot b \times c}, \; g_3 = \frac{c \times a}{a \cdot b \times c}$$

With the concept of the reciprocal lattice, the position of diffraction spots can be explained by Bragg's law in terms of the Ewald sphere construction. This is a sphere which intersects the origin of the reciprocal lattice, and describes the relationship between the wave vector of the incident and diffracted x-ray or electron beams, the diffraction angle for a given reflection, and the reciprocal lattice of the crystal (figure 2.5).

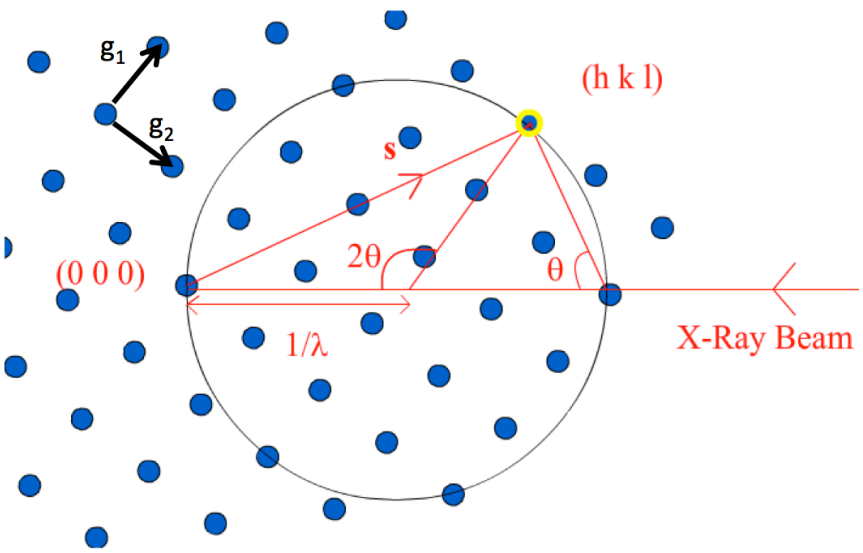

Figure 2.5: All the possible diffraction peaks can be found for a known reciprocal lattice and wavelength of radiation using the Ewald sphere when Bragg's condition is satisfied. Modified from [93]

2.4 High resolution X-ray diffraction (HRXRD)

XRD is a non-destructive technique that is commonly employed to examine the crystalline quality of the materials. In the field of III-nitrides, XRD is a relatively rapid means of measuring the interplanar spacing, lattice parameters and is consequently an indirect method of measuring the composition of heterostructure layers based on Bragg's law [91].

In order to obtain as much information as possible from semiconductor heterostructures, for instance, the signal from MQWs, it is often required to use a number of precision components in the XRD apparatus to acquire high-resolution measurements [92] (*i.e.* to resolve the width of the rocking curve to within a few arc seconds).

The resolution of XRD can be related to the divergence (δθ) of the X-ray beam, which is expressed as:

$$\delta\theta = \frac{h+s}{a}$$

Where *h* is the X-ray source size, *s* is the slit size and *a* is the source-specimen distance (Figure 2.6). For a typical low-resolution case where h = 0.4 mm, s = 1 mm and a = 500 mm, δθ ~ 500 arc seconds, however, the width of the rocking curve for highly perfect crystals is a few arc seconds.

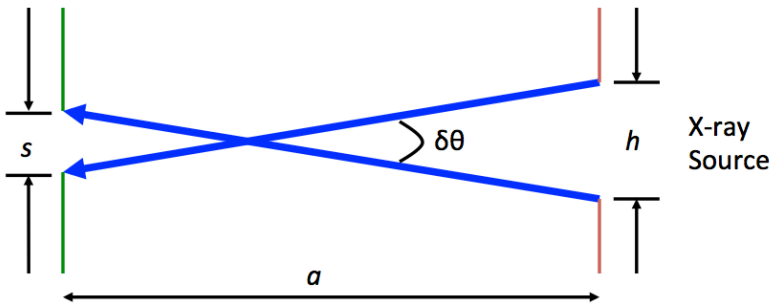

Figure 2.6: Relationship between the divergence with source size, slit size and distance between source and specimen.

High-resolution XRD (HRXRD) measurements therefore require a small divergence and a small wavelength spread of the beam incident upon the specimen, as well as a narrow acceptance angle with the detector. The HRXRD measurements carried out throughout this thesis were performed on a Philips PW3050/65 high-resolution X-ray diffractometer. A CuKα X-ray radiation source was used due to its high intensity and relatively large wavelength (λ(CuKα) = 1.540562 Å) so the spacing of reciprocal lattice points is similar to the radius of the Ewald sphere (*i.e.* only one or two reciprocal lattice points can be at the Bragg condition).

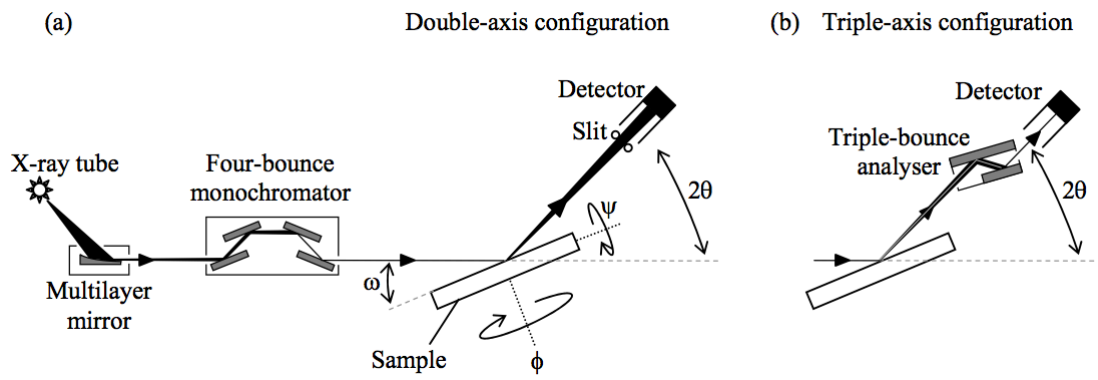

Figure 2.7: Schematic of key components for HRXRD configuration. (a) Double-axis configuration for lower resolution (open detector) and (b) triple-axis configuration for high-resolution (with analyser). Reproduced from [93].

HRXRD measurements may be taken in either of two modes: double- or triple-axis configuration (figure 2.7) to achieve different angular resolutions. In double-axis configuration, the first axis is used for the adjustment of the beam conditioner (comprising optical elements such as a monochromator) and the second axis is used to scan the specimen through the Bragg angle. In triple-axis configuration, the additional third axis allows the adjustment of the analyser in front of the detector (in a similar way as the monochromator reduces the angular spread of the X-ray source). This provides the fine-scaled information necessary to obtain the highest resolution, but at the expense of intensity, and hence requires an increased time for acquisition. The movement along the three axes of measurement determines the precision and accuracy of the instrument [94]. Almost all of the measurements in this thesis were carried out in triple-axis configuration to obtain the highest resolution possible.

Two types of scan are typically performed for III-nitride semiconductors. ω-scans measure the film quality by scanning the diffraction spot in an arc. The broadening of the peak is related to dislocations and wafer curvature. ω-2θ scans are required for lattice parameter determination. Both ω and ω-2θ scans are also known as rocking curves, *i.e.* the crystal is "rocked" about the ω-axis perpendicular to the incident beam, the resulting plot giving the intensity variation through the reciprocal lattice point. The following table provides an overview of the information that can be derived from rocking curves obtained from HRXRD measurements.

Table 2.1: Effect of substrate and epilayer parameters upon the rocking curve [12]

Material parameter	Effect on rocking curve	Distinguishing features
Mismatch	Splitting of layer and substrate peak	Invariant with sample rotation
Tilt or misorientation	Splitting of layer and substrate peak	Changes sign with sample rotation
Dislocation	Broadens peak	- Broadening invariant with beam size - No shift of peak with beam position on the sample
Mosaic spread	Broadens peak	- Broadening may increase with beam size up to mosaic cell size - No shift of peak with beam position on the sample
Wafer curvature	Broadens peak	- Broadening increases linearly with beam size - Peak shifts systematically with beam position on sample
Relaxation	Changes the splitting	Different effect on symmetrical and asymmetrical reflection
Thickness	- Effects intensity of peaks - Introduces interference fringes	- Integrated intensity increases with thickness up to a limit - Fringe period is controlled by the thickness
Inhomogeneity	Effects vary with position on sample	Individual characteristics may be mapped

Although peak broadening can be related to several factors as listed above, for HRXRD measurements performed on high dislocation density films, the broadening from lattice rotations at dislocations dominates [95] and can be used as a measure of dislocation density. A simple relation between the dislocation density and broadening of the rocking curve is expressed as [96]:

$$\rho = \frac{\beta^2}{9b^2}$$

Where ρ is the dislocation density in cm^{-2}, β is the broadening of the rocking curve in radians and b is the Burgers vector for the dislocation in cm.

2.5 Scanning electron microscopy (SEM) / Cathodoluminescence (CL)

Cathodoluminescence (CL) is light emitted by a material due to irradiation by an electron beam. The beam of a scanning electron microscope (SEM) is ideal for this purpose. The SEM-CL measurements in this work were performed on a FEI XL30s with a field-emission gun (FEG-SEM) for providing a high brightness and small probe size for a given beam current. In a typical SEM set-up, the electron gun is positioned at the top of the column (figure 2.8). Electrons are generated when a high voltage (adjustable between 1 to 50 kV) is applied between the anode and cathode. The focused electron beam can be achieved by demagnifying the beam through sets of electromagnetic lenses. The system, including the sample and detectors, is kept under high vacuum to avoid electron scattering or the build up of any contamination to the sample or electron source [97]. Two deflection coils positioned below the condenser lens are used to control the scanning of the electron beam probe across the sample.

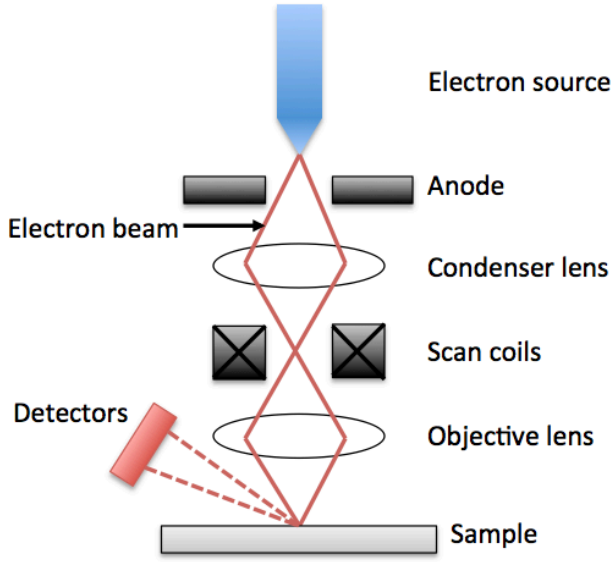

Figure 2.8: Schematic of basic components and configuration of a scanning electron microscope.

The impingement of a SEM electron beam with typical energies of 1 keV to 30 keV can result in many different inelastic scattering processes as beam electrons lose energy in the solid (figure 2.9). These scattering processes can be extracted and detected by various detectors [97]. The secondary electrons (SE) can be used for evaluating topographic information. The back-scattered electrons (BSE) can be used for structural analysis of solids, since the image contrast depends on atomic number. X-rays provide compositional information of the sample. These beam electrons are also able to excite electrons from the valence band (VB) to the conduction band (CB) in semiconductors and leave behind holes. These electrons and holes can recombine (electrons fall back down to the VB) and emit photons and the process is termed cathodoluminescence (CL) emission.

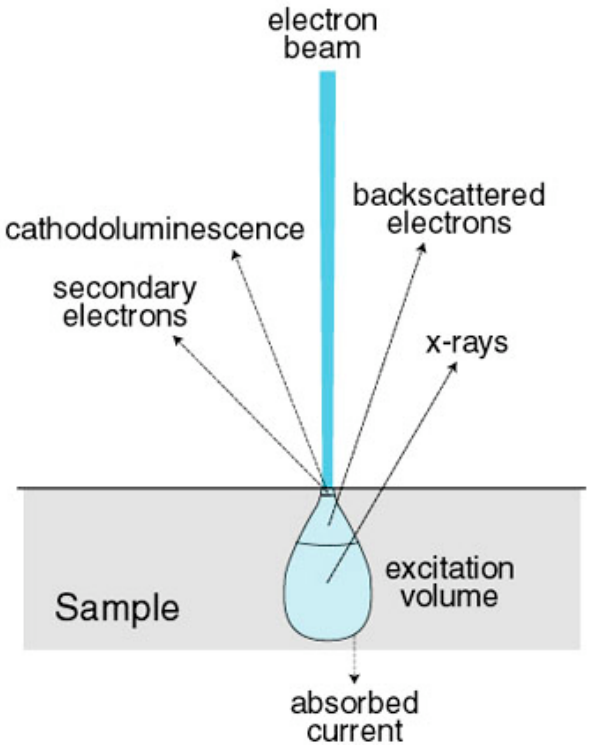

Figure 2.9: Interaction between electron beam and the sample.

The CL emission therefore is characteristic of the electronic transitions in semiconductors, and is able to provide high spatial resolution information on a variety of material properties. The main CL applications include: identifying luminescence centre concentrations and distributions, estimation of material composition [98], estimation of carrier diffusion length from the dependence between CL intensity and electron beam energy [99], and determining carrier lifetime from time-resolved CL measurements [100].

Two kinds of information can be obtained in SEM-CL: microscopy information (CL images or maps) and spectroscopy information (CL spectra). Throughout this thesis, the CL measurements were taken in an SEM to give optical and structural information about defects in III-nitride semiconductors.

The emitted photons (CL emission) are collected through a precision diamond-turned paraboloidal aluminium mirror (up to 85% light collection efficiency [98]) positioned directly above the sample in the Gatan MonoCL4 (figure 2.10). The DigiScan II beam control system is attached to the MonoCL4 to enable imaging of multiple channels

(*i.e.* CL and SEM) and to enable control over pixel density and pixel dwell time. The MonoCL4 consists of a chamber-mounted monochromator and a highly sensitive photomultiplier tube (PMT) with a wavelength detection range of 160 nm to 930 nm. The incident photons are converted into electrons as a consequence of the photoelectric effect in the PMT. This electrical signal is then enhanced and amplified by the high voltage electron multiplier before entering the microscope. The gain of the PMT detector increases with increasing applied voltage up to about 75% of the maximum high tension (HT); further increase in HT would result in increasing noise. This high collection and transmission efficiency allows the CL to be performed without excessive beam injection voltages or currents, and hence high spatial resolution CL is achievable. Cryogenic temperatures at ~ 7K or ~ 90K using a Gatan CF302 continuous flow liquid helium cold stage or a nitrogen cold stage respectively can also be employed to achieve further enhancement of the CL resolution. This is possible because the CL emission can often be enhanced significantly due to radiative recombination being favoured at this temperature, so more signal can be collected at low injection condition.

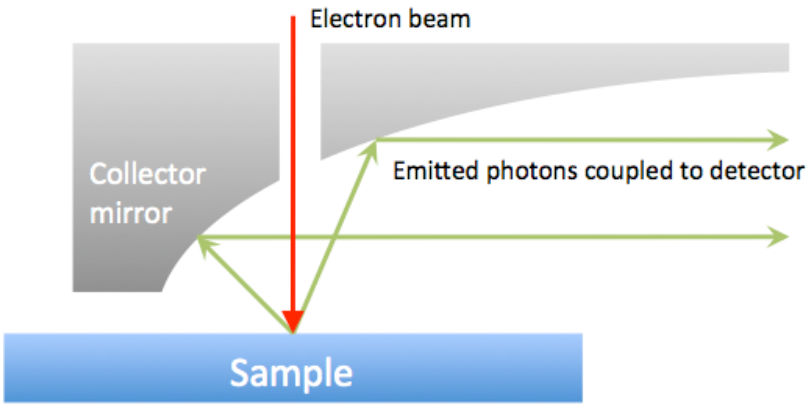

Figure 2.10: Schematic of emitted photons coupled to a detector via a paraboloidal mirror located directly above the sample surface.

In the CL imaging mode, the system is able to operate in panchromatic or monochromatic setup. In panchromatic mode, all the transmitted light bypasses the monochromator and is collected directly by the PMT detector (figure 2.11, blue light path), providing a map of the total light output from the scanned area on the specimen. In monochromatic mode, a map of the light output at a specific wavelength

can be acquired by dispersing the light through a diffraction grating (figure 2.11, red light path). The small range of wavelength (the bandpass) is controlled by the magnitude of the exit slit before entering the PMT.

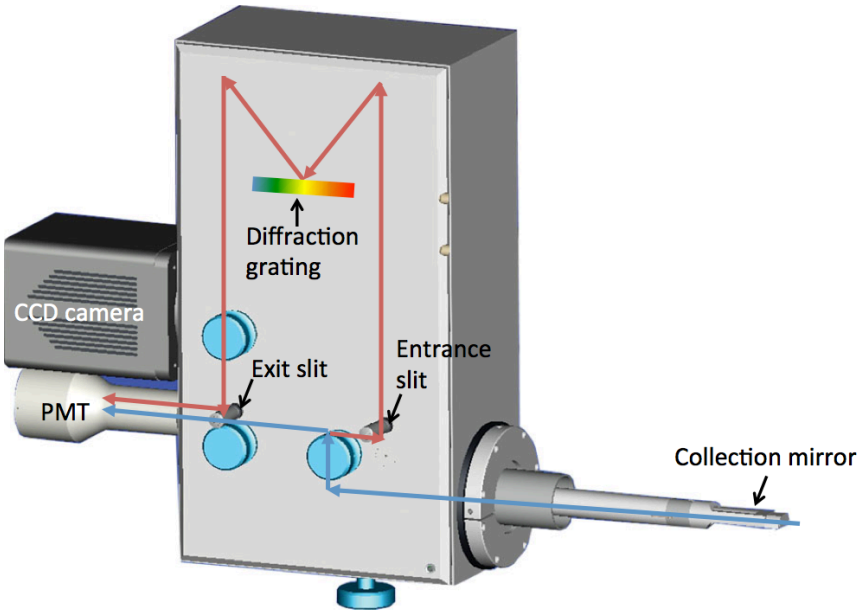

Figure 2.11: Schematic illustrating the path of emitted light in panchromatic (blue) mode and monochromatic (red) mode.

The CL spatial resolution is determined theoretically by the size of the electron beam and by the beam-specimen interaction volume. Specimen characteristics such as specimen morphology, surface states (including dead layers present due to specimen preparation techniques) [101] and material-specific absorption characteristics can also influence the result obtained [102]. Higher electron beam energy provides a larger interaction volume and signal-to-noise ratio at the expense of spatial resolution

Monte Carlo simulations were used to estimate the beam-specimen interaction volume, which as a result provides a guide to the approximate CL spatial resolution that can be obtained from the samples [103]. The simulation results shown here were carried out using CASINO [104] software. The simulation of the sample was generated using the sample C2691D growth recipe (see chapter 7 for sample details), which has 10 repeated layers of AlGaN/GaN quantum wells. Figure 2.12 shows the simulation of an electron beam with 1 keV and 5 keV beam energy, indicating that the interaction volume has an approximate radius of 25 nm at 1 keV, to over 200 nm at 5

keV. Although the theoretical interaction volume for 5 keV exceeds 200 nm, most of the light output is concentrated and emitted from the top centre layer of the film. Therefore, the practical effective interaction volumes are less than the estimated values and hence the lateral resolution is on average slightly higher.

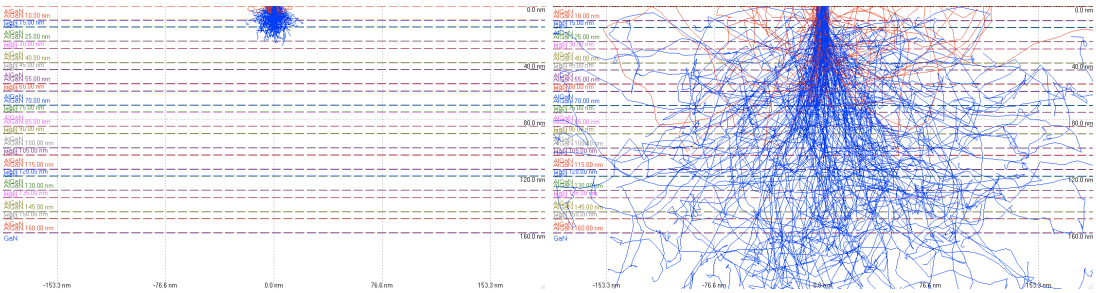

Figure 2.12: A Monte Carlo simulation of electron beam and sample interaction volume for sample C2691D with a 1 keV (lef) and 5 keV (right) beam voltage.

In CL spectroscopy mode, spectral analysis can be obtained by passing the CL emission through the entrance slit of a monochromator to a diffraction grating. A wavelength range is then selected for light passing through the exit slit to the detector. The CL intensity is then analysed as a function of wavelength. Spectral acquisitions can be achieved with a PMT (serial spectroscopy) or an array detector (parallel spectroscopy).

In serial spectroscopy mode, the electron beam remains stationary at the region of interest and a stepper motor rotates the diffraction grating (dwell time and increment steps are adjustable) to change the wavelength of the light before reaching the PMT (figure 2.13). The CL intensity of the selected wavelength is collected from each rotation for a certain period of time (known as the exposure) to record the CL spectrum as a function of wavelength in nanometres.

In parallel spectroscopy mode, the diffraction grating remains stationary. The light is collected with a multi-channel charge-coupled device (CCD) camera instead of a PMT (figure 2.13). Each pixel in the CCD camera acts as an exit slit which responds to a particular wavelength of the light dispersed from the monochromator. The signal from every pixel can be recorded and integrated simultaneously. Hence parallel spectroscopy acquisition is much faster (in milliseconds) in comparison to serial CL

mode. This is beneficial for analysing electron beam sensitive materials, such as InGaN [93].

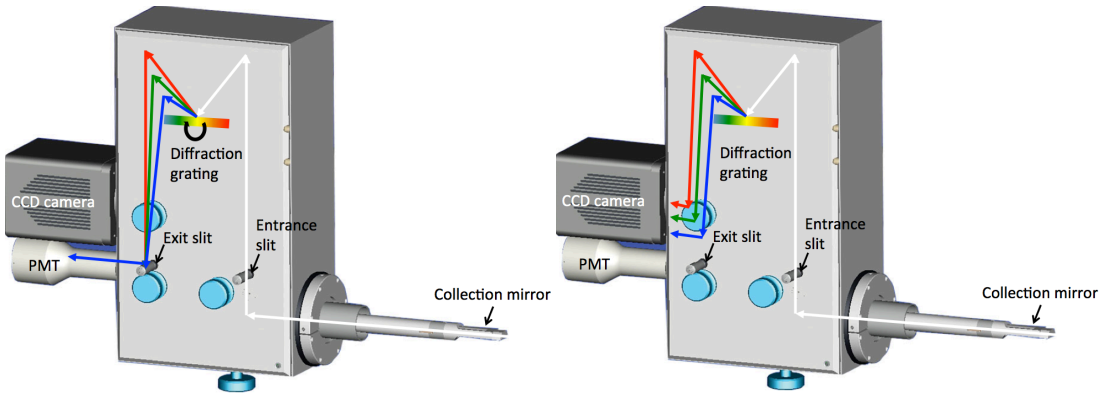

Figure 2.13: Schematic illustrating the light path for serial CL acquisition (left). The diffraction grating is rotated to select a specific wavelength before entering the PMT. In parallel CL acquisition (right), all the light diffracted from the diffraction grating is collected with a CCD array detector in a parallel manner.

It is also possible to acquire both spatial and spectral information in a single data set with spectrum imaging (SI) [98]. This is achieved when the electron beam is rastered across the region of interest in either 3D mode for full spectrum imaging or in 2D mode for a spectrum line scan (figure 2.14). The region of interest is selected from a standard CL image acquired with the PMT to achieve a high pixel density. The spatial information is then obtained in SE imaging mode and spectral information is obtained using parallel CL with a CCD camera in a “spectrum per pixel” manner within this region of interest to form a spectrum image.

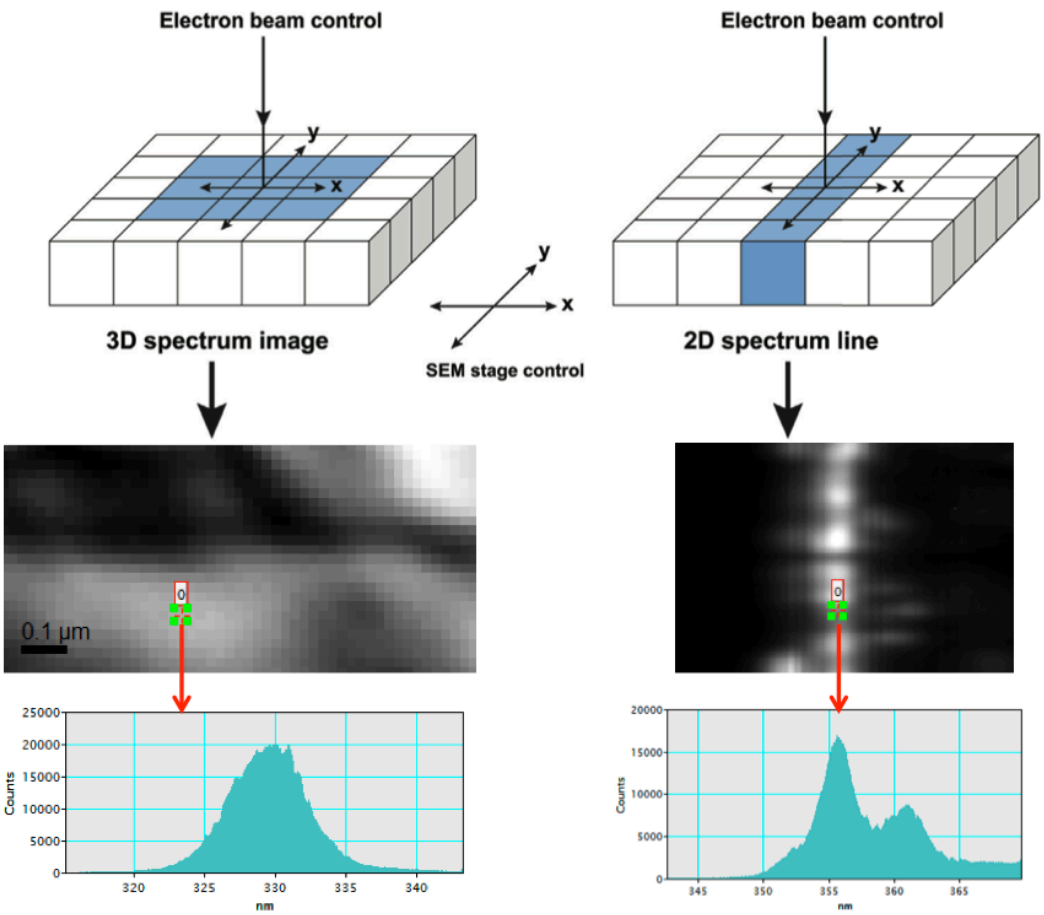

Figure 2.14: Schematic diagram of a 3D spectrum image (left) and a 2D spectrum image (right)

The CL spectral resolution depends on the luminescence properties and temperature of the sample, and the detection capability of the CL system. Materials related dependency could be minimised with the aid of cryogenic temperatures as mentioned earlier. Therefore, the spectral resolution is mainly limited by the detection capability of the CL system, such as the width of the diffraction grating, the width of the entrance and exit slits and the spatial resolution of the detector.

Figure 2.15 shows the calculated correlation between slit width, the bandpass and the width of the diffraction grating. A 1200 g/mm and a 2400 g/mm grating has been used for this work.

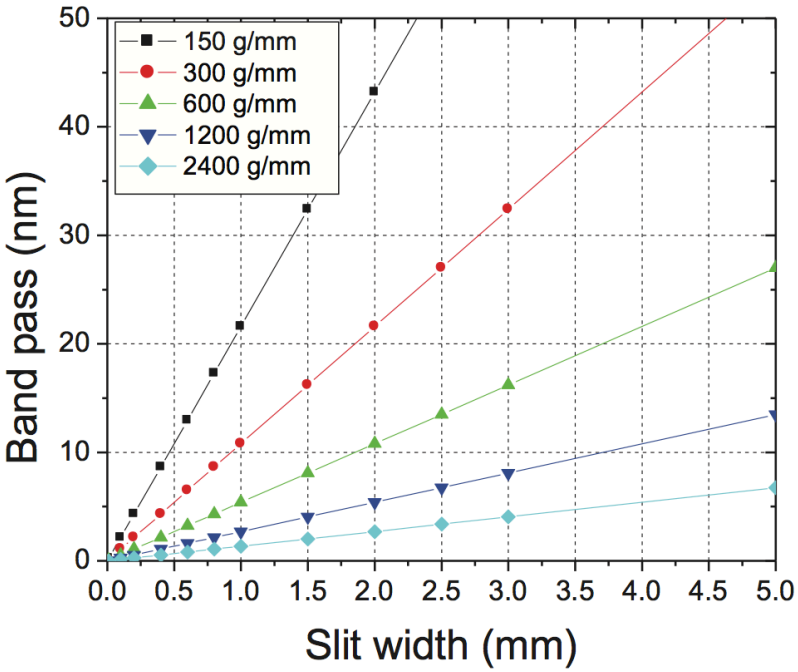

Figure 2.15: Calculated bandpass as a function of the widest width of either the entrance or the exit slit. (Reproduced from [98])

CL is a therefore powerful technique used to investigate the structural and optical properties of semiconductors. In some of this work (chapter 7), both CL and TEM are performed on the same areas of samples. By doing this, a correlation between areas with defects in TEM and maps of the CL intensity and wavelength can be obtained, thus providing further understanding of the luminescence properties of the defects.

2.6 Transmission electron microscopy (TEM): Sample preparation

In order to study the microstructure of the material in TEM, a very thin sample with thickness less than 100 nm should be prepared so it is electron transparent. However, artefacts and damage can be generated at each stage of preparation, which may result in misleading features being observed in the TEM.

The TEM samples used throughout this thesis were prepared with mechanical polishing followed by argon milling in a Gatan Precision Ion Polishing System

(PIPS). Two types of samples were used: Plan-view (the sample was thinned in the growth direction) and cross-sectional samples (the sample was thinned in a direction perpendicular to the growth direction). Cross-sectional samples were prepared by sandwiching two specimens together with a relative 90° in-plane rotation such that the [1-100] and [11-20] zone axes ([1-100] and [0001] for nonpolar material) are readily accessible in the TEM.

Two different preparation processes for cross-sectional samples were used to investigate the quality of the samples. The first is by conventional mechanical polishing, using the CHREA method (by Dr P. Vennéguès, CNRS-CHREA, France). The second process is carried out using the Focused Ion Beam (FIB) microscope.

CHREA method

The CHREA method involves cleaving two strips of wafer (~ 4mm by 10mm) one with the long edges running parallel to $[11\text{-}20]_{GaN}$ and $[1\text{-}100]_{GaN}$ directions for c-plane samples ($[0001]_{GaN}$ and $[11\text{-}20]_{GaN}$ for nonpolar samples). These cleaving directions are approximated relative to the wafer flat. The two strips were then glued together with the GaN sides facing each other using an epoxy resin (Araldite). This sandwich was then pressed firmly to minimise the thickness of the glue line and cured for 20 minutes at ~ 100°C. G2 epoxy (Gatan) was used to glue the sandwich piece inside a brass fork and the whole assembly placed together into a brass tube. This tube was also cured for 20 minutes at ~ 100°C. The tube was then sliced into 1 mm discs using a rotating saw with a diamond-coated blade.

A maximum of four prepared discs can be polished simultaneously by using a Gatan disc grinder. The large-scale jaggedness was polished away with silicon carbide grinding paper (240 grade) until the samples were at an even thickness. A rotating grinding wheel with different grades of diamond lapping films was then used to thin down and polish the samples. The first side of the samples was polished using successive grades of 30, 15, 6, 3 and 1 μm lapping films, each grade removing approximately three times the grain size of the previous film, *i.e.* the 15 μm film was used to remove 90 μm of material. After a mirror surface finish was achieved, the samples were inverted to polish the second side. Again the same subsequent grades of

diamond lapping films were used and 30 µm lapping film was used to remove material until the sample was at ~ 150 µm. 15 µm film was then used until the sample reached ~ 100 µm thickness and 6 µm was used for the final polish to a thickness of ~ 50 µm. The thickness achieved during each stage was estimated with an optical microscope. The samples were then polished down further with a Gatan dimple grinder. This reduced the thickness at the centre of the sample to less than ~ 20 µm and the final mirror surface finish was also achieved using a dimple grinder with 1 µm diamond paste for ~ 2 minutes at the maximum speed. The samples were then removed from the grinder stub and cleaned with acetone for a few hours. Next, each cross-sectional sample was then attached to a spring clip PIPS holder for the ion milling stage. Plan-view sample preparation starts with a square of wafer with ~ 3 mm diamond length. The samples were polished with the same procedures as for the cross-sections but only from the sapphire side. Samples were adhered to the PIPS plan-view sample holder with the GaN side facing down.

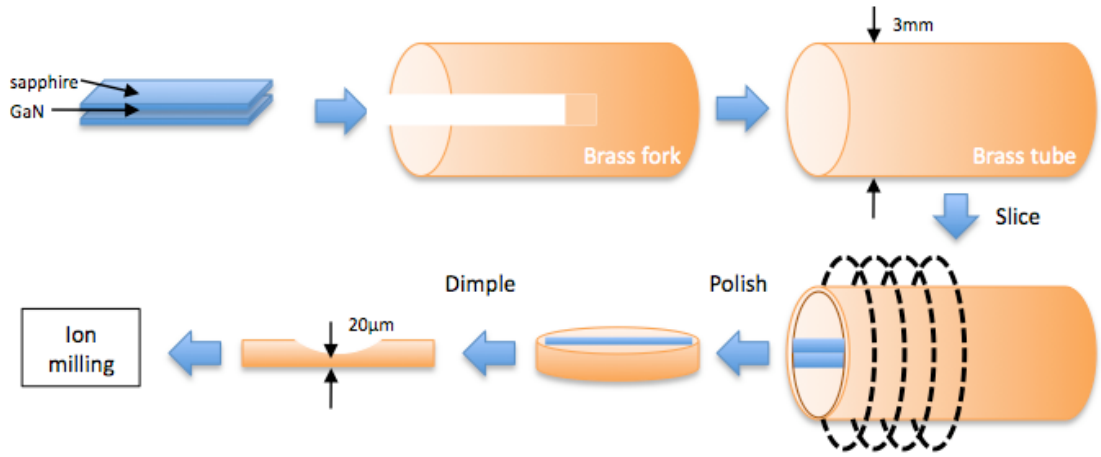

Figure 2.16: Schematic of CHREA sample preparation procedures.

In the PIPS, the argon milling guns were set to a shallow angle at -4° on the flat side and +6° for the dimpled side to achieve a wide electron-transparent thin area for cross-sectional samples (for both guns were set to +7° to mill away the sapphire for plan-view samples). Double beam modulation was used for cross-sectional samples to avoid milling the sample holder. Material was milled at a rate of ~ 5 µm per hour at a 5 kV beam voltage. Once a small hole was generated at the centre of the sample, the beam voltage was then reduced to 2.5 kV for 10 minutes to remove the surface

amorphous region caused by the high beam voltage. Fringes around the hole were visible under the optical microscope (figure 2.17) and these indicated the presence of electron-transparent thin areas to be investigated in the TEM.

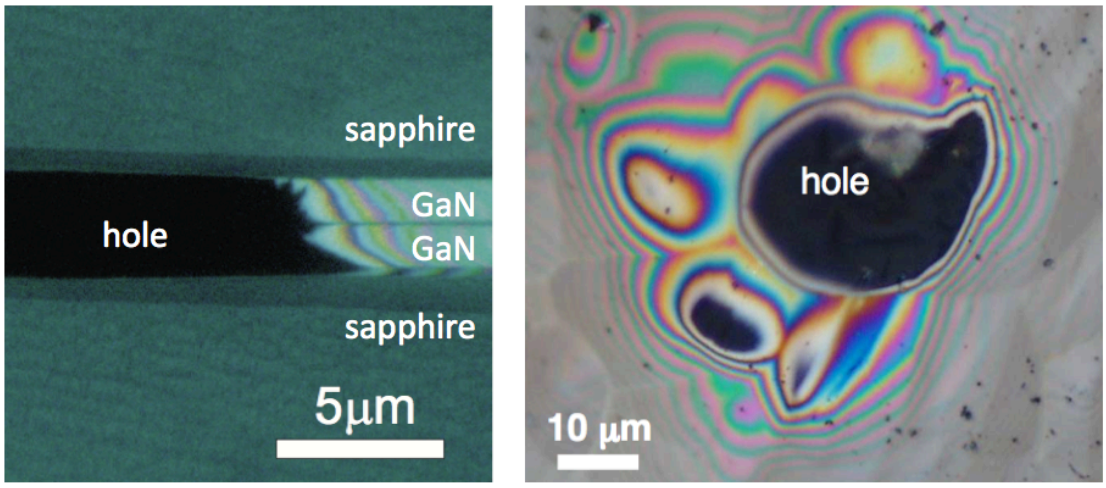

Figure 2.17: Optical micrograph of a completed TEM cross-sectional sample (left) and plan-view sample (right). The regions with thickness fringes are suitable for TEM analysis.

Focused Ion Beam (FIB) method

Focused Ion Beam (FIB) microscopy is a widely used materials science research technique for site-specific analysis, material deposition and ablation. Because high-energy gallium ions are used, its sputtering capability also allows the FIB to be used as a TEM sample preparation technique [105]. The FIB used in this work is a dual-beam system consisting of an electron beam and a gallium ion beam allowing real-time viewing of the sample area during ion milling.

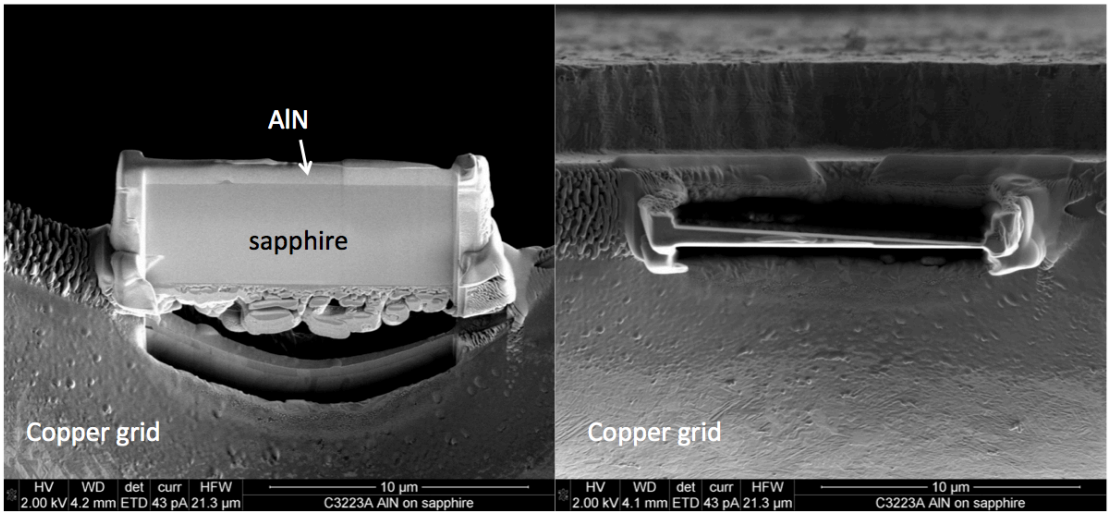

Figure 2.18: Side view (left) and top-down view (right) images of sample C2691D prepared with FIB to create a wedge shape with 3° angle from thinner region (<100 nm) to thicker region (~ 500 nm)

In contrast to the PIPS mentioned earlier, although both are capable of producing electron transparent thin TEM samples, the FIB method has the additional benefit of creating specific sample shapes, such as micro-machining a sample to a wedge shape with custom thickness and angle (figure 2.18). The benefit of this sample shape is that the thicker region can be used for CL analysis whilst the thinner region can be used for TEM analysis (more detailed in chapter 7). More importantly, the nanometre-scale resolution of the FIB allows selected sample regions to be investigated, and TEM specimens of specific sample features to be prepared. For example, the exact region of interest in the sample can be "marked" by the FIB such that the region of interests can be found easily using both CL and TEM, allowing a direct correlation between both data sets on a specific defect to be established.

The drawbacks of FIB sample preparation are the surface damage caused by the high-energy ions (which sputter atoms from the surface), and the effect of gallium ions being implanted into the surface [106]. This causes the top few nanometres of surface to become amorphous (dead layer), which affects both CL and TEM observations (chapter 7). This dead layer can be removed by using lower FIB milling voltages at the end of preparation.

2.7 Transmission electron microscopy (TEM)

TEM is an invaluable tool for providing a wealth of information about crystalline materials. An excellent overview of TEM and related techniques may be found in Williams et al [107]. This section highlights the use of conventional TEM techniques to obtain structural information about the crystalline defect types in c-plane and nonpolar III-nitride specimens. Three different TEM techniques are most commonly used: diffraction patterns (DP), bright field (BF) and dark field (DF) imaging. Diffraction patterns can be used to determine lattice parameters of the material and to provide crystallographic information such as the orientation of the wurtzite structure of GaN. Bright field and dark field imaging are used to image dislocations and stacking faults.

Fundamentals of TEM

A Philips CM30 TEM was used to obtain most of the images in this thesis. The CM30 is capable of accelerating electrons up to maximum energy of 300 keV and the electron source is a thermionic LaB_6 crystal source. Figure 2.19 below highlights the simplified layout of the key optical components in a conventional TEM. Modern TEM columns have many more lenses in their imaging systems, which give greater flexibility in terms of the magnification and focusing range for both images and DPs.

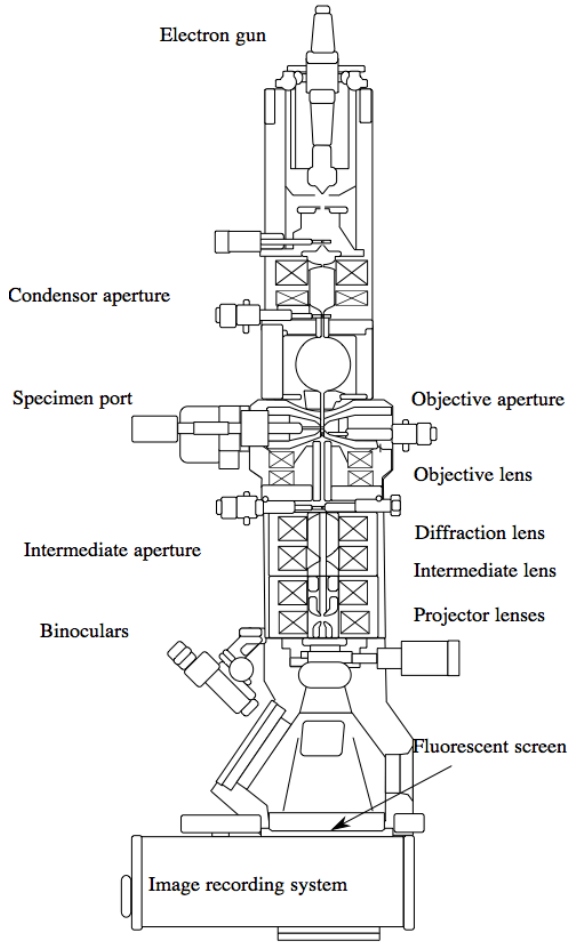

Figure 2.19: Schematic of a conventional TEM showing optical components. (Reproduced from [108])

The CM30 microscope consists of three stages of lenses. They are the condenser lenses, the objective lenses, and the projector/diffraction lenses. The condenser lenses are responsible for the primary beam formation. The objective lenses magnify the image of the specimen and they should be optimally aligned and stigmated as they deal with largest range of angles, which can present the worst aberrations. The projector lenses further magnify the image of the specimen.

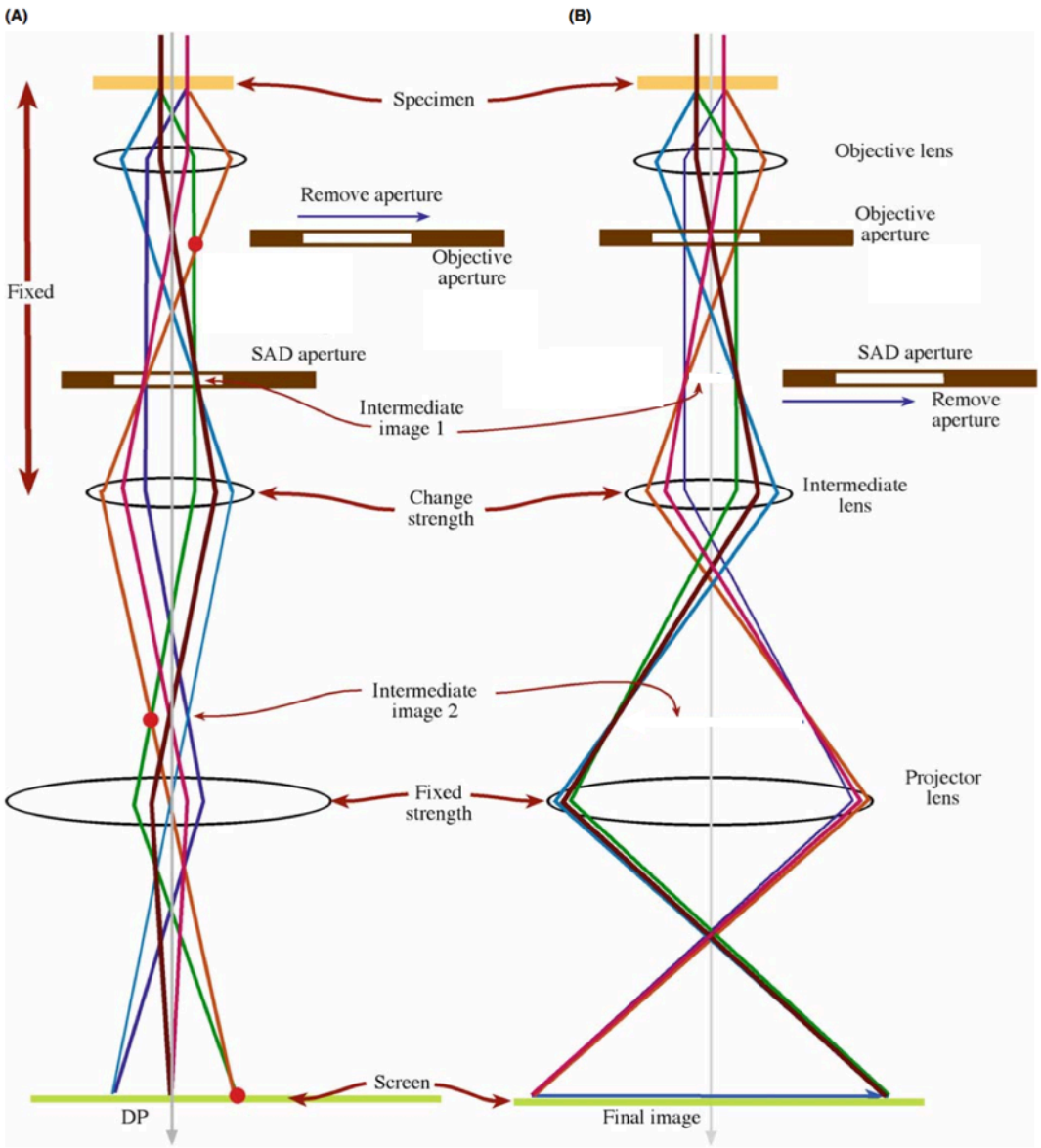

Figure 2.20: The two basic operations of the TEM imaging system involve (A) diffraction mode: projecting the DP onto the viewing screen and (B) image mode: projecting the image onto the screen. (Reproduced from [107])

Figure 2.20 is a highly simplified schematic, which illustrates the two basic operation modes in TEM: imaging mode and diffraction mode. In imaging mode, the electron beam is focused by a condenser lens onto the specimen. The electrons passing through the specimen are focused by the objective lens to form an image called the first intermediate image. The first intermediate image forms the "object" for the next lens, the intermediate lens, which produces a magnified image of it called the second intermediate image. This again becomes the object for the projector lens, which forms

the greatly magnified final image on the viewing screen of the microscope. In diffraction mode, the diffraction pattern that is formed at the back focal plane of the objective lens can be viewed on the viewing screen by weakening the intermediate lens.

Diffraction patterns

In TEM, two types of electron diffraction patterns (DP) can be obtained: selective area diffraction (SAD) patterns or convergent beam electron diffraction (CBED) patterns. Figure 2.21 illustrates the optics involved in obtaining these two DPs. The SAD pattern is acquired when a parallel electron beam is incident on the specimen with diffraction spots formed in the back focal plane (BFP) of the objective lens. The selective area aperture is placed in the first intermediate image plane to select a small region of the sample for diffraction contrast imaging, a technique that is commonly used to characterise the structure of III-nitride materials.

The CBED pattern is acquired when the electron beam converges to form a spot on the specimen by adjusting the condenser lens, resulting in diffraction disks formed in the BFP. The main application of CBED in this work is to extract information on the polarities of the III-nitride samples (reviewed later in this section).

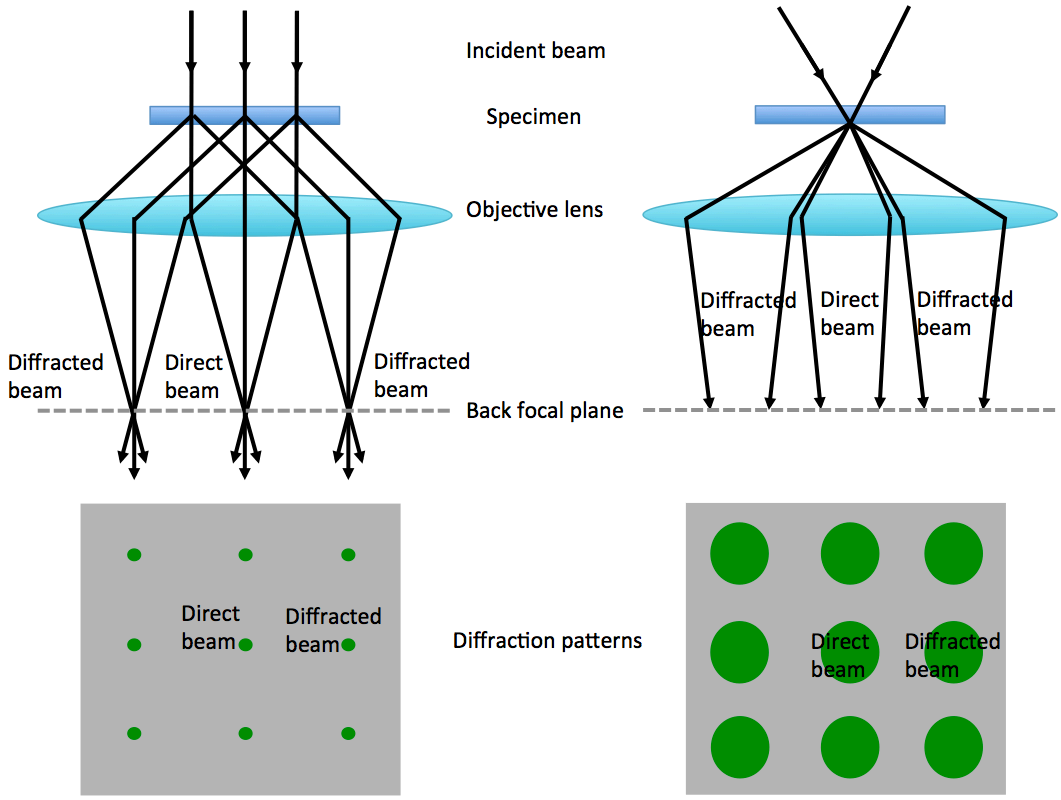

Figure 2.21: Schematic of the optical rays in selected area diffraction (SAD) (left) and convergent beam electron diffraction (CBED) (right).

The basic concepts of diffraction and the reciprocal lattice in TEM are the same as for X-ray diffraction, which has already been reviewed in sections 2.2 and 2.3. The important difference between X-ray and electron diffraction is the wavelength of the beam source. In TEM, the emitted electrons have a wavelength (depending on the microscope, $\lambda \approx 0.00370$ nm ~ 0.00164 nm at 100 keV ~ 400 keV accelerating voltage) shorter than that of X-rays, resulting in a much larger Ewald sphere, (almost planar according to the radius of the sphere = $1/\lambda$). In addition, the electron transparent TEM specimen is normally very thin in the direction of the incident beam. The actual shape of the reciprocal lattice points is elongated in this direction to form rel-rods [107] (figure 2.22). The electron interact much more strongly with matter than X-rays, and therefore reciprocal lattice points do not have to be at the exact Bragg conditions to intersect the Ewald sphere. The combination of these effects results in more reciprocal lattice points being intersected by the Ewald sphere. The diffraction spots observed in TEM are therefore projections of these intersected reciprocal lattice points.

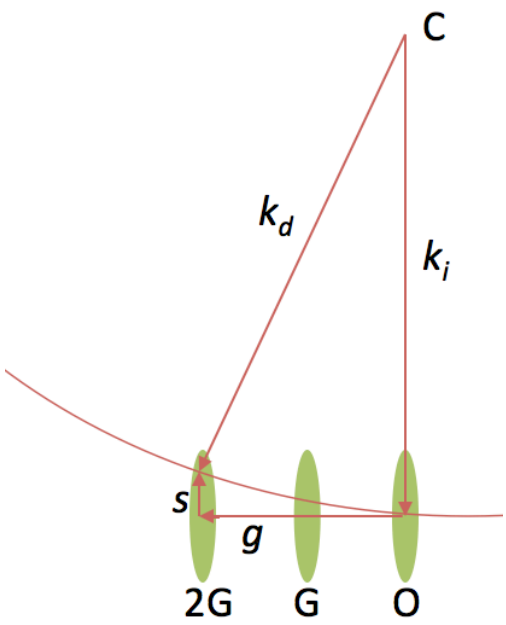

Figure 2.22: An Ewald sphere intersecting reciprocal lattice points "rel-rods". C is the centre of the sphere, k_i is the incident wave-vector, k_d is any diffracted wave-vector that satisfied the Bragg diffraction condition, and s is the excitation error that corresponds to the distance from the Ewald sphere to the reflection.

Bright field and dark field imaging

Diffraction contrast imaging is a conventional TEM technique that has been used to study the defects in the III-nitride materials throughout this thesis. The contrast in a TEM image arises due to the different Bragg conditions at the regions of the specimen that are disrupted by the presence of defects. In the bright field (BF) condition, the objective aperture that lies below the objective lens is placed at the optic axis allowing only the direct beam to pass through to form an image. In thin specimen the defects appear dark in the image due to the scattering of the electron beam by the defects, disrupting the crystallographic planes. In the dark field (DF) condition, the objective aperture is placed around a diffracted beam and in thin specimen the defects appear bright on a dark background. However, the diffracted beam is sometimes far away from the optic axis, which increases the degree of astigmatism and other aberrations due to the TEM lenses being imperfect. Therefore, the image beam is usually tilted onto the optic axis for higher resolution 'off-axis' dark field images.

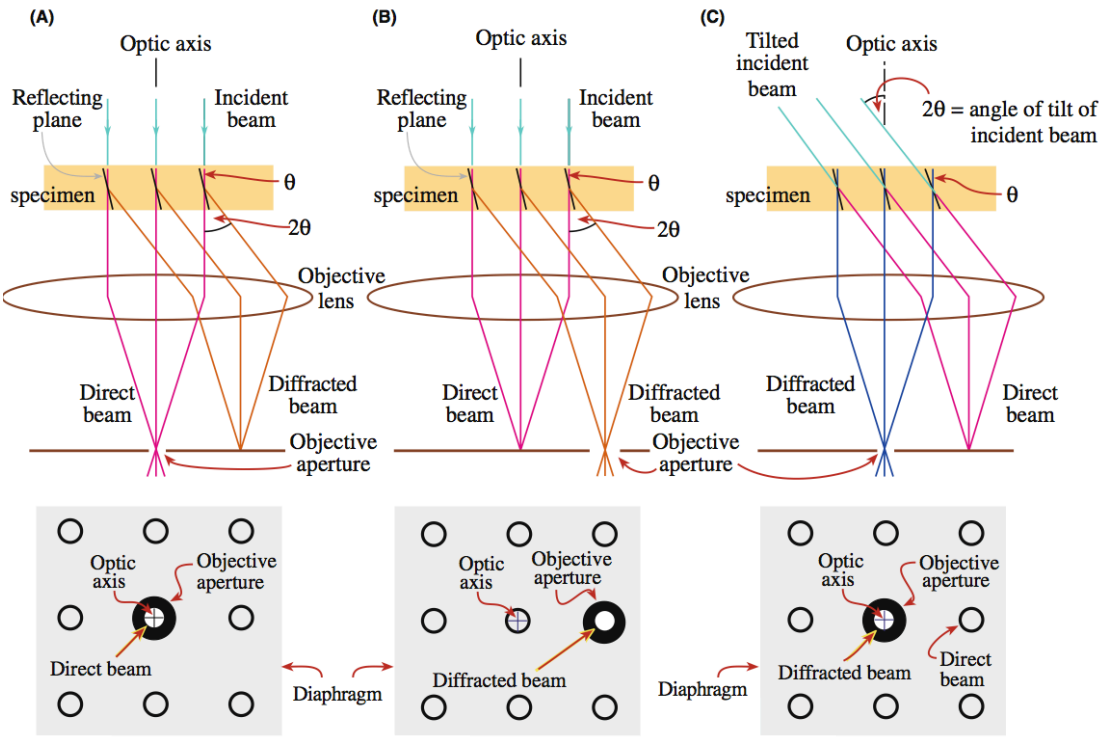

Figure 2.23: Ray diagrams showing the combination of objective lens and objective aperture used in producing (A) a BF image formed from the direct electron beam, (B) a DF image formed with aperture centred at the deflected beam, and (C) a 'off-axis' DF image where the incident beam is tilted so that the deflected beam emerges on the optic axis. (Adapted from [107]).

Weak beam dark field imaging (WBDF)

An alternative approach to dark field imaging is weak beam dark field imaging (WBDF). WBDF has become the most widely used technique for imaging high dislocation density III-nitride materials since the observed dislocation lines appear narrower (~ 1.5 nm wide [109]) and less sensitive to the specimen thickness contrast, [109] and hence the positions of these lines are well defined with respect to the dislocation cores, which is extremely useful for studying high dislocation density films. The WBDF approach has been used for this analysis because it provides higher contrast: white dislocation lines on a dark background.

The dislocations appear very narrow compared to the dislocations in the BF or DF images because only the highly strained lattice planes close to the dislocation core are sufficiently tilted to be in the Bragg condition for the incident beam.

The diffraction condition used in WBDF is slightly different from that in the on-axis DF as shown in figure 2.24a. WBDF images can be obtained when tilting the specimen far from **g**. Typically the **g**(3**g**) condition is used as it is a good compromise between obtaining good dislocation visibility at low n**g** (n = integers) and high resolution at high n**g**. For a **g**(3**g**) diffraction condition (figure 2.24b), the specimen is tilted to make the excitation error ***s*** large and the 'new' strongly excited reciprocal lattice point is now at the 3**G** position where the Ewald sphere intersects. A small objective aperture is then placed around the **G** diffracted beam to form a WBDF image. As the excitation error ***s*** increases, the intensity decreases as $1/s^2$ and the beam in the DP appears as a weak spot, hence the name, weak-beam.

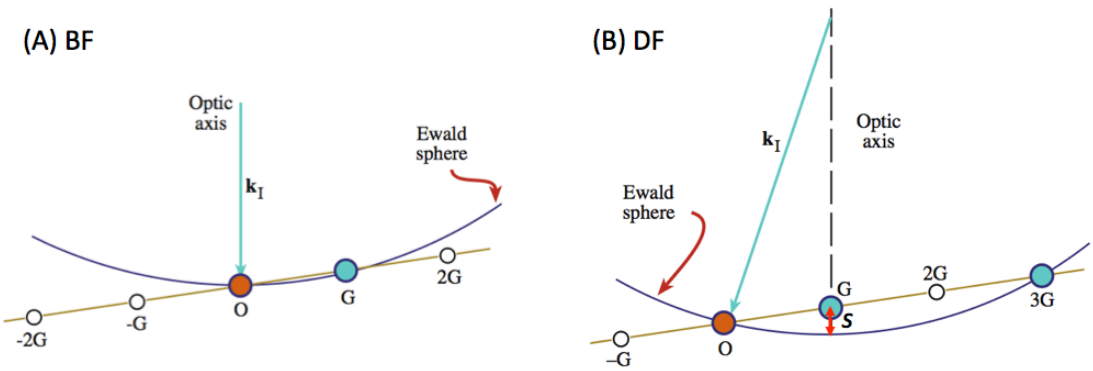

Figure 2.24: Diffraction conditions for (A) a BF image and (B) a WBDF image with **g**(3**g**) condition (adapted from [107]).

The contrast of the defects is determined by the appropriate invisibility criterion, which is derived from the dynamical theory [110] *e.g.* **g**.**b** and **g**.**b**×**u**=0, where **b** is the Burgers vector of the dislocation and **u** is a unit vector along the dislocation line. For a screw type dislocation, the **g**.**b**≠0 condition will result in the dislocation being **visible** and **g**.**b**=0 will result in the dislocation being **invisible**. For edge or mixed type dislocations, visibility will depend on both **g**.**b** and **g**.**b**×**u**. This is an extremely useful criterion for imaging particular types of dislocations. Stacking faults also produce contrast due to the disruption of the crystal lattice and their visibility depends on **g**.**R**, where **R** is the lattice translation associated with the stacking faults. These invisibility criterions is summarised in Table 2.2.

Table 2.2: Invisibility criteria used for distinguishing between different types of dislocation or stacking faults.

Defects	Characteristic	Visible g vector =
BSF	**R** = ⅓[1-100]	[1-100], [11-20]
PSF	**R** = ½[10-11]	[0002], [1-100], [11-20]
a-TD	**b** = ⅓[11-20]	[1-100], [11-20]
c-TD	**b** = [0001]	[0002]
PD	**b** = ⅙[20-23]	[0002], [1-100], [11-20]

Zone axis	**g** = 0002	**g** = 1-100	**g** = 11-20
[0001]	n/a	BSF, PSF, PD	PSF, PD, a+c-TD
[1 $\bar{1}$00]	BSF, PD, a+c-TD, c-TD	n/a	PSF, PD, a+c-TD, a-TD
[11 $\bar{2}$0]	PD, a+c-TD, c-TD	BSF, PSF	n/a

The **g**-vectors needed for the invisibility of edge dislocations are perpendicular to those needed for screw dislocations. Hence the best specimens to use for Burgers vector determination are cross-sectional specimens. The [11-20] and [1-100] zone axes are readily accessible in c-plane material and the [0001] and [1-100] zone axes are accessible in nonpolar material. Examples of the diffraction patterns obtained along each zone axis are shown in figure 2.25.

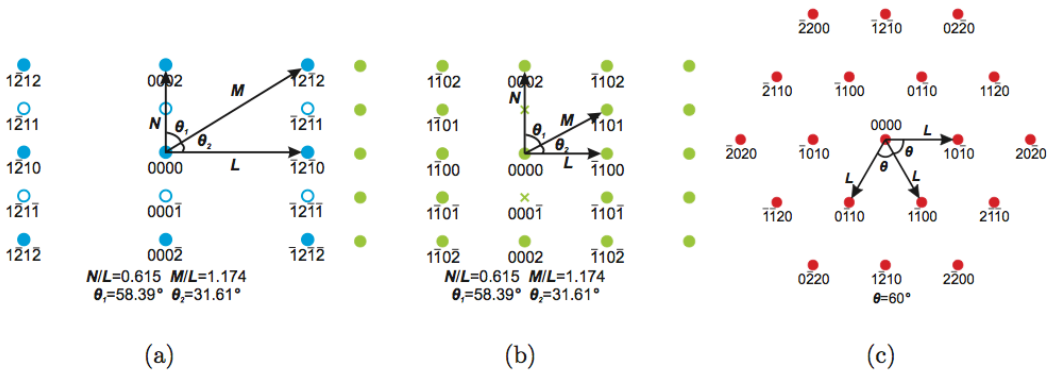

Figure 2.25: Three commonly used diffraction patterns for wurtzite III-nitrides on the (a) [1-100] (b) [11-20] and (c) [0001] zone axes. Open circles represent forbidden

reflections. Crossed reflections are present due to dynamical diffraction. (Adapted from [111]).

Convergent beam electron diffraction

CBED is a powerful technique that can be used to extract many kinds of structural information from a very localised area in a specimen, such as film thickness measurements [112]. In this work, CBED is used to determine the bond symmetry (polarity), rather than to characterise defects in III-nitride materials with cross-section samples. As mentioned in figure 2.21, the diffracted disks are formed when converging the electron probe on the specimen. An example of such a CBED pattern in GaN viewing along the [1-100] zone axis is shown in figure 2.26 (further details in Chapter 6).

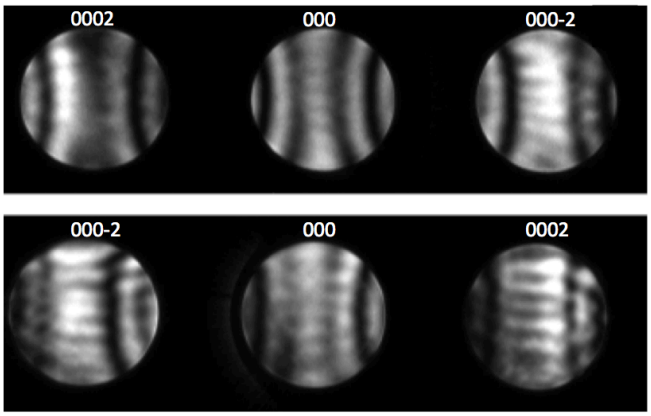

Figure 2.26: Two CBED patterns of GaN viewed along the [1-100] zone axis taken at the either side of an inversion domain boundary. Contrast is different for the (0002) and (000-2) disks due to the non-centrosymmetric crystal.

The CBED patterns exhibit opposite contrast due to the polarity of GaN, *i.e.* the crystal is non-centrosymmetric in real space. This method has been successfully used in the literature to determine the polarity of the inversion domains present in a GaN epilayer [113] and also the work in Chapter 6. However, the contrast of the disks also varies with TEM specimen thickness; the bright band in the centre of the (000-2) disk can swap with the dark band in the centre of the (0002) disk and vice-versa for certain specimen thicknesses. Therefore it is preferable to carry out the CBED measurements

at the regions that have at least 100 nm thickness and only small variations in thickness.

To determine the absolute polarity of the layer, CBED patterns must be compared to simulated patterns using Bloch wave calculations in the EMS software [114]. Detailed experimental and modelling techniques can be found in the work by Sharma *et al.* [115]

2.8 Scanning transmission electron microscope (STEM)

In contrast to conventional TEM where a parallel incident electron beam is used, a converged electron beam is used in STEM. A much smaller and a brighter electron probe can be achieved by the FEI Tecnai F20 TEM with a field emission gun source (FEG) operating at 200 kV due to more spatially localised electron emission. This small electron probe is then used to scan the specimen and build up an image on a point-by-point basis. An annular dark-field (ADF) detector is used to collect electrons from an annulus around the beam, sampling far more scattered electrons than in conventional dark-field imaging where only diffracted electrons can pass through the objective aperture. This provides an advantage in terms of signal collection efficiency. A high angle ADF detector (HAADF) collects electrons that are scattered inelastically by thermal diffuse scattering to large angles (figure 2.27). The contrast in STEM-HAADF images is therefore most strongly influenced by compositional variation (the signal varies approximately as the square of atomic number [107]) and is often termed z-contrast imaging.

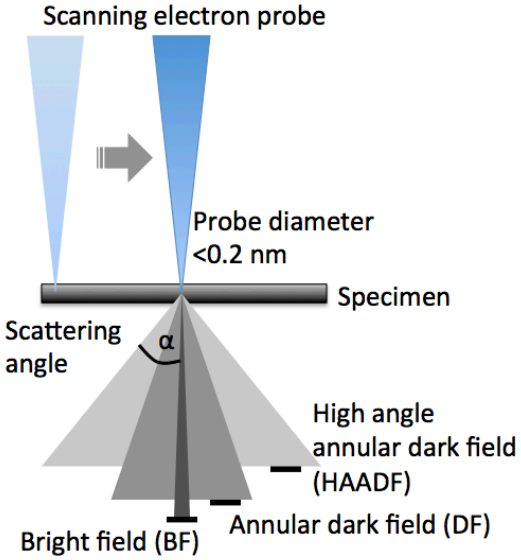

Figure 2.27: Schematic of the arrangement of sample and high angle dark-field (HAADF) detector in STEM.

STEM-HAADF is used to image the nonpolar GaN/AlGaN quantum wells in Chapter 6. The GaN wells appear brighter than AlGaN barriers due to gallium's higher atomic number (figure 2.28).

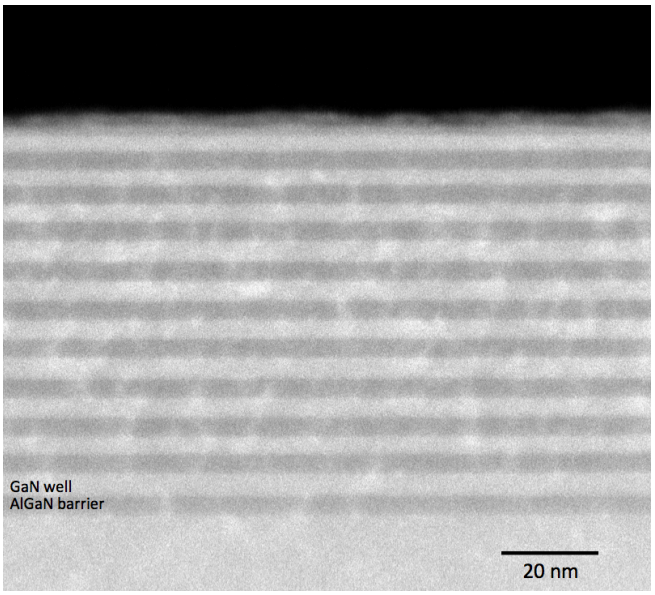

Figure 2.28: A STEM-HAADF image of GaN/AlGaN MQWs grown on a nonpolar GaN template. GaN well appear brighter due to higher gallium atomic number.

3

c-plane AlGaN grown on AlN template: Defect analysis

3.1 Background

The growth of AlGaN alloys of high aluminium content on a thick AlN buffer layer has attracted much interest recently because AlN buffer layers are optically transparent for deep UV radiation (sub-290nm). They also prevent cracking as AlGaN layers grown epitaxially on AlN are under compressive strain, due to the different lattice mismatch between GaN (a=3.1893Å) and AlN (a=3.1130Å). However, there is a large lattice mismatch strain between AlN and the sapphire substrate and the strain is relaxed by the generation of dislocations. Therefore AlN films usually have a very high density of threading dislocations. These dislocations are observed to extend into the succeeding AlGaN layer, which can degrade the device performance as dislocations are thought to be nonradiative recombination centres.

It is well known that when a strained layer exceeds a critical thickness [116], misfit dislocations are generated by interfacial migration of pre-existing threading dislocations, or by the nucleation and subsequent glide of dislocation loops, or by direct nucleation of new dislocations in nearly perfect crystal materials [117][118]. The strain relaxation process in AlGaN/GaN heterostructures has been discussed extensively in the literature [24] and is dominated by the combined processes of interfacial misfit dislocations and cracks [119]. It has been suggested that the cracks are introduced to the film first and help promote nucleation of dislocation half loops,

which consequently determine the quantity of misfits presented at the interface. However, in the case of little-discussed AlGaN/AlN heterostructures cracks are normally suppressed due to the compressive strain. Instead, these compressively strained heterostructures are largely relaxed by the generation of bent threading dislocations in addition to the misfit dislocations.

These threading dislocations bend away from their original [0001] direction and, in conjunction with the misfit dislocations, they are the dominating strain relaxation mechanisms in these films, as reported by several authors [119][120][121]. However, for heterostructures that have much higher lattice mismatch (e.g. $Al_{0.2}Ga_{0.8}N$ epilayer grown on AlN), other defects such as dislocation multiplication mechanisms (e.g. Frank Read sources) and inclined dislocation arrays (discussed in the next chapter) and hillocks on the layer surface can also occur in these structures, as reported in this work. These additional defects are rarely discussed in the literature. The Frank-Read sources, for example, have been reported for SiGe on Si cubic systems [122][123] but are not discussed in AlGaN/AlN systems. Inclined dislocation arrays have not been reported before. Their origins and how they interact with other defects in the materials is unclear but all these additional defects present in the epilayer can contribute to the strain relaxation processes. It is necessary to understand their properties and the influences on the film quality in order to reduce or eliminate these defects that are detrimental to the device performance.

3.2 Aim

Specific aims of this chapter include:

1. To study the microstructural properties of each type of defect using characterisation techniques such as (S)TEM, XRD and SEM-CL.

2. To investigate the effect of AlGaN epilayer composition on the distribution of these defects.

3. To evaluate the strain attributed to each type of observed defect using in-situ wafer curvature measurement in conjunction with the microscope data.

3.3 Experimental details

All samples studied in this chapter were grown by Dr. Menno Kappers at the University of Cambridge, using metalorganic vapour phase epitaxy (MOVPE) in a Thomas Swan 6 x 2" close-coupled showerhead reactor with trimethylaluminium (TMA), trimethygallium (TMG) and ammonia (NH_3) as precursors and hydrogen as carrier gas. Initially, 4 µm thick AlN layers were deposited on c-plane sapphire substrate (0.25° ± 0.10° towards $(11\bar{2}0)$) for all the samples. For this, the sapphire substrates were thermally cleaned for 7 minutes in a flow of hydrogen, followed by a predose of 56 µmol TMA in the absence of ammonia, and the growth of a 30 nm thick AlN nucleation layer at a pressure of 200 Torr, a V-III ratio of 250 all at a temperature of 1050 °C, followed by high-temperature AlN growth at 50 Torr, 1130 °C and a V-III ratio of 60. These templates were re-introduced in the reactor and were overgrown with a ~2 µm $Al_xGa_{1-x}N$ layer at 1100 °C and 50 Torr, where x = 0.23, 0.44, 0.72 and 0.87, for sample C3901A, C3902A, C3903A and C3905A, respectively (see Table 3.1). A schematic of the sample is shown in figure 3.1.

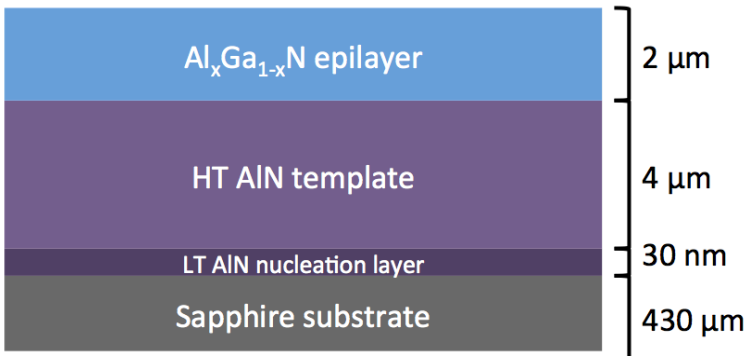

Figure 3.1: Schematic of the structure for a deep UV emitter.

Table 3.1: Aluminium contents in the samples determined by XRD.

Sample	Aluminium content in $Al_xGa_{1-x}N$ epilayer
C3901A	0.23
C3902A	0.44
C3903A	0.72
C3905A	0.87

3.3.1 Growth of high quality thick AlN template

The TMA predose method in the initial AlN growth was used to create an Al-polar coverage of the substrate before growth. This predose method was found greatly to reduce the number of inversion domains in the film beyond these of the conventional continuous growth method (mixed polarity) [124][125]. This enables us to grow a thicker AlN layer without cracking, and at the same time achieve a low threading dislocation density, favourable to the growth of the succeeding AlGaN hetero-epilayer. Figures 3.2 and 3.3 give an example of a low magnification overview of the sample microstructure under cross-sectional TEM. Defect reduction is apparent in these images as the film thickness increases (see Chapter 6 for further details on the growth of high quality AlN template)

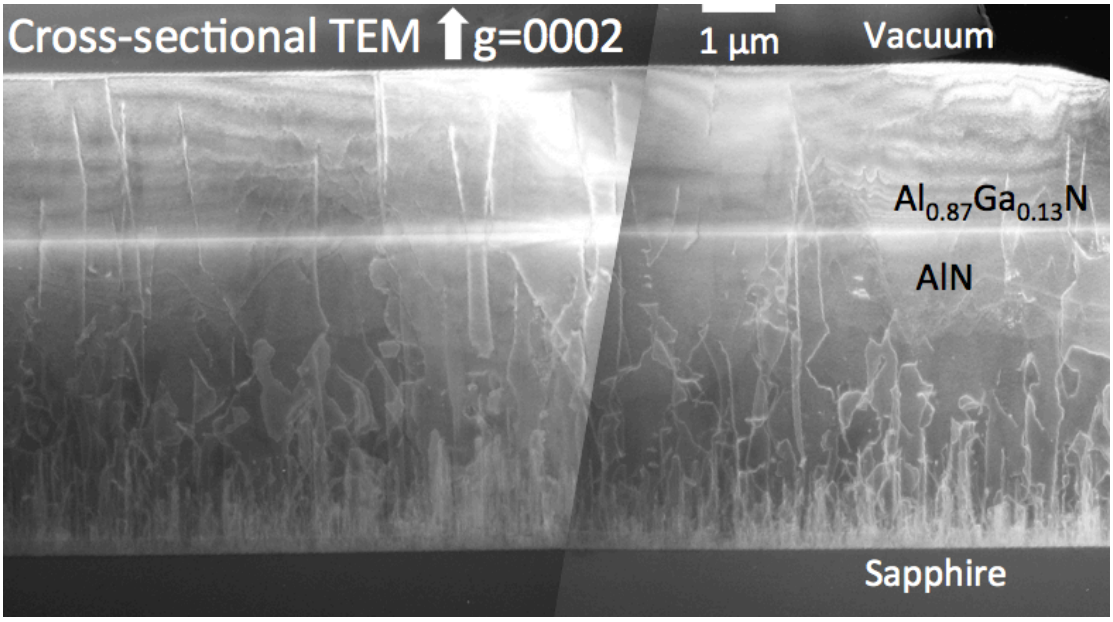

Figure 3.2: Cross-sectional TEM image of C3905A, viewed along [1-100] using g=0002 condition , showing reduced *a*+*c* and *c*-type dislocations and annihilation as the AlN layer thickness increases.

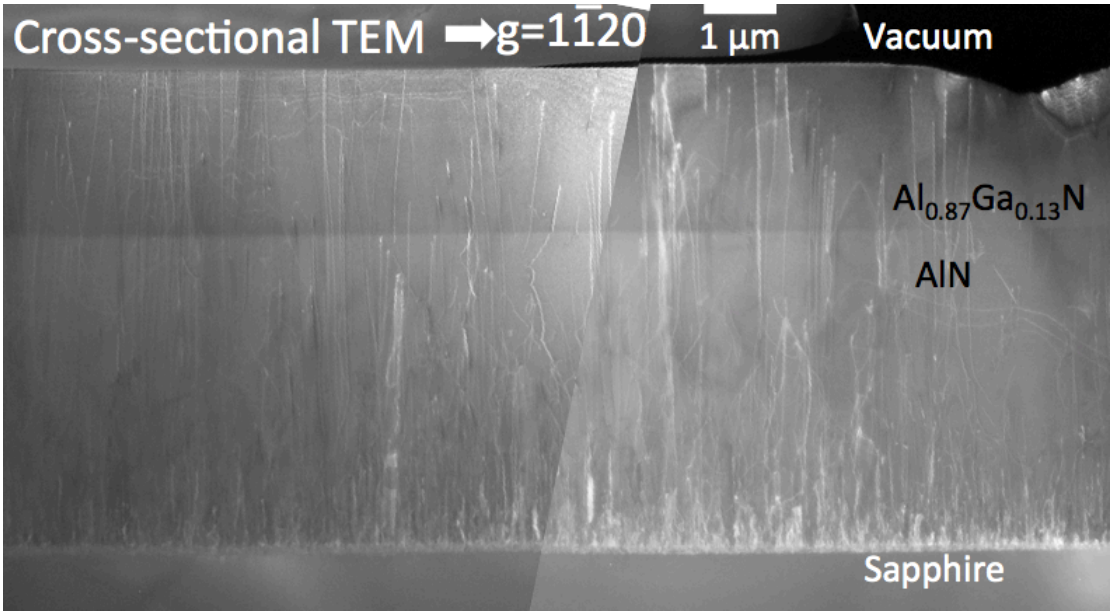

Figure 3.3: Cross-sectional TEM image of C3905A, viewed along [1-100] using g=11-20 condition, showing reduced *a*+*c* and *a*-type dislocations and annihilation as the AlN layer thickness increases.

3.4 Results

3.4.1 XRD results

The following table summarises the XRD data collected by Dr. Clifford McAleese from this set of AlGaN epilayers grown on AlN templates. The threading dislocation density was calculated from the plan-view TEM results. The difference between C3901A, C3902A, C3903A and C3905A is the aluminium content used for the AlGaN growth, 23%, 44%, 72% and 87%, respectively.

Table 3.2: Summary of XRD FWHM values and threading dislocation densities for the samples used in this work.

Sample	$Al_xGa_{1-x}N$ x =	AlGaN relaxation wrt AlN	ω scan FWHM				TD Density /cm^{-2}
			AlGaN (002)	AlGaN (101)	AlN (002)	AlN (101)	
C3901A	0.23	77%	256	679	251	445	$1.6\pm0.1\times10^{10}$
C3902A	0.44	68%	246	570	254	449	$3.4\pm0.2\times10^{9}$
C3903A	0.72	21%	219	431	218	462	$3.3\pm0.2\times10^{9}$
C3905A	0.87	6%	200	411	219	465	$4.3\pm0.1\times10^{9}$

The AlGaN composition and strain state were determined from reciprocal space maps of the (0002) and (10-11) reflections. In AlGaN layers where significant strain relaxation has taken place clear strain/compositional variations are present. In such cases the analysis was carried out for the highest intensity peak as this is likely to be most representative of the surface region to be measured by PL.

Lower Al content AlGaN layers have broader (101) ω peaks (the AlN templates are largely consistent in the series), which, in conjunction with the TEM analysis (shown in the next section) confirmed there was an increase in edge-type threading dislocations, as a result of the strain relaxation process.

The FWHM values for both AlGaN and AlN layers indicated that the film quality improves as the aluminium content increases in the AlGaN layer, as expected from the smaller lattice mismatch with respect to AlN. All the samples studied in this work showed improvement on older samples that did not employ the TMA predose method. This again confirms the importance of the high quality AlN template for the succeeding AlGaN epilayer growth.

3.4.2 Electron microscopy

Dislocation reduction and annihilation as well as various types of dislocations were observed in the epilayer. With low-aluminium content, high lattice mismatched samples such as C3902A, several types of dislocations were observed, as shown in figures 3.4 and 3.5.

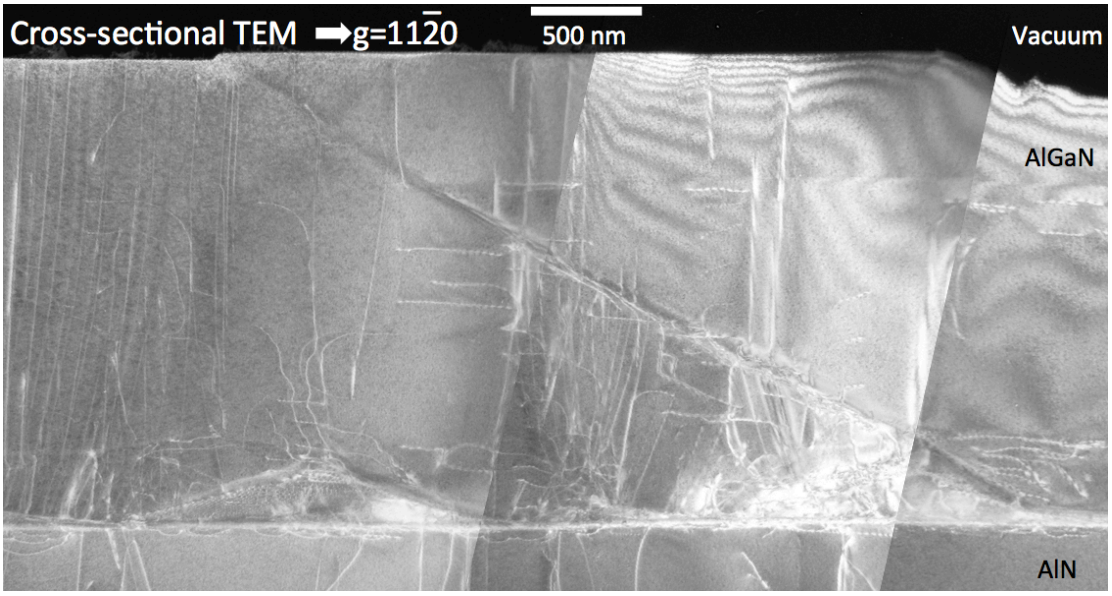

Figure 3.4: Cross-sectional TEM image of C3902A, viewed along [1-100] using g=11-20 condition. Four different types of defect were observed in the AlGaN epilayer.

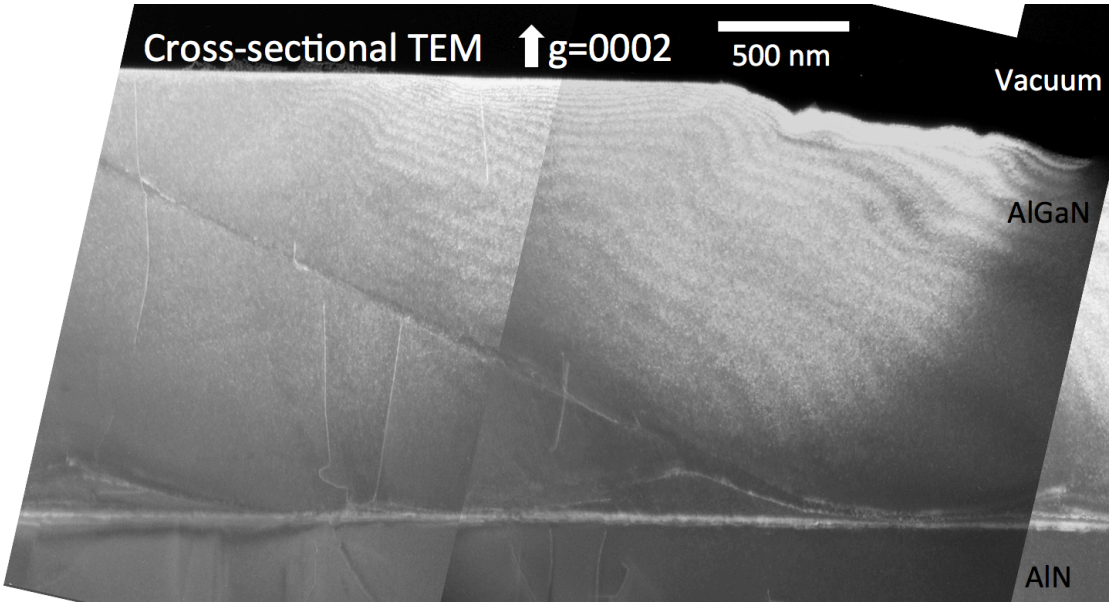

Figure 3.5: Cross-sectional TEM image of C3902A, viewed along [1-100] using g=0002 condition. Only an inclined dislocation array and a few a+c-type dislocations are visible.

Using *g.b* criteria, these figures indicated that most of the dislocations were *a*-type and only a few were *a*+*c* or *c*-type dislocations. The micron-scale inclined dislocation array (discussed in chapter 4) remained visible in both imaging conditions.

Figures 3.6 and 3.7 show the cross-sectional TEM images of the high aluminium content and low lattice mismatch sample, C3905A. Again most of the dislocations were *a*-type.

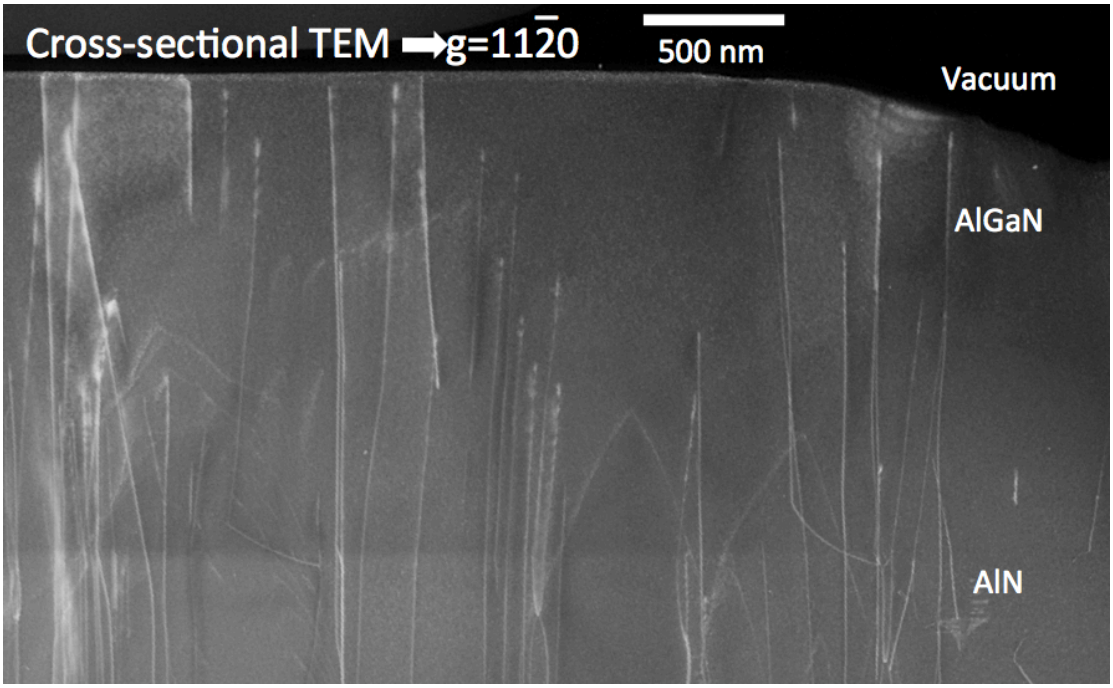

Figure 3.6: Cross-sectional TEM image of C3905A, viewed along [1-100] using the g=11-20 condition, showing *a*+*c* and *a*-type dislocations.

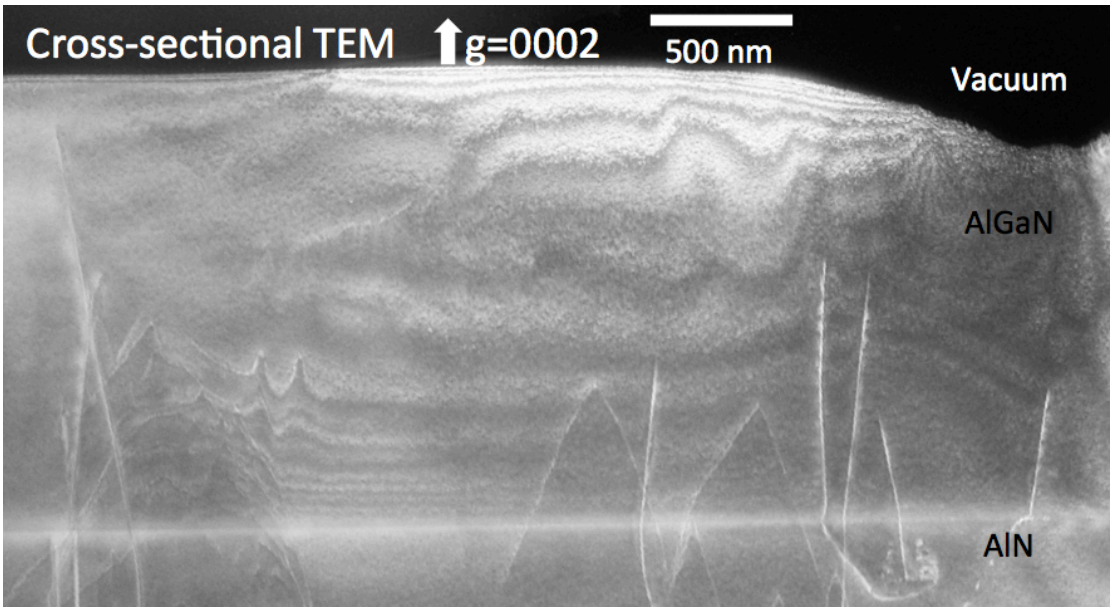

Figure 3.7: Cross-sectional TEM image of C3905A, viewed along [1-100] using the g=0002 condition, showing *a*+*c* and *c*-type dislocations.

This high Al-content sample had a much "cleaner" microstructure than that of the low Al-content sample showing just TDs in the AlGaN epilayer, as was expected with

slight relaxation. Most of the dislocations propagated through the heterointerface from the pre-existing dislocations in the AlN template.

Cross-sectional TEM of these samples shown above identified 4 types of defects. All the characterisation techniques used in this chapter identified a total of 6 types of defects in the AlGaN film. These include:

1. Helical threading dislocations
2. Bent threading dislocations
3. Inclined dislocation arrays
4. Misfit dislocations (shown later using large angle TEM tilt)
5. Frank-Read sources
6. Flat and spiral hillocks (shown later using plan-view SEM-CL)

The following sections focus on the observations on each of the 6 types of defect.
The effect of different AlGaN compositions on the distribution of these defects will be discussed extensively in chapter 3.5.

3.4.2.1 Threading dislocation half-loops

Some of the a-type threading dislocations thread up from the AlGaN/AlN heterointerface and form half loops in the AlGaN epilayers, as shown in figure 3.8.

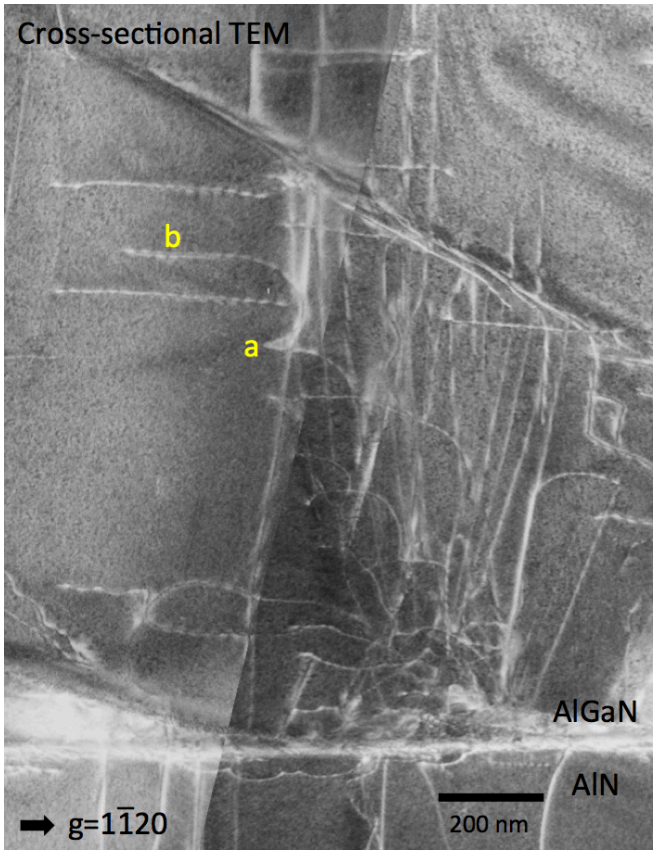

Figure 3.8: Higher magnification image focused on the helical threading dislocations.

The sharp angle of the dislocation line at position **a** could indicate a turning point of a helical circle. The distinctly oscillating contrast of the dislocation line at position **b** is due to diffraction contrast varying with depth as the inclined dislocation passes through the specimen thickness. This indicates that the dislocation line was going into or out of the page. These observations suggest that these TDs could be helical TDs. The presence of helical threading dislocations is not very common in the III-nitride films. Dislocation movements, such as climb, probably govern the formation mechanism as suggested by Fu et al. [126], using finite element simulations (more details in chapter 3.5). This type of threading dislocation was observed only in the two low-Al content samples, C3901A and C3902A and the density of this defect was higher in the C3902A sample. Another interpretation of the observed features could be that the dislocations are pinned by impurities and as dislocations glide, half-loops are formed similarly to those seen in dislocation multiplication processes, such as Frank-Read sources.

3.4.2.2 Bent threading dislocations

All four epilayers of different AlGaN composition studied in this work showed some TDs inclined away from the [0001] direction (figure 3.9).

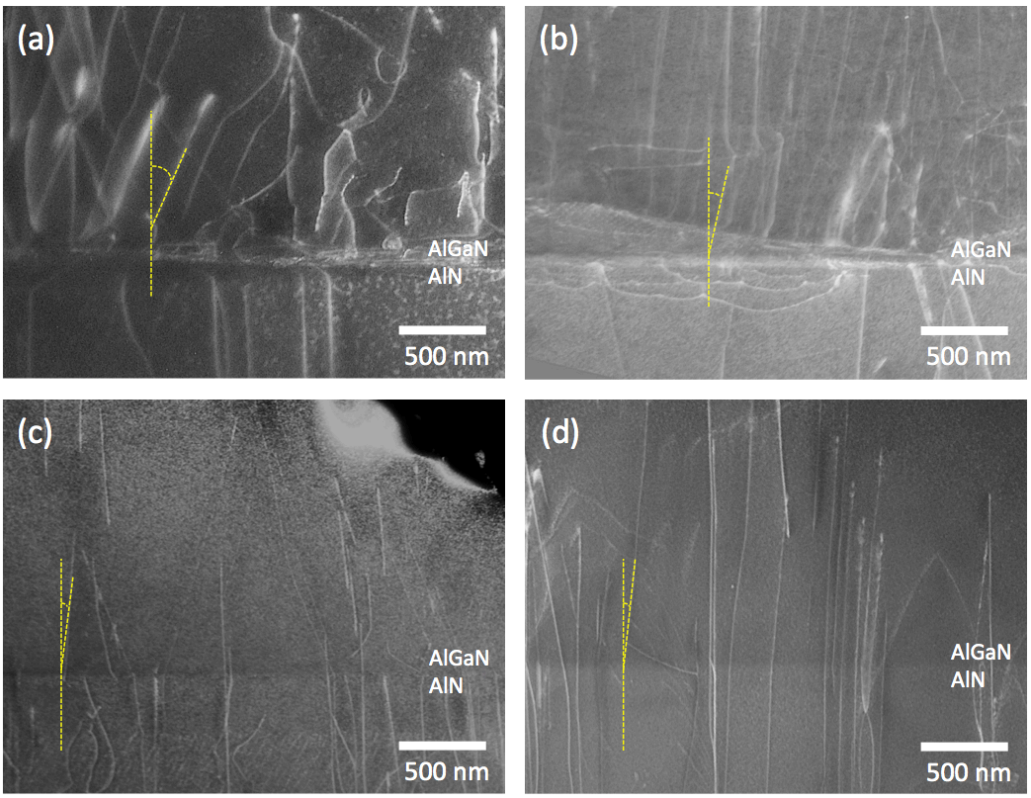

Figure 3.8: Cross-sectional TEM images all viewed along [1-100] with g = 11-20, showing a-type threading dislocations bend away from their original [0001] direction. The bend angle increases as Al-content decreases, as shown in the (a) 23%, (b) 44%, (c) 72% and (d) 87% $Al_xGa_{1-x}N$ epilayer.

Table 3.3: Average bend angles, α, of the bent threading dislocations against AlGaN layer compositions.

Sample	$Al_xGa_{1-x}N$, x =	ρ_{BTD} / cm^{-2}	α / °
C3901A	0.23	$1.6\pm0.1\times10^{10}$	22.1
C3902A	0.44	$3.4\pm0.2\times10^{9}$	15.6
C3903A	0.72	$3.3\pm0.2\times10^{9}$	15.2
C3905A	0.87	$4.1\pm0.1\times10^{9}$	8.3

From these TEM images it was clear that the pre-existing threading dislocations in the AlN template were inclined at certain angles upon entering the compressively strained AlGaN epilayer. The degrees of inclination (α, averaged over 30 TDs) were dependant on the Al-content of the AlGaN layers. These bent threading dislocations have been noted in the literature in similar AlGaN/AlN heterostructures [120]. They also suggested the compressive strain in the AlGaN film could be relieved by bending these threading dislocations away from the [0001] direction. The inclination direction of these *a*-type TDs is not random as confirmed by the plan-view TEM data from the similar structures in the literature [120][121]. They always incline toward <1-100> directions, perpendicular to their Burgers vector ***b***= 1/3<11-20>. The misfit components of these bent threading dislocations can either add to or relieve the strain in the compressively strained film depending on the sign of the Burger's vectors. For instance, if two misfit components with opposite Burger's vectors move into coincidence, the sum of the Burger's vector will be zero (two opposite extra half planes would cancel), and the overall strain relieve may be less than expected. Thus it is important to determine the sign of Burger's vector in order to carry out an accurate quantitative strain analysis. However, determining the sign of Burger's vector would require the use of LACBED [178], high-resolution TEM or simulation of the stress field from a plan-view TEM image, these techniques can be complicated and beyond the scope of this chapter, therefore the characterization of the Burger's vectors will be done in the future work.

The cause of this inclination is not very well understood, as bending cannot be caused by conventional dislocation movements such as glide or climb (further details in section 3.5). Faceted growth could be a possible reason for the TD bending (e.g. 3D to 2D growth, details in chapter 1.3.6), however this kind of bending normally only occur at the initial growth stage and no longer bend after the initial TD reduction and annihilation. Thus, this cannot explain the reason for the bent TDs having line directions that continue linearly to the sample surface.

3.4.2.3 Inclined dislocation arrays

The micron-scale inclined dislocation arrays are observed for samples with relatively low Al-content, such as C3901A and C3902A (see figure 3.9). These dislocation

arrays appear to be related to the surface steps of the AlN template. The direction of the bent threading dislocations changes (inclined toward the original [0001] direction) when they encounter these arrays, which might suggest strain-relief related mechanisms between the TDs and arrays. Detailed studies of these inclined dislocation arrays are shown in chapter 4.

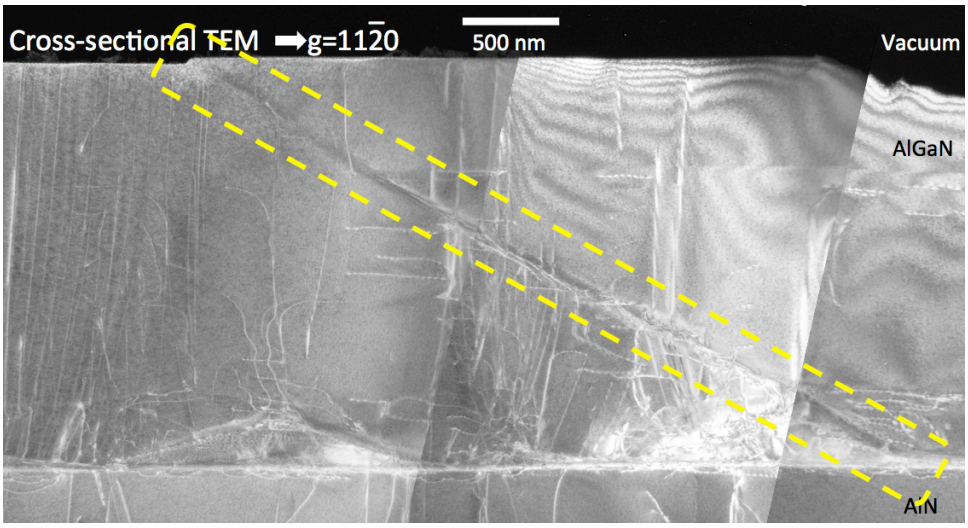

Figure 3.9: Cross-sectional TEM image of C3902A showing a large scale inclined dislocation arrays running across the entire AlGaN epilayer.

3.4.2.4 Misfit dislocations

Misfits dislocations can be imaged using both plan-view and cross-sectional electron microscopy. For plan view samples the buffer layer has to be very thin (<100 nm) in order to reveal the triangular grid of misfit dislocations on the interface. They are normally observed as a triangular grid since each misfit dislocation can have one of the three <1-100> line directions and hence each pair forms a 60-degree angle.

For samples that have thicker buffer layers on top of the interface, cross sectional electron microscopy has to be used. Misfit dislocations can be imaged with the sample tilted to a large angle (over 35-degree) from the usual imaging zone axis, e.g. [11-20] or [1-100] to broaden the projection of the interface. The resulting zone axis after the tilting is a [10-11] zone axis (see figure 3.10). This is useful as misfit dislocations lying on the interface that is normally parallel to the electron beam appear as dots on the image and become very difficult to identify. With tilting, the

misfit dislocations will appear as short lines across the tilted interface and are easy to identify as they appear as an unique dotted line due to the distinctly oscillating contrast (see figure 3.11). The oscillations are produced by the diffraction contrast varying with depth in the TEM specimen as the misfit dislocations pass through its thickness [107].

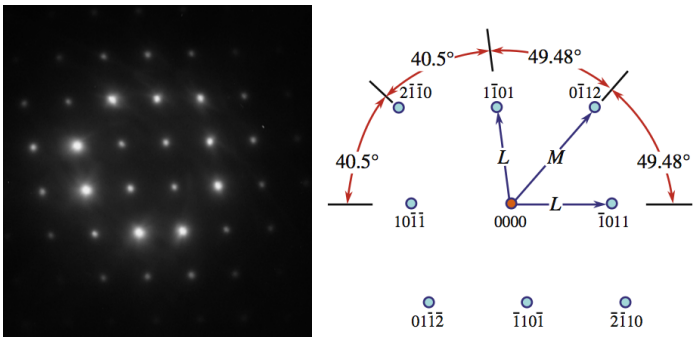

Figure 3.10: Diffraction pattern of the 10-11 zone axis.

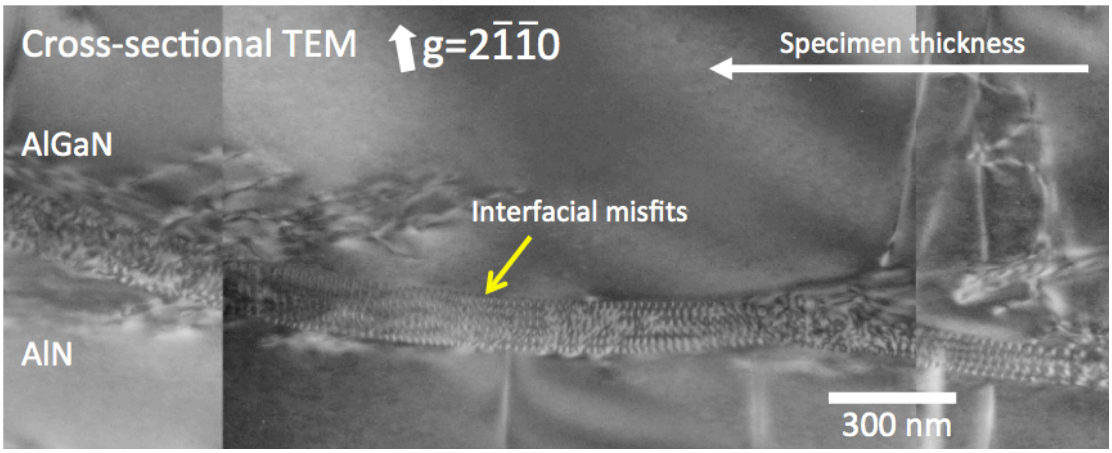

Figure 3.11: Cross-sectional TEM image of C3902A after a large angle tilt to reveal the interfacial misfit dislocations (indicated by the yellow arrow).

The length of the interfacial misfits observed in this imaging condition is directly proportional to the specimen thickness due to 3D to 2D projection. The misfit length increases as the specimen thickness increases.

High resolution XTEM has been used to confirm the spacing between each extra half plane, which represents the true misfit dislocations.

An image at 500kx magnification was taken from a very thin sample area, which contains the interface of AlGaN and AlN. The interface was identified from the change in contrast (figure 3.12).

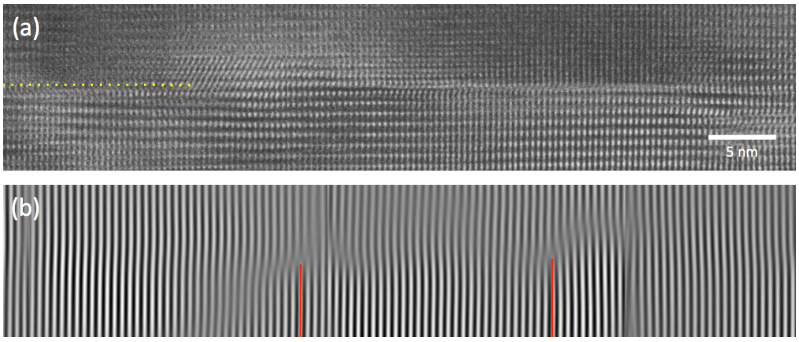

Figure 3.12: (a) High resolution XTEM image at the AlGaN/AlN heterointerface indicated by the yellow dotted line. (b) corresponding Fourier transformed image showing two extra half-planes indicated by the red lines.

A total of 14 images of 512 pixel-squares was taken continuously across the sample for Fourier Transform purposes. The masks were applied to show only the contrast perpendicular to the interface, i.e. showing the extra half planes normal to the interfaces.

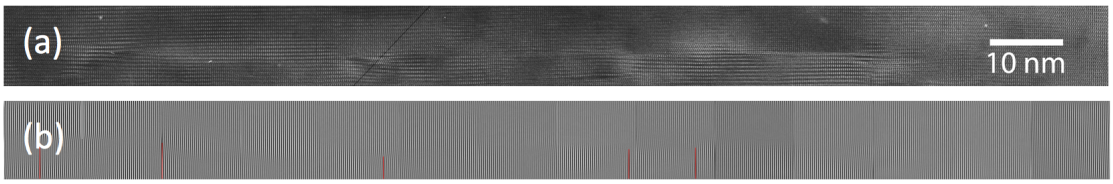

Figure 3.13: (a) A total of 14 HRTEM images at the interface. (b) Corresponding Fourier transformed image showing 5 extra half planes as indicated by the red lines.

Over the total image length of 150 nm across 14 images (figure 3.13), there were 5 misfit dislocations identified resulting in 30 nm spacing between each misfit dislocation. This is consistent with the observation from a dark field XTEM image, where the spacing average was found to be around 33 nm. This also confirms that the well-defined short dotted lines were indeed misfit dislocations, consisting of extra half planes on the AlGaN/AlN interfaces. Note that the extra half-planes are mostly below the interface indicating that the material below the interface has smaller lattice spacing and therefore is AlN.

Misfit dislocations were observed for the low Al-content samples in C3901A and C3902A. The distance between each misfit dislocation was estimated to be around 33 nm (averaged over 50 misfits) for both samples. However, I did not see any interfacial misfit across a few microns of the sample area for samples with higher Al-content

(figure 3.14). This was expected from the small relaxation determined from XRD earlier. However, for C3903A with 73% Al-content, the critical thickness is still much less than ~10 nm (according to the critical thickness calculation on the similar compressively strained InGaN/GaN system by Holec et al [33]) and normally misfits should be generated above this critical thickness. It is likely that other mechanisms, such as bent threading dislocations, dominate the strain relaxation in this case.

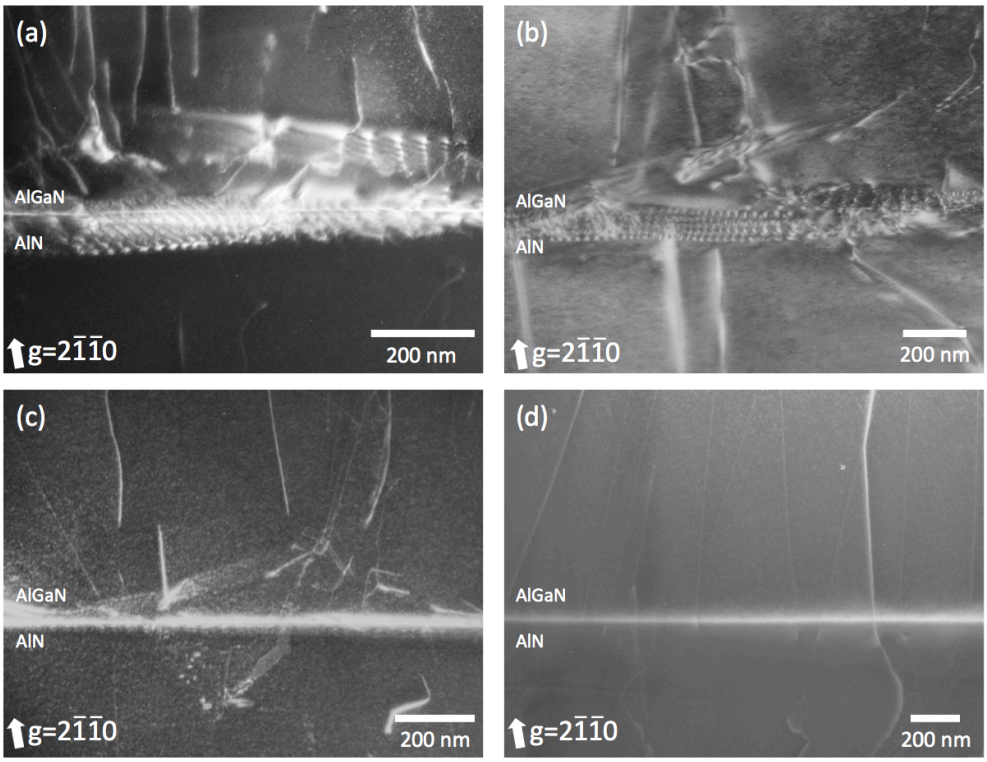

Figure 3.14: Cross-sectional TEM image of (a) 23%, (b) 44%, (c) 72% and (d) 87% of Al-content in the AlGaN epilayers. All the images were taken with large angle tilt under the [10-11] zone axis condition.

Table 3.4: Average distance between misfit dislocations, d_m, against AlGaN composition.

Sample	$Al_xGa_{1-x}N$, x =	AlGaN relaxation wrt AlN	d_m / nm
C3901A	0.23	77%	33±5
C3902A	0.44	68%	33±5
C3903A	0.72	21%	n/a
C3905A	0.87	6%	n/a

3.4.2.5 Frank-Read multiplications

Frank-Read sources were observed using WBDF TEM at the interface between AlGaN and AlN. These dislocation multiplication processes can occur in systems such as SiGe film grown on Si substrate [127]. A Frank-Read source occurs when a dislocation (figure 3.15) is pinned in the basel plane at two ends either by impurities or an immobile non-basal dislocation. If a shear stress is resolved onto the basel plane, the dislocation line becomes unstable and begins to bow. With increasing stress, the line bows back onto itself to produce a new loop that is free to progagate, and a section that remains pinned, which may initiate more loops. In these AlGaN/AlN samples the origins of the Frank-Read sources are the interfacial misfit dislocations.

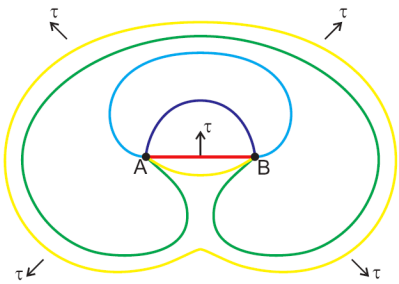

Figure 3.15: Schematic of a Frank-Read source. A dislocation (red line) bows out due to the local shears associated with nearby defects and is locally pinned [128].

A similar observation in the literature was reported by Floro et al [119] and showed interfacial dislocation multiplication in an AlGaN/GaN film, due to misfit segments gliding in the basal plane and pinned by propagating threading dislocations from the underlying GaN. However, there is little explanation in the literature of why Frank Read Sources operated in a non-basal plane and extended into the underlying AlN layer (figure 3.16). Frank-Read sources that operated below the interface at the AlN region were not observed from pure AlN template growth on sapphire (not shown), which implied that they must have occurred during or after the succeeding AlGaN growth.

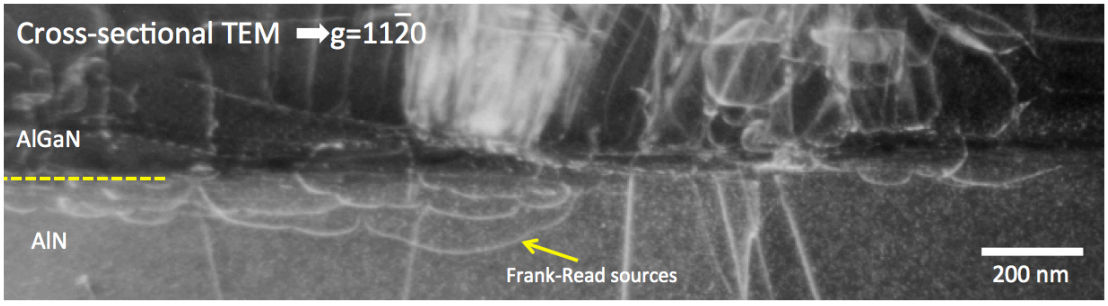

Figure 3.16: Cross-sectional TEM image of C3902A taken with g=11-20 condition. Yellow dashed line indicated the heterointerface of AlGaN/AlN layers. Yellow arrow shows the Frank-Read sources under the heterointerface.

These Frank-Read sources were only observable under the g=11-20 imaging condition, suggesting they were pure *a*-type dislocations, consistent with their sources of origin, the *a*-type interfacial misfit dislocations.

The reason for these Frank-Read sources operating in the underlying AlN template may be found in the work on SiGe on the Si system by M. Albrecht et al. [127] who suggested that the stress can concentrate at the trough of the surface features (e.g. surface steps), which generates a positive stress. If this positive stress is great enough, it can cause the underlying misfit dislocations, pinned by the pre-existing threading dislocations, to inject the misfit dislocations into the substrate. Such an observation has not been reported for hexagonal crystal structures.

In our results, it is notable that most of the Frank-Read sources occurred when there was a triangular area (bounded by the inclined dislocation arrays, see figure 3.17) present above the interface. There were no evidences of troughs at the heterointerface, suggesting that the formation of Frank-Read sources was different compared to the study by Albrecht *et. al.* An alternative explanation might involve strains occurring due to a thermal gradient across the template and the epilayer. However, further work is required to understand whether this would be the case.

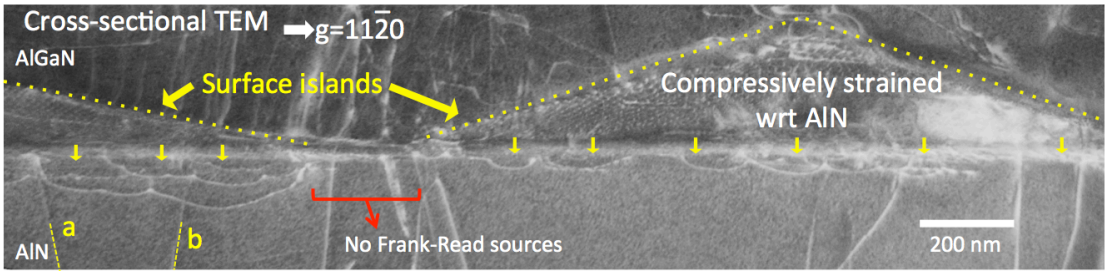

Figure 3.17: Cross-sectional TEM image of C3902A taken with g=11-20 condition. The yellow dashed line indicates the surface islands above the heterointerface. Positions **a** and **b** show two yellow dotted lines indicating two pre-existing threading dislocations in the AlN template that pinned the interfacial misfit dislocations.

It is interesting that Frank-Read sources occurred only in the sample with 44% Al-content AlGaN layer (C3902A), but not in any other sample. It was expected that the Frank-Read sources would also occur in the 23% Al-content AlGaN sample (C3901A) due to similar relaxation and high number of dislocations that could give raise to large stress to generate these Frank-Read sources.

This inconsistency might be due to the amount of triangular areas on the heterointerface. These areas were formed when two inclined dislocation arrays with opposite inclined directions coalesce. Since there were far fewer inclined dislocation arrays in the 22% Al-content AlGaN sample, and therefore there was no triangular area presented in the film (at least over a few micron of area under XTEM), we did not observe any Frank-Read sources. This suggests that Frank-Read sources only occur when a significant quantity of inclined dislocation arrays were generated in the AlGaN epilayer.

3.4.2.6 Flat and spiral hillocks

Plan-view spatially resolved CL analysis was carried out for this set of samples. In plan-view, C3901A, which has the lowest aluminium content of 23%, showed a very rough surface as expected due to large relaxation of 77% from the XRD data. C3902A was similar to C3901A where a large number of surface step edges (figure 3.18) were observed due to the relatively low aluminium content and large relaxation. The surface steps were much less radiative than the surrounding materials. (The steps are

associated with inclined dislocation arrays, discussed in chapter 4). In addition to these surface steps, a large number of hillocks were observed in C3901A but not on other samples (figure 3.20), some unusual micron sized crystals were observed in the centre of each hillock. These crystals seemed to oriented at either <1-100> or <11-20> directions (figure 3.20a). Our data were insufficient to explain their occurrence. Further work will be required to understand whether they were reactor-related impurities or were intrinsic to the materials. C3905A with 87% aluminium content showed a much smoother (atomically flat) surface with uniform surface emission, which is again expected from the slight relaxation of 6% (figure 3.19).

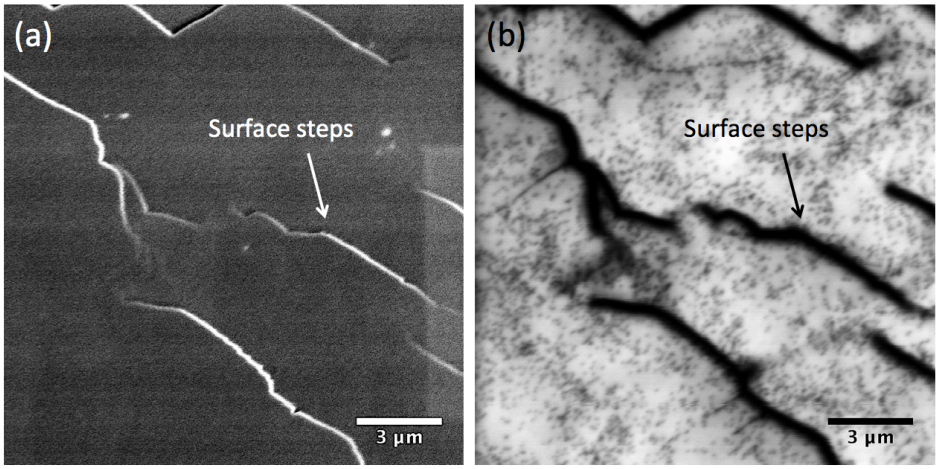

Figure 3.18: (a) Plan-view SEM and (b) corresponding panchromatic CL images of C3902A taken at 75K. Arrows indicate surface steps that are non-radiative recombination centres.

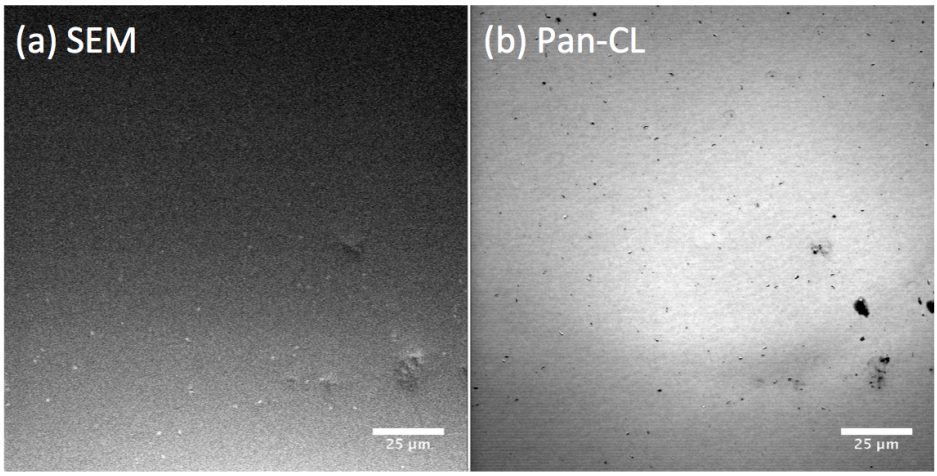

Figure 3.19: (a) Plan-view SEM and (b) corresponding panchromatic CL images of C3905A taken at 75K.

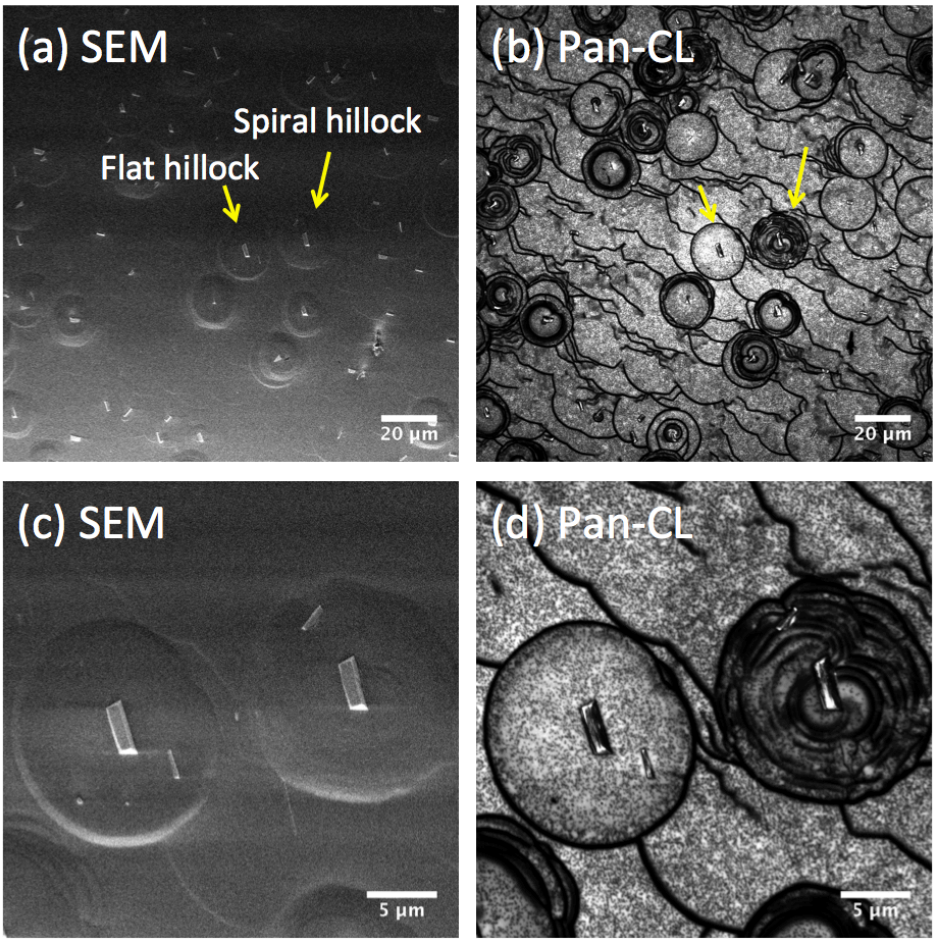

Figure 3.20: Low magnification images of (a) plan-view SEM and (b) corresponding panchromatic CL of C3901A taken at 75K . Higher magnification images of (c) plan-view SEM and (b) corresponding panchromatic CL images of the flat and spiral hillocks.

The C3901A plan-view CL results showed two types of hillocks, flat and spiral. For the spiral hillock, emission from the centre of the hillock was redshifted by 7±3 nm relative to that of the flat hillock (figure 3.21 b). Both types of hillock have longer emission wavelength on the hillock edges (figure 3.21 c), which is likely due to the absence of QCSE at these semipolar facets.

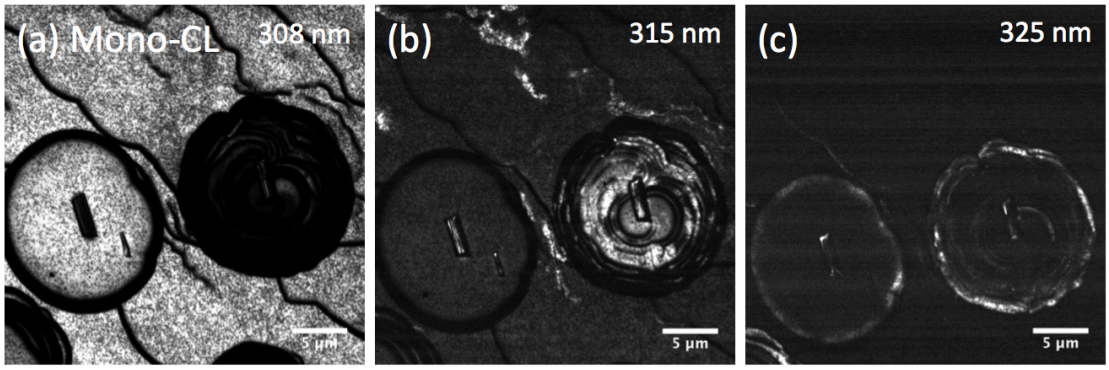

Figure 3.21: Monochromatic CL images taken at (a) 308 nm, (b) 315 nm and (c) 325 nm wavelength.

These spiral hillocks were often reported for MBE GaN films but not for MOCVD films (shown later). It is well known that control of the growth surface is very important to the device fabrication. A rough surface can lead to poor film quality and ultimately affects the device performance. These spiral hillocks can cause variations in surface height that may lead to a non-uniform quantum well thickness and the spiral structure may lead to fluctuations in the composition of nitride alloys and dopant concentration. It is important to understand the origin of these surface non-uniformities and how they can be controlled.

An early theoretical study by Burton, Cabrera and Frank [129] predicted that when a mixed threading dislocation intersects with the atomically smooth free surface, a pinned step is created from the dislocation slip plane with ends of the step fixed to the mixed dislocation. In certain growth conditions, these pinned steps can elongate and bow out from the dislocation with one end fixed at a mixed dislocation and wind into a spiral centre. The continuous growth of a pinned step can result in spiral hillocks.
Heying et al. [130] observed such formations on the GaN surface grown by MBE (figure 3.22), similar to the observation in this work. Heying et al. and Merlin et al. [131] found a simplified condition in which spiral hillocks form. The condition is defined by the relation between the miscut terrace width, w_{MC} and the width of a terrace on the two interlocking spiral ramps that create a spiral hillock, w_s.

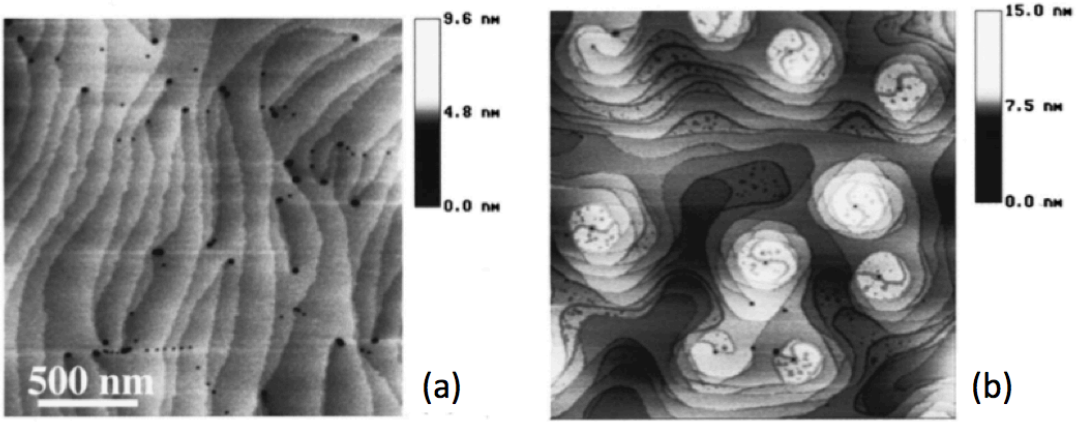

Figure 3.22: The AFM images from Heying *et al.* show the morphologies of an (a) MOCVD and (b) MBE grown GaN film. [130]

They concluded that if w_{MC} was smaller than w_s, the miscut steps would annihilate the spiral steps faster than the spiral could spread on the surface and therefore spiral hillocks form when $w_{MC} >> w_s$.

In our case the terrace widths w_{MC} and w_s can be measured by plan view SEM images (w_s is measured and averaged by taking the diameter of the hillocks and dividing by the number of spiral layers). w_{MC} is measured to be around 15 μm and w_s to be around 2.5 μm. And indeed the $w_{MC} >> w_s$ is satisfied. w_s is also proportional to the curvature of the initial step line connected to the mixed dislocation. It was reported that the decrease in curvature (which is related to the step energy) is proportional to decreasing III/V ratio. Therefore the lower the III/V ratio, the larger w_s and once it is larger than w_{MC} the formation of spiral hillocks should be inhibited. This also explains why the formation of spiral hillocks was not normally observed in samples grown by MOCVD. The III/V ratio of MBE is much higher than that in MOCVD but for low Al% AlGaN grown on AlN, the III/V ratio is also higher, which can lead to smaller w_s satisfying the spiral formation condition. It might be possible to prevent the formation of these hillocks in the AlGaN samples by using smaller substrate miscut steps. However, in Heying's model, the spiral hillocks were around 5 nm in diameter, whereas the diameter can be as large as 10 μm in our case. Detail work will be required in the future to determine the limitations of application of Heying's model to these data.

3.5 Discussion

Stress is known severely to affect the film quality and consequently the device performance due to wafer bending and defect formation. Although for AlGaN/AlN heterostructures, cracking is usually suppressed due to the compressive stress, dislocation formations can become very complicated due to the presence of several types of defect, as shown in the results section. It has also been shown that the AlGaN epilayers with different Al-content significantly influence how these different types of defects are produced and distributed in the film. Those observed defects could have their own influences on relaxation of the heterostructures.

Table 3.5 summarises the observations on how each type of defect was distributed in all four AlGaN epilayers with different Al-content. It can be seen that most of the defect types were observed in samples of low-Al content. Only bent threading dislocations were observed for high-Al content.
The main differences of C3902A compared with C3901A were (a) higher HTDs density, (b) smaller BTDs angle, (c) larger IDA angle, (d) larger degree of Frank-Read sources bowing and (e) no surface hillocks. The main difference between C3905A and C3903A was only a smaller BTDs angle.

Because several types of defects were generated concurrently in the film (especially for the low-Al content AlGaN epilayers), understanding of how they interrelated and influenced the film quality can be complex. In order to understand accurately and in detail why they were distributed in this way, a quantitative strain analysis on each of the defects was required.

Table 3.5: Summary of the distributions of each type of defect observed in four AlGaN compositions.

Sample	C3901A (23%Al)	C3902A (44% Al)	C3903A (72% Al)	C3905A (87% Al)
Relaxation wrt AlN	77%	68%	21%	6%
TDD / cm^{-2}	$1.6\pm0.1\times10^{10}$	$3.4\pm0.2\times10^{9}$	$3.3\pm0.2\times10^{9}$	$4.3\pm0.1\times10^{9}$
Helical threading dislocation	Low density of HTDs occurs at around half way up the AlGaN layer	Relatively higher density of HTDs occurs at the heterointerface and up to around 2/3 of the AlGaN film	None observed	None observed
Bend threading dislocation	Relatively large bend angle initially (~22.1°) up to around 0.45 µm thick. Smaller angle afterward (~8.3°)	Relatively large bend angle initially (~15.6°) up to around 0.83 µm thick. Smaller angle afterward (~4.3°)	Average bend angle across the entire AlGaN film ~15.2°	Average bend angle across the entire AlGaN film ~ 8.3°
Inclined dislocation arrays	IDA observed across the entire AlGaN layer with ~15° inclination	IDA observed across the entire AlGaN layer with ~30° inclination	None observed	None observed
Misfit dislocations	High density of misfits with ~33 nm spacing between each misfits	High density of misfits with ~33 nm spacing between each misfits	None observed	None observed
Frank-Read sources	FR sources observed operating in the underlying AlN template	The same as C3901A. The degree of bowing is larger compared to C3901A	None observed	None observed
Surface morphology	In addition to surface steps, both flat and spiral hillocks observed on the surface	Surface steps (related to the IDA)	Atomically flat surface	Atomically flat surface

This discussion section aims to describe how the AlGaN composition affects the distribution of the defects based on quantitative strain analysis, with the aid of in-situ wafer curvature measurement.

This description is explained in the following sub-sections:

3.5.1: Purposes of using in-situ wafer curvature measurement for this work.
3.5.2: Estimate of total strain, ε_T.
3.5.3: Estimate of strain associated with misfits, ε_m and BTDs, ε_{BTD},
3.5.4: Estimate of strain associated with other types of defects.

The main assumption used in this work is that the total strain relieved ε_T is equal to the strain relieved from all different types of defects observed in the epilayers.

$$\varepsilon_T = \varepsilon_{HTD} + \varepsilon_{BTD} + \varepsilon_{IDA} + \varepsilon_{misfit} + \varepsilon_{FR}$$

where ε_{HTD}, ε_{BTD}, ε_{IDA}, ε_m and ε_{FR} is the strain relieved by helical threading dislocations, bent threading dislocations, inclined dislocation arrays, misfit dislocations and Frank-Read sources respectively.

On this assumption, the total strain ε_T may be estimated using the in-situ wafer curvature measurement. ε_{BTD} and ε_m may be estimated using the same approach. Once these values are known the strain associated with other types of defects can be extracted from this equation. Using this approach it is possible to understand why certain types of defects are generated only in certain AlGaN compositions.

3.5.1 In-situ wafer curvature measurement

In recent years, in-situ wafer curvature measurement has become popular in measuring the stresses in films. It has very frequently been reported in the literature that strain engineering via wafer curvature measurement has been successfully

employed to develop crack-free AlGaN on GaN buffer layers [132] and optimise the growth recipes for GaN on Si close to zero wafer bow [133].

This technique also has the advantage of characterising the stress at the growth temperature, unlike other techniques such as XRD, where the determined stress state is at post-growth stage. Effects from cooling have to be taken into account and may complicate the overall strain analysis.

Most importantly, in-situ wafer curvature measurement has the advantages of determining the strain at a specific thickness of the sample, whereas XRD averages the strain across a macroscopic scale. It is useful, for instance, to obtain the strain state at the AlGaN/AlN heterointerface where most of the strain is relieved by the interfacial misfit dislocations, or to obtain the strain state close to the sample surface, where most of the strain is relieved by bent threading dislocations. This gradual decrease in strain state toward the surface of the sample can only be determined using this in-situ curvature measurement. With this information to hand, it is possible to determine quantitatively the effects of different types of dislocations on relaxation processes at different stages of growth (see figure 3.23).

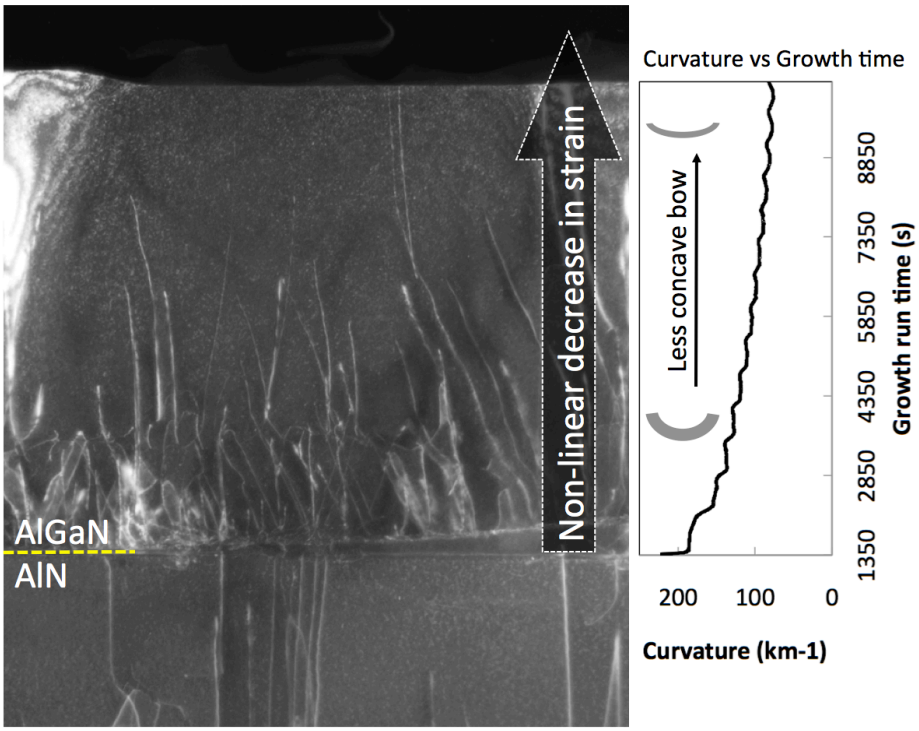

Figure 3.23: XTEM image of C3901A with corresponding curvature to the right. A non-linear decrease in strain was observed from beginning to the end of the growth.

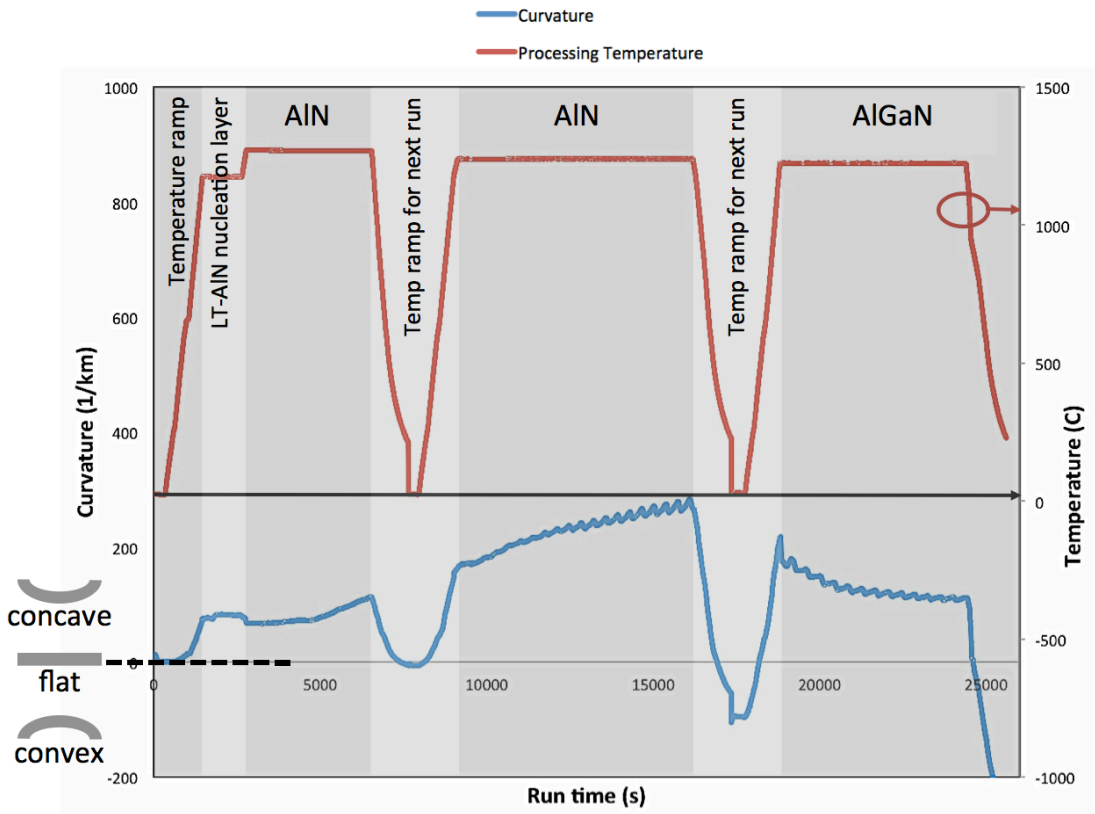

Figure 3.24: Temperature and curvature during growth of sample C3902A.

Figure 3.24 above shows an example of temperature and wafer curvature measurement of sample C3902A during growth. The growth recipe is shown in the previous experimental details section (section 3.3). Several templates were produced with the same growth recipes, hence the breaks (cool down and re-heat) due to sample batches between different growth stages. The AlN template grown on a sapphire substrate is under tensile stress and therefore the wafer becomes concave as expected and shown in the figure. An AlGaN epilayer grown on an AlN template is under compressive stress and therefore the wafer curvature decreases and bows toward the original flat wafer.

In theory, if the AlGaN epilayer was fully strained (without any relaxation) with respect to the AlN template, the wafer curvature would stay the same with increasing layer thickness (for a relatively thin epilayer). In practice, relaxation occurred most of the time by generating a high density of defects. This process relieved some of the strain in the heterostructures and therefore the wafer curvature decreases. Given this relationship, strain in the film can be estimated (shown in next section). In the case of

C3902A shown above (figure 3.24) the decreasing curvature was not linear; the gradient also decreases as the film thickness increases. This indicated that the interfacial misfit dislocations relieved a relatively greater degree of strain initially and a lesser relaxation then took place after a certain layer thickness but at a lower rate, which might be correlated to the bent threading dislocations and other types of defect observed in TEM.

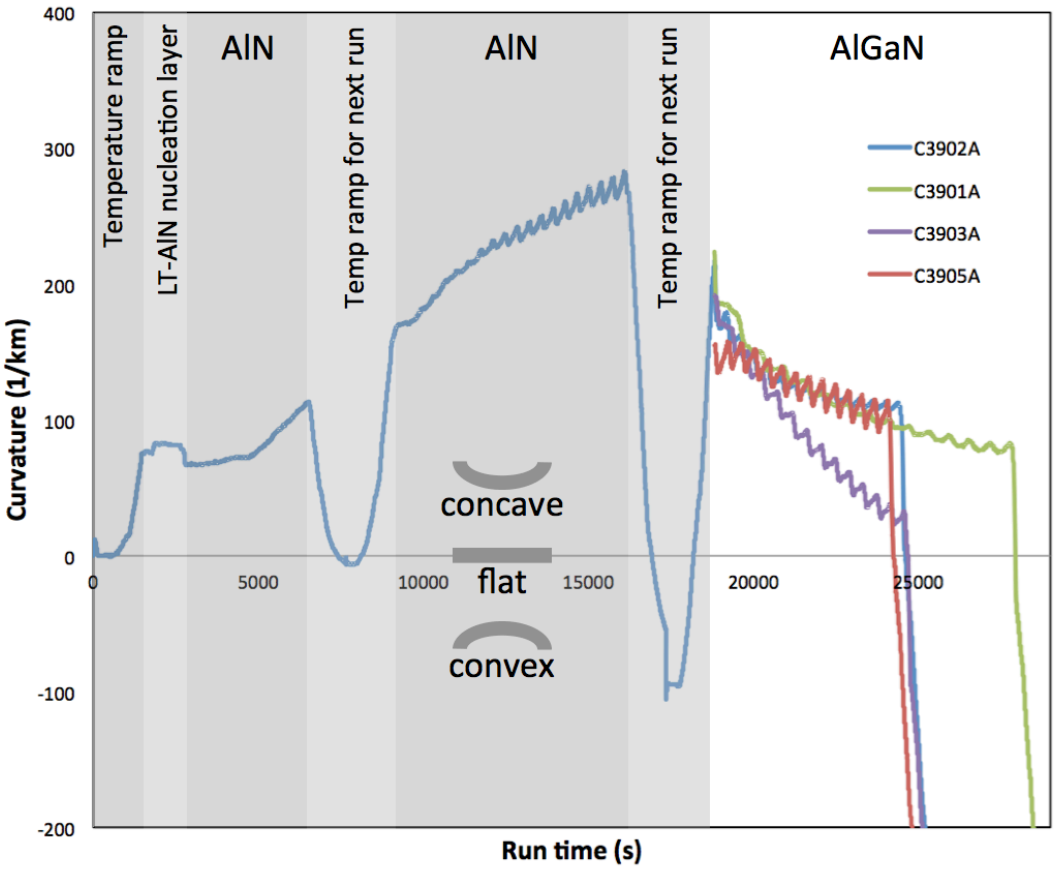

Figure 3.25: Wafer curvature measurements during growth of C3902A (blue), C3901A (green), C3903A (purple) and C3905A (red).

Figure 3.25 compares AlGaN compositions grown on top of the same AlN templates. Sample C3901A had a larger overall change in wafer curvature than C3902A did, which was expected from the largest lattice mismatch. The curvature trend was similar to that of C3902A, suggesting a relatively large degree of strain was relieved initially due to interfacial misfit formation. In C3905A the overall change in curvature was the smallest, as expected from the much smaller lattice mismatch. Its wafer

curvature decreased linearly, which reflected the observations from TEM images, where bent threading dislocations provided the only strain relaxation mechanism. However, sample C3903A showed an even greater change in wafer curvature despite the defect distributions being similar to those of C3905A.

3.5.2: Estimate of total strain, ε_T.

There are 4 contributions to wafer bowing:

(a) The initial bow of the sapphire substrate. This value is very small and can be disregarded in this calculation.
(b) Curvature change caused by a vertical temperature gradient. When the temperature is ramped to the desorption temperature (in order to desorb volatile surface contamination) the bowing of the sapphire substrate due to a difference in the vertical temperature gradient across the thickness of the sapphire (430 μm) i.e. the temperature difference between top and bottom of the substrate. The in-situ curvature measurement showed a linear increase of substrate bowing between 650°C to 1050°C (see figure 3.23). Since the growth temperature for AlGaN and AlN is similar and the curvature caused by the vertical temperature gradient can be treated as a constant, this value can also be disregarded.
(c) Thermal mismatch. Since the layer is grown at constant temperature, the difference of thermal expansion coefficient between an epilayer and substrate is also constant and can be ignored in this calculation.
(d) Lattice mismatch induced change in curvature during growth at a constant temperature. This change is directly associated to the strain in the film and is used for strain analysis.

This change in curvature is based on the measurement of the substrate curvature κ in the centre of the wafer. The data are normally interpreted using the classical Stoney formula [134].

$$\kappa = \frac{6M_f h_f}{M_s h_s^2} \times \varepsilon$$

Where κ is the curvature measured in situ, M_f and M_s are the biaxial modulus of the film and substrate respectively, ε is the mismatch strain and $h_{f,s}$ is the thickness of film layer and substrate. M_f and M_s can be calculated using:

$$M_{f,s} = C_{11} + C_{12} - 2C_{13}\left(\frac{C_{13}}{C_{33}}\right)$$

However, the elastic constants of AlGaN at the growth temperature are not readily available in the literature and several different values have been reported [135]. They are assumed to be similar to the biaxial modulus of GaN at high temperature, i.e. 449.6GPa. (For comparison, M for AlN is 470 GPa)

The mismatch strain ε can also be expressed as:

$$\varepsilon = \frac{a_f(T) - a_s(T)}{a_s(T)} = \frac{\Delta a_f}{a_s}$$

$$\Rightarrow \frac{\Delta a_f}{a_s} = \text{Gradient of the curvature} \times \frac{h_s^2 M_s}{6M_f}$$

Thus the lattice parameters of the epilayer can be estimated with the curvature gradient data obtained from the in-situ measurements (the gradient is the change of curvature over a certain film thickness). The curvature gradient must be measured cautiously due to the artefacts arising from oscillations in the reflected light laser (reflections and resonances with the substrates) [136]. Also it is necessary to use the gradient values at the very beginning of the growth before significant relaxation has occurred (when curvature becomes nonlinear) since this method can become complicated and unreliable if the gradient was averaged over a nonlinear trend line due to relaxation.

Total strain is then determined from these estimated lattice parameters. In order to calculate the lattice parameters at the growth temperature, the two-step effective substrate method has to be used [137] because all the multilayers grown on sapphire

are affected by the strain associated with the layers underneath. The strain, a_f, in each layer has to be determined first and applied to the next layer, a_f^*. (see figure 3.26 for schematic).

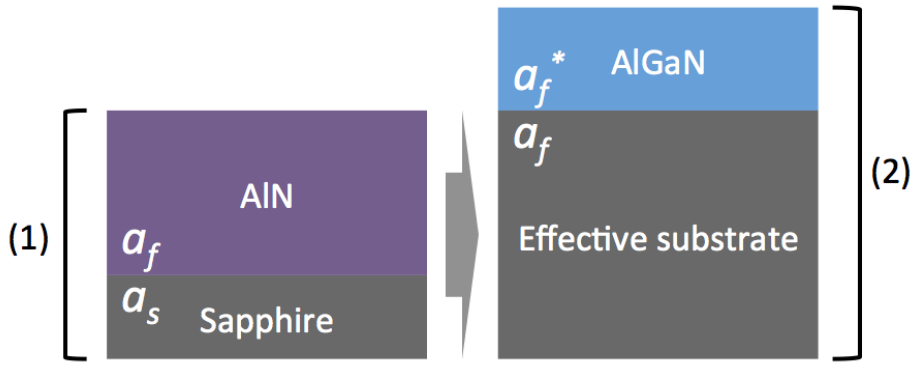

Figure 3.26: Schematic of two-step effective substrates method

Table 3.6 summarises the total strain in each AlGaN composition calculated from the lattice parameters determined from curvature data.

Table 3.6: Lattice parameters of AlN, a_f, and AlGaN, a_f^* using in-situ wafer curvature measurements. The composition, x, of $Al_xGa_{1-x}N$ and the total strain relieved were resolved using the calculated lattice parameters of AlN and AlGaN.

Sample	XRD $Al_xGa_{1-x}N$, x =	Calc. AlN a_f / nm	Calc. AlGaN a_f^* / nm	Calc. $Al_xGa_{1-x}N$, x =	Calc. total ε
C3901A	0.23	0.3117±1E-4	0.3181±5E-4	0.104±0.035	0.0204
C3902A	0.44	0.3117±1E-4	0.3156±1E-4	0.429±0.005	0.0124
C3903A	0.72	0.3117±1E-4	0.3131±5E-5	0.753±0.002	0.0044
C3905A	0.87	0.3117±1E-4	0.3120±5E-5	0.896±0.002	0.0026

The calculated AlN lattice parameter, a_f, is the actual lattice parameter at the growth temperature on sapphire; for reference, the bulk lattice parameter for AlN is 0.3112 nm [135]. Using the two-step effective substrate method the calculated AlN lattice parameter then become the effective substrate lattice parameter for the calculation of the AlGaN layers. Therefore the calculated AlGaN lattice parameter should represent the actual lattice parameter at the growth temperature. The errors were produced when

measuring the best-fit lines for the gradient of the curvature. The errors were larger for lower Al% AlGaN layers due to larger changes in curvature.

The calculated AlGaN compositions were in good agreement with the XRD results. However, in the case of C3901A the calculated composition was markedly inconsistent with the XRD. This might be due to the error terms or to the finding mentioned earlier that XRD averages over the entire AlGaN film to obtain the lattice parameters, whereas wafer curvature measures the lattice parameters at the heterointerface where the strain is at its maximum.

3.5.3: Estimate of strain associated with ε_m and ε_{BTD}.

The strain relaxation produced by the misfit dislocations is given by [137]:

$$\varepsilon_m = \frac{3}{2} \times \frac{a}{\lambda}$$

Where a is the lattice parameter of the layer below the interface, in this case the AlN. The strain is corrected by a factor of 3/2. The reason for this is that there are three <1-100> misfit directions on the (0001) basal plane. However, we can only image two out of 3 misfit directions using cross-sectional TEM images (section 3.4.2.4) and assuming the misfit dislocations have equal densities in all three directions (which is the case with hexagonal crystal structures), therefore a factor of 3/2 has to be taken into account. λ is the spacing between each misfit dislocation (~33 nm in both C3901A and C3902A, see section 3.4.2.4). In order to yield good statistics of the spacing, 100 data points are collected cross several cross-sectional TEM images to obtain averaged values.

Table 3.7: Misfit strain calculations.

Sample	XRD $Al_xGa_{1-x}N$, x =	Calc. AlN a_f / nm	Calc. total ε	Misfit strain
C3901A	0.23	0.3117	0.0204	0.0141
C3902A	0.44	0.3117	0.0124	0.0141
C3903A	0.72	0.3117	0.0044	n/a
C3905A	0.87	0.3117	0.0026	n/a

This calculation suggests that for C3901A, over 2/3 of the total strain was relieved by the interfacial misfit dislocations. For C3902A, the interfacial misfit dislocations relieve almost all of the strain. Note that the estimated misfit strain was larger than the total strain. This may be for two reasons, (a) errors caused by the oscillating artefacts of the curvature data were significant, or (b) additional misfit dislocations were being generated after growth during cool down or even during TEM sample preparation due to large shear stresses associated with grinding and polishing.

Bent threading dislocations were first reported by Cantu et al [120], where edge dislocations were found to bend away from the vertical upon entering the compressively strained AlGaN layer. They have also found that these edge dislocations inclined along $[1\bar{1}00]$ lines (if viewed projected onto the (0001) growth plane), which lie perpendicular to the **b=a** Burgers vectors of the dislocations and that the bent dislocations are not in their glide planes. Thus the bending must result from climb or by some other mechanism. Romanov and Speck [121] subsequently proposed a theoretical energy-balancing model to describe these inclined dislocations. They predicted that dislocation bending occurs once the critical thickness is exceeded and therefore the bending becomes energetically favourable. However, more recent work by Follstaedt [137] found that the bending of dislocations occurs almost at the interface before the critical thickness has been reached, and the same finding was reported in this work (see cross-sectional TEM images in results section). Dislocation climb by bulk defect diffusion is too slow at the growth temperature, which is not sufficient for inclination to occur. This contradicts the model Romanov and Speck proposed (which assumes sufficient climb exists). Accordingly, bending of a dislocation takes place by another process at the growth surface, which Follstaedt described as 'surface-mediated climb', where an existing dislocation overgrows a surface vacancy without filling the vacancy, as illustrated by the schematic (figure 3.27). This is likely because the formation energy for an interstitial is much larger than for a vacancy. This makes the dislocation move away by one atomic unit length and continue up until the dislocation core again meets another surface vacancy. This surface process may provide the reason for inclination initiation below the critical thickness. However, this model only holds for the initial stage of growth, because it

does not explain why bent dislocations are inclined at a fixed angle (with fixed amount of strain relieved) even after the strain decreases nonlinearly (figure 3.23) further away from the interface.

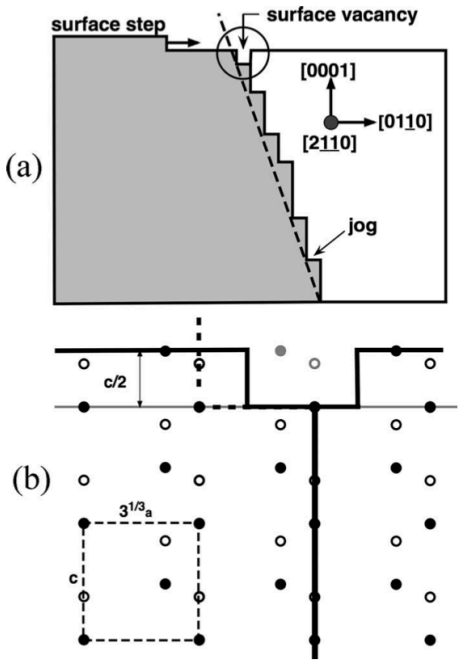

Figure 3.27: (a) A cross-sectional view of an AlGaN layer showing the extra (2-1-10) half plane produced by a bent threading dislocation. The dashed line represents the average bend of the thread. A surface vacancy is attached to the terminated dislocation core. The area inside the circle is enlarged in (b) to show the atomic structure. The vertical black line is the existing thread and the heavy dashed line shows the jog that would be created if the surface vacancy is overgrown without filling [137].

These bent threading dislocations are inclined away from the [0001] direction and therefore their projections to the basal plane actually consist of misfit components (figure 3.28). These misfit components are equivalent to interfacial misfit dislocations, which also effectively relieve the strain in the film. Thus the bend angles were observed to increase as the lattice mismatch increases (relieving more strain).

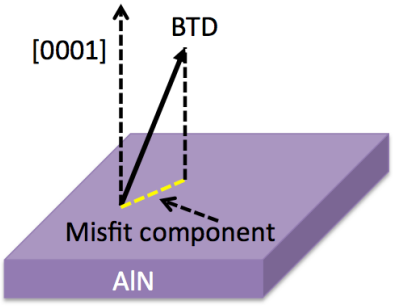

Figure 3.28: A schematic showing a bent threading dislocation that has a misfit component (yellow dashed line) due to its projection to the basal plane.

The strain relieved by these bent threading dislocations can be estimated using the following equation [137]:

$$\varepsilon_{BTD} = \frac{1}{2} b \rho_{BTD} L$$

$$L = h \tan \alpha$$

where b is the magnitude of the dislocation's Burgers vector (b=0.318 nm [135]), ρ_{BTD} is the density of inclined dislocations (assuming all dislocations are bent). L is the projection of the inclination to the basal plane, which is the misfit component. h is the thickness of the layer and α is the average angle of inclination.

In the case of samples C3901A and C3902A, because the inclinations were not linear across the entire film, BTD strain evaluation was separated into 2 layers where the inclinations were relatively consistent in each layer (see figure 3.29). The strains calculated from these two layers were then added and represent the total ε_{BTD} for the sample.

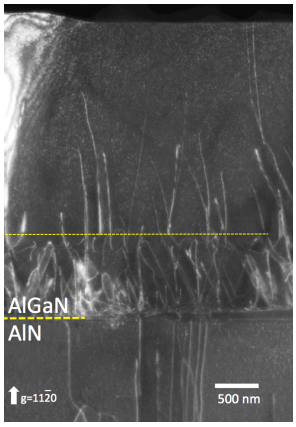

Figure 3.29: XTEM image of C3901A. The thin yellow dashed line marked the position where most of the BTDs had a change in bend angles

Table 3.8: BTDs strain calculation in different AlGaN compositions.

Sample	$Al_xGa_{1-x}N$ x =	ρ_{BTD} / cm^{-2}	h / μm	α / °	ε_{BTD}
C3901A	0.23	$1.6\pm0.1\times10^{10}$	0.45(1.35)	22.1(8.3)	0.00966
C3902A	0.44	$3.4\pm0.2\times10^{9}$	0.83(1.11)	15.6(4.3)	0.00170
C3903A	0.72	$3.3\pm0.2\times10^{9}$	2.10	15.2	0.00299
C3905A	0.87	$4.1\pm0.1\times10^{9}$	1.90	8.3	0.00181

As expected the amount of strain relieved by these inclined dislocations (Table 3.8) was less than the amount relieved by pure misfit dislocations (Table 3.7).

In sample C3901A the BTD strain was the largest due to much greater inclined angles and a larger number of TDs, which contributed to more misfit segments when projected onto the basal plane. Interfacial misfits accounted for about 3/5 of the total strain relieved whereas BTDs accounted for 2/5. The sum of the strain relieved by these two mechanisms was greater than the calculated total ε (Table 3.7), which is similar to C3902A suggesting some post-growth generated interfacial misfit dislocations.

In sample C3902A the strain contributed from BTDs was the least among all samples due to a smaller averaged incline angle, despite the lattice mismatch being still quite large. This might suggest that the inclined dislocation arrays (discussed in chapter 4) also relieved a significant amount of strain as it can be seen that the threading dislocation bend angles decreased significantly once they encountered the arrays. Therefore both the interfacial misfits and the dislocation arrays have already relieved most of the strain.

In C3903A and C3905A, the total strain is largely accommodated by these BTDs, which is consistent with the observations from XTEM, where BTDs were the major relaxation process in the samples.

Bent threading dislocations were observed in all cases since the formation of misfit dislocations is related to the critical thickness of the layers. This indicates that the energy required to cause threading dislocations to bend was much lower than that for misfit dislocation generation. Their misfit segments were not constrained to the critical thicknesses of the samples. This also suggested that these bent threading dislocations were probably inconsequential to the formation of the misfit dislocations.

3.5.4: Estimate of strain associated with other types of defect.

From the calculations shown above, it can already be seen that most of the strain in the AlGaN film was relieved via generation of both misfits and BTDs in the low Al-content layer or just simply BTDs in the high Al-content layer. Therefore on the assumption mentioned earlier:

$$\varepsilon_T = \varepsilon_{HTD} + \varepsilon_{BTD} + \varepsilon_{IDA} + \varepsilon_{misfit} + \varepsilon_{FR}$$

The strains associated with helical threading dislocations and Frank-Read sources were almost non-existent. However, they were observed in the TEM images. The reason for their presence might be partly that helical (or half-loops) threading dislocations also have misfit components when projected onto the basal plane, and essentially these helical (or half-loops) TDs were similar to the BTDs, which have already been taken into account in the previous calculation. As for the Frank-Read sources, these were essentially misfit dislocations that bowed out due to the local shear stress (discussed in section 3.4.2.5) and therefore their associated strain has also already been taken into account in the misfit strain calculations.

Table 3.9: Comparison (column 3 and 4) between the amount of strain that XRD suggests has been relaxed with the amount of calculated strain that can be relaxed by the defect, and (column 5 and 6) between the total strain determined by XRD prior to relaxation with that measured from the in-situ curvature data (also before relaxation).

Sample	$Al_xGa_{1-x}N$ x =	Calc. strain relaxed by BTD and misfits	Strain that XRD suggests has been relaxed	Calc. total ε	XRD total ε
C3901A	0.23	0.0238	0.0146	0.0204	0.0190
C3902A	0.44	0.0158	0.0094	0.0124	0.0138
C3903A	0.72	0.0030	0.0015	0.0044	0.0071
C3905A	0.87	0.0018	0.0002	0.0026	0.0032

The XRD measured total strain prior to relaxation was comparable to the calculated total strain (Table 3.9 column 5 and 6), indicating the in-situ curvature data were overall in a good agreement with the XRD data.

However, the amount of strain that XRD suggests has been relaxed (according to the relaxation in Table 3.2) was only about half the amount of strain calculated from in-situ curvature data that can be relaxed by the defects (Table 3.9 column 3 and 4). This discrepancy was expected since the calculation assumed that every misfit components of the bent TDs relieve the strain (i.e. all extra half planes occur at one side of the dislocations), whereas in reality, some bent TDs can also add to the strain if the misfit components have opposite sign of the Burger's vector (see section 3.4.2.2). Therefore further studies on the characterisation of the Burger's vectors will be necessary to correct this inconsistency.

3.6 Conclusion

In this chapter different types of defects seen in compressively strained AlGaN on AlN have been examined and discussed. Stress relaxation in these films occurred by the combined processes of interfacial misfit dislocations and bent threading dislocations. In-situ wafer curvature measurement in conjunction with other characterisation techniques has demonstrated that interfacial misfit dislocations dominate the strain relaxation processes while bent threading dislocations also relieve a fraction of the strain due to their inclined projection on the basal plane, equivalent to interfacial misfits. The strain associated with other types of defects was much smaller than that of the previous two types. In addition we have found that these bent threading dislocations occurred in all different AlGaN compositions studied ranging from 22% to 87% aluminium content. This suggests that their projected misfit segments were unrelated to the critical thicknesses of the layer and therefore the density of bent threading dislocations was probably inconsequential to the formation of the misfit dislocations.

Frank-Read sources can occur at the interfaces in AlGaN/AlN films, not so far reported in the literature. Our data here were insufficient to determine their exact formation mechanisms. However, the results from conventional TEM studies showed that some of these dislocation multiplication sources originated from pre-existing interfacial misfit dislocations. Hence we hypothesised that the Frank-Read sources are interfacial misfit dislocations that bow out due to a local positive stress concentration

arising from surface islands or steps, which force some misfits to glide into the underlying AlN layer.

Flat and spiral hillocks on the surface of highly lattice-mismatched films ($Al_{0.23}Ga_{0.77}N$ on AlN) can be detrimental to the optical properties of the structure as the emitted wavelength is red-shifted. We also hypothesised that the formation of hillocks should be prevented by using a low III/V ratio and large substrate miscut steps, based on the model described by Heying et al. An atomically flat surface can be achieved with a high aluminium content AlGaN alloy so the lattice mismatch is small with respect to AlN and hence there is a small relaxation. However the dislocation density does not decrease further with a smaller lattice mismatch, because dislocation inclination angles become smaller and without surface steps or islands, dislocations are less likely to meet each other to reduce or annihilate.

There are some limitations to the in-situ wafer curvature analysis. The most problematic are the difficulties in accurately determining the slope gradient when the sample is relaxed (small critical thickness) and the periodic oscillation artefacts caused by the interaction between the laser and the wafer, which can be extremely complex to correct.

Additional inclined dislocation arrays, which also cause shifting in the emission wavelength, were also noted in low Al-content samples with a high density of surface steps. Detailed optical and structural studies of these inclined dislocation arrays are discussed in the next chapter.

4

Inclined dislocation arrays in AlGaN/AlN structures.

4.1 Background

III-nitride materials are usually grown on foreign substrates such as sapphire, due to the lack of lattice-matched bulk substrates. The relaxation induced by the large lattice mismatch in these heteroepitaxially grown films generates a significant amount of dislocations, which hinder the performance of the devices (see literature). Numerous growth techniques have been developed in order to reduce the dislocation density, such as epitaxial lateral overgrowth (ELOG) [138] and the use of interlayers (SiN or ScN) [38]. However, these techniques can be complicated, such as requiring additional patterning, re-growth, etc. These additional growth steps can increase the overall manufacturing costs. Therefore another approach has been proposed in the literature [139] by simply using vicinal substrates. It has been reported that the miscut steps on the substrates lead to the formation of macro-scale inclined dislocation networks, which are able to lock and drag threading dislocations within the network, creating areas that are dislocation-free. This is very similar to the ELOG process but with a simpler approach and without the need of ex-situ patterning. However, the dislocation reduction and annihilation mechanisms at these macro-scale inclined

networks are not very clearly understood. Also the properties of these networks have not been thoroughly studied, for instance, even though they are able to reduce the dislocation density. However the steps induced by these network on the surface can have detrimental consequences for the succeeding quantum well growth, for instance, non-uniform active region heights.

Most of the reports in the literature have focused on the studies of inclined dislocation networks in the first layer of the template, e.g. AlN or GaN on vicinal sapphire, or AlN on vicinal Si(111) substrates. However, so far there are no reports on the studies of these inclined dislocation networks on the succeeding grown buffer layers.

As mentioned in the previous chapter, we have observed similar inclined dislocation network in the AlGaN buffer layer in our AlGaN/AlN heterostructures grown on sapphire. These features occurred without the use of vicinal substrates but occurred solely on the growth induced surface steps of the AlN template. How these inclined dislocation networks interact with other types of dislocations in the materials is rather complicated. In order to understand their influence on device performance, another reference sample with slightly different growth (with a thinner AlN layer and a GaN interlayer) was employed for comparison between the surface step densities, threading dislocation densities, and inclined dislocation arrays.

4.2 Aim

This chapter aims to explain the formation mechanisms and investigate the optical and structural properties of these inclined dislocation networks and their influence on device performance.

4.3 Experimental details

All samples were grown by metalorganic vapour phase epitaxy (MOVPE) in a Thomas Swan 6 × 2” close-coupled showerhead reactor using trimethylaluminium (TMA), trimethygallium (TMG) and ammonia (NH_3) as precursors and hydrogen as carrier gas. Initially, 1 μm thick and 4 μm thick AlN layers were deposited on c-plane

sapphire substrates (0.25º ± 0.10º towards $(11\bar{2}0)$) for Samples A and B, respectively. For this, the sapphire substrates were thermally cleaned for 7 min in a flow of hydrogen, followed by a predose of 56 μmol TMA in the absence of ammonia, and the growth of a 30 nm thick AlN nucleation layer at a pressure of 200 Torr, a V/III ratio of 250 all at a temperature of 1050 ºC, followed by high-temperature AlN growth at 50 Torr, 1130 ºC and a V/III ratio of 60. For Sample C, the 1 μm thick AlN template (sample A) was re-introduced in the reactor and a 20 nm GaN interlayer was introduced for defect reduction purposes [140] and was grown at 1100 °C, 50 Torr and V/III=3880, followed by a 1.0 μm $Al_{0.46}Ga_{0.54}N$ layer at 1100 °C and 50 Torr. For Sample D, the 4 μm thick AlN template (sample B) was overgrown with a 1.5 μm $Al_{0.43}Ga_{0.57}N$ layer at 1100 °C and 50 Torr. For sample E, the $Al_{0.46}Ga_{0.54}N$/AlN template (Sample C) was overgrown with an AlGaN connecting layer with the same composition and a 10-period $Al_{0.30}Ga_{0.70}N/Al_{0.46}Ga_{0.54}N$ QW structure. For sample F, the $Al_{0.44}Ga_{0.56}N$/AlN template (Sample D) was overgrown with an AlGaN connecting layer with the nominally same composition (however, XRD analysis showed it to have an Al fraction of 0.49) and a 10-period $Al_{0.35}Ga_{0.65}N/Al_{0.49}Ga_{0.51}N$ QW structure. A schematic of the different sample growth stages for Samples E and F is shown in Figure. 4.1.

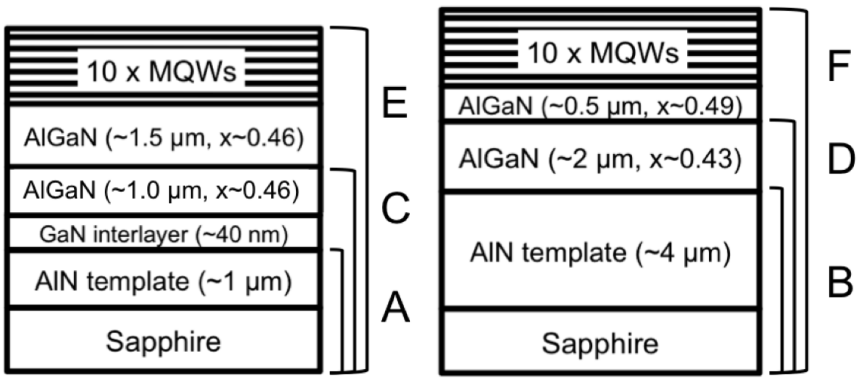

Figure 4.1: Schematic of the two sample structures.

4.4 Results and Discussion

4.4.1. X-ray diffraction

The AlGaN/AlN 'template' layers (Samples C and D) were characterised first, in order to determine their compositions and to evaluate their dislocation densities.

Table 4.1: Summary of the XRD data collected from Samples C and D.

Sample	$Al_xGa_{1-x}N$ Composition x	AlGaN Relaxation (wrt AlN)	ω scan FWHM arcsec			
			AlGaN (0002)	AlGaN (10-11)	AlN (0002)	AlN (10-11)
C	0.46	84%	584	1062	638	861
D	0.43	75%	224	537	242	468

Table 4.1 shows a summary of the XRD data collected from the two template layers: the full width at half-maximum (FWHM) values were obtained from ω-scans of the 0002 and $10\bar{1}1$ reflections for both samples. The FWHM values for the AlN as well as the AlGaN 0002 and $10\bar{1}1$ reflections were reduced by a factor of 2 or more in the layers used in Sample D, compared to those used in Sample C. In all cases, the 0002 FWHM was less than the $10\bar{1}1$ FWHM, indicating that edge-type dislocations were predominant in the layers and that Sample D contained a significantly lower dislocation density than Sample C, primarily due to a lower dislocation density in the AlN buffer layer. Comparison between the AlGaN and AlN FWHM values within the same sample shows that the AlGaN layers have broader (101) ω peaks, suggesting an increase in edge-type threading dislocations at the AlGaN/AlN interface. Cross-sectional TEM measurements (discussed below) will confirm this result. The AlGaN compositions and strain states were determined from reciprocal space maps (RSMs) of the 0004 and $10\bar{1}5$ reflections. The data in Table 4.1 indicate that significant strain relaxation has taken place in the AlGaN layers, which may be linked to the increase in edge-type TD density at the AlGaN/AlN interface. Because clear strain and/or compositional variations were visible from the RSMs for both AlGaN layers, the analysis was carried out for the highest intensity peak. Figure 4.2(a) and (b) show the RSMs of the $10\bar{1}5$ reflection for the MQW structures, respectively Sample E and F.

The data clearly indicated that (a) the AlGaN layers have relaxed significantly with respect to the AlN buffer layers and (b) the AlN reciprocal space point of sample F, i.e. from the 4 μm-thick AlN layer is much smaller that that of sample E, i.e. from the 1 μm-thick AlN layer. The lower AlGaN RSP in Figure 4.2(b) indicates the compositional mismatch between the $Al_{0.44}Ga_{0.56}N$ layer of Sample D and the $Al_{0.49}Ga_{0.51}N$ connecting layer for the growth of Sample F.

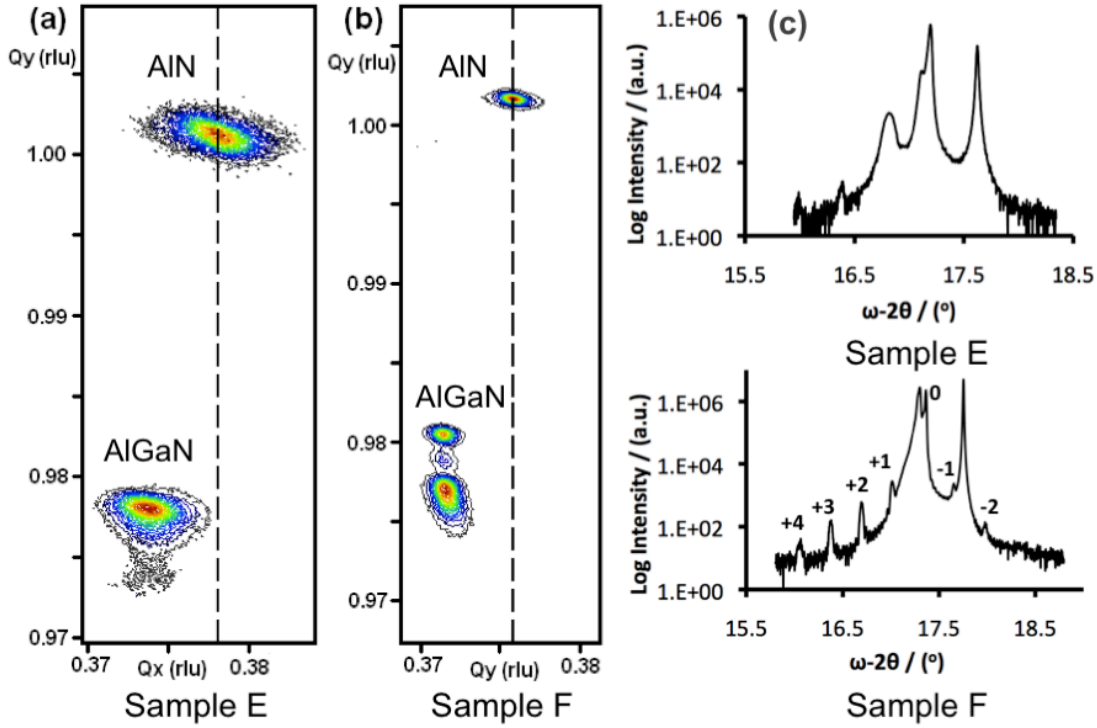

Figure 4.2: X-ray diffraction reciprocal space maps of the AlGaN and AlN 10-15 reflections from the 'templates' used in (a) Sample E and (b) Sample F, with the dotted lines indicating the AlN in-plane lattice parameter. (c) ω−2θ scans of the 0002 AlGaN reflection, showing interference fringes due to the AlGaN/AlGaN multiple quantum wells.

Figure 4.2(c) shows ω−2θ scans for both samples. The sharper fringes observed in the ω−2θ scan for Sample F indicate the smooth, high-quality interfaces within the MQWs, while the 'smearing' of the fringes in the ω−2θ scans from Sample E indicates rougher or more diffuse interfaces [12]. However, in both cases, the data were sufficient to enable simulations to be performed in which the QW and barrier compositions and thicknesses could be extracted.

4.4.2. Atomic force microscopy

The surface morphology of both the AlN layers, Samples A and B, was investigated using atomic force microscopy. No cracks were observed in any of the layers. The surface roughness of Sample A (RMS = 1.96±0.05 nm, over 5 x 5 μm area) was higher than that of Sample B (RMS = 1.64±0.10 nm, over 5 x 5 μm area) due to a higher density of bunched surface steps (Figure 4.3). Surface step densities were 0.30 ± 0.04 μm^{-1} and 0.24 ± 0.02 μm^{-1} for Sample A and B, respectively. The surface step densities (μm^{-1}) were calculated by measuring the total length of the steps (in μm) within a 20 μm x 20 μm area of the sample as revealed by plan-view SEM-CL data. The height of the bunched steps in Sample A and B is about 20 nm and 10 nm on average, respectively.

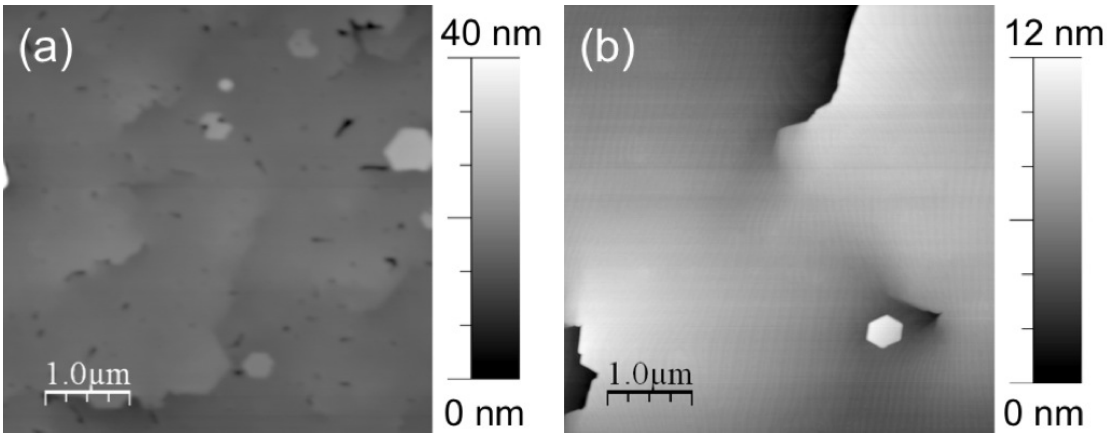

Figure 4.3: 5 μm x 5 μm atomic force microscopy height images of the surface of (a) the 1 μm AlN buffer layer used in Sample A (RMS = 1.94±0.05 nm), (b) the 4 μm AlN buffer layer used in Sample B (RMS = 1.69±0.10 nm).

4.4.3. SEM-cathodoluminescence

Plan-view SEM-CL imaging of the surface morphology of Sample E and F indicate that the MQWs in the region of the bunched surface steps have a reduced cathodoluminescence intensity compared to the rest of the sample. Dark spots are also observed in the CL image; these are most likely due to non-radiative recombination at

threading dislocations (TDs) [141]. However, the CL spectra taken from sample F (Figure 4.4) showed a small shoulder around 300 nm. A plan-view monochromatic CL image taken at 302 nm (Figure 4.4) showed that this longer-wavelength, lower intensity emission originated from the step edges. This step-edge-related emission was also observed in Sample E (spectra not shown). The intensity of the shoulder peak in Sample E is stronger than that in Sample F suggesting the step density is higher for Sample E, which is consistent with the higher surface step density measured by AFM.

Dark features running at an angle of 30º across the entire AlGaN region of both samples were observed in cross-sectional panchromatic CL measurements (not shown). Careful comparison with the corresponding SEM images of the same areas showed that the features were intrinsic to the sample and not due to morphological features of the cleaved surface.

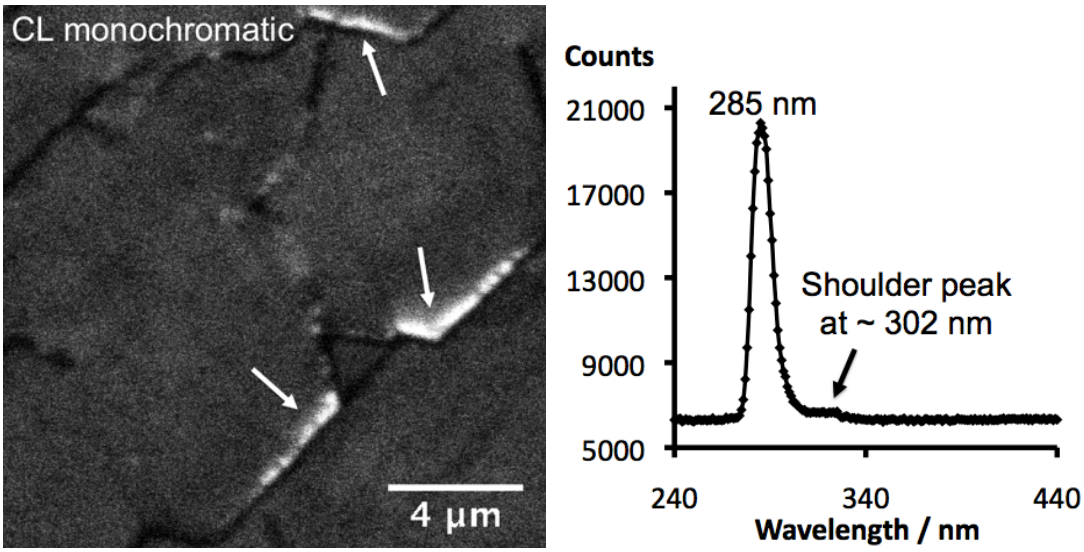

Figure 4.4: Plan-view monochromatic CL image (302 nm) obtained from Sample B, along with a CL spectrum obtained from this area.

4.4.4. Transmission electron microscopy

The inclined features observed in SEM-CL in the Samples E and F can also be seen in STEM-HAADF, as shown in Figure 4.5. In these low-magnification images, the inclined features are observed to meet, annihilate or overgrow one another. The

contrast in the HAADF images may be caused by a change in strain state and/or a local change in composition. To further characterise these inclined features, conventional cross-sectional TEM studies were carried out on Sample F and the results are shown in Figure 4.6. First of all, a significant number of pure edge-type TDs were generated at the AlGaN and AlN interface, confirming the broadening of the AlGaN X-ray rocking curves compared to those of the AlN layer as discussed previously. The formation of extra TDs at the AlGaN/AlN interface is likely the result of the significant lattice mismatch between AlN and AlGaN [137]. The dislocation density in Sample E was determined at $(3.6\pm0.1)\times10^{9}$ cm^{-2} and that in Sample F at $(1.7\pm0.1)\times10^{9}$ cm^{-2}, which is consistent with both the plan-view CL data and XRD data. Also observed in Figure 4.6 is the bending of all types of TDs occurring at the inclined features, which has already been discussed extensively in the previous chapter. Plan-view TEM images taken with the **g** = 1-100 diffraction condition revealed arrays of inclined dislocations in addition to conventional threading dislocations aligned perpendicular to the substrate (Figure 4.7). These correspond to the intersection of the inclined features with the sample surface; indeed, thickness fringes corresponding to a surface step can be detected running along the edge of the array. Clearly, the inclined features consist of arrays of dislocations, which terminate at bunched surface steps. These inclined bundles of dislocations show up as dark features in both plan-view and cross-sectional SEM-CL images.

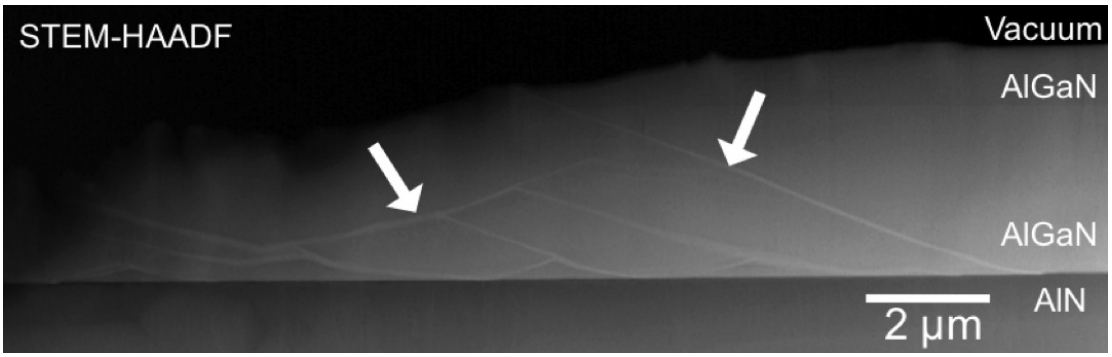

Figure 4.5: Cross-sectional STEM-HAADF image of Sample F.

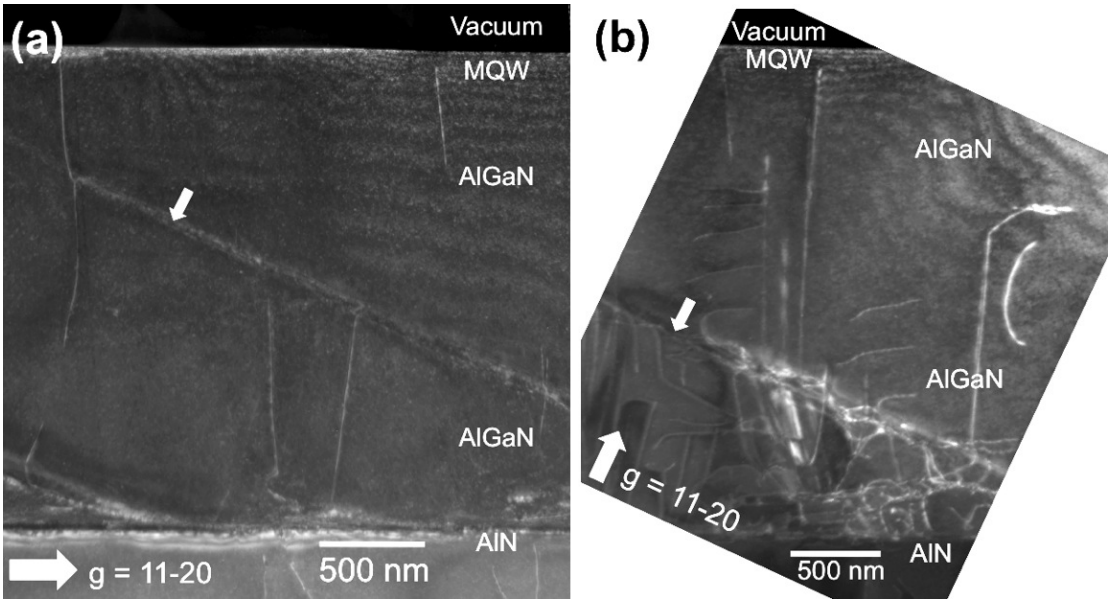

Figure 4.6: Cross-sectional weak beam dark field TEM images of Sample F taken with diffraction conditions using (a) **g** = 11-20 (revealing *a* and (*a*+*c*)-type dislocations) and (b) **g** = 0002 (revealing (*a*+*c*) and *c*-type dislocations).

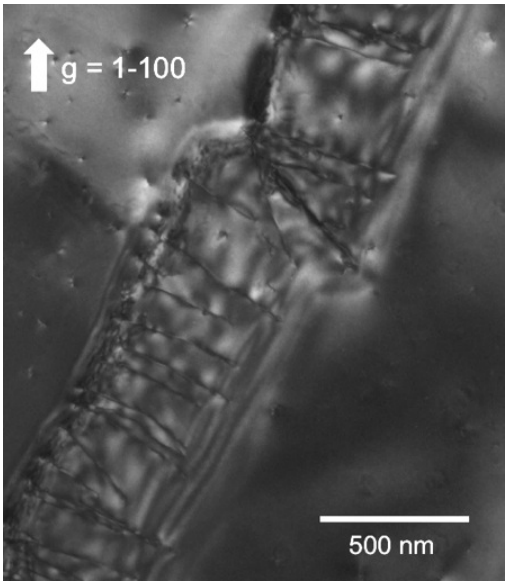

Figure 4.7: Plan-view weak-beam dark field TEM image taken with the **g** = 1-100 diffraction condition from Sample F, showing an inclined dislocation array terminating at a surface step.

However, plan-view CL data (Figure 4.4) showed that the surface steps were associated with luminescence at both lower intensities *and* longer wavelengths compared to the bulk. While the lower intensities are explained well by the presence

of the inclined dislocation arrays, the shift in emission wavelength is not. However, STEM-EDX measurements showed that the region around the inclined dislocations in both the AlGaN epilayer and the quantum wells also had lower aluminium content (Figure 4.8). The inclined dislocations also produced an increase in the thickness of the wells and barriers in the succeeding MQW region as seen in Figure 4.9. In conjunction with the additional Ga in the wells, this was likely to be responsible for the emission wavelength shifts in CL emission spectra (Figure 4.4). The low-aluminium content regions (containing the inclined dislocation arrays) were solely generated at the side facets of the surface steps at the AlGaN/AlN interface, suggesting differences in the relative incorporation rates of Al and Ga on these inclined facets [142][143]. It is not clear whether the dislocation arrays formed independently, or whether they are misfit dislocations produced as a result of the lattice mismatch of the low-Al content region with respect to the surrounding higher-Al content AlGaN.

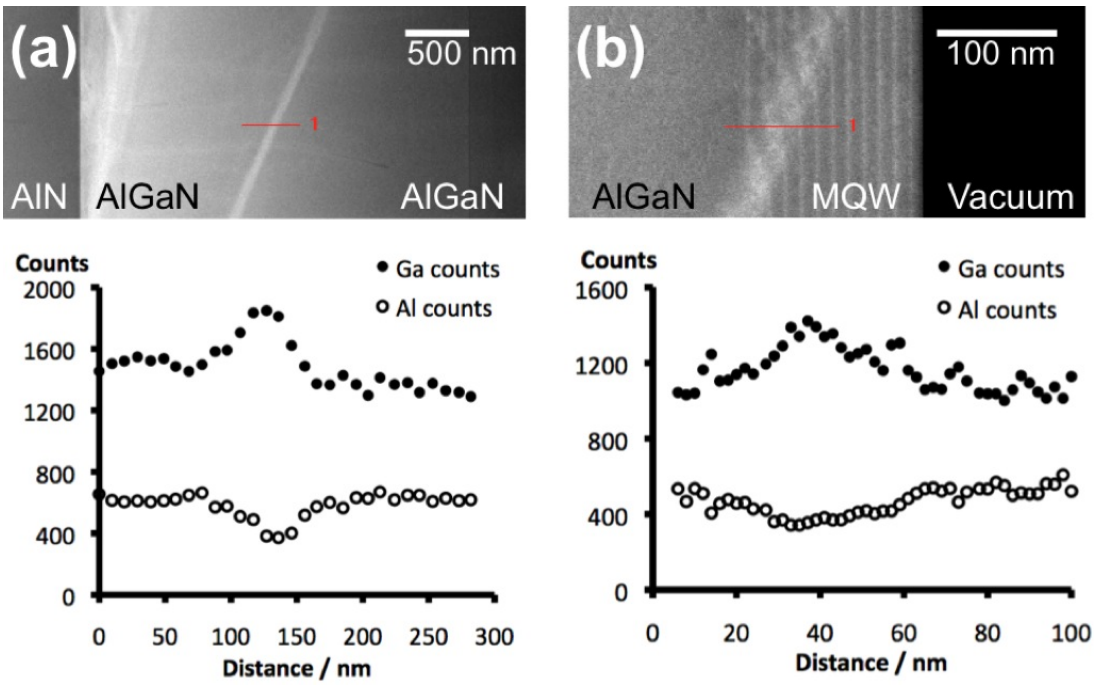

Figure 4.8: STEM-EDX maps and corresponding line profiles indicating the relative proportions of Ga (filled circle) and Al (open circle) in the region surrounding the inclined defect in (a) the AlGaN 'template' layer and (b) the quantum wells.

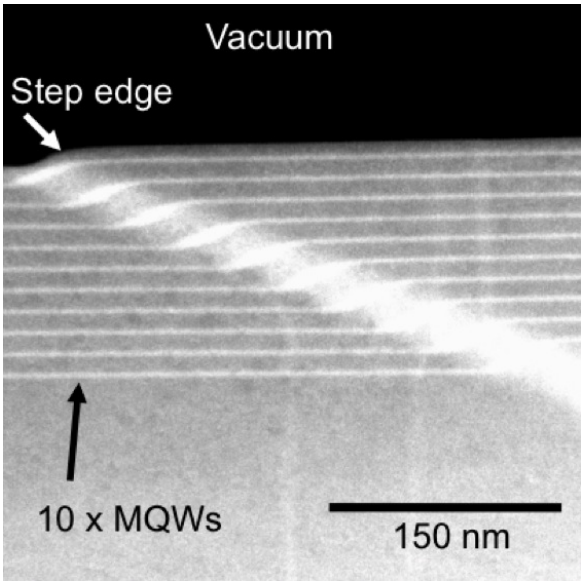

Figure 4.9: Cross-sectional STEM-HAADF image of the inclined defect within the MQWs region in Sample F.

4.5 Discussion

A similar inclined dislocation network was observed by Shen *et al.* [139] in the AlN film grown on a 2.0° miscut (0001) sapphire substrate as mentioned in section 4.1. Figure 4.10 shows the dislocation reduction mechanism induced by these inclined dislocation networks.

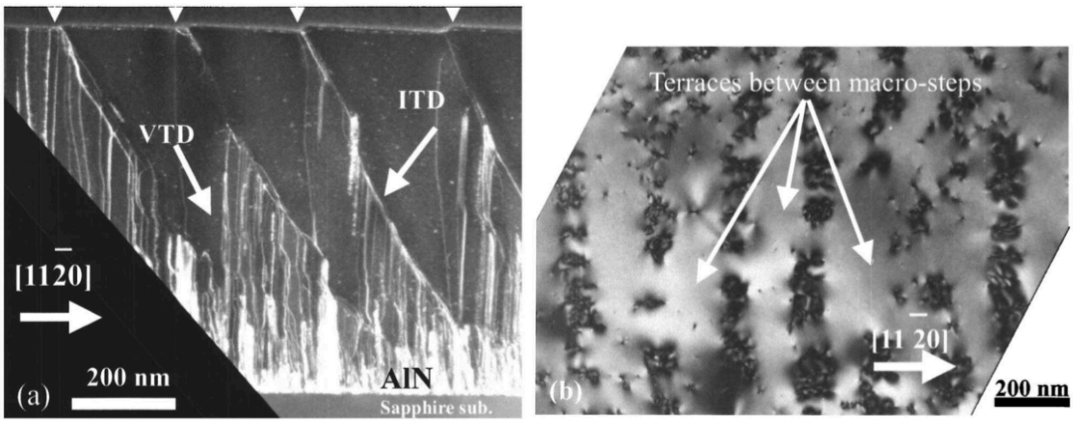

Figure 4.10: (a) Cross-sectional TEM image of the AlN film grown on a 2.0° miscut sapphire substrate. Dislocation reduction was observed at the inclined dislocation networks region. (b) Plan-view TEM image of the same sample showing an ELOG-like structure. (Results from [139])

The inclined dislocation arrays observed in this work were similar to Shen's work. However, dislocation reduction did not occurred in our cases, which was clearly evident in figure 4.11.

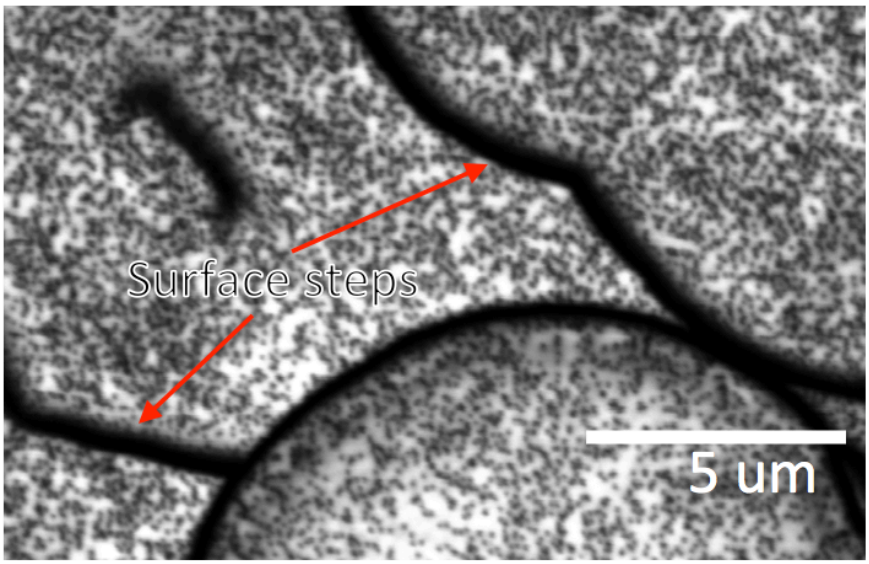

Figure 4.11: Plan-view panchromatic CL image of sample F. Surface steps that are associated with inclined dislocation arrays were marked by red arrows. Dislocation densities seem to remain unchanged at the vicinity of the steps.

Although the inclined dislocation arrays may lead to local TDD reduction similar to Shen's result, the inclined dislocation arrays observed in this work were associated with a change in composition (more gallium as shown in STEM-EDX data), causing a change in lattice parameters in comparison to the surrounding material. Therefore, it is likely that the lattice mismatch at these arrays can also lead to the generation of misfit dislocations and hence an overall dislocation reduction was not observed. The dislocations were revealed as dark spots in plan-view CL images and the density remained unchanged at either side of the surface steps, indicating the inclined dislocation arrays had no effect on the overall TDD of the sample.

Since the TDD did not change, it also suggested that the inclined dislocation arrays probably have an insignificant effect on the stress relaxation in the film, and therefore are insignificant in the strain calculation in Chapter 3. A future study involves the determination of the magnitude and sign of the Burger's vector of dislocations (in

figure 4.7) would be useful to clarify the effect of the inclined dislocation arrays on the stress relaxation.

Figure 4.12 showed evidence that the low-Al content inclined dislocation arrays were likely to originate from the surface steps on the AlN template as mentioned earlier. Since the inclined dislocation arrays were detrimental on the device (causing a shift in emission wavelength, changing the active region's heights and possibly generating additional dislocations due to lattice mismatch), reducing the density of surface steps on the AlN template may directly reduce the amount of inclined dislocation arrays and improve the AlGaN film quality.

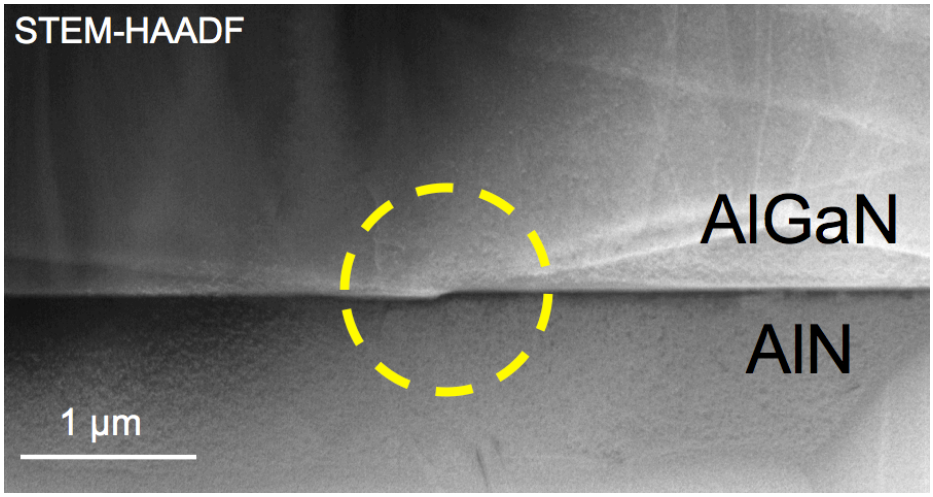

Figure 4.12: Cross-sectional STEM-HAADF image showing an inclined dislocation array originated from a surface step on AlN template.

4.6 Conclusion

Throughout the course of this chapter, we have compared two AlGaN/AlGaN MQW structures emitting at around 290 nm, which were grown using two different defect reduction methods, one with a GaN interlayer and one with a thicker AlN buffer layer. The optical and structural properties of the buffer layers and MQW structures were investigated by a number of complementary characterisation techniques. The use of a thick (4 um) AlN buffer layer was found to be more effective in reducing overall defect densities, as shown in the XRD data, and in increasing the internal quantum

efficiency, as shown in the PL data, compared to a 1 um AlN buffer layer plus a GaN interlayer. This was mainly due to the improvement in AlN template growth. Both AlN layers contained bunched surface steps, which led to the formation of arrays of inclined dislocations in the AlGaN buffer and MQW layers. The GaN interlayer did not prevent the formation of these inclined dislocations.

The inclined dislocation arrays were found to be lower in aluminium content possibly being generated during AlGaN growth on the inclined facets at the step edges due to differences in the relative incorporation rates of Al and Ga on different facets. The inclined dislocation arrays would be detrimental on device performance; they distorted the quantum well and barrier heights and changed the composition leading to a shift in emission wavelength. Additional misfit dislocations could probably be generated due to the lattice mismatch with the surrounding AlGaN materials.

The inclined dislocation arrays seem to originate from the surface steps on the AlN template. We hypothesise that reducing the step density of the AlN film may directly reduce the density of inclined dislocation arrays and result in an improved AlGaN film. This leads to the investigation of AlN template growth optimisation in Chapter 5.

5

AlN growth

5.1 Background

The use of AlN as the template for UV optoelectronic device structures has attracted much attention in recent years [144] due to AlN having the largest direct band gap in the conventional III-V nitrides and thus being transparent to UV emission. However, the growth techniques for AlN are not very well established, as it is relatively more difficult to grow, in comparison to GaN, due to the low aluminium adatom mobility, slow lateral growth rate and the requirement for a higher growth temperature etc. (see chapter 1 for more details). AlN layers grown on sapphire substrates therefore usually exhibit a large degree of surface roughness with a high threading dislocation density, of the order of 10^{10} cm^{-2} often being reported [145]. This greatly affects the quality of the succeeding epilayers and growth of the active region. For instance, the surface steps on the AlN template can lead to the generation of inclined dislocation arrays as shown in chapter 4.

Several growth techniques for AlN have been reported in the literature which were developed in an attempt to improve the materials quality: these include high temperature growth using hot-wall MOCVD [146], epitaxial lateral overgrown AlN [147], patterned sapphire prior to AlN growth [148], pulsed atomic layer epitaxy growth (PALE) [149], mid-temperature nucleation layers [150] and pre-dose methods [150]. McAleese *et al* [150] in Cambridge achieved substantial improvements in material quality by combining the TMA pre-dose method and nucleation layer technique leading to a high quality 4 μm thick AlN layer with XRD ω scan FWHM

values of 272 arcsec and 473 arcsec for the (002) and (101) reflections, respectively. These values are comparable to conventional GaN layers on sapphire, suggesting these AlN templates are indeed promising candidates for deep-UV optoelectronic applications. For instance, 2 µm AlGaN epilayers growth on these high quality templates have shown the narrowest XRD peak widths of any method to date with dislocation densities of order of low - mid 10^8 cm^{-2} (see chapter 3 for more details).

Although high quality AlN templates have been successfully used to achieve the growth of succeeding high quality AlGaN epilayers, it has been shown in chapter 4 that further reduction in the amount of surface steps on the AlN templates should eliminate the generation of inclined dislocation arrays and further enhance the quality of succeeding epilayers. In addition, the growth of high quality AlN templates is not as reproducible as the growth of GaN templates due to several growth-related issues. For instance, under the exact same growth condition, the AlN surface morphology can vary significantly (Figure 5.1) depending on "memory effects" associated with the history of the reactor's usage, (e.g whether a H_2 bake prior to a TMA pre-dose is used, whether impurities are left over from previous runs, or contaminants are incorporated from the showerhead/susceptor). Thus, it is believed that there is scope for AlN growth techniques to be further optimised to achieve atomically flat surfaces and high reproducibility.

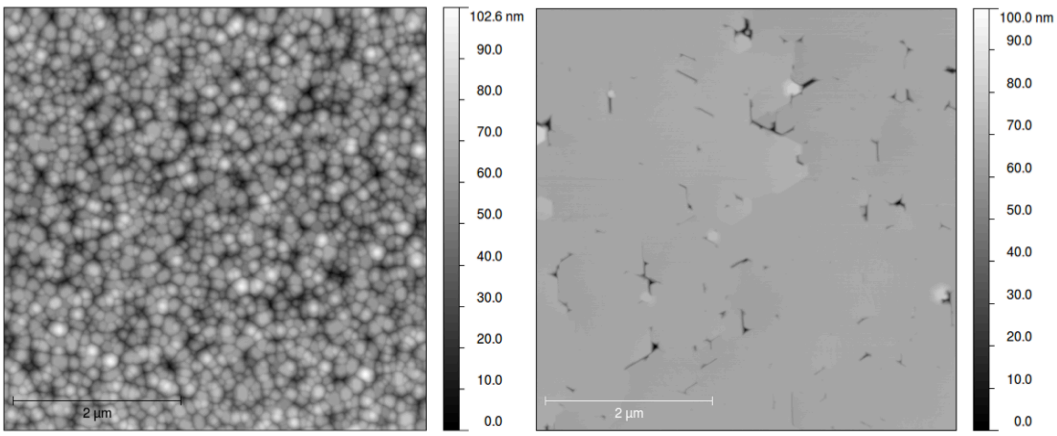

Figure 5.1: AFM images of 1 µm AlN templates grown under the same conditions except for the use of a hydrogen bake prior to the TMA pre-dose. The left hand image shows sample C4162 grown using such a hydrogen bake whilst the right hand image shows sample C4164 grown without a hydrogen bake.

5.2 Aim

Specific topics covered in this chapter include:

1. Further understanding of the influence of the bake recipe and reactor history effects prior to pre-dose.

2. Optimising the bake recipe and the TMA pre-dose step for AlN growth.

3. Microstructural analysis of the AlN films.

5.3 Pre-existing results from the Cambridge GaN centre

5.3.1 MOCVD growth conditions for AlN

The Al-N bond strength (E_B = 2.88 eV) is greater than that of Ga-N (E_B = 2.2 eV) [151], as a consequence AlN has a higher melting point of ~3200°C in comparison to GaN, which melts at ~2500°C, thus the Al adatoms have less mobility on the growth surface at a given temperature than do Ga adatoms, which leads to slower lateral growth rates and a higher dislocation density. Therefore AlN is normally grown under the highest reactor temperature possible to increase the adatoms mobility [152]. However, the maximum temperature achievable in our MOCVD is ~1130°C, which is still insufficient to reach the comparable lateral growth rate as for GaN.
Also TMA and NH_3 precursors undergo strong parasitic reactions in the gas phase to form low volatility addition compounds, which consequently lowers the growth rate under high V/III ratio [153]. Therefore, low ammonia flows and reactor pressures are normally used during AlN growth to minimise the parasitic reactions in the gas phase and to increase the growth rate.

5.3.2 TMA pre-dose step

Early works on AlN growth exhibit very rough surfaces [154], which were unsuitable for epitaxial growth of further heterostructures or active regions. This is because the growth rate of Al- and N-polar materials is significantly different and therefore the surface morphology is highly sensitive to the presence of inversion domains in the layers (mixed polarity, Figure 5.2). Therefore, films exhibiting a single polarity are preferred for obtaining smooth AlN surfaces. N-polar material can be obtained by extensive nitridation of the sapphire substrate and has been demonstrated to give a very narrow XRD ω scan FWHM values of less than 50 arcsec [150]. However, the surface roughness is still very high due to non-uniform and incomplete coverage of N-polar material on the sapphire substrate surface even after 1-hour of nitridation.

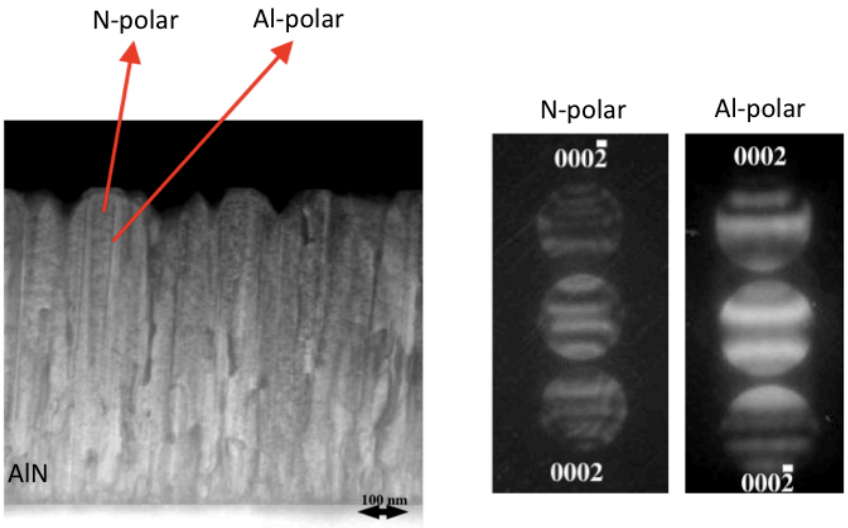

Figure 5.2: STEM-HAADF image and CBED patterns from AlN layer without pre-dose step. Data from Dr. McAleese *et al* [150].

The surface roughness can lead to MQW thickness fluctuations and is therefore unsuitable for further heterostructure growth.

Al-polar AlN material can be obtained by injecting ("predosing") the group III precursor (TMA) into the reactor prior to the introduction of the ammonia [155]. This deposits a thin layer of Al metal on the sapphire surface initially producing an Al-polar surface for the subsequent material growth. Nitridation can be also prevented when the ammonia flow is introduced after this TMA pre-dose. Al-polar AlN was

found to represent the only option to achieve a smooth surface (Figure 5.3) but with the trade-off of incurring a higher defect density (ω scan FWHM values of ~800 and ~1000 arcsec in the (002) and (101) reflections, respectively).

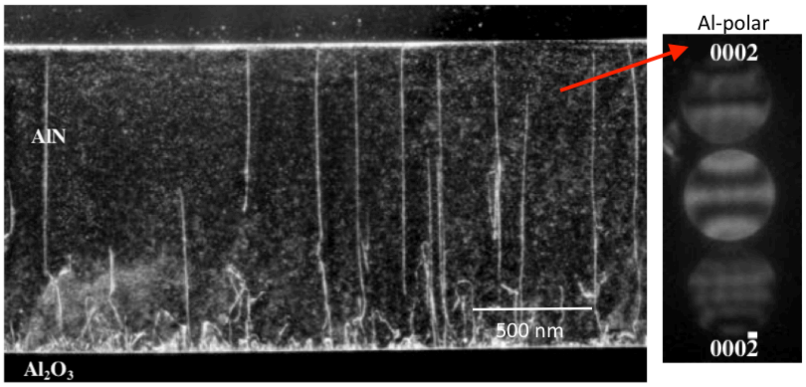

Figure 5.3: WBDF image (g = 0002) of an Al-polar AlN layer with TMA pre-dose. Data from Dr. McAleese *et al*. [150]

The thickness of the AlN layer grown using a TMA pre-dose step is limited to around 1 μm or less to avoid cracking, leading to difficulties in the developments of dislocation reduction methods [156].

5.3.3 Low temperature nucleation layer

The use of a low V/III ratio nucleation layer (~30 nm thick grown at 700°C) in the initial stage of growth can prevent nitridation before growth commences to create an Al-polar film. The surface was also smooth in comparison to the pre-dose method. In addition, AlN layers grown on this nucleation layer were found to be under compression at 1 μm thickness (in comparison, standard AlN growth at 1130°C was under tensile strain and generally cracked at thickness > 1 μm).

An alternative method that combines the merits of both the TMA pre-dose step and an intermediate temperature nucleation layer was developed in Cambridge by Dr. McAleese in order to maintain the crystal quality whilst allowing thicker layers to be grown. The TMA flow was reduced to 30 sccm with a 120s pre-dose time for the initial stage of growth. The nucleation layer was then grown at 1050°C with an NH_3 flow of 75 sccm and a V/III ratio of 255, all at a reactor pressure of 200 Torr. The

growth temperature was then raised to 1130°C and pressure lowered to 50 Torr to commence the growth of the main AlN layer at a higher growth rate of up to 1.3 µm/hour and a low V/III ratio of 42.

As a result, a high quality AlN layer with a smooth surface was successfully produced. Such layers exhibited decreasing XRD ω scan values (Figure 5.4) with increasing layer thickness due to dislocation bending and annihilation, as shown in chapter 3 (in comparison, the thickness of GaN makes no difference to the ω scan peak width, and the TDD is stable after the initial 500 nm or so). However, some occasional large step bunches are still apparent in wide area images. These caused generation of large-scale inclined dislocation arrays in the succeeding AlGaN layers as shown in chapter 4. A further improvement on the surface morphology will certainly lead to a very promising future for many UV applications that utilise AlN templates, as the material quality is clearly approaching that of high quality GaN/sapphire templates.

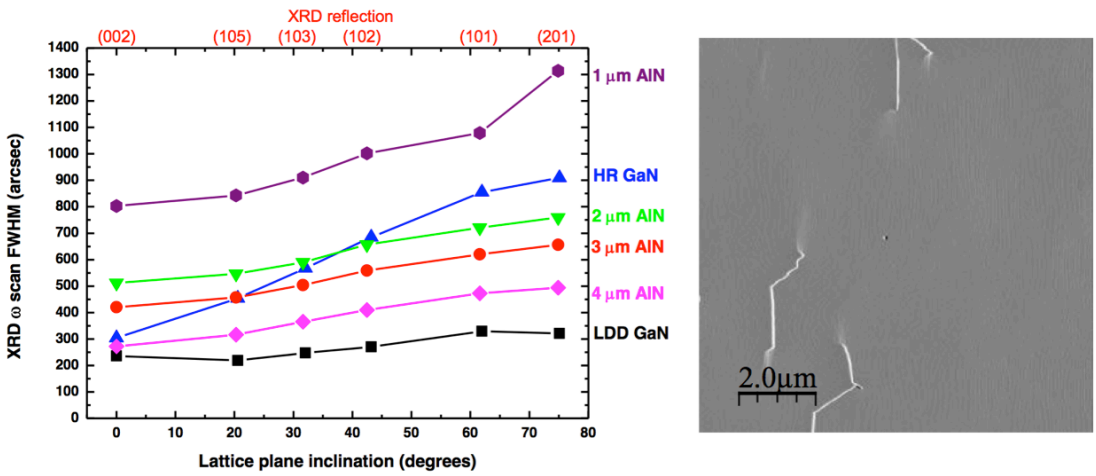

Figure 5.4: Evolution of XRD ω scan peak widths with increasing layer thickness and data for highly resistive (HR) and low dislocation density (LDD) GaN templates as a comparison. AFM amplitude image on the right shows the surface of a 4 µm thick AlN layer. Data from Dr. McAleese *et al* [150].

5.4 Experimental details

The AlN template growth procedure was based on the same conditions as described in chapter 3 (see chapter 3.3 for detailed growth procedures). Therefore most of the parameters remained unchanged, the only differences were introduced at the very beginning of the growth, i.e. modifying the TMA pre-dose flux, and commencing growth with or without a pre-bake. The following table (Table 5.1) summarises the samples used in this chapter. All the samples were grown in The Cambridge Centre for Gallium Nitride by Dr Menno Kappers (reference samples) and Dr Fabrice Oehler (new pre-dose and AlN samples).

Table 5.1: Sample descriptions.

Sample	Pre-growth treatments	TMA pre-dose @ 30 sccm	Description
Reference samples			
C3899	No-bake	120s	4 µm AlN template used in chapter 3
C4154	No-bake	0s	Test samples
C4155	No-bake	10s	Test samples
C4157	No-bake	60s	Test samples
C4156	No-bake	120s	Test samples
C4159	No-bake	180s	Test samples
C4158	No-bake	240s	Test samples
C4169	H_2 baked	120s	Hydrogen baked C4156
C4164	No-bake	120s	1 µm AlN grown on C4169
C4162	H_2 baked	120s	1 µm AlN grown on C4156
TMA pre-dose on sapphire			
C4604	30 min H_2 bake	120s	Beginning of 1 week growth session
C4619	Idle in reactor overnight	120s	Day before end of the growth session
C4624	30 min H_2 bake	120s	End of the growth session
C4606	After an AlN run	120s	Bake-like recipe
C4607	Modified H_2 bake	120s	5 min of NH_3 introduced during cool down after H_2 bake

C4608	Modified H_2 bake	120s	30 min NH_3 introduced during cool down after H_2 bake
C4617	Full N_2 bake	120s	Nitrogen bake
AlN grow after TMA pre-dose			
C4610	Modified H_2 bake (5 min NH_3)	120s	Rough surface, incomplete coalescence
C4612	After an AlN run	120s	Rough surface, incomplete coalescence
C4615	H_2 bake	120s	Rough surface, incomplete coalescence
C4621	H_2 bake	60s	Rough surface, incomplete coalescence
C4623	After a previous AlN run	Double TMA flux	Direct NH_3 injection, fully coalesced, large random crystals
C4626	After a previous AlN run	Double TMA flux	Slow NH_3 ramp, fully coalesced, smaller random crystals

5.5 Results

The following work attempts to verify the hypothesis on the effect of baking, (based on the observations from two 1μm AlN reference samples shown in Figure 5.1). With baking, the reactor should be free from any nitrogen containing impurity left over from the previous growth run. As mentioned earlier, under the exact same recipe, the AlN surface morphology can vary significantly depending on whether or not a pre-bake was used prior to growth. The AlN islands did not coalesce when a H_2 bake was used, whereas the AlN was almost completely coalesced when no H_2 bake was employed. However, additional work needs to be carried out to further understand the effect of baking on the final AlN layer surface morphology.

5.5.1 Pre-dose of aluminium on sapphire wafers

- Optimising TMA pre-dose duration
  Sample studied: C4154 – C4159

The effect of varying the TMA pre-dose duration between 0 to 240 seconds using a fixed 30-sccm flow was investigated with AFM (Figure 5.5). An optimum pre-dose duration of 120s has been determined. 60s pre-dose was insufficient to fully cover the surface with Al, which could lead to partial substrate nitridation resulting in mixed polarity films. A 180s pre-dose was too long and resulted in large scale Al blobs and a rougher pre-dosed sapphire surface, making defect generation more likely once the AlN begins to grow. It should be noted that the surfaces observed using AFM under ambient conditions were not necessarily representative of the surfaces at the growth temperature (since aluminium metal melts at ~550°C). However, significant differences in the surface morphology were apparent when the pre-dose time was varied.

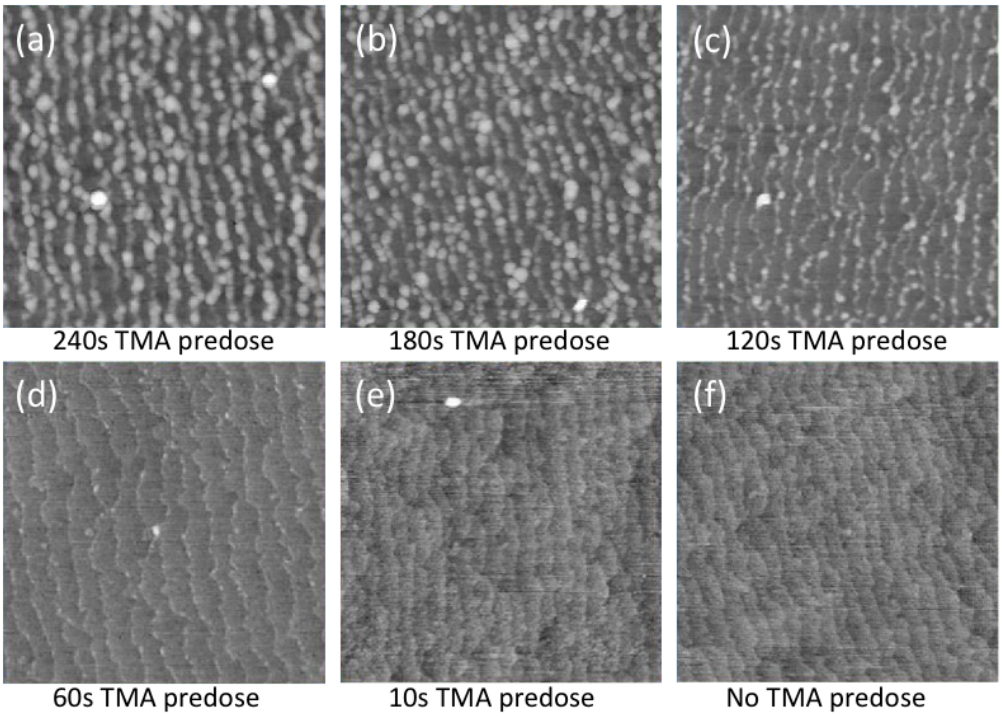

Figure 5.5: AFM images, 1 μm square, of Al coverage on sapphire wafers with varying TMA pre-dose time (sample C4154-C4159). Image z ranges are (a), (b), (c) 20 nm, (d) 10 nm and (e), (f) 5 nm.

- <u>Reactor evolution over time</u>

  Samples studied: C4604, C4619, C4624

The growth session which provided the new pre-dose and AlN samples lasted ~ 1 week and consisted of over 23 growth runs. It was reasoned that the state of the reactor will be different between the beginning and the end of the growth session, i.e. the showerhead can be contaminated with metallic precursors and impurities can be left behind on the susceptor, and that these may influence the growth mode.

At the beginning of the growth session with a new susceptor and a cleaned showerhead, the TMA pre-dosed sapphire surface was smooth. As the growth mode evolves over several runs, relatively large-scale Al blobs start to appear on the TMA pre-dosed sapphire surface (Figure 5.6) prepared using exactly the same bake recipe as the one used initially.

This suggests that the TMA pre-dosed sapphire surface morphology after H_2 bake varies not only with the previous growth recipe but also with the full reactor history, i.e. the state of the susceptor and the degree of contamination on the showerhead.

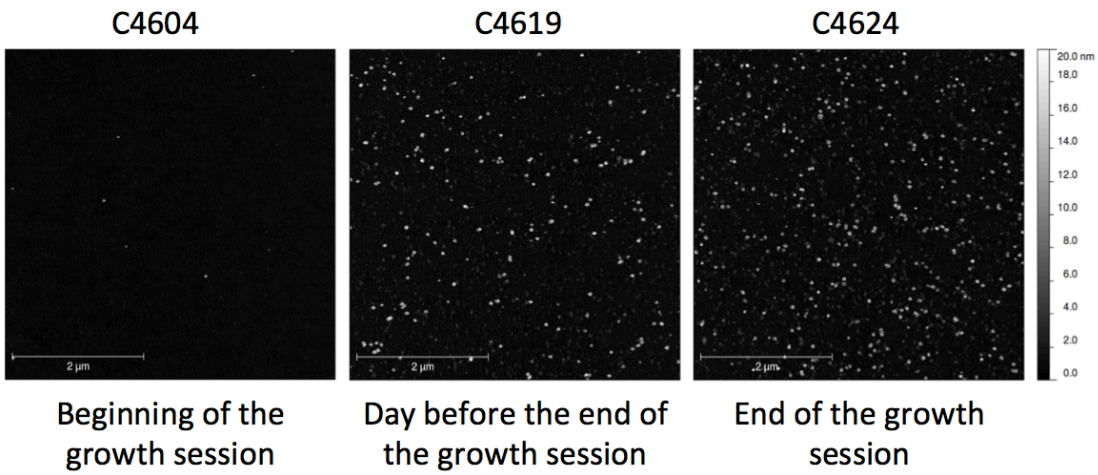

Figure 5.6: AFM images, 5 µm square with 20 nm z scale, of three TMA pre-dose on sapphire samples grown using the same H_2 bake, taken at the beginning of the growth (C4604), day before the end of growth (C4919) and end of growth (C4624). Number of aluminium blobs increased over time. (Courtesy of Dr Oehler)

- Effect of different bake recipes

  Bake recipes used for the TMA pre-dosed sapphire samples:

  C4606: After a AlN growth run (i.e. without H_2 bake)

  C4607: H_2 bake and an introduction of ammonia (NH_3) during final cool down for 5 minutes.

  C4608: H_2 bake and an introduction of ammonia (NH_3) during final cool down for 30 minutes.

  C4617: 30 min nitrogen (N_2) bake

Since we have hypothesized that baking affects the amount of nitrogen containing impurities left over from the previous growth run or the state of the reactor, for example, a contaminated showerhead (refer to previous section), which leads to the variation in surface morphology. Therefore, four different bake recipes were investigated for a study of modified bake processes.

The TMA pre-dosed sapphire sample after an AlN growth run, C4606, (i.e. without a H_2 bake) had a rougher surface than any of the H_2 baked samples shown in the previous section. It also appeared different than the old reference sample C4156 (Figure 5.5 c) grown under the same conditions without a H_2 bake. Surprisingly this non-baked C4606 sample was similar to the old baked sample C4169 (Figure 5.7), suggesting the morphology of the Al film deposited on sapphire wafers may greatly depend on the reactor history in addition to the bake recipe.

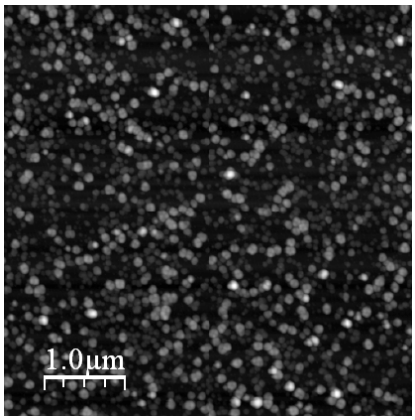

Figure 5.7: AFM image of C4169 (C4156 with H_2 bake), the image z scale was 40 nm.

Interestingly, if the samples (C4607 and C4608) were introduced to an ammonia flow, during the final cool down, their surface morphologies appear to be similar to C4606 (Figure 5.8). The longer duration of the ammonia flow introduced during cool down, C4608, seems to increase the size of the blobs on the sapphire surface (the blobs may be AlN nuclei due to the thermophoretic force between TMA and NH_3, more details in section 5.6). This suggests that either the NH_3 or the compound related to the introduction of NH_3 may produce a memory effect in the reactor.

The sample subjected to a nitrogen (N_2) bake before the TMA pre-dose (C4617) showed similar morphology to a sample grown with a H_2 bake, suggesting that pure nitrogen has an insignificant effect on the surface and only the introduction of ammonia would affect the size of the blobs. However, sample C4617 was grown a few days after the other 3 samples and it was difficult to verify this analysis due to the reactor evolution over time as shown in the previous section.

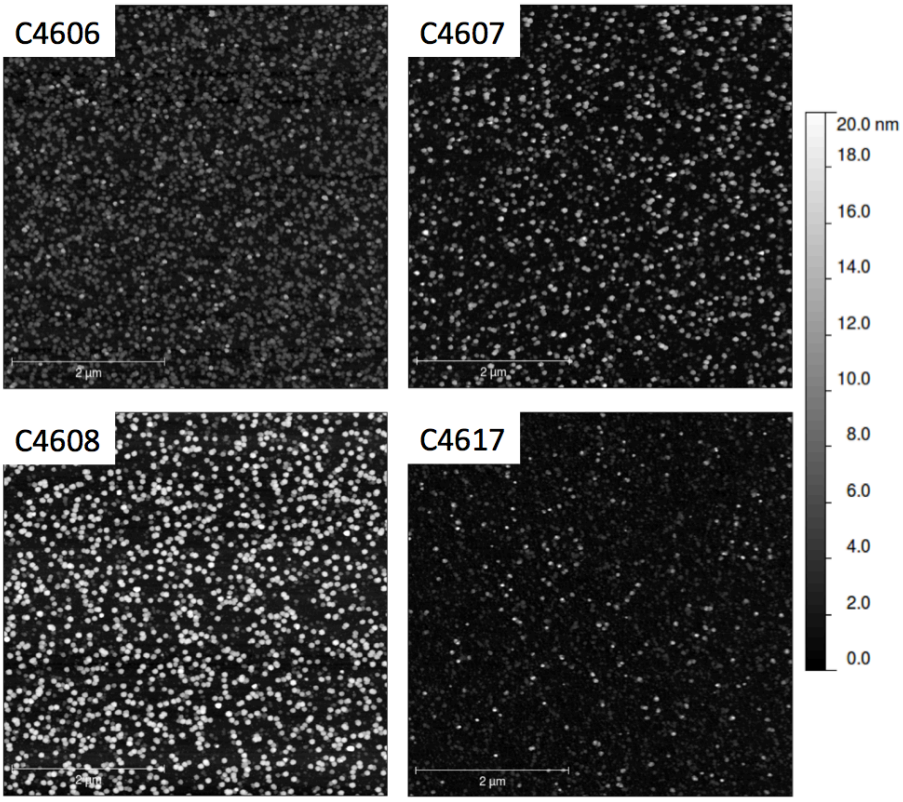

Figure 5.8: AFM images, 5 µm square with 20 nm z scale, of TMA pre-dosed on sapphire samples with different bake recipe. (Courtesy of Dr Oehler)

5.5.2 AlN growth

The difference between a smooth and a rough AlN layer surface as shown in Figure 5.1 seems to be related to the lateral spreading of the surface features (Figure 5.9). Both samples showed a very similar height difference between the flat surfaces and uncoalesced regions.

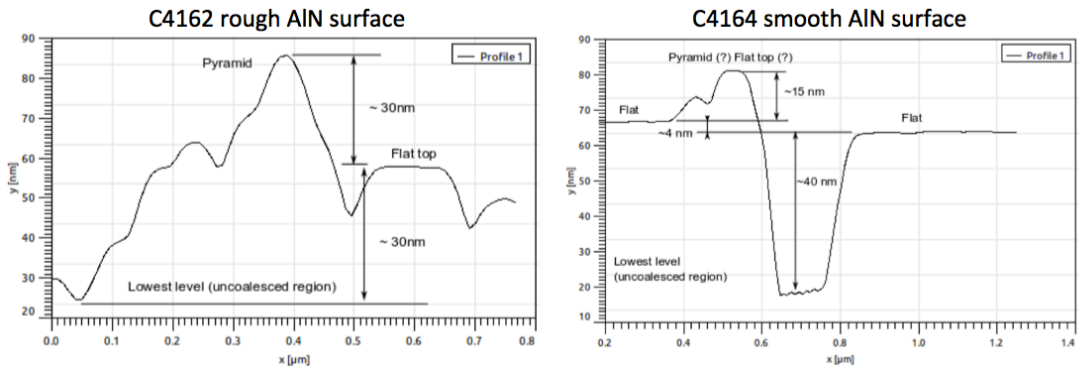

Figure 5.9: Line profiles of the surface feature height extracted from AFM data in figure 5.1.

This in conjunction with the study on the TMA pre-dose and bake recipe in the previous section suggests that the AlN surface morphology may be indirectly related to the bake recipe, but instead directly associated with the variation in the density or nucleation time of the surface blobs (AlN nuclei). In another words, although the lateral growth rate is the same for both samples (the same V/III ratio, pressure and temperature), it is possible that the AlN sample can still have a coalesced surface due to more nuclei being available at the beginning of the growth. If that assumption holds, we would expect to see a coalesced surface when grown on the TMA pre-dosed sapphire sample with a high blob density, such as C4608 (Figure 5.8).

Figure 5.10 shows three 1 µm AlN layers (all grown with intermediate temperature AlN nucleation layers prior to the main layer grown) grown after three different bake recipes: an H_2 bake with an additional 5 min NH_3 flow during cool down, and without an H_2 bake (grown straight after a previous AlN run), and a H_2 bake.

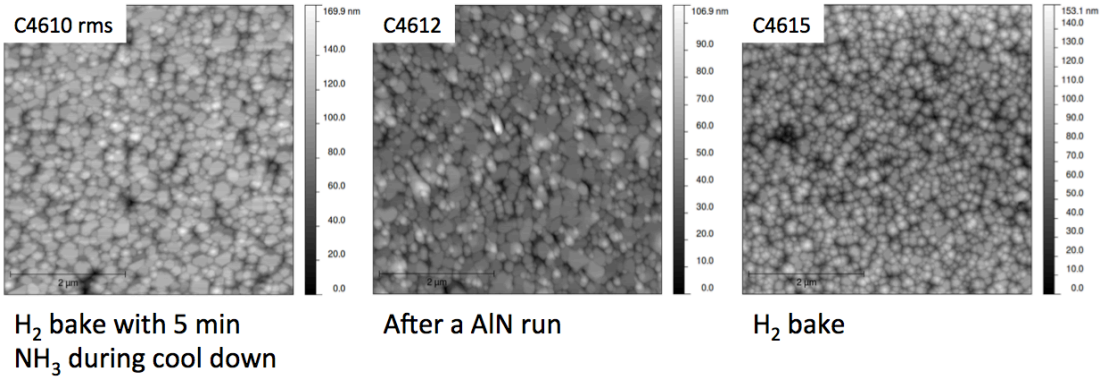

Figure 5.10: AFM images (5 µm square) of three 1 µm AlN templates grown after different bake recipes. RMS values were 17.9 nm, 10.2 nm, and 18.8 nm for C4610, C4612 and C4615, respectively. (Courtesy of Dr Oehler)

These three samples showed a result inconsistent with the assumption made earlier: The RMS value of the AlN surface grown on a high blob density pre-dose sample was actually higher than the AlN sample grown on a non-baked (lower surface blob density) pre-dose sample, and all samples had uncoalesced surfaces. This indicated that the lateral spreading of the surface features did not significantly affect the final AlN layer surface morphology and therefore other parameters should be considered and tuned to achieve a smooth surface.

Varying the duration and molar concentration of TMA used for the pre-dose was initially considered. The same AlN main layers were grown on a 60 s TMA pre-dose sample and a double TMA flux (changed 30 sccm to 60 sccm) sample for C4621 and C4623, respectively. The AlN layer with a 60 s TMA pre-dose grown after an AlN run (without bake) showed a similar morphology (Figure 5.11) compared to the sample prepared using a 120 s TMA pre-dose with a H_2 bake (C4615, Figure 5.10). This indicated that both a 60 s and a 120 s pre-dose were probably insufficient to produce a completely Al-polar surface.

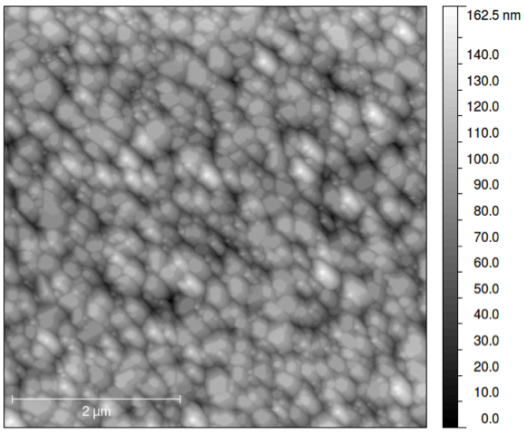

Figure 5.11: A 5 µm square AFM image of C4621 grown with a 60 s TMA pre-dose time. RMS = 19.4 nm

Doubling the TMA flux (with the same pre-dose duration) may lead to a more complete coverage of TMA on the surface at growth temperature (1130°C) according to a thermodynamic study made by Dr Oehler. It was noted that doubling the TMA flux does not necessarily correspond to a doubling of the amount of Al metal being deposited onto the surface. In real life, when the mass flow controller is set to 60 sccm flow, approximately 20 sccm of TMA is required in the gas phase before any material is deposited on the surface.

This AlN layer grown with a doubled TMA flux was grown after another AlN run (without bake), which makes it comparable to sample C4612 with a standard 120 s TMA pre-dose. Figure 5.12 shows the AFM image of this new sample C4623, it seems that the double TMA flux was sufficient for the AlN to coalesce fully and an atomically smooth surface was achieved. The typical surface steps related to the substrate miscut (0.25° toward *a*-Al_2O_3) were visible.

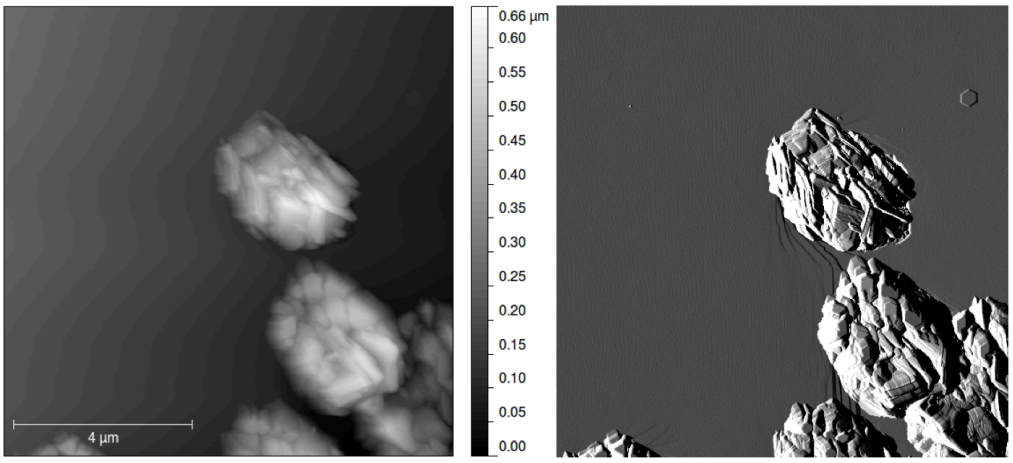

Figure 5.12: A 10 µm square AFM height image of C4623 (left) and an amplitude error image of the same region (right) showing typical surface steps following the substrate miscut. Large-scale structures were also observed with no particular crystal arrangements.

However, there were also a significant number of large-scale structures on the surface being approximately 300 – 500 nm higher than the flat surface. These structures showed a random crystal arrangement (more details on these structures are shown later).

The final AlN layer surface morphology seems to depend greatly on the pre-dose and the early stage of growth. In the next growth run, C4626, an attempt was made to maintain this atomically smooth surface and reduce these large-scale structures by using the same double TMA flux and by optimising the initial nucleation layer growth recipe.

C4626 used the same recipe as C4623; the only difference was how the nucleation layer was grown. For comparison, C4623 had the NH_3 switched directly from vent to inject at 75 sccm, and the TMA was ramped from 60 sccm (pre-dose) to 30 sccm (NL) with NH_3 in 1 min. Whereas C4626 had the NH_3 put to 0 sccm (leaking rate[1]) to vent, and then switched to inject into the reactor (run) for 5 seconds (still at "0 sccm") and ramped slowly to 50 sccm in 1 min and then instantly switched to maximum

[1] At a set point of 0 sccm, the ammonia flow is not completely turned off, so a very small of flow rate (<5 sccm) could still occur

value of 75 sccm flow. The TMA was switched instantly from 60 sccm to 30 sccm during the 5-second window when the NH_3 was switched from vent to run.

Figure 5.13 shows the AFM height and amplitude error image of the improved sample. Again, an atomically smooth surface was observed, however the sample still showed the similar large-scale features. In contrast to the previous run, these features were actually smaller and surrounded by a number of hexagonal hillocks that raised above the surface and the "indents" that extended tens to hundreds of nanometres below the surface.

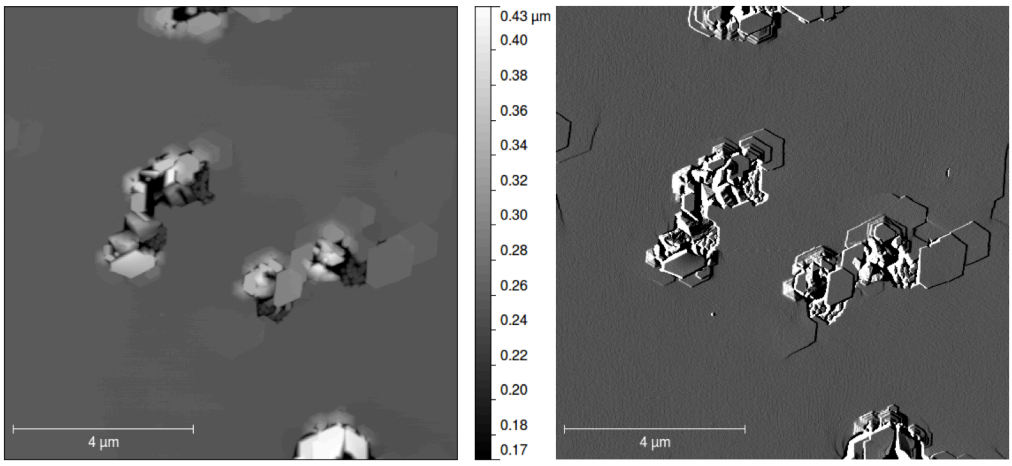

Figure 5.13: A 10 µm square AFM height image of C4626 (left) and an amplitude error image of the same region (right) showing an atomically smooth surface. Relatively smaller structures were also observed surrounded by hillocks and indents.

The HR-XRD scan data (Table 5.2) of the two samples with double TMA flux showed relatively narrow peaks in comparison to the old high quality samples (C4164 and the 4 µm templates used in chapter 3).

Table 5.2: HR-XRD ω scans data.

Sample	AlN layer thickness	ω scan FWHM (002)	ω scan FWHM (101)	Description
C4623	1 µm	402	693	Double TMA flux
C4626	1 µm	522	1090	
C4164	1 µm	616	773	Old recipe
C4162	1 µm	660	1495	
C3899	4 µm	254	462	

The reference samples C4164 (without bake, smooth surface) showed a narrower peak width in (10-11) reflection in comparison to C4162 (bake, rough surface), suggesting a reduced edge-type threading dislocation density, as confirmed with cross-sectional TEM studies in Figure 5.14 and 5.15. The higher threading dislocation density in C4612 was related to the high number of inversion domains present in the mixed polarity layer.

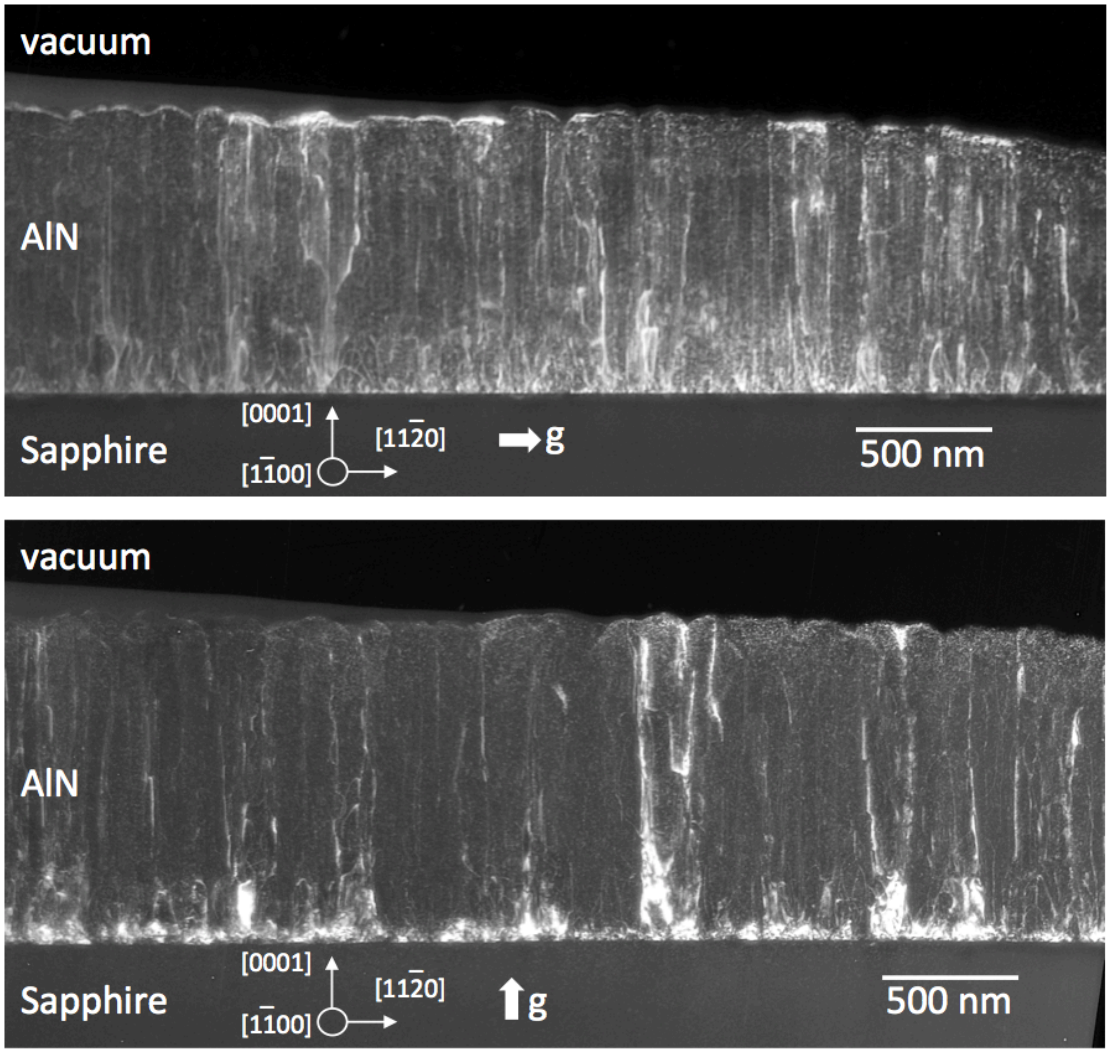

Figure 5.14: Cross-sectional TEM images of sample C4162 showing rough surfaces with high threading dislocation densities associated with inversion domains in both g = 11-20 (*a*+*c*- and *a*-type) and 0002 (*a*+*c*- and *c*-type) conditions.

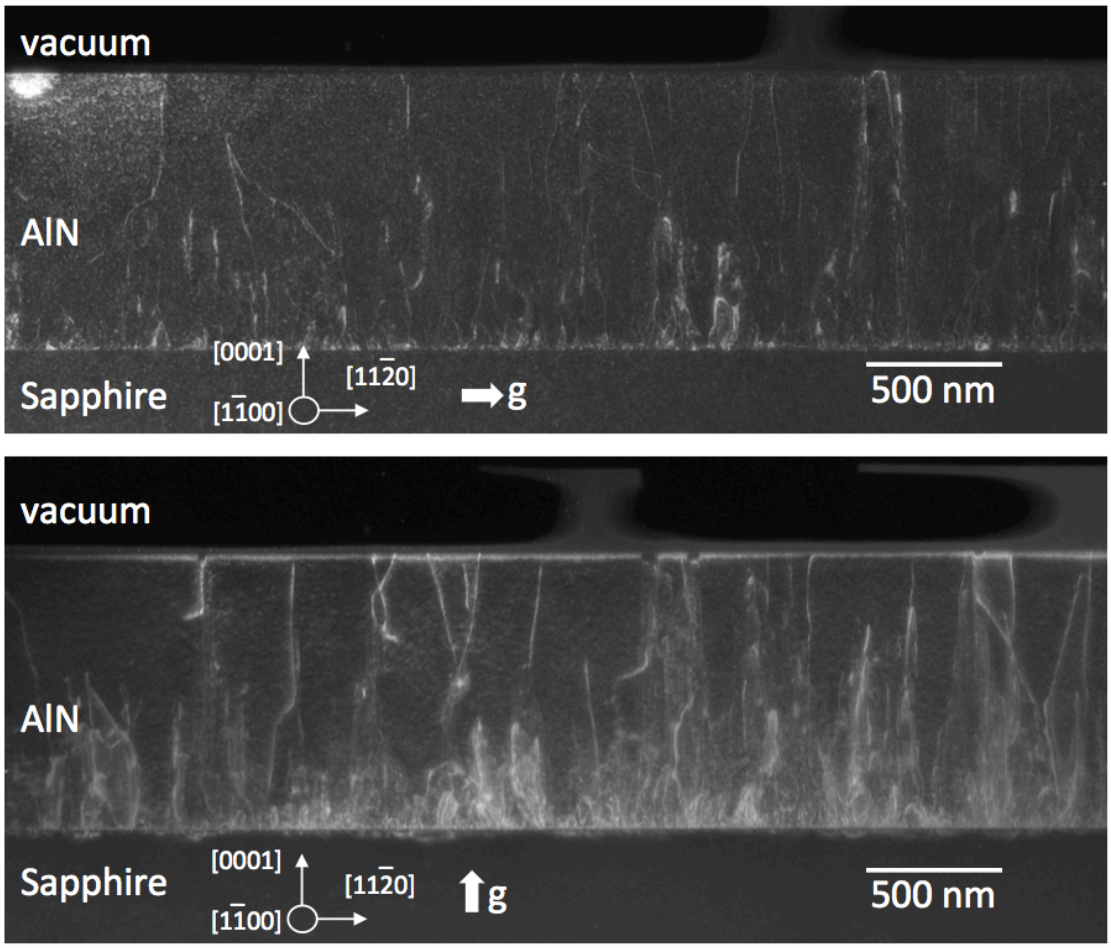

Figure 5.15: Cross-sectional TEM images of sample C4164 showing smooth surfaces with relatively lower threading dislocation densities in both g = 11-20 (*a*+*c*- and *a*-type) and 0002 (*a*+*c*- and *c*-type) conditions.

The AFM image of C4164 (Figure 5.1) shown earlier indicated that the surface was not fully coalesced, there were some regions with "indents" that extended up to 90 nm below the surface. The cross-sectional TEM image (Figure 5.16) showed the higher threading dislocation density was associated with these indents and were possibly inversion domains (i.e. N-polar materials embedded in Al-polar AlN). This suggested that the old reference sample with a standard 120 s TMA pre-dose was insufficient to fully cover the substrate surface, or that the way the ammonia was injected into the reactor was not optimised so that slight nitridation still occurred on the substrate surface.

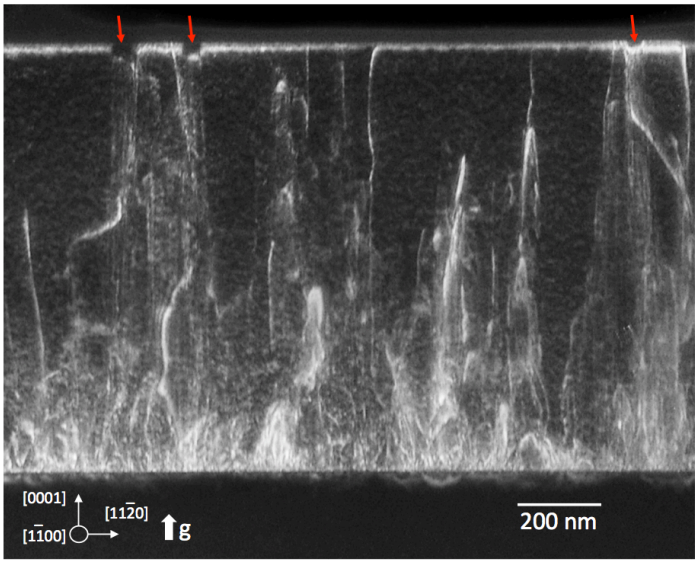

Figure 5.16: Cross-sectional TEM image of C4164 showing the regions with higher threading dislocation densities were associated with the "indents" (marked by the red arrows) on the layer surface.

Sample C4623 with larger surface features was of better crystalline quality than C4626, especially in the (10-11) reflection, which also suggested a reduced edge-type threading dislocation density (Figure 5.17), similar to the observation of C4162 and C4164: the XRD ω scan peak width value was higher for C4626, which was related to a higher density of inversion domains in a cross-sectional TEM image (Figure 5.18). These inversion domains corresponded to the raised hexagonal hillocks observed earlier in the AFM data in Figure 5.13.

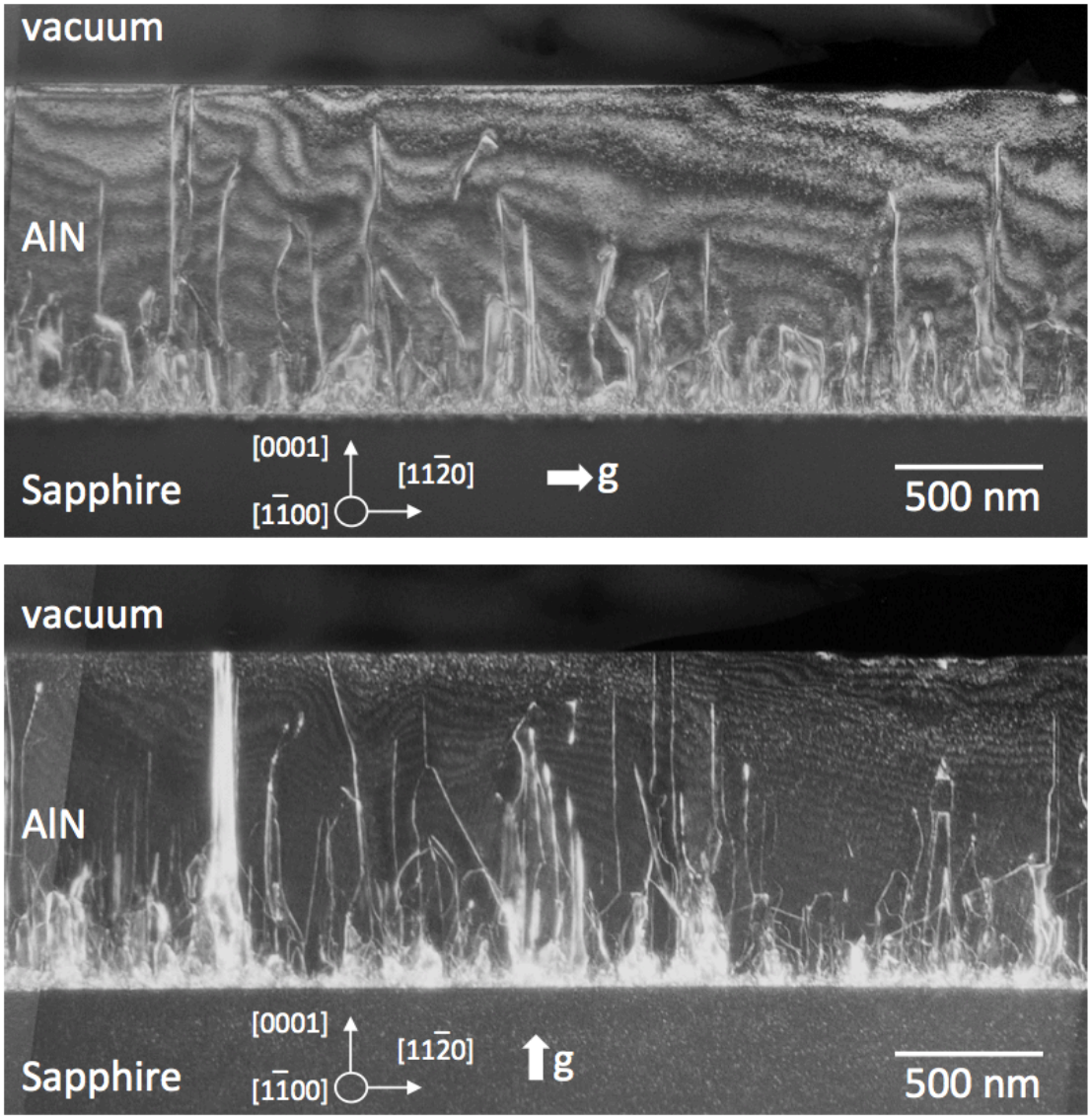

Figure 5.17: Cross-sectional TEM images of sample C4623 showing threading dislocations reduction in both g = 11-20 (*a*+*c*- and *a*-type) and 0002 (*a*+*c*- and *c*-type) imaging conditions.

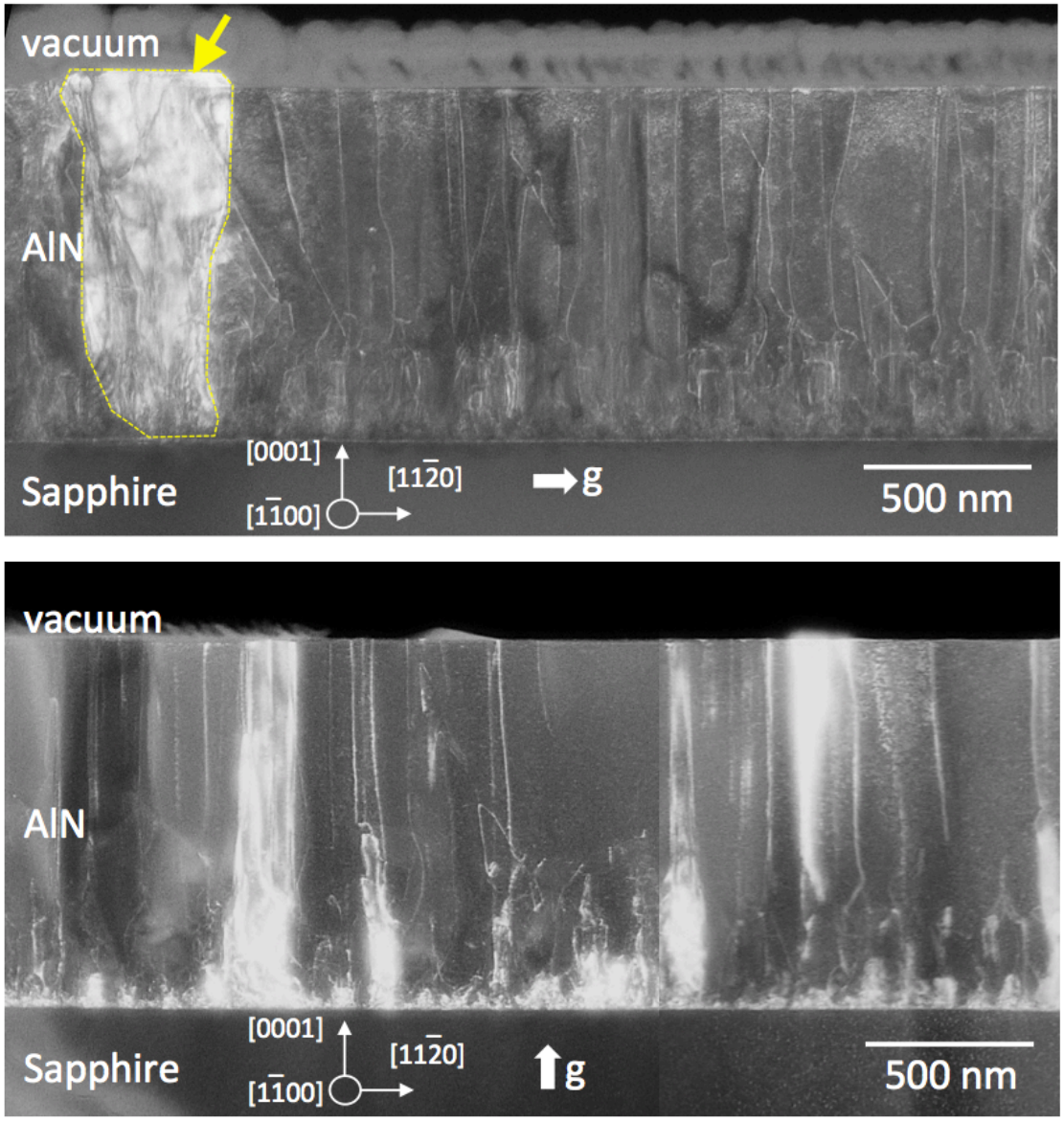

Figure 5.18: Cross-sectional TEM images of sample C4626 showing slightly higher threading dislocation densities than C4623 in both g = 11-20 (*a*+*c*- and *a*-type) and 0002 (*a*+*c*- and *c*-type) conditions. Inversion domain (marked by the yellow dashed line) was observed as an opposite contrast (brighter) in the WBDF imaging condition.

Both double TMA pre-dosed sapphire samples were slightly better than the older samples C4164 and C4162 grown with the standard 120 s TMA pre-dose. Figure 5.19 summarises the XRD ω scan FWHM values of the samples studied (including additional low dislocation density GaN and different AlN layer thicknesses for comparison).

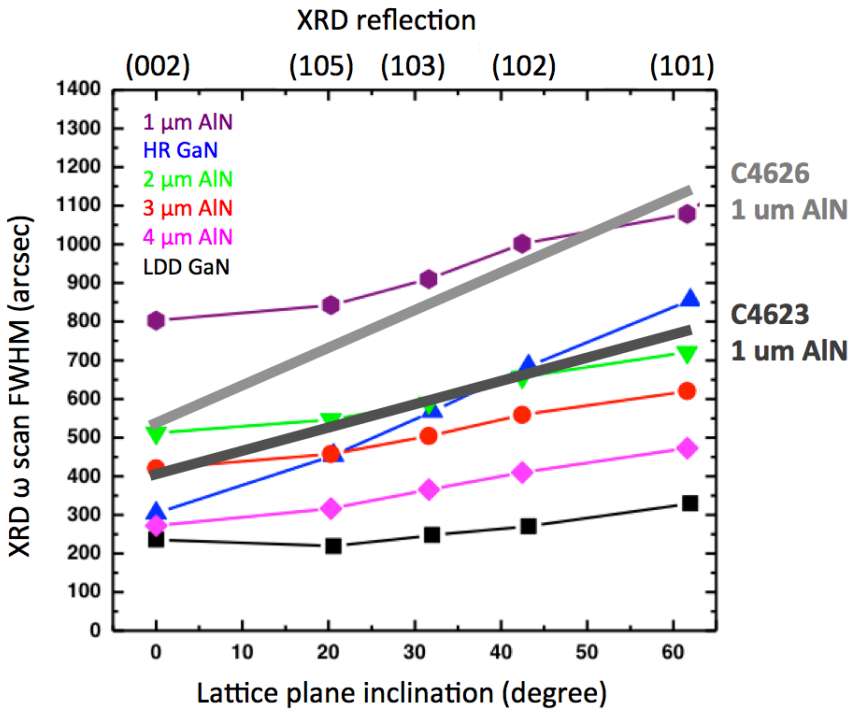

Figure 5.19: HR-XRD ω scan peak widths of the AlN samples with doubled TMA pre-doses compared to reference samples.

The crystalline quality of the 1 µm AlN layer (C4623) was comparable to the old reference 2 µm AlN layer despite the presence of the large-scale structures. It is expected that growing a 4 µm layer with the new recipe would result in a film quality that exceeds the original high quality AlN layer and will become comparable to the LDD GaN template.

5.6 Discussion

- **Influence of the bake process and the reactor history**

The early hypothesis based on the observation of C4162 and C4164 stated that the final film surface morphology greatly depends on the initial bake process, i.e. a smooth and coalesced film would be produced if the layer were grown without a bake

providing impurities such as nitrogen containing compounds were present in the reactor after the previous run.

In this work, some variations in the island morphology during the initial growth stage were observed depending on whether a hydrogen bake was used prior to growth (after a previous AlN growth). However, the surface never achieved coalescence with any bake recipe. This suggested that the final surface morphology did not depend only on the bake, but instead on the entire initial growth process including the effects from the pre-dose step.

The evolution of the reactor performance overtime suggested that the H_2 bake was not always able to fully remove the influence of historical effects in the reactor. Nitrogen containing compounds were able to stay in the reactor between the runs. These compounds would affect the size of the blobs on the TMA pre-dosed sapphire surface. The presence of the residual NH_3 contamination could originate from the previous run or the residual GaN decomposition at 900°C in the H_2 ambient. However the result was not able to differentiate between these two hypotheses and further experiments are required.

- **Influence of the TMA pre-dose flux and the presence of the "blobs"**

Coalescence was achieved with a significant increase in the TMA pre-dose. This new pre-dose was not optimized and it is likely that a smaller pre-dose could achieve a similar result. The double TMA pre-dose final surfaces were fully coalesced whereas the final surfaces of the standard TMA pre-dose were near complete with the presence of some elongated indents in the layer.

The "blobs" observed on the TMA pre-dosed sapphire surface might be AlN islands that arise from the reaction between the ammonia and the molten Al layer, resulting from the TMA pre-dose, at high growth temperature. Another explanation might be due to the thermophoretic force, reported by Creighton *et. al.* [158], that convert the precursors, TMA and NH_3, into nanoparticles in gas phase, a co-ordination compound $(CH_3)_3Al{:}NH_3$, where some of the lone-pair electron distribution on the ammonia is donated to the Lewis acid of the TMA [159]. Creighton *et. al.* suggested this conversion process was significant, 20-80% of the input aluminium is lost from the MOCVD process because of nanoparticle formation. This degree of conversion could

also explain the decline in AlN growth rates at high temperature. However, at this stage, it is not clear whether these nanoparticles are able to stay on the sample surface as nuclei that lead to the presence of AlN islands ("blobs") at high temperature, and potentially lead to the formation of large randomly orientated crystals.

- **Large features on the coalesced surfaces**

Both AlN samples with doubled TMA pre-doses contained large (> 1 µm wide) pyramidal agglomerates of crystals. The cross-sectional TEM images (Figure 5.20) suggested these features start growing at the same time as the main AlN layer growth. They do not seem to be epitaxially related to the surface and the agglomerates were randomly orientated as indicated by the diffraction pattern.

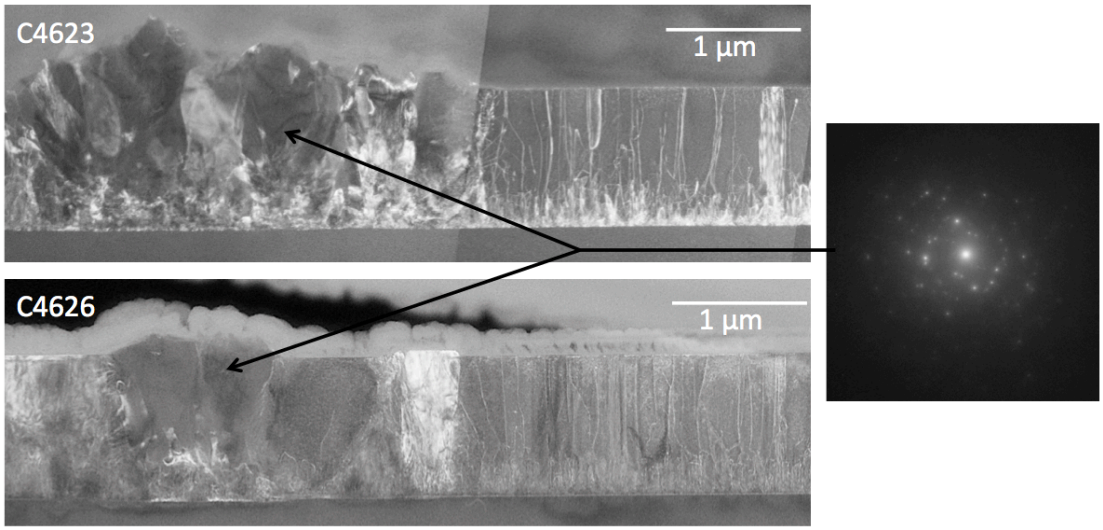

Figure 5.20: Large features were observed in both AlN samples with doubled TMA pre-doses. Diffraction pattern at these regions showed randomly orientated crystals.

Unlike the formation of inversion domains, the "alien" nature of these large crystals suggest that they do not form on the surface but instead nucleate in the gas phase (powder formation) before impinging on the sapphire substrate. Powder formation in the gas phase is favoured when a high reactor pressure (200 Torr) used during the nucleation layer growth is coupled with the high TMA reactivity [157]. These seed with random orientations, which impinge on the surface, then lead to various configurations of the large crystals. Further investigation would be required to

understand whether this powder formation is related to the nanoparticles mentioned in the previous section.

STEM-EDX measurements were employed to study the composition of these large polycrystalline features. Figure 5.21 shows the change in ratio of oxygen and nitrogen signals from a 200 nm EDX line profile acquired between the sapphire and the main AlN layer. A clear transition from Al_2O_3 to AlN was observed as the oxygen signal decreases and nitrogen signal increases at the heterointerface.

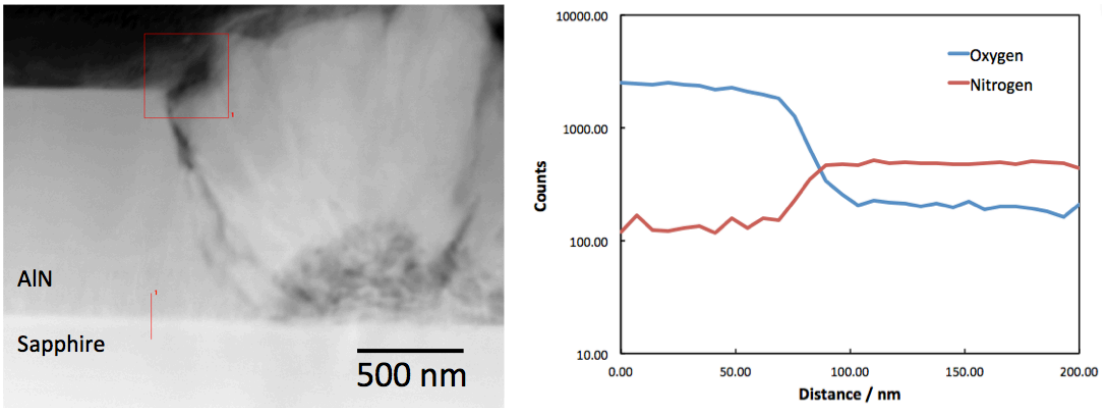

Figure 5.21: A cross-sectional STEM-EDX map of the structure (left). The red line profile was extracted to show the oxygen and nitrogen signals against measurement position (right). The red square was the spectrum drift correction.

Figure 5.22 shows the EDX line profile acquired when moving from the sapphire substrate to the polycrystalline features. The change in oxygen and nitrogen signals was similar to the previous result indicating that these large polycrystalline features were AlN compounds, the same composition as the rest of the AlN layer. However, above the heterointerface, there were regions showing darker z-contrast (lower atomic number) in the STEM map. The change in oxygen and nitrogen signals at this region was similar thus making it difficult to differentiate the composition at the interface.

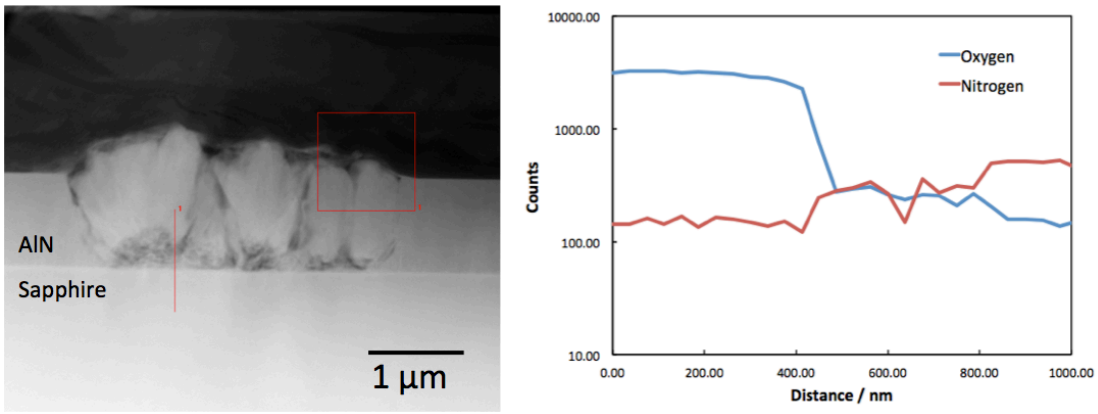

Figure 5.22: A cross-sectional STEM-EDX map of the structure (left). The red line profile measured the oxygen and nitrogen signal transition from sapphire to polycrystalline features (right).

An EDX line profile with smaller pixel step (the same 30 acquisitions as previously but acquired within 400 nm length instead of 1000 nm) was measured just above the heterointerface (Figure 5.23). At this scale, the oxygen and nitrogen signals were still difficult to differentiate. However, an additional peak was distinguishable corresponding to elemental carbon. The TEM image of the exact same region (Figure 5.20) did not show any void at the interface, suggesting that these darker z-contrast regions just above the interface contain oxygen, nitrogen, carbon or their related compounds. The presence of carbon was possibly due to a broken valve of the reactor exhaust system leading to back-flow of residual contaminants and causing an increase in chamber pressure. Alternatively, this carbon trace might also indicate the presence of nanoparticles $(CH_3)_3Al{:}NH_3$ as suggested earlier. Again, further detailed EDX analysis on the surface blobs would be required to understand the role of the nanoparticles formed in the gas-phase. As mentioned earlier, high TMA flux coupled with high reactor pressure often leads to powder formation. Thus further optimising the TMA pre-dose duration and flux and careful control of the chamber pressure should prevent the formation of AlN powder in the gas phase.

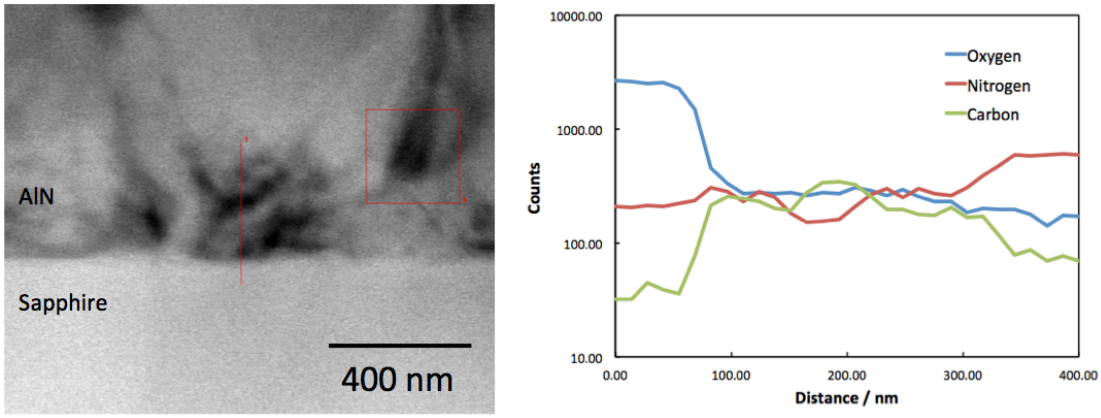

Figure 5.23: A cross-sectional STEM-EDX map of the structure (left). The red line profile measured the oxygen and nitrogen signal transition at the heterointerface with a smaller pixel step.

5.7 Conclusion

The effect of a bake process on the final AlN film surface morphology was more complicated than expected. The pre-dose study suggested that the final surface morphology depends not only on the bake process but also the reactor state since a H_2 bake could not always fully remove the impurities in the reactor. Residual nitrogen containing compounds could stay in the reactor between runs and cause partial nitridation at the initial pre-dose step that breaks up the coverage of the thin Al film on the substrate surface.

Doubling the TMA pre-dose enabled a better Al coverage to be achieved leading to a fully coalesced AlN film at 1 µm thickness (the old high quality reference sample was only nearly completely coalesced at this thickness). An atomically smooth surface was achieved over a large 10 x 10 µm AFM scale (the old high quality sample still showed large surface steps even at 4 µm thickness at this scale). The XRD ω scan peak width of this new 1 µm AlN film was comparable to the older 2 µm thick reference sample. It was expected that using this approach, a 4 µm AlN film could achieve an even better ω scan result that would be comparable to a typical LDD GaN film.

Large polycrystalline AlN compounds were observed initiating at the heterointerface. Their “alien” nature suggested that they originated from powder formation in the gas

phase due to high TMA flux coupled with high reactor pressure during the initial stage of growth (pre-dose step and nucleation layer). Randomly oriented seeds drop onto the surface and enlarge during the main AlN layer growth. Further optimising the TMA pre-dose duration and flux and a careful control of the chamber pressure should prevent the formation of these large polycrystalline features.

6

Nonpolar a-plane GaN/AlGaN MQW structures.

6.1 Background

The lack of symmetry in the Wurtzite III-nitride unit cell leads to macroscopic spontaneous polarisation P_{SP} induced along the polar [0001] c-axis. This in conjunction with the piezo-electric polarisation P_{PZ} introduced by the strain at hetero-interfaces, results in the Quantum Confined Stark Effect (QCSE), which redshifts the recombination energy and decreases the electron-hole wavefunction overlap with increasing QW width (figure 6.1), which ultimately reduces the optical efficiency due to non-radiative recombination processes.

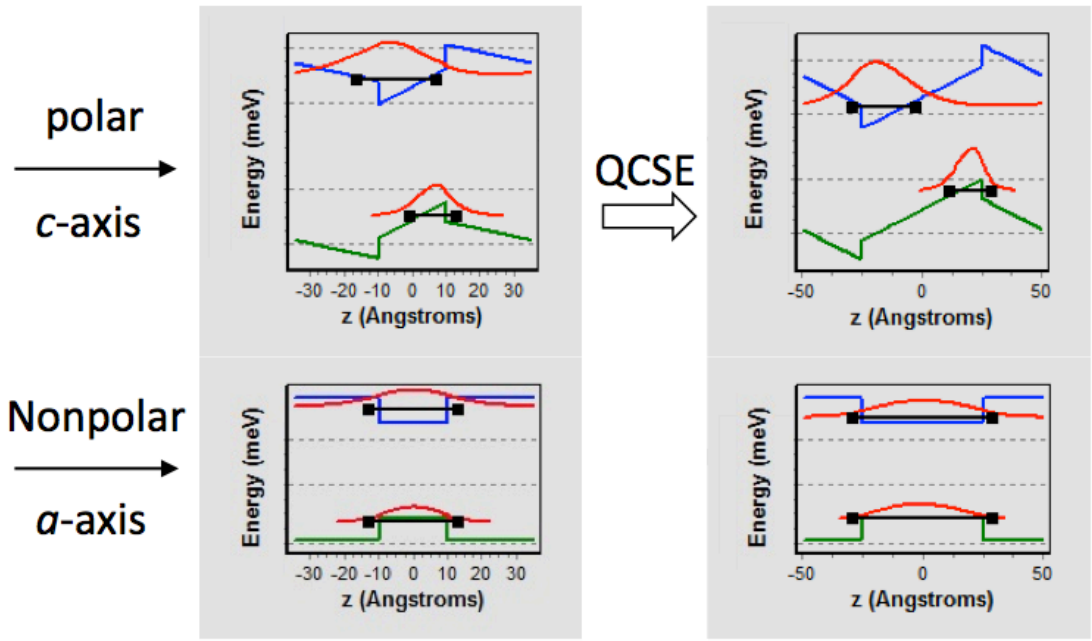

Figure 6.1: Effect of quantum wells thickness on polar and nonpolar III-nitride band structures.

As mentioned earlier in Chapter 1, growth in the nonpolar crystal orientation eliminates the QCSE and restores e-h wavefunction symmetry. This has been confirmed by many reports [38] in the literature and also by photoluminescence (PL) studies on the nonpolar AlGaN/GaN MQW structures used here. Figure 6.2 shows that nonpolar (11-20) AlGaN/GaN QWs are not subject to a significant electric field.

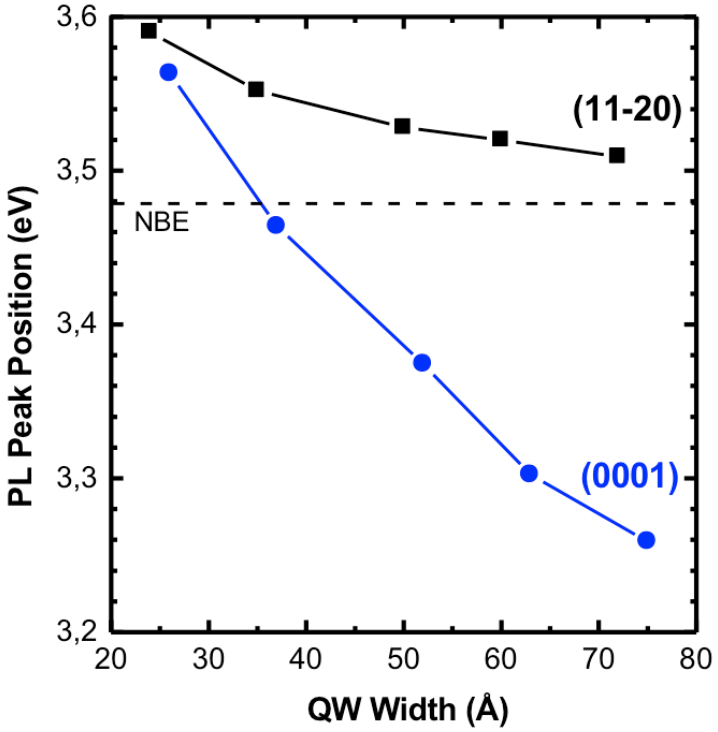

Figure 6.2: Results of polar and nonpolar QW structures on PL peak positions against quantum well thicknesses. Nonpolar (11-20) QWs are not subjected to a significant electric field (Courtesy of Dr. Tom Badcock).

Nonpolar a-plane GaN/$Al_xGa_{1-x}N$ multiple quantum wells (MQWs) are promising for use in ultraviolet light-emitting diodes, due to the reduced quantum confined Stark effect expected for nonpolar structures [54]. Many works on nonpolar or semipolar structures have been reported in the literature in the past few years and have shown successful reduction in the QCSE [38]. However, the consequence of growing in an off-basal-plane crystal orientation is that much higher defect densities are produced due to the nature of nonpolar growth as mentioned in Chapter 1.

Epitaxial lateral overgrowth (ELOG) was found to be effective at reducing the defect density of nonpolar and semipolar structures as reported by [38] and many other groups [160]. However, the ELOG technique requires a number of ex-situ process steps, including mask deposition and lithography. In addition, the materials are only improved over the overgrown wings but the defect density remains high in the window regions.

An alternative solution is to employ an in-situ SiN_x interlayer to reduce the defect density. The SiN interlayer produces inhomogeneous nucleation and lateral growth of the overlayer, causing bending of dislocations towards facet walls, and it also blocks some dislocations from entering the overlayer. The interlayer is deposited on the templates by in-situ deposition of silane (SiH_4) and ammonia (NH_3) and it has been shown to be effective at reducing defect densities from 10^9 to 10^7 cm^{-2} in c-plane GaN [161]. It has also been recently used successfully in nonpolar growth [162], where significant reduction in partial dislocations has been observed. However, the defect reduction mechanism of the SiN interlayer is not very well understood and detailed studies are required to optimise the use of these interlayers in nonpolar structures.

It is also interesting to study the MQW structures grown on these reduced defect density nonpolar templates, especially for UV-emitting GaN/AlGaN QW structures, where most of the studies on UV structures are still based on more mature c-plane growth techniques, and much less work has been reported on nonpolar UV structures. This chapter reports on a series of GaN/$Al_xGa_{1-x}N$ MQW structures grown on reduced defect density a-plane (11-20) GaN on r-plane (1-102) sapphire substrates, in which the QW thickness, t, was varied between t = 1 and 5 nm and the $Al_xGa_{1-x}N$ barrier composition, x, was varied between x = 0.22 and 0.41, while the barrier thickness was kept constant at 5 nm. This series of samples were designed in collaboration with the University of Manchester. Their role was to used temperature dependent PL to study the enhancement in the exciton binding energy and the reduction in radiative lifetime and therefore possibly higher IQE. Our role was to study the structural information such as defect analysis.

6.2 Aim

Specific aims throughout the course of this chapter include:

1. To study the optical and microstructural differences between samples with varying well thicknesses and barrier compositions.

2. To study the effects of a SiN interlayer on the quality of an *a*-plane GaN template.

6.3 Experimental details

All samples were grown by metalorganic vapour phase epitaxy (MOVPE) in a Thomas Swan 6 × 2" close-coupled showerhead reactor using trimethylaluminium (TMA), trimethygallium (TMG), silane (50 ppm SiH_4 in H_2) and ammonia (NH_3) as precursors and hydrogen as carrier gas. The nonpolar (11-20) GaN epilayers were grown as follows: (a) r-plane (1-102) sapphire was heated in a flow of hydrogen and ammonia to 1050 ºC for 3 min at a reactor pressure of 100 Torr followed by 3 min with an additional silane flow of 200 nmol/min; (ii) a GaN nucleation layer with a thickness of 30 nm was deposited at 540 ºC and 500 Torr; (iii) a 600 nm-thick GaN epilayer was deposited using a flow of 660 μmol/min at 1030 ºC, 100 Torr and a V–III ratio of 34; (iv) the GaN growth was interrupted for the incorporation of in-situ SiN_x interlayer using a flow of 200 nmol/min silane and ammonia at 860 ºC for 900s; (v) the GaN overgrowth was recommenced at 1000 ºC and 300 Torr for 300s using a TMG flow of 270 μmol/min and a V-III ratio of 1650 followed by 2300s using a TMG flow of 660 μmol/min at 1010 ºC, 100 Torr and a V–III ratio of 34. The pseudo-templates grown as such were stored in wafer boxes in a dry nitrogen atmosphere of a glove box. The growth of the 15 different GaN/AlGaN 10QW structures was started with a GaN connecting layer of 700 nm thickness to bury the regrowth interface. Three sets of MQW structures were grown in which the Al composition of the AlGaN barrier was set at 22, 32 and 41%, while the nominal QW thickness was varied between 1 and 5 nm with a step size of 1 nm by varying the well growth time. The quantum wells were grown at 1020 ºC and 50 Torr using a TMG flow of 106 μmol/min giving a GaN growth rate of 0.263 nm/s, while the barriers were grown under the same conditions with the same TMG flow of 106 μmol/min and either a TMA flow of 38 μmol/min for 13.7s for 5nm thick $Al_{0.22}Ga_{0.78}N$ barriers, or a TMA

flow of 65 μmol/min for 11.4s for 5nm thick $Al_{0.32}Ga_{0.78}N$ barriers, or a TMA flow of 102 μmol/min for 9.8s for 5nm thick $Al_{0.41}Ga_{0.78}N$ barriers.

A schematic of the sample growth is shown in figure 6.3.

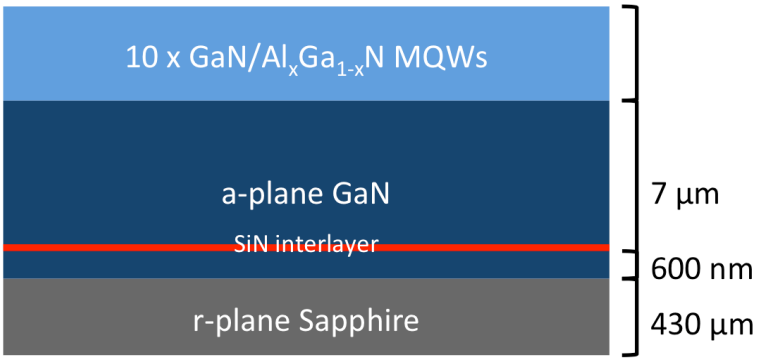

Figure 6.3: A schematic of the sample structure. GaN QW thickness ranged between 1 to 5 nm. AlGaN QB composition ranged between 22%, 32% and 41%, at constant 5 nm thicknesses. A 900s SiN interlayer was grown 600 nm above the substrate.

Both cross-sectional and plan-view TEM samples were prepared by an argon ion beam thinning technique using a Gatan precision ion-polishing system. For microstructural characterisation of the TEM samples, a Philips CM30 (300 kV) TEM and a Tecnai F20-G2 (200 kV) TEM with STEM-HAADF facilities were used. A PANalytical MRD PW3050/65 HR-XRD diffractometer was used to determine the full width at half-maximum (FWHM) values from ω-scans of the 11-20 reflections, and to determine strain-states and alloy compositions of AlGaN buffer layers from reciprocal space maps around 11-22 and 11-20 reflections. The cathodoluminescence (CL) data were acquired from a Gatan MonoCL4 system attached to a Philips XL30s field emission gun scanning electron microscope. Panchromatic images (displaying intensity collected over a broad wavelength range of about 200 - 600 nm) and monochromatic images (displaying intensity collected over a narrow wavelength range of about 10 nm, centred on a specified wavelength) and CL spectra were acquired at an operating voltage of 5 kV using liquid nitrogen cooling to reach low temperatures of 90 K. Surface morphologies were studied using a Veeco Dimension 3100 atomic force microscope (AFM) in TappingMode™ with a standard uncoated silicon tip.

Table 6.1: Sample descriptions. Samples selected for detailed studied are printed in bold.

GaN QW / nm	5 nm $Al_{0.22}Ga_{0.78}N$ barrier	5 nm $Al_{0.32}Ga_{0.68}N$ barrier	5 nm $Al_{0.41}Ga_{0.59}N$ barrier
1	**C4284B**	**C4289B**	**C4294B**
2	C4286B	C4291B	C4296B
3	C4283B	C4288B	C4293B
4	C4285B	C4290B	C4295B
5	**C4287B**	**C4292B**	**C4297B**

PL measurements were carried out for all 15 samples. 6 out of the 15 samples were selected for further SEM-CL, AFM and (S)TEM studies.

6.4. Results

6.4.1 Optical studies

QW emission energies were calculated using in-house simulation software, BlueCalc, (shown as dotted lines in figure 5.4). Room temperature PL and CL measurements were carried out and compared with the theoretical values. It should be noted that the slight blue shifts in the CL peak positions compared to PL may be due to calibration differences between the detectors in the different instruments.

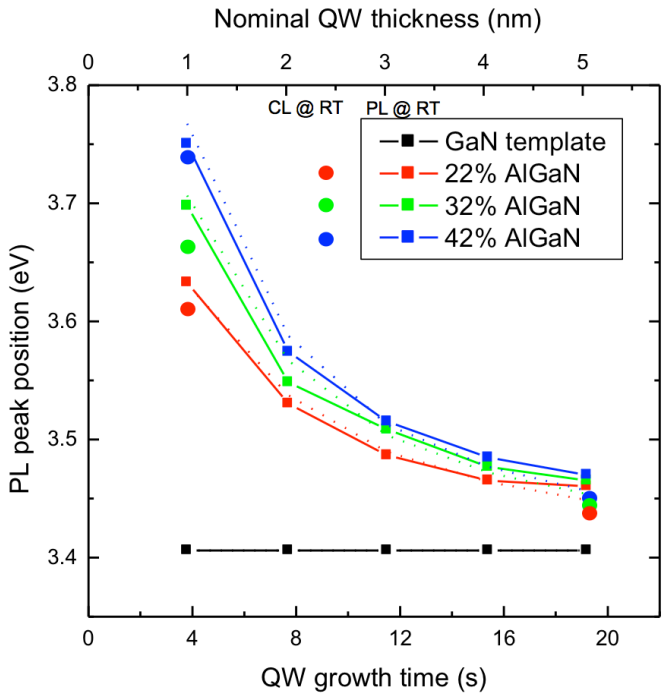

Figure 6.4: BlueCalc simulations (dotted lines) and experimental (data points and drawn lines) CL and PL results on peak positions against quantum wells thicknesses.

The QW confinement decreases as the well thickness increases, which is expected from the calculation by [163] and confirmed by the PL and CL results. This leads to similar peak positions for the 5 nm well thicknesses even when the aluminium content varied between 22% and 42% in the AlGaN barriers. This also indicates that the simulated quantum well and barrier thicknesses are in a good agreement with the actual growth. However, the variation between the simulated well thicknesses (t = 1 and 5 nm) and $Al_xGa_{1-x}N$ compositions (x = 0.22, 0.32 and 0.41) may affect the growth of the active region due to differences in strain and critical thicknesses. Therefore, accurate experimental determination of the thicknesses was still required in order to correlate to the band gap energy measured from the optical studies.

X-ray diffraction was employed to measure the actual layer compositions and thicknesses. These can be easily measured for c-plane oriented III-nitrides as the films are under symmetric biaxial stress and a reliable set of calculated elastic constants are available [135]. However, in the case of the nonpolar orientation, the two in-plane elastic constants are no longer the same, and tilt might occur in the film. Also commercial XRD simulation software does not exist yet for off basal plane

orientations. Therefore an alternative approach has to be used instead. A method developed by Hollander and McAleese [164] described the transformation from conventional (c-plane) calculated elastic constants into new values appropriate for the nonpolar orientation. They have derived an equation based on the transformation, the *d*-spacing of the III-nitride template and the strained alloy layer (determined from well-to-barrier thickness ratio from low-angle X-ray reflectivity measurement), which successfully measured the composition of a layer.

Reciprocal space maps of (11-20) at both phi = 0° and 90° confirmed that there was no presence of tilt in the film (figure 6.5).

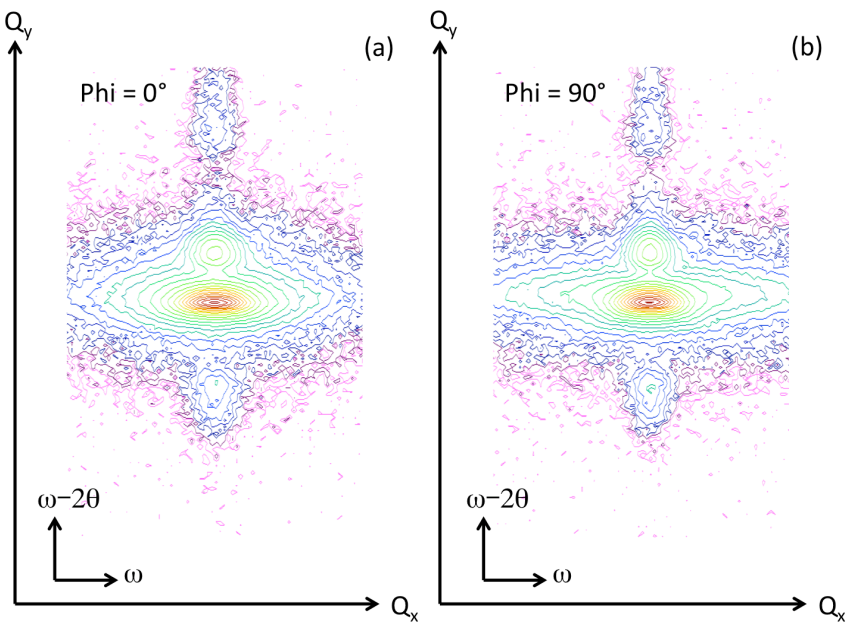

Figure 6.5: Reciprocal space maps (RSM) of C4287B taken at (11-20) reflection with (a) [0001] (phi = 0°), and (b) [1-100] (phi = 90°) crystal orientations.

Unfortunately, the peak intensities from the ω–2θ scans (figure 6.6) and low angle reflectivity (not shown) measurements were too low to accurately determine the well-to-barrier thickness ratio. This can be attributed to the surface morphology of the samples being fairly rough with a few hundred nanometres difference in heights in the vicinity of the striations (figure 6.7).

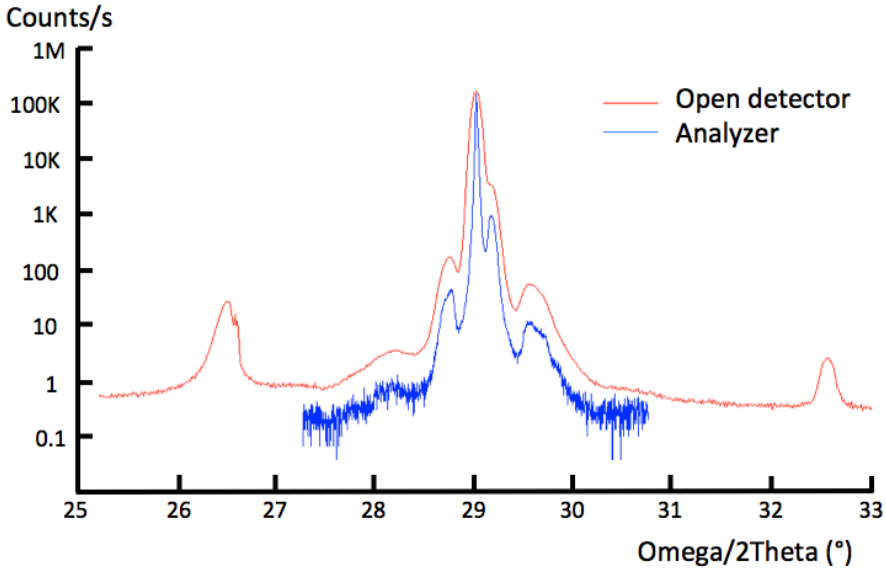

Figure 6.6: 11-20 ω–2θ scans with an open detector (blue line) and with an analyser crystal (red line) of sample C4287B. Both could not detect MQW fringes.

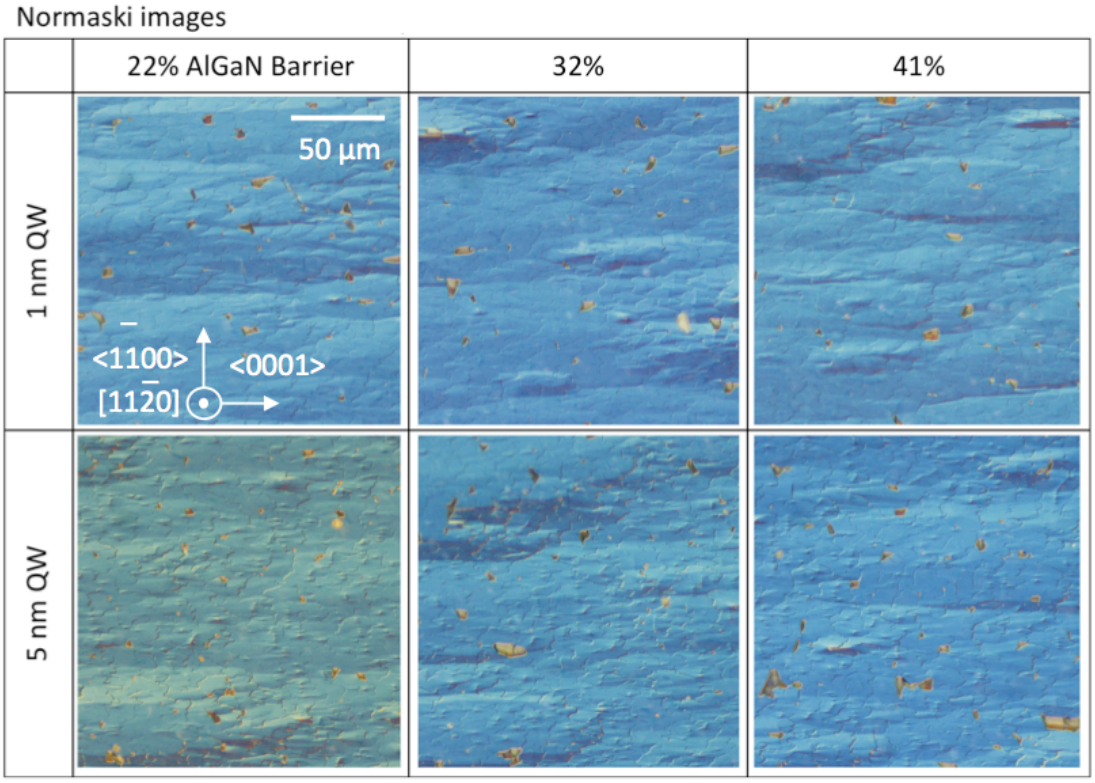

Figure 6.7: Nomarski plan-view images of the sample surfaces showing surface striae run in the <0001> direction.

XRD scans taken at both beam incident directions (i.e. <0001> and <1-100> sample directions) could not detect MQW fringes, suggesting the key issue that caused such

low signal intensities was because X-ray diffraction is highly sensitive to the local nano-scale changes in surface steps. If there was a significant amount of nano-scale (~ 5 nm) surface steps presented in the film, the peak intensities 'smear-out' and drop significantly. The presence of these nano-scale surface steps was confirmed from the AFM results (figure 6.8) and cross-sectional electron microscopic images shown later. These samples were therefore unsuitable for X-ray diffraction analysis of layer compositions and thicknesses. Alternative characterisation techniques, such as cross-sectional STEM-HAADF were required to determine these values.

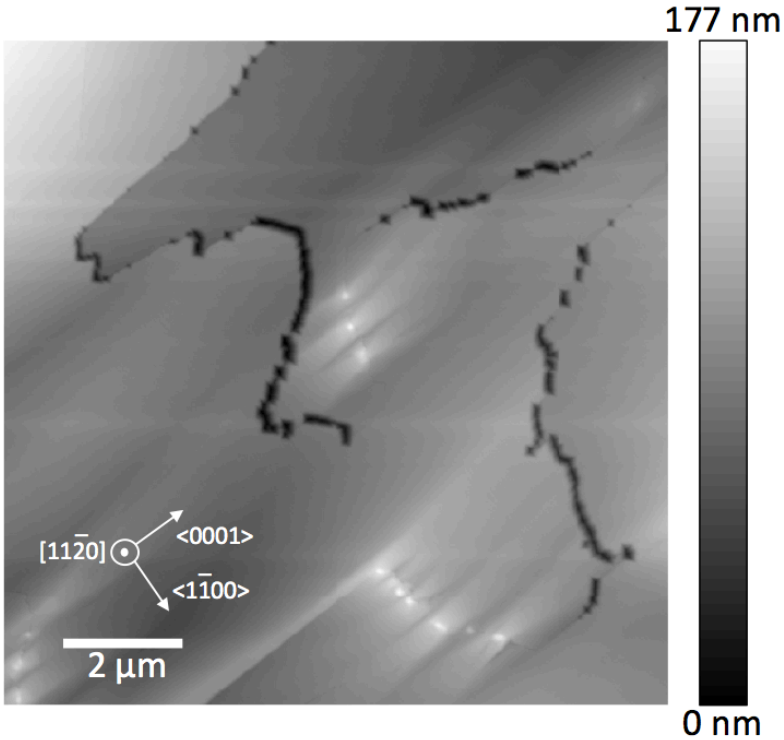

Figure 6.8: AFM images of C4287B with high roughness consisting of surface striations, pits and steps.

Plan-view SEM-CL images were used to compare the structural differences between these samples, such as threading dislocations (appear as dark spots) and distributions and possible misfit dislocations (appear as dark lines) if the well or barrier layer extend beyond the critical thickness.

Six out of fifteen samples (1 nm and 5 nm quantum wells with 3 different AlGaN composition barriers) were selected for this study.

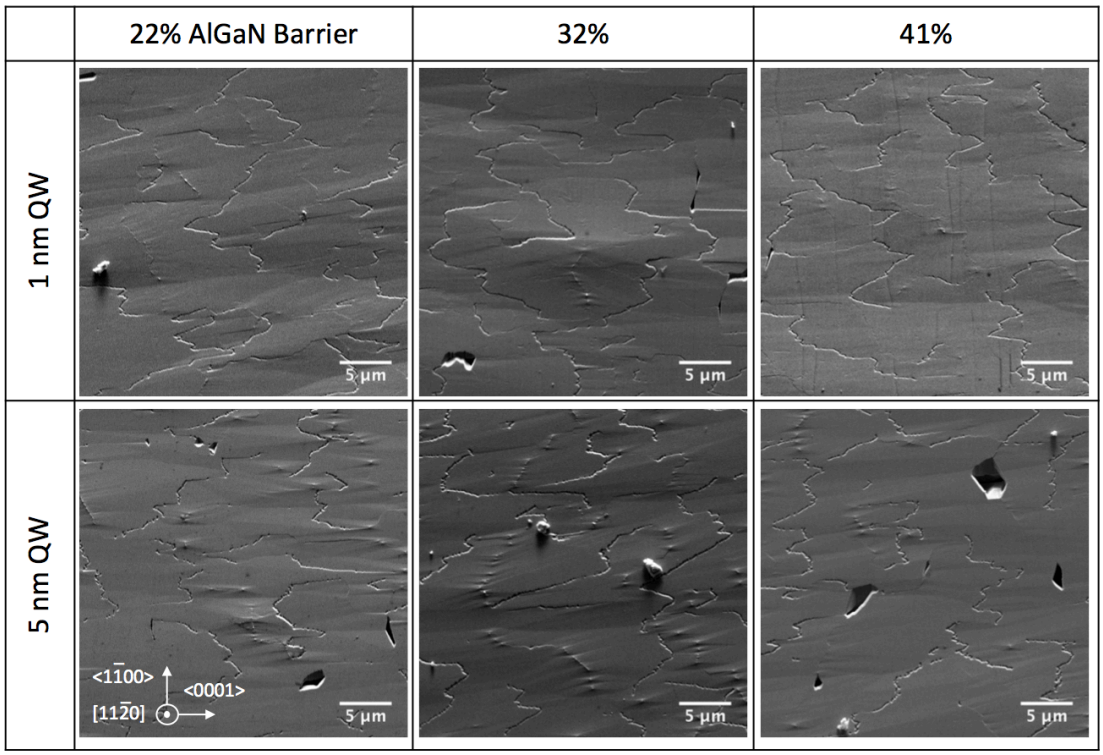

Figure 6.9: Room temperature SEM images of selected samples.

Both SEM (figure 6.9) and CL (figure 6.10) data were acquired at the same time at the same imaging areas at room temperature. From the plan-view SEM images, in all cases, coalescence boundaries were clearly visible, which consist of many pits that run along the boundaries (figure 6.11). Large surface striations were apparent and run in the [0001] direction. Additional smaller scale striations (pyramidal shape with ~2µm in length) were also observed, which are related to the coalescence boundaries (as shown later in the plan-view TEM images in a later section). The only apparent difference between these samples in SEM was the additional surface steps that run in the [1-100] direction observed in the 1 nm QW samples. These steps become more obvious as the aluminium content in the AlGaN barriers increases, suggesting they are basal plane stacking faults that run in the typical [1-100] direction in the nonpolar materials [38] and their density increases as the mismatch between the QW and barriers increases.

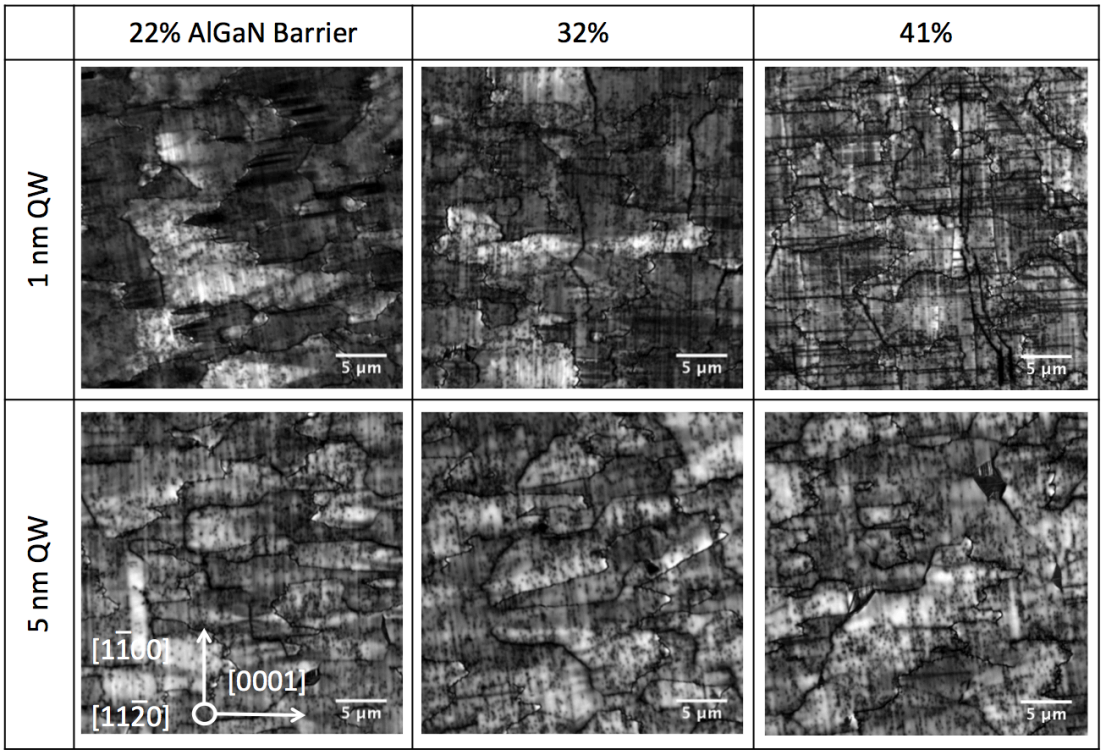

Figure 6.10: Corresponding room temperature panchromatic CL images of selected samples.

From the CL images, in all cases, the coalescence boundaries, dislocations and the stacking faults (running in the typical [1-100] direction) were associated with non-radiative recombination, appearing as dark spots and lines in the CL data. For the 1 nm QW with 22% AlGaN sample, the surface emission was less uniform compared to the others. The non-uniformity was not caused by the surface morphology (i.e. surface striations) but was instead due to the coalescence boundaries since the brighter and darker emission areas are separated by these boundaries. This suggests the presence of inversion domains [165].

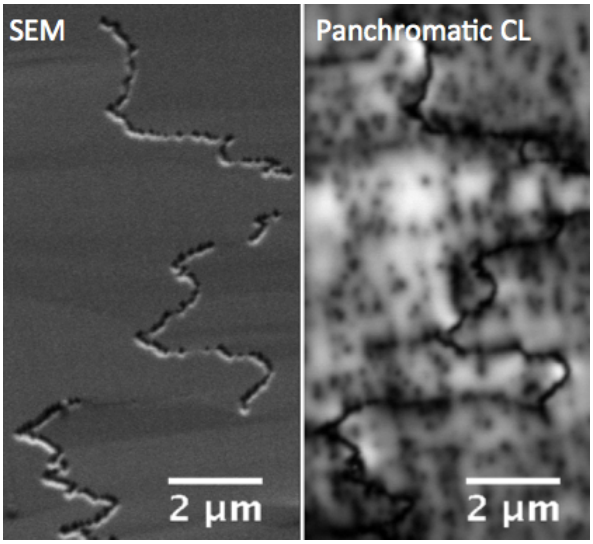

Figure 6.11: Higher magnification SEM and CL images of the coalescence boundaries that consisted of pits and surface steps.

From the 1 nm QW samples, the uniformity of the panchromatic CL emission across the surface improves as the aluminium content in the barriers increases. However, for the 5 nm QW samples, the aluminium content had no apparent effect on the emission uniformity.

One interesting observation was the presence of additional horizontal non-radiative lines that run perpendicular to the stacking faults, and both defects formed a cross-pattern-like defect network. These networks were most apparent in the 1 nm QW with the highest 41% AlGaN barriers. Some were observed in the 1 nm QW with 32% AlGaN sample and all three of the 5 nm QW samples. And is least obvious in the 1 nm QW with 22% AlGaN sample. There can be two possible explanations for these additional defects:

(a) Micro-cracks that result in non-radiative dark lines: We have already disregarded this reason as both SEM (figure 6.9) and AFM (figure 6.8) images did not showed any cracks present on the surfaces.

(b) Misfit dislocations: Since the 41% aluminium content AlGaN barrier thickness (5 nm) may already exceeds its critical thickness based on the calculated values from c-plane GaN/AlGaN [171] (the a-plane GaN/AlGaN critical thickness is not readily available), relaxation was expected in the active region. For nonpolar GaN/AlGaN heterostructures, the lattice mismatch in the *a*-plane direction [1-100] is larger compared to the *c*-plane direction, which

might cause misfit dislocations being generated only in one direction. (In polar materials, misfits can exist equally in <1-100> and <11-20> directions due to the symmetry of biaxial stresses). In addition, the amount and rate of relaxation is likely to be different between 5 nm MQBs grown on 1 nm MQWs in comparison to 5 nm MQBs grown on 5 nm MQWs. And therefore, based on these two influences, the misfit dislocation density should be the highest in the 1nm QW with 41% AlGaN barrier, which could be reasonably consistent with the observation in the CL data. It was however, difficult to confirm the presence of misfit dislocations in the plan-view SEM-CL data. Further investigations, such as plan-view and cross-sectional TEM were required.

6.4.2 Linear defects perpendicular to the stacking faults

The plan-view SEM-CL results from the previous section revealed additional dark lines (defects) running in the [0001] direction perpendicular to the typical stacking faults direction [1-100]. Cross-sectional TEM (figure 6.12) was used to confirm whether these additional defects were misfit dislocations. Two different **g** vectors (**g** = 0002 and **g** = 11-20) were used for a [1-100] zone axis orientation to image all types of threading dislocations in the film.

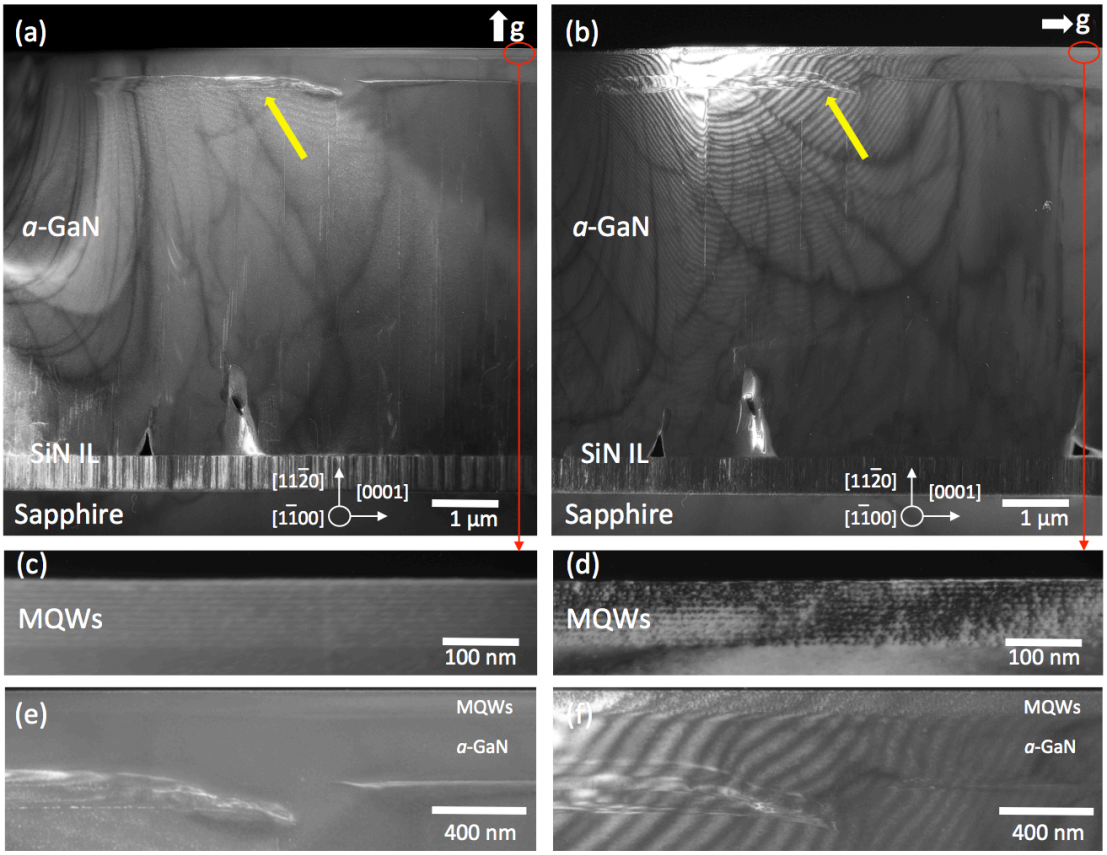

Figure 6.12: Cross-sectional TEM image of C4297B with 41% AlGaN QBs and 5 nm GaN QWs. (a) viewed along [1-100] using g = 11-20 (b) viewed along [1-100] using g = 0002. (c) and (d) are the corresponding active regions. (e) and (f) are the corresponding areas marked the yellow arrows indicating the linear defects.

Interestingly, no misfit dislocations were observed in the active regions for all the samples used in TEM studies. Instead, linear defects were found around 250 nm below the active regions. These defects are *a*+*c* type and run in the [0001] direction perpendicular to the stacking faults. Plan-view TEM (figure 6.13) also revealed these [0001] linear defects. They originated from the corners of the void sidewalls, possibly due to stress concentration [166]. These voids were observed in all the nonpolar GaN templates due to overgrowth of GaN above the SiN islands in the interlayer. The size of the voids can vary between a few hundreds of nanometres to a few microns in height. The voids (also shown as large silver features in the Nomarski image in Figure 6.7) seemed to be randomly distributed across the entire film and were found to be roughly tens of microns apart from each other.

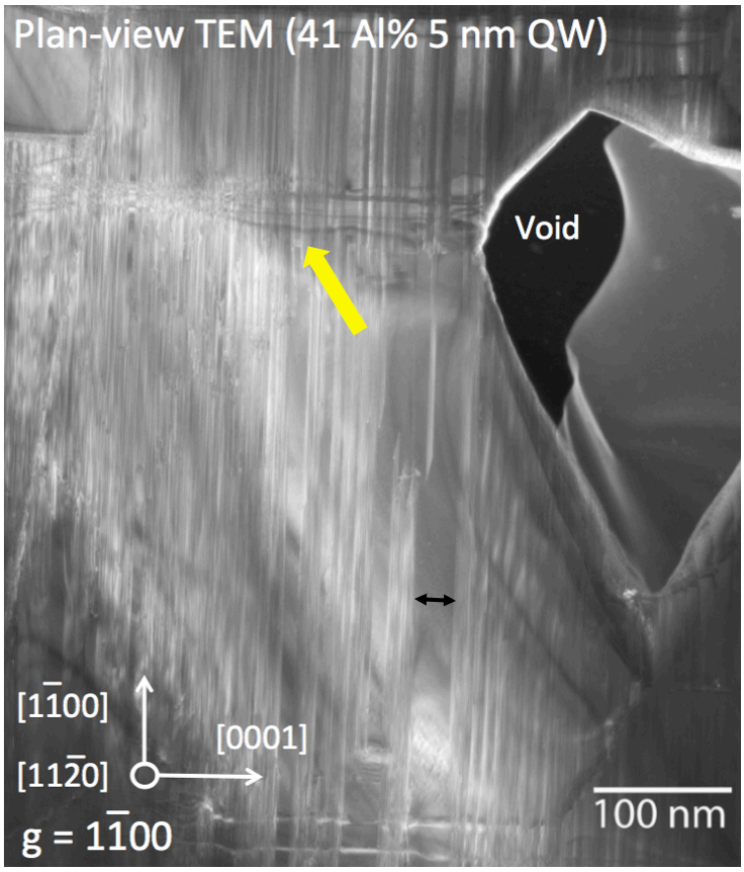

Figure 6.13: Plan-view TEM image of C4297B with 41% AlGaN QBs and 5 nm GaN QWs viewed along [11-20] using g = 1-100. Yellow arrow highlights the linear [0001] defect originated from the corners of the void sidewalls. Black arrow highlights the region that is BSF free.

These defects can be generated at different layer depths depending on the dimensions of the voids. They only existed in [0001] directions possibly due to the stress concentration at the corners of the voids in conjunction with larger lattice mismatch in the [1-100] direction as mentioned earlier. If some of these defects were generated closer to the surface, they could be imaged by the SEM-CL (electrons from a 5kV electron gun accelerating voltage have around 250 nm penetration depth) and corresponded to the additional linear dark lines observed in the CL data. Since there were no misfit dislocations found in the MQW as shown in the cross-sectional TEM images in a later section, this indicated that these additional lines indeed occurred in the template and were unrelated to the QW structure.

6.4.3 Inversion domains

In addition to the linear defects originating from the voids, inversion domains were also observed above the SiN interlayer. These inversion domain boundaries form when islands coalesce with opposite in-plane polarities on either side of a void [167]. Noted that the sample preparation technique (e.g. ion-milling) might preferentially etch the void and boundaries, therefore caution should be taken when studying TEM samples. However, inversion domain boundaries were evident in these cross-sectional TEM images (figure 6.14), where the periodic oscillating contrast of the domain boundaries is produced due to the diffraction contrast varying with depth in the TEM specimen as the boundary passes through its thickness.

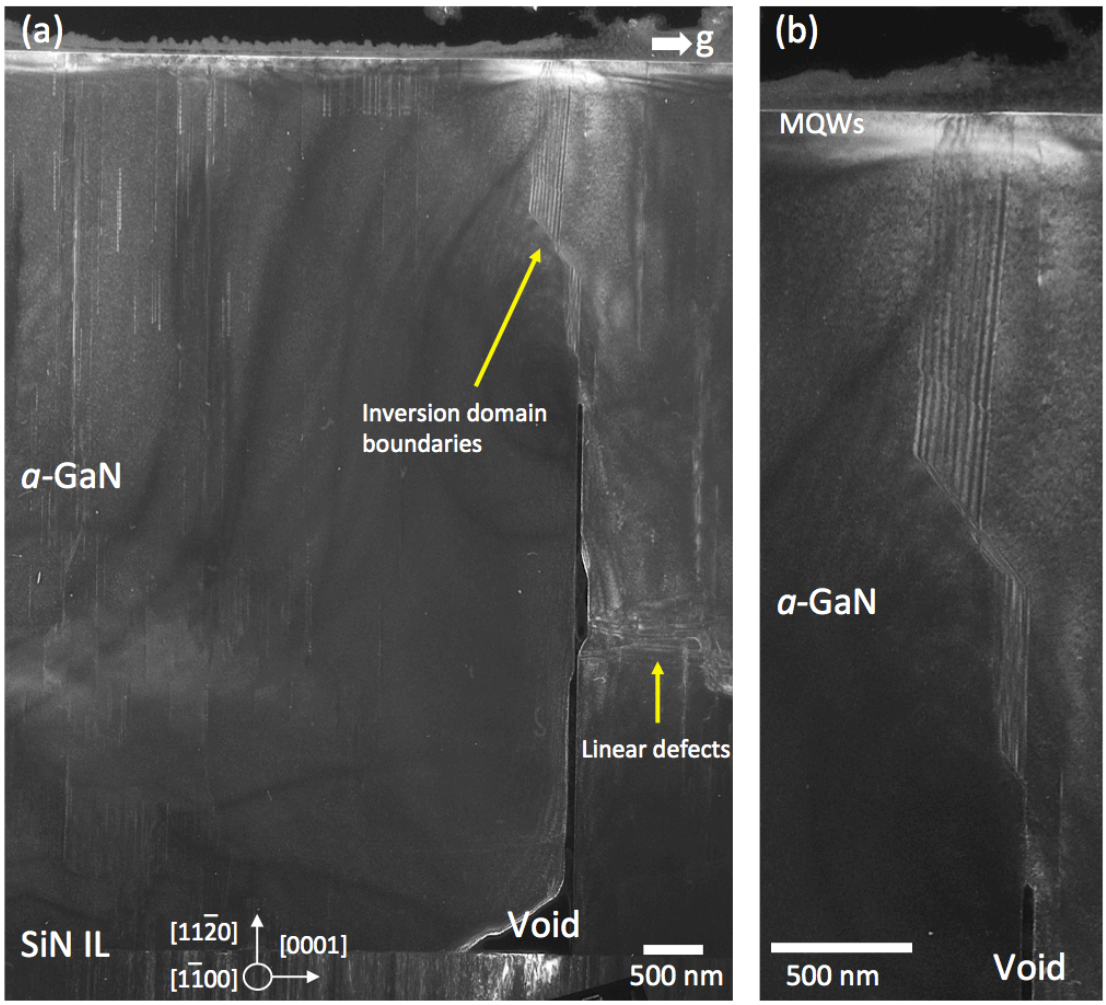

Figure 6.14: Cross-sectional TEM image of C4284B viewed along [1-100] using g = 0002. Linear defects were found generating from the void's sidewall. Inversion

domain boundaries were observed above the void tip. (b) shows an enlarged image of the inversion domain boundaries.

Since the growth rate of –*c* direction ([000-1]) was very slow as confirmed by the ELOG studies [170] and selective area growth [172], the elongated shape of the void shown in the image above suggested that the domains at either side of the void were probably both running in the –*c* direction, hence only coalesced after several microns of growth.

Convergent beam electron diffraction (CBED) measurements were used to suggest the presence of inversion domains at either side of the void (figure 6.15). However, an accurate determination of the polarities would require both thickness map (CBED contrast is highly sensitive to the thickness variation at the sampling area) and a full simulation of the CBED patterns.

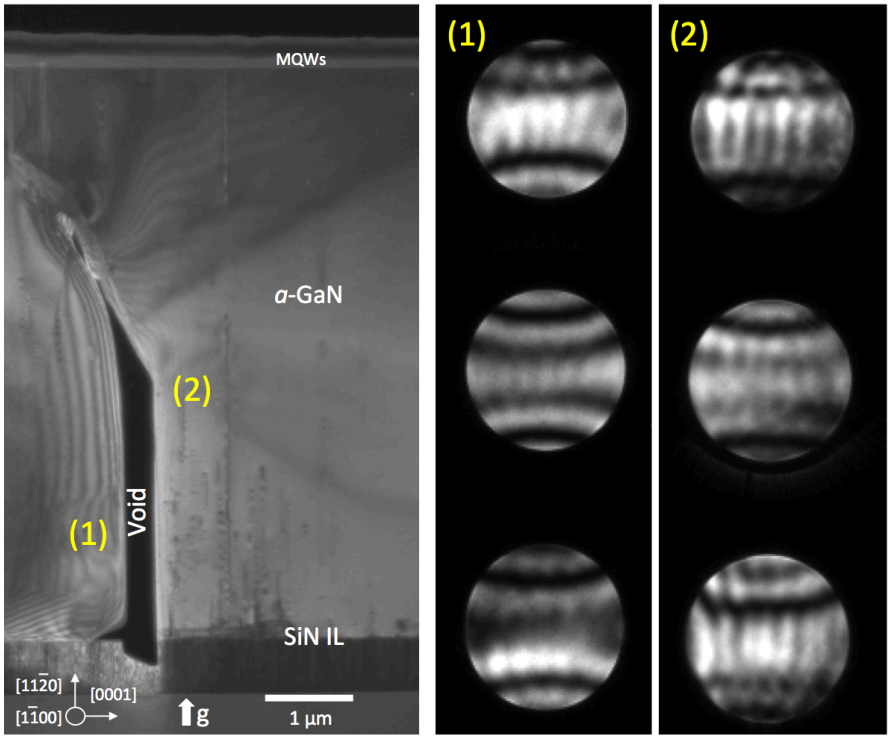

Figure 6.15: Cross-sectional TEM image of C4292B viewed along [1-100] using g = 11-20. CBED measurements were taken at position (1) and (2) and confirmed inversion domains at either side of the void. [Courtesy of Dr Lewis Liu]

The same oscillating contrast of these inversion domain boundaries was also observed in plan-view TEM (figure 6.16). The termination of BSFs was also an evidence of inversion domain boundaries.

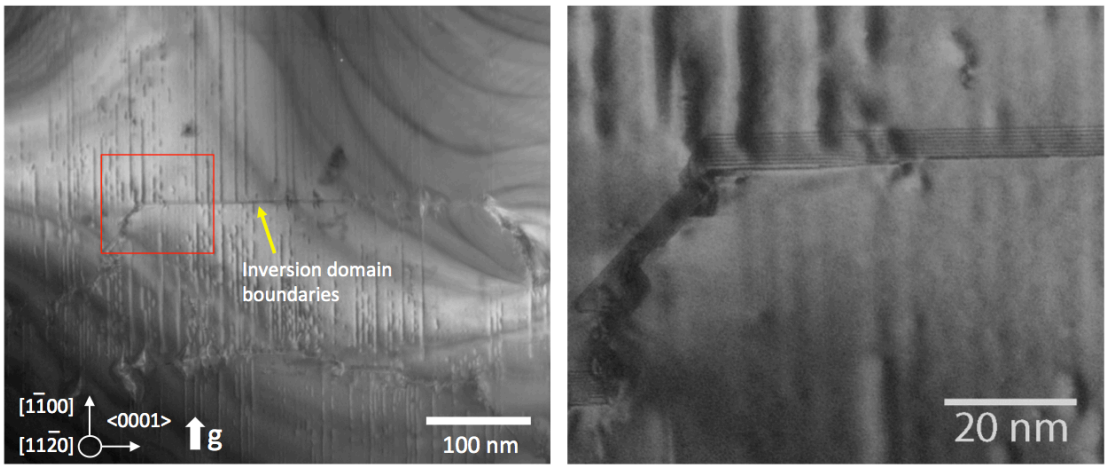

Figure 6.16: Plan-view TEM image of C4292B viewed along [11-20] using g = 1-100. Yellow arrow highlights the inversion domain boundaries run perpendicular to the stacking faults. Image to the right is the enlarged area of the red box.

Although the inversion domain boundaries were often reported to be irregular in size and crystallographic directions in the epilayer [167], however, it was observed that some of the domain boundaries aligned linearly in the [0001] directions perpendicular to the stacking faults in the scale of few hundreds of nanometres. These inversion domain boundaries could be imaged by the SEM-CL and corresponded to the irregular curvy dark lines observed in the CL data (figure 6.11).

6.4.4 V-defects and domain boundaries at quantum wells

As described earlier, the presence of a significant amount of local changes in surface height was the reason for XRD measurement not being able to collect enough signal to carry out QW thickness analysis. The local scale roughness could already be seen from the AFM and CL data where the surface consisted of v-defects and surface steps. Cross-sectional STEM-HAADF was used to confirm the presence of these defects.

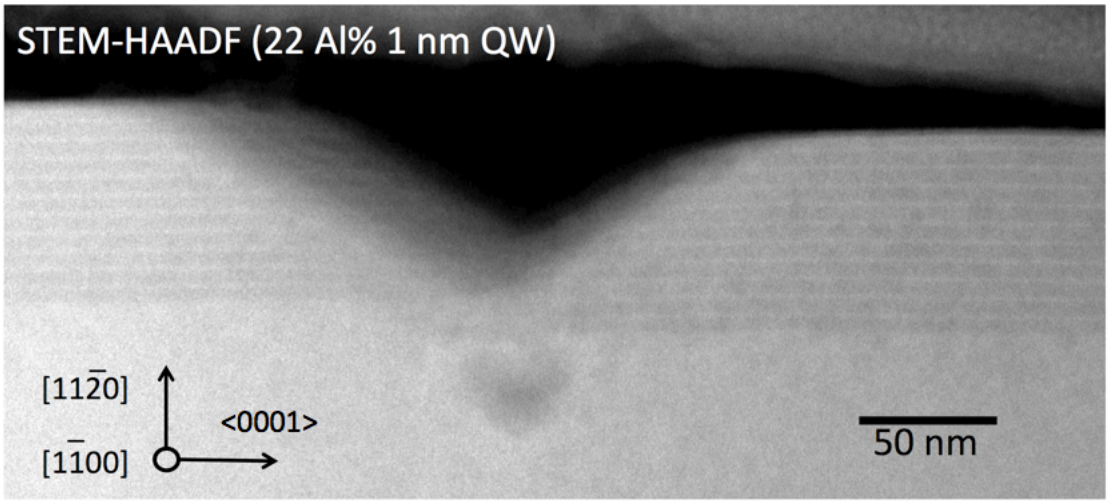

Figure 6.17: Cross-sectional STEM-HAADF image of C4284B viewed along [1-100] showing a v-pit at the MQWs.

The quantum wells orientation and thickness remained unchanged in the vicinity of the v-defects. This was unlike our observation for *a*-plane InGaN/GaN MQW structures [167], where the MQWs orientation and thickness followed the shape of the v-defect. In Figure 6.17, the dark spot located in the image below the v-defect was a void. Figure 6.18 shows another v-defect with a more apparent void underneath.

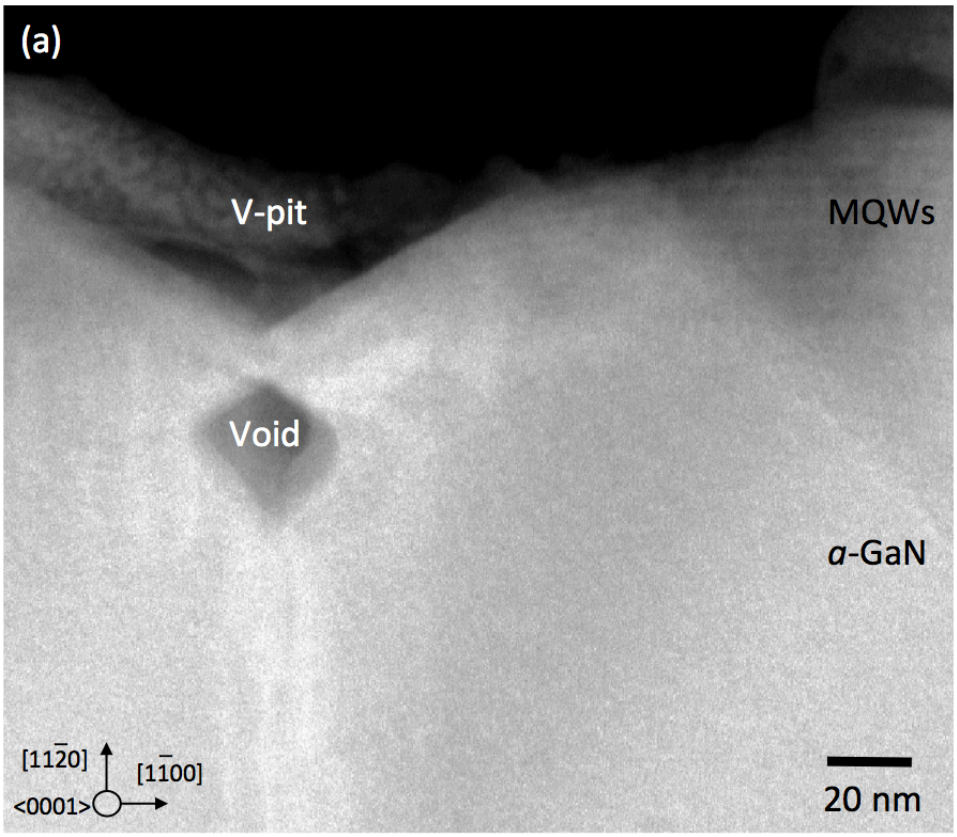
(a)
V-pit
MQWs
Void
a-GaN
[11$\bar{2}$0]
[1$\bar{1}$00]
<0001>
20 nm

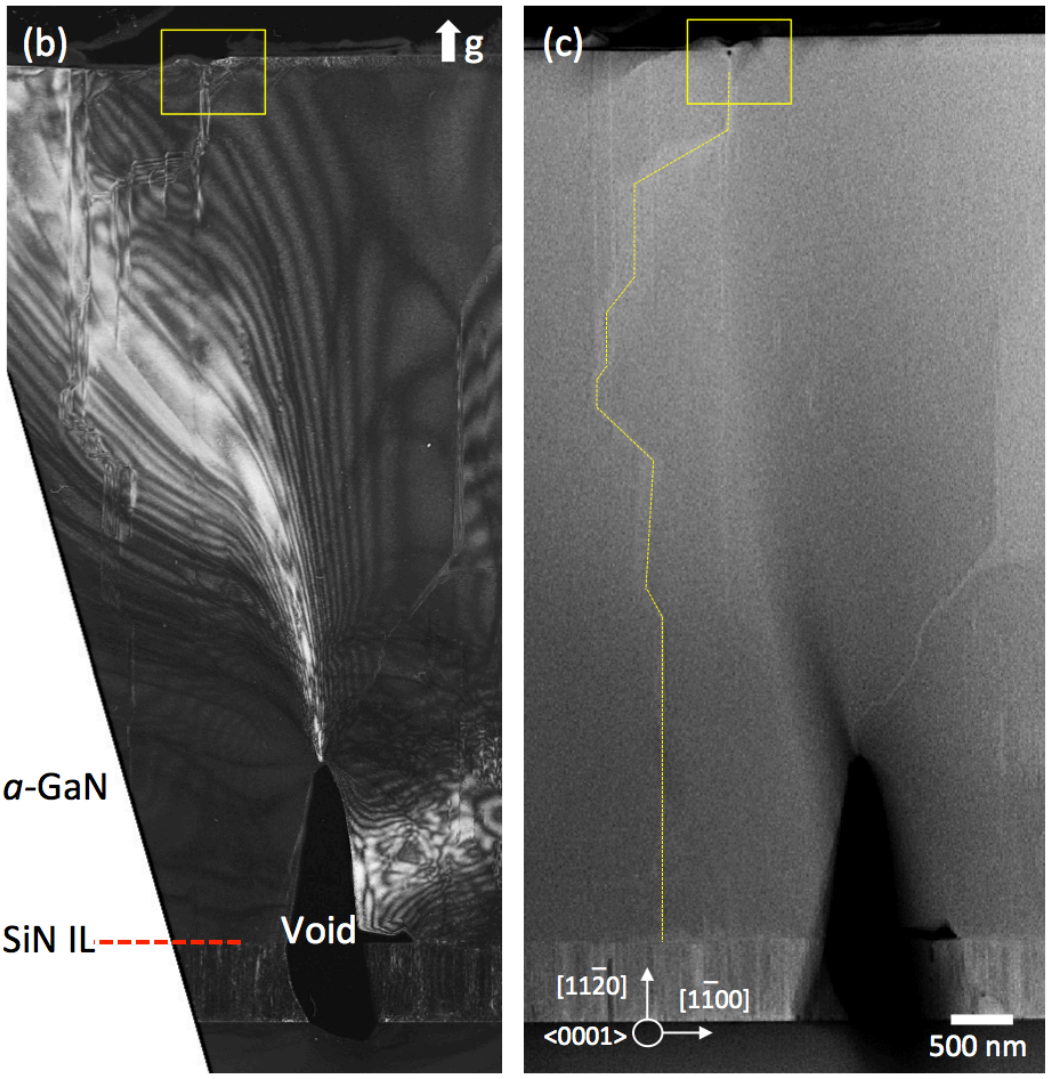

Figure 6.18: (a) Cross-sectional STEM-HAADF image of C4284B viewed along [0001] showing a v-defect at the MQWs and a void underneath the v-defect. (b) and (c) are the lower magnification images of (a) under WBDF TEM and STEM-HAADF, respectively, showing an inversion domain boundary linked between the SiN interlayer and the void.

A void was observed underneath the apex of the v-defect below the MQW region and was correlated with the inversion domain boundary. The boundary was more apparent in the above images when viewed along the [0001] direction, since the majority of boundaries were aligned along [0001] as shown previously in the plan-view STEM image (figure 6.16). This observation suggested that the v-defects, voids and inversion domain boundaries were interrelated.

However, the inversion domain boundaries do not always lead to the formation of voids and v-defects in some cases (figure 6.19).

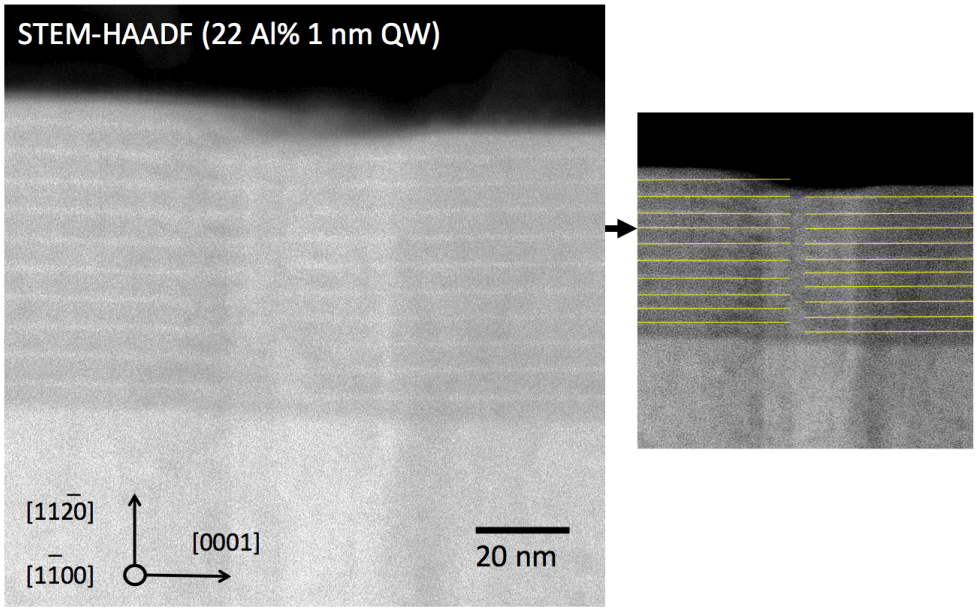

Figure 6.19: Cross-sectional STEM-HAADF image (left) of C4284B viewed along [1-100] direction showing an inversion domain boundary intersect with the MQWs. The yellow lines highlight the 10 repeats of GaN QWs (right).

The inversion domain boundary shown in Figure 6.19 was not associated with a v-defect or void. Instead it caused a variation in the MQW's registry on either side of the IDB. From the image in Figure 6.19 it can be seen that for the same 10 repeats of MQWs, there was a ~ 5 nm difference in the total active region height at either side of the inversion domain boundary. Since the interface of the *a*-GaN template and MQWs was step-free, it suggests that the MQW thickness was different for opposite domains (polarities). An alternative explanation for this could be due to a void (e.g. figure 6.17) hidden underneath the active region causing a misinterpretation of the TEM image.

6.4.5 Relationship between the observed features

The observations shown previously suggest that the linear defects, inversion domains, v-defects and voids below v-defects were all interrelated and all these features could

be correlated and referred back to the voids originated above the SiN interlayer when GaN coalesced. Schematic below summarised the relationship between the observed features.

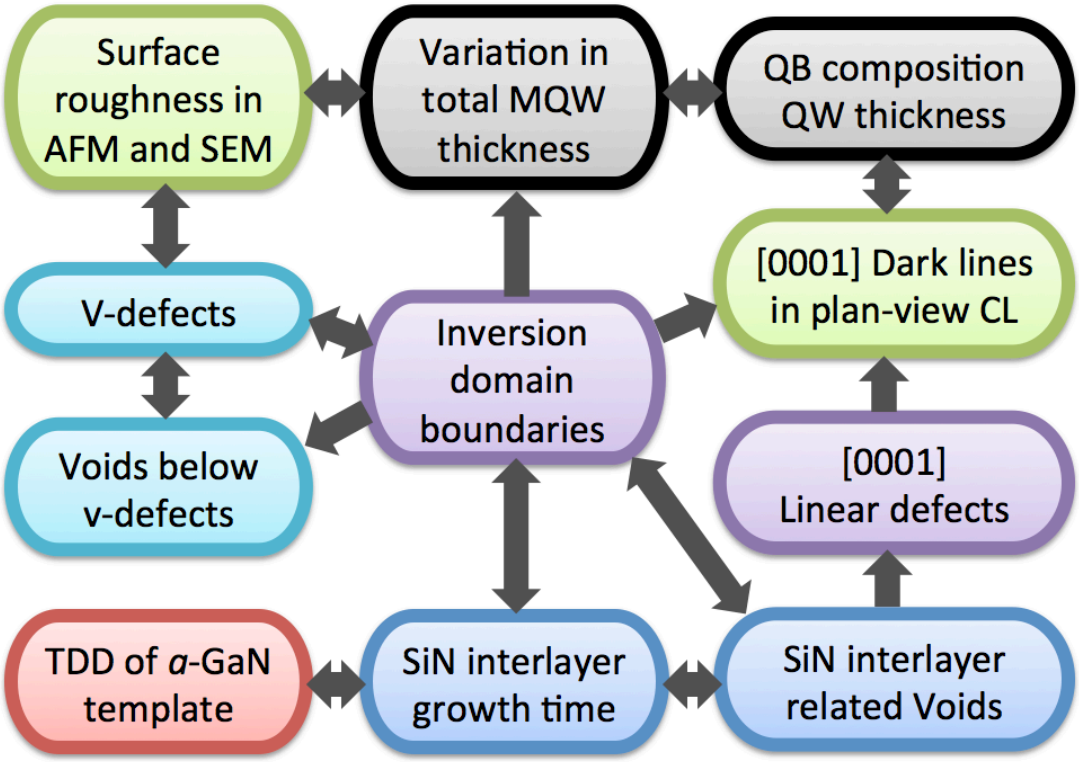

Figure 6.20: Summary of the relationship of each features observed in all samples.

The use of SiN interlayers was able to significantly reduce the BSF and dislocation densities in the non-polar material as mentioned in the background section. Johnston et al. [38] compared an *a*-plane GaN template without an SiN interlayer to three other templates with different single SiN interlayers for which the silane dosing time was varied from 600 s, 900 s to 1200 s. The 900 s SiN interlayers were found to be the optimum condition, where 600 s had a high TDD and 1200 s did not reduce the TDD further compared to the 900 s dose.

The templates with 900 s SiN interlayers used in this work gave a reduction in the dislocation density of two orders of magnitude to ~3.5 × 10^8 cm^{-2}, and the BSF density was reduced by an order of magnitude to ~4.0 × 10^5 cm^{-1} (courtesy of R. Hao) compared to the template without the interlayer. There were also regions, extending for ~500 nm along [0001], that were free from BSFs (figure 6.13). The defect density

reduction was due to both blocking of dislocations by the interlayer and dislocation bending at the interlayer.

6.4.6 MQW optical analysis: effect of thickness fluctuation

The MQW thickness analysis was carried out using cross-sectional STEM for each sample, 15 data sets were collected for each sample (3 data sets from each image over 5 images, see figure 6.21). Each data set (the well and barrier thickness) was calculated by measuring the FWHM values of the peaks in the count vs. distance graph. The counts (i.e. signals arise from the z-contrast image in STEM) were integrated over an area of a 200 integral-width for sufficient signal. Quantum wells and barrier thickness values were averaged over 15 points and standard deviations were presented as the error bars in figure 6.22 and 6.23.

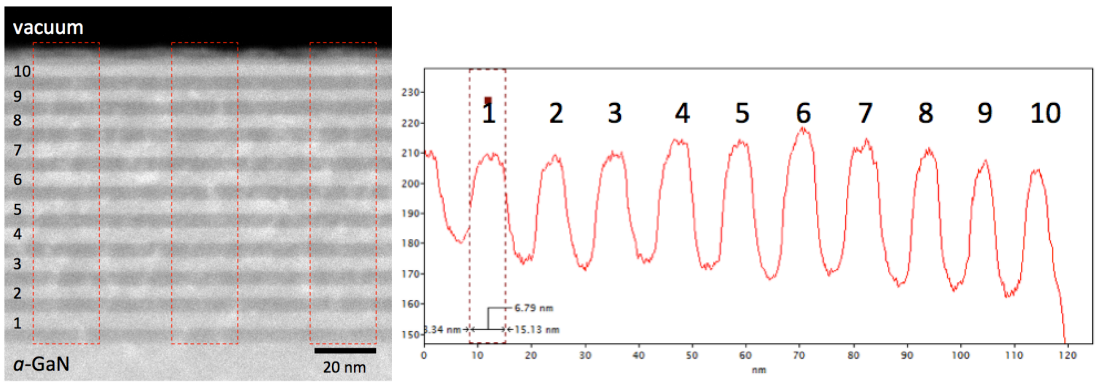

Figure 6.21: Cross-sectional STEM-HAADF image for the MQW thickness analysis. This example shows sample C4297B with 41% AlGaN QBs and 5 nm QWs. One red dashed box with a 200 integration-width was used to calculate one data set as shown in the graph. QW and QB thickness was obtained from the FWHM (marked by the red dotted lines) values of the peaks in the graph.

Figure 6.22 and figure 6.23 show the MQW thickness analysis of 1 nm and 5 nm GaN quantum wells thickness, all with three different AlGaN barriers compositions.

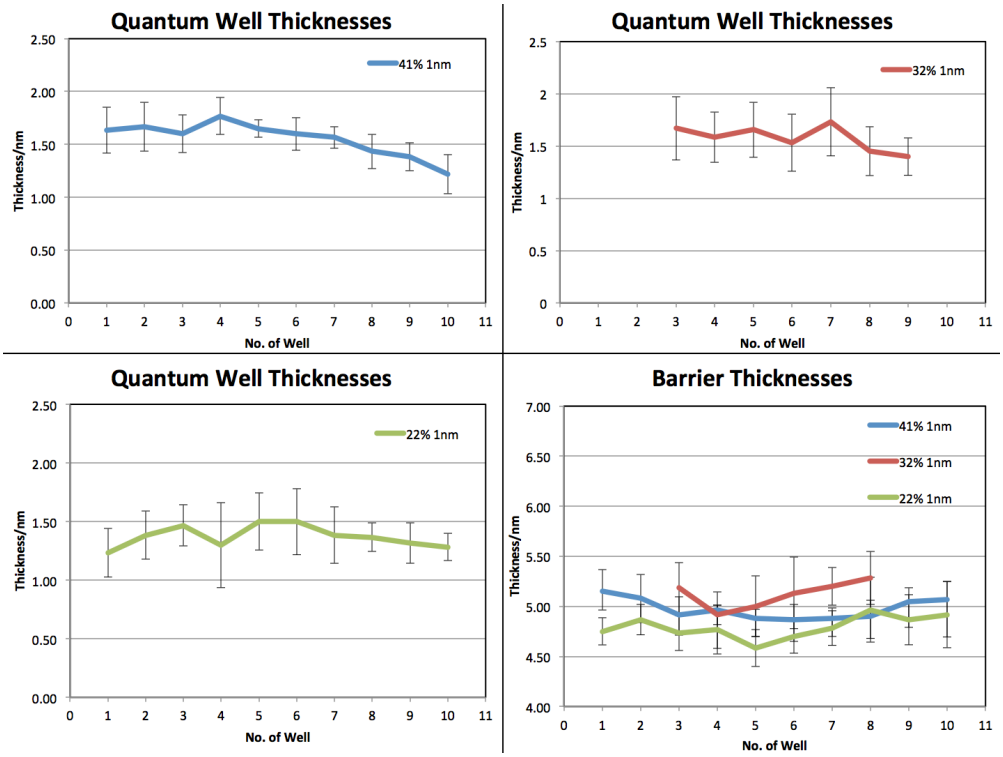

Figure 6.22: MQW thickness analysis of 1 nm QWs with 3 different 5 nm AlGaN barriers compositions.

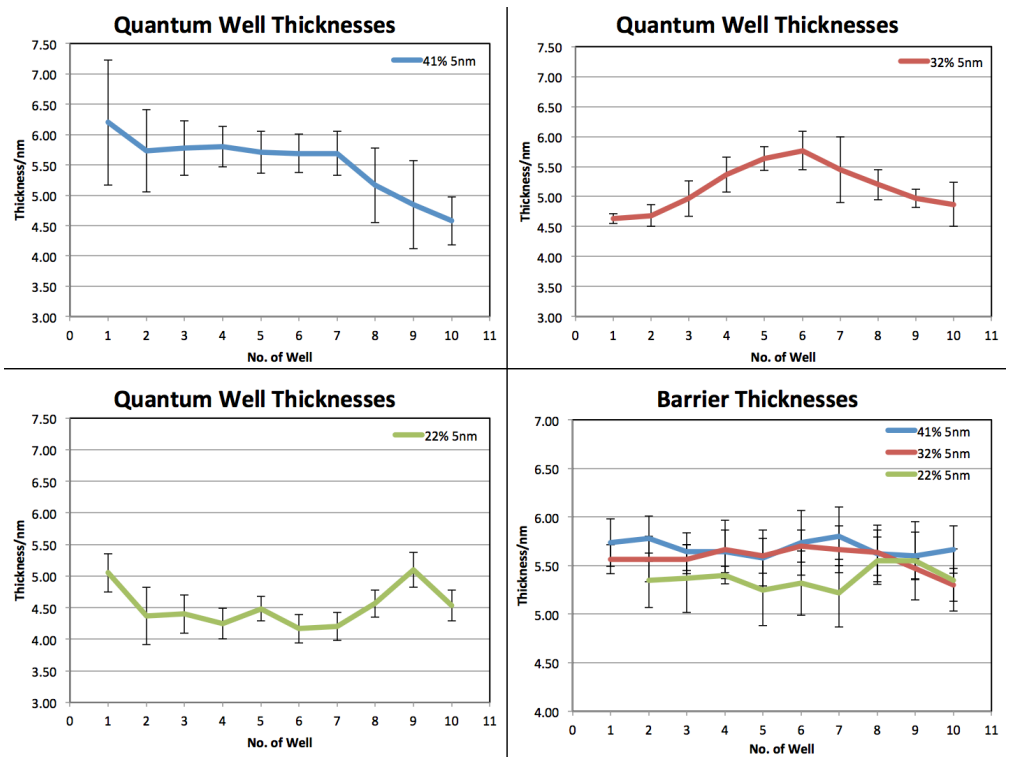

Figure 6.23: MQW thickness analysis of 1 nm QWs with 3 different 5 nm AlGaN barriers compositions.

The quantum barrier thickness remained constant for all 6 samples. The 1 nm quantum well samples showed random distributions of thicknesses, however all of the wells were around 1.5 nm in thickness instead of 1 nm as predicted by the growth recipe. The 5 nm quantum well samples showed trends of thickness distributions, especially for the sample with 41% AlGaN barriers, where the initial well growth was thicker (near the interface) at around 6 nm and decreased toward the surface to around 4.5 nm. This could be attributed to increasing strain in the active region as more stacks of MQW were grown, which caused a reduction in the growth rate.

As discussed earlier, opposite in-plane material polarities might cause a change in the MQW thickness, this can be correlated with the error bars in the graph above. These error bars represent the standard deviations of the 15 data points for each quantum well. The errors were quite significant, varying between 0.2 nm to 0.7 nm for the 1 nm QW samples and between 0.2 nm to 2 nm for the 5 nm QW samples. Since it is likely that over 5 STEM images (approximately 1-3 microns imaging distance) would contain a certain amount of inversion domain boundaries intersecting the MQWs (as judged by the spacing between the IDBs in Figure 6.16). The deviations in MQW thickness might be associated with different growth rates for different domains. Therefore, apart from the fluctuation in thickness between quantum wells, there was also a fluctuation in thickness within each quantum wells (standard deviation). This can lead to fluctuating quantum confinement within a single quantum well, leading to a broader QW PL emission peak (figure 6.24) compared to the older sample (chapter 7) with higher defect density but fewer inversion domains (and therefore fewer quantum well fluctuations).

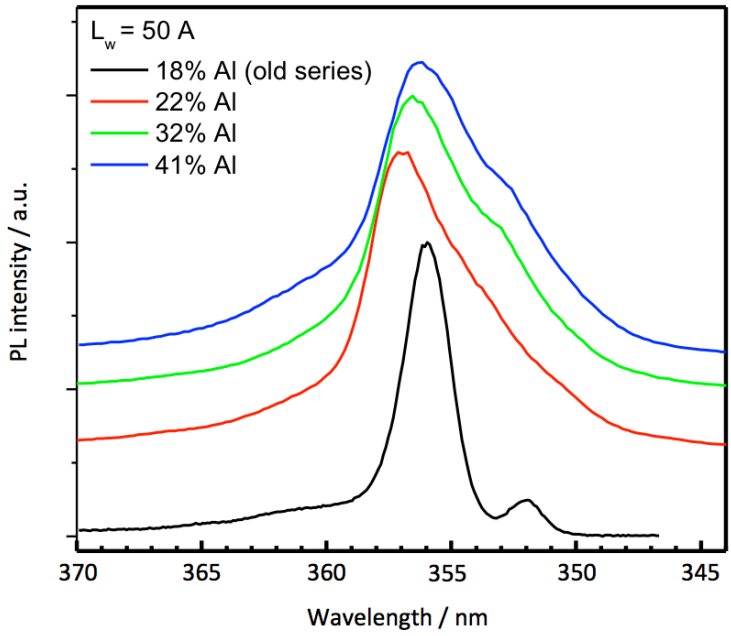

Figure 6.24: 6 K PL spectra of 5 nm QW samples with 3 different AlGaN barriers compositions compared to higher defect density sample (black line). Main peak was associated with emissions of the quantum wires produced by BSF intersecting QWs (Courtesy of Dr. T. Badcock)

BSFs in nonpolar structures are optically active [84] and can act as carrier localization centres. These BSFs can play a dominant role in the QW recombination process at low temperature. Stacking faults in bulk wurtzite GaN can be considered as narrow (~8 Å) type II zinc blende QWs in the wurtzite GaN host. In these MQW structures, the perpendicular intersection of the wurtzite GaN QWs and the zinc blende BSFs produces quantum wires along <1-100>. Recombination of electrons and holes in these BSFs intersecting the QWs region is responsible for the dominating emission peak at 354 nm in the low temperature PL result shown above.

While PL spectra provided an optical overview of the sample, CL spectrum imaging (figure 6.25) was employed to study both spatial and spectral information on a more refined scale. 100 CL spectra were acquired within a distance of 2.2 μm with each spectrum acquired 22 nm apart in order to distinguish different emissions.

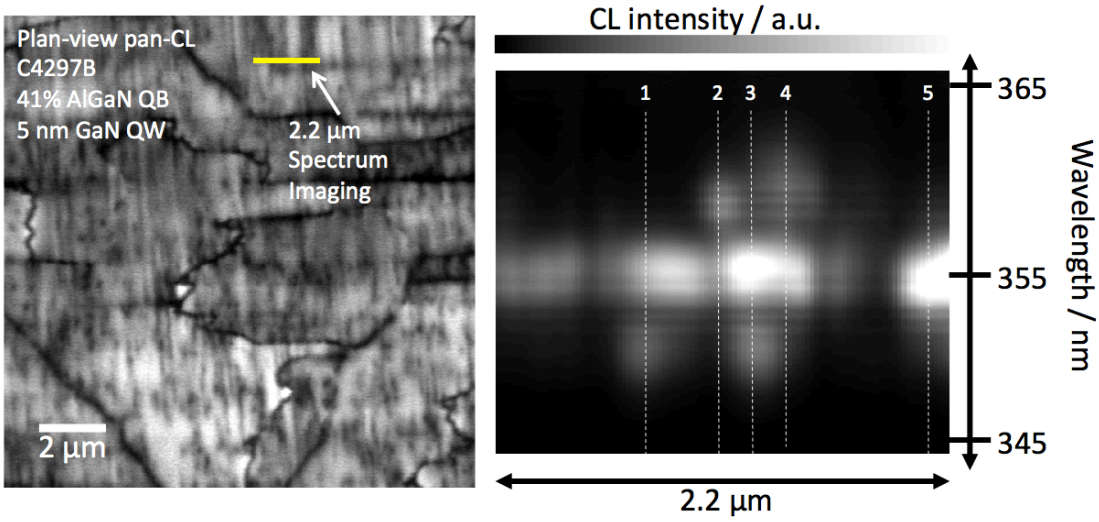

Figure 6.25: Liquid nitrogen temperature CL spectrum imaging across a length of 2.2 µm as indicated by the yellow line in the SEM image. 100 spectrums (22 nm apart) were taken and 5 were selected for further analysis.

The spatial resolution of the CL measurements in SEM is limited by the electron probe size, how the material interacts with the electron beam (generation volume) and the minority carrier diffusion. For a 5kV SEM electron gun accelerating voltage used for the GaN template, the interaction volume is estimated to be around 200 nm wide, according to the Monte-Carlo simulations (see chapter 2).

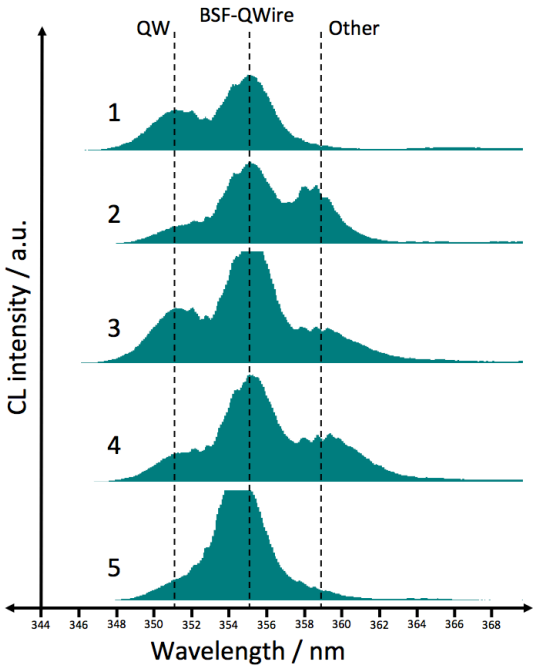

Figure 6.26: 5 spectra taken at 90K at different region within 2.2 µm imaging distance showing significant variation in CL emission.

The spectrum imaging showed a significant variation in emission wavelengths on a local scale (figure 6.26). PL temperature dependency should be taken into account when comparing with the CL results. Paskov *et. al.* [173] reported that the peak positions were comparable between PL and CL if both spectra were acquired below 100K. Three peaks were identified from the CL results in comparison to the PL data and were responsible for QW emission at 351 nm, BSF-Qwire emission at 355 nm and a possible impurity-related [170] emission at 359 nm.

Thickness fluctuations within the well due to either alloy disorder or effects from inversion domains might be responsible for the 2 nm wavelength blue shift of the BSF-related quantum wire emission peak at spectrum position 5. Thickness fluctuations between the wells should also demonstrate a shift in wavelength when acquiring the spectra using different accelerating voltages (i.e. varying the interaction volume to pick up emissions from the wells at different level). Plan-view TEM results (figure 6.13) showed that for the BSF free regions, the BSFs were at most 50 nm apart from each other. This indicated that, for a 200 nm interaction volume, every CL spectra acquired from this spectrum imaging would pick up the quantum wire emissions originating from a BSF intersecting QWs. This was consistent with the spectrum imaging result.

6.5 Discussion

The presence of the interlayer can lead to the generation of voids after the material coalesces. The size and amount of the voids possibly depend on the morphology of the SiN islands (see figure 6.27). Some voids can be seen below the interlayer, however this is likely due to the preferential etching of the PIPS during TEM sample preparation.

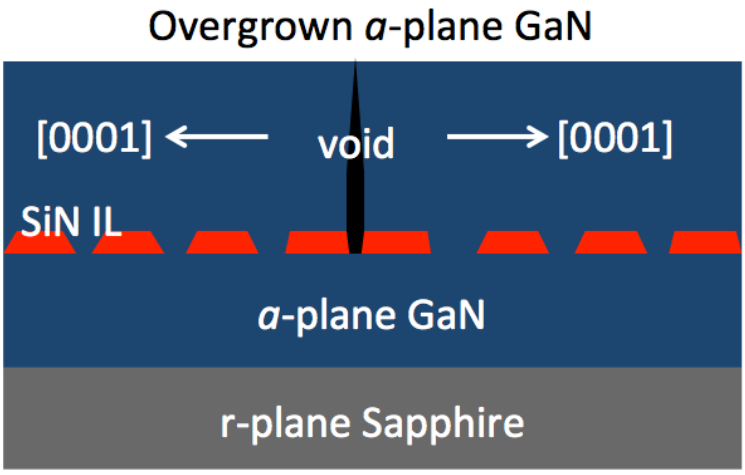

Figure 6.27: Schematic of the coalescence boundary between two islands with opposite in-plane polarity. Red trapezoid represents the portion of the SiN interlayer on the GaN.

The exact mechanism for void formation is unclear with the available data. However, since the number of voids increases with increasing SiN growth time (courtesy of Dr. Johnston), it is expected that the larger SiN islands (due to longer SiN growth time) in conjunction with the different growth rate between $[0001]_{GaN}$ and $[000\text{-}1]_{GaN}$ (growth rate of [000-1] is slower [172]) may increase the coalescence time of the materials, which leads to void formation if the lateral growth rate is not fast enough.

All the templates studied in this work have a significant amount of voids generated above the SiN interlayers. Some of these voids were found to associate with the generation of linear defects that run in the [0001] direction and also the inversion domain boundaries (see figure 6.15). These two defects were observed in the plan-view panchromatic SEM-CL data, producing cross-patterned defect networks. The thickness and composition of the MQWs contribute greatly to the formation of these defects. They were most apparent with the highest Al% barriers and thinnest wells. This was possibly due to the combination of (i) highly lattice mismatched active regions leading to highly strained heterostructures, which were observed to generate additional [0001] linear defects instead of misfit dislocations (this also might suggest the possibility of dislocation movements [126][168]) and (ii) a thinner overall active region thickness leading to electrons in the SEM penetrating deeper into the template

and picking up more emissions from dislocations, this can be tested in future work with different beam currents as well as Monte-Carlo simulations.

Since the nonpolar GaN materials probably started with random in-plane polarity on the sapphire substrate at the beginning of the growth, these in-plane opposite polarities continue when GaN is overgrown on top of the SiN interlayer. Therefore inversion domain boundaries were clearly observed originating at the interlayer and also the tips of the voids in cross-sectional TEM (not every void is associated with inversion domains, since islands may also have the same in-plane polarity).

Where the inversion domain boundaries intersected with the active regions, a difference in total MQW thickness could be produced at the either side of the boundary. This suggested that the growth rate could be different with in-plane opposite material polarities and this could have two effects on the films: (i) causing a difference in the thicknesses of quantum wells and barriers (more details in section 6.4.1) and (ii) causing a difference in surface height and leading to a rougher surface on a nano-scale as observed in the AFM (figure 6.8) and SEM (figure 6.11) data.

V-pits were observed in all the MQW samples. Cross-sectional STEM indicated that the v-defects were associated with surface steps in the GaN template of the order of 10 nm in height. These in conjunction with the surface steps caused by inversion domain boundaries lead to significant nano-scale MQW thickness variations across the sample, which indirectly confirmed the reason for the XRD scans not being able to pick up enough MQW signal for thickness analysis (section 6.4.1). The reason for the QW orientation remaining unchanged in the vicinity of the v-defect was unclear, but the voids underneath the tip of the v-defects might suggest that material decomposition might occur.

6.6 Conclusions

A SiN interlayer is well known for reducing the TDD in the templates, however these interlayers' additional consequences on the film properties were not often reported in the literature. This chapter observed and examined how these interlayers lead to the generation of voids and consequently the generation of linear defects and the relation with inversion domain boundaries and their associated v-defects and the variation in the MQW growth rate. These observations were all interrelated. Although the 900 s SiN interlayer significantly reduced the defect density in the *a*-GaN template, high amounts of voids lead to the generation of additional linear defects and cause fluctuations in MQW thicknesses due to inversion domains and v-defects, which is detrimental towards their optical properties. Therefore a 600 s SiN interlayer might be a better choice for reducing the void density. This suggested that there is a compromise between obtaining a low defect density film and good quality MQWs.

7

Defect luminescence from non-polar a-plane GaN/AlGaN MQWs

7.1 Aim

In order to improve the performance of nonpolar optical devices, it remains crucial to understand the influence of defects on the optical properties of the active region. The objective in this section was to carry out a comparative study of the defect properties at the same area of the specimen by using both spatially resolved CL and TEM. This could establish a direct correlation between the defects and their luminescence properties and thus clarify the nature of the different emission bands in the spectra.

7.2 Experimental details

The older sample C2691D studied here has a similar structure compared to the ones mentioned in the previous chapter. The sample was grown in a 6x2 in. Thomas Swan CCS-MOVPE reactor using trimethylgallium (TMG), trimethylaluminium (TMA), silane (50ppm SiH_4 in H_2) and ammonia (NH3) as precursors, and hydrogen (H_2) as

carrier gas. The (11-20) GaN pseudo-template was grown in a standard two-step growth process, as follows: (i) r-plane (1-102) sapphire was heated in a flow of hydrogen and ammonia to 1050 ºC for 3min at a reactor pressure of 100 Torr followed by 3min with an additional silane flow; (ii) a GaN nucleation layer with a thickness of 30nm was deposited at 540 ºC and 500Torr; and (iii) the GaN epilayer was deposited at 1020 ºC, 100 Torr and a V–III ratio of 200. The growth of the GaN epilayer with a total thickness of 6 µm was interrupted three times for the incorporation of in-situ SiN_x interlayers using a flow of silane and ammonia at 860 ºC. The surface of the GaN pseudo-template showed some triangular-shaped pits and a strong corrugation aligned along the [0001] or c-direction. High-resolution X-ray diffraction (11-20) omega-scans taken along the different in-plane [0001] and [1-100] crystallographic directions show good in-plane isotropy with FWHM values as low as 540 arcsec [174]. The GaN/$Al_{0.18}Ga_{0.82}N$ 10xQW structure was grown on the (11-20) GaN pseudo-templates for which the GaN QW thickness was set at 6.0 nm at a constant barrier thickness of 10.8nm.

A schematic of the sample growth is shown in figure 7.1.

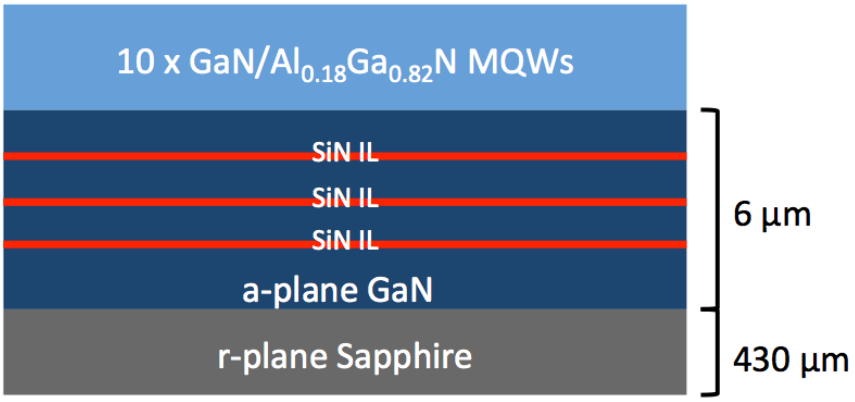

Figure 7.1: A schematic of the sample structure. 10 GaN QW thicknesses were set 6.0 nm at a constant barrier thickness of 10.8 nm. 3 SiN interlayers were grown during the a-plane GaN template growth.

The well and barrier widths were determined by X-ray diffraction and X-ray reflectivity measurements taken on a P'Analytical high-resolution MRD instrument. The results from the X-ray analysis were in good agreement with thickness measurements from transmission electron microscopy (TEM) images. The barrier

composition was determined from X-ray measurements assuming bi-axial strain of the barriers to the template. TEM studies have shown that the incorporation of SiN interlayers effectively reduces the density of defects (mainly partial dislocations, Figure 7.2) in nonpolar materials. The dislocation and BSF density was (6.6±0.4) × 10^9 cm^{-2} and (3.0±0.3) × 10^5 cm^{-2}, respectively, after the third SiN interlayer [38].

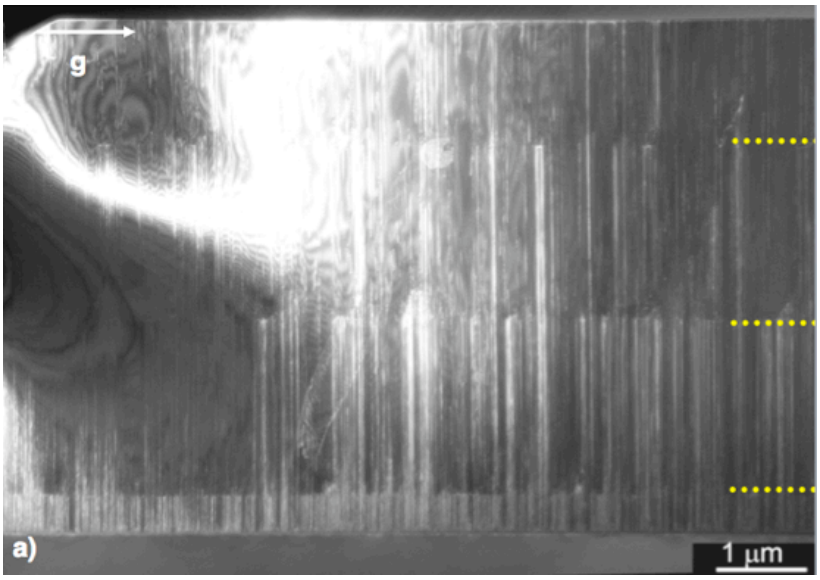

Figure 7.2: Cross-sectional TEM images of the nonpolar GaN 'template' sample with three SiN interlayers viewed along [1-100] using g = 0002. [38]

CL measurements require a relatively thick sample area (>200 nm) for sufficient light emission, however TEM analysis requires a very thin sample area (<100 nm) to be electron transparent. Therefore it is also important to choose a suitable sample thickness for carrying out both CL and TEM on the same region of the sample and to ensure that the thickness of any amorphous 'dead layers' on the specimen surface is minimised. Thus, specimens were prepared with both focused-ion beam (FIB) and mechanical polishing methods, in order to determine the optimal sample preparation technique for carrying out this type of experiment.

7.3 Results and discussions

The FIB preparation technique allowed us to produce a very thin sample that is electron transparent. In this work, a wedge shaped sample with a thin region less than 100 nm and thicker region at around 500 nm was produced. The CL measurement was carried out at 7K (figure 7.3). However, the CL panchromatic image acquired using a 5 kV electron beam voltage was poorly resolved. The SEM image showed some degree of image drifting induced by surface charging, possibly due to poor electrical contact with the stub. This is one of the main factors limiting the CL resolution, however the sample surface damage due to the FIB preparation technique may also have greatly influenced the CL result.

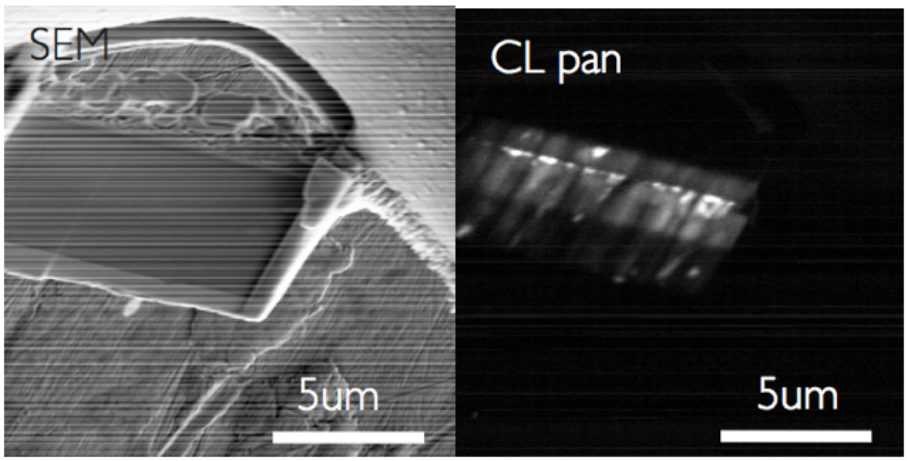

Figure 7.3: SEM and CL panchromatic images of sample C2691D (nonpolar GaN film with GaN/AlGaN MQWs) prepared by the FIB method.

The cross-sectional sample prepared with the conventional mechanical polishing and ion-milling method was also investigated by CL at ~ 7K (figure 7.4). This cross-sectional sample consists of two wafer pieces glued with the GaN sides facing each other and there is a 90° in-plane misorientation of the two pieces relative to each other. The CL measurement was much better resolved than in the FIB sample: CL panchromatic images clearly revealed layers of luminescence features.

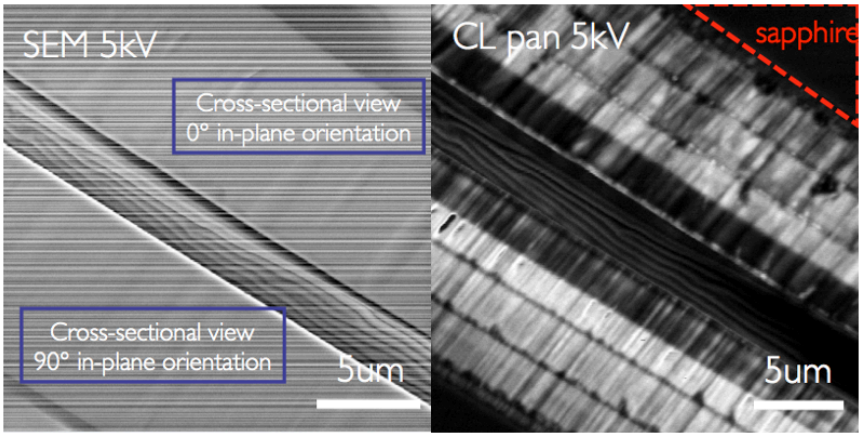

Figure 7.4: SEM and CL panchromatic images of sample C2691D prepared by the conventional mechanical polishing method.

The luminescence features could be identified according to the growth recipe. The layers of luminescence features were introduced by the presence of SiN interlayers (indicated by dark lines running parallel to the sample surface). The dark layer close to the quantum wells was the high temperature low V/III ratio GaN layer (~1.5 μm), followed by an overgrown low temperature high V/III ratio GaN layer (~200 nm) and multiple quantum wells (~150 nm with 10 repeated GaN/AlGaN QWs) to complete the structure. It also showed many defects propagating vertically from the GaN/substrate interface to the quantum well region.

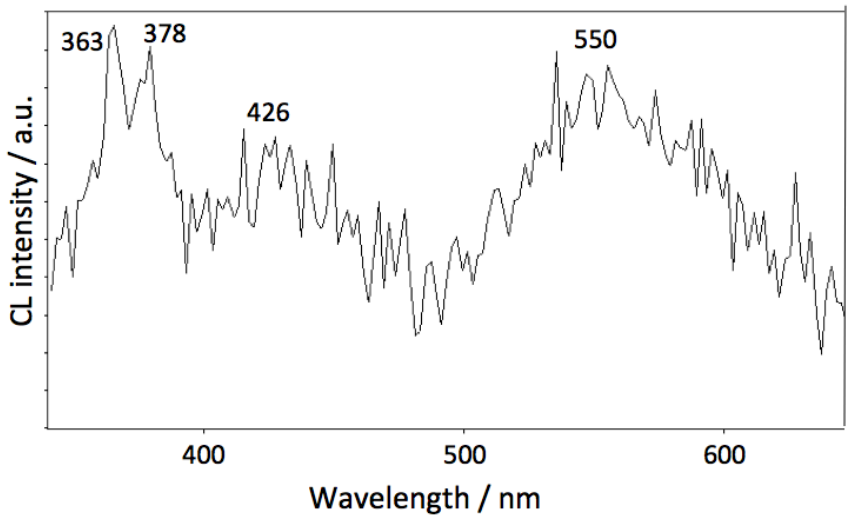

Figure 7.5: Serial CL spectra acquired from throughout the whole scanning region.

A serial CL spectrum was acquired from the total scanned area (figure 7.5). Four peaks were revealed at around 363, 378, 426 and 550 nm. The peaks at 363 nm and 378 nm corresponded to the BSF- and PSF-related emission [141]. The source of the 426 nm and 550 nm peak emission wavelengths was unclear, but is likely to be related to point defects. Since the spectrum was summed over the entire scanning area of the sample, it was difficult to relate the luminescence to specific defects. Therefore detailed analysis was required, as follows.

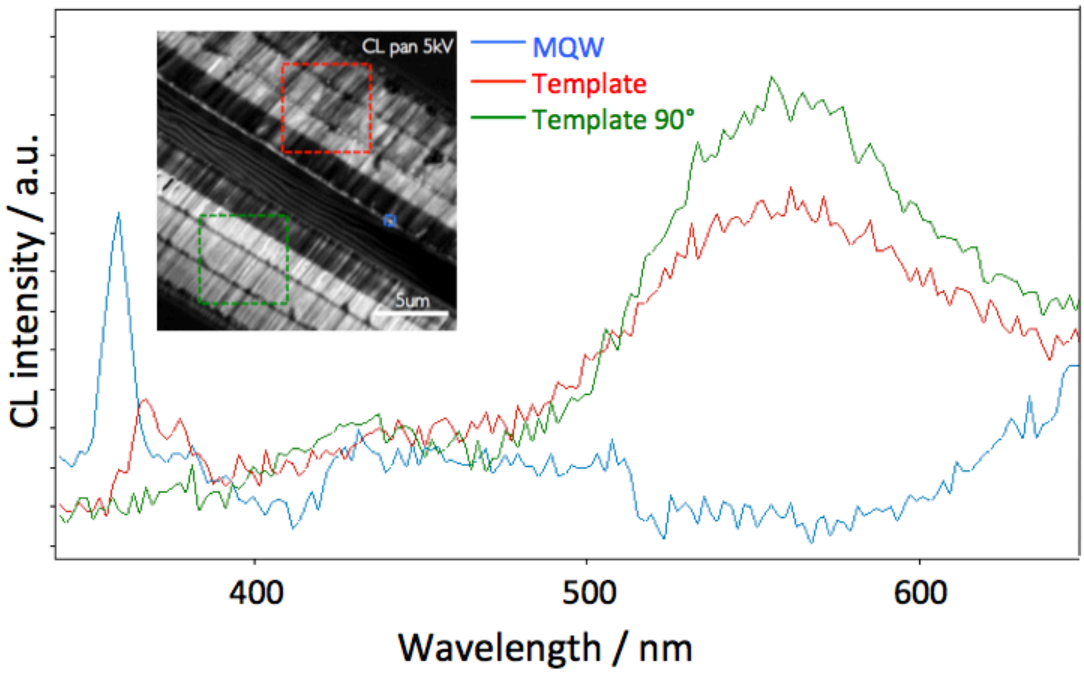

Figure 7.6: Serial CL spectra acquired from the quantum wells region (blue), the template below the active region (red) and the template below the active region with a 90° relative in-plane orientation (green).

Three further serial CL spectra were acquired from the MQWs region, the template below the active region and the template on the relative 90° in-plane rotated sample section (figure 7.6).

The spectrum at the quantum wells showed a high intensity 358 nm emission peak, related to the quantum wire emission originating from the BSF intersecting QWs as shown from PL studies (figure 6.25) [84]. The presence of PSFs in this quantum wells region was confirmed with a cross-sectional TEM study using the sample prepared by FIB (figure 7.7) and these suggest near band emission at ~ 380 nm. The sample

prepared by the conventional mechanical polishing method was not thin enough to carry out TEM analysis. (Note that an image showing the BSFs image was not acquired, as only the [1-100] zone axis was accessible in the FIB sample).

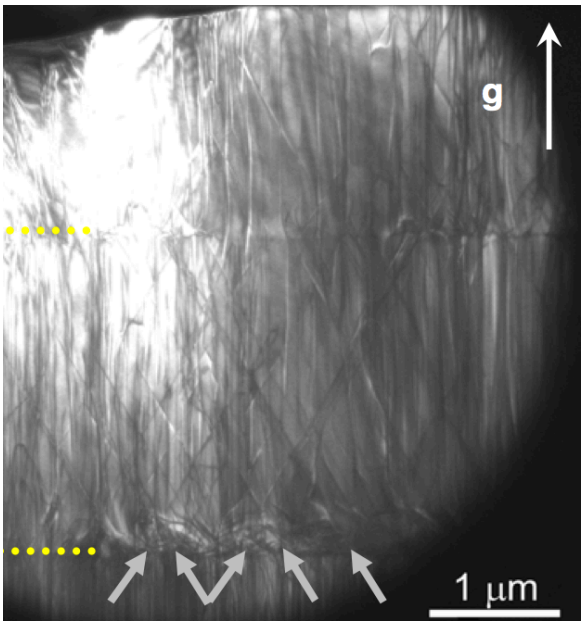

Figure 7.7: Cross-sectional TEM image of the nonpolar sample prepared with the FIB method. The image was viewed along [1-100] using g = 10-10. TDs, PDs and PSFs (white arrows) are visible.

The spectrum taken from the template showed similar peak positions and intensities compared to the overall spectrum (figure 7.5), however, for the 90° in-plane rotated sample, the stacking fault related emissions were not observed in the spectrum. This might suggest an orientation dependency of the sample luminescence. These spectra also confirmed that the 426 nm and 550 nm yellow luminescence originated from radiative recombination centres outside of the quantum wells.

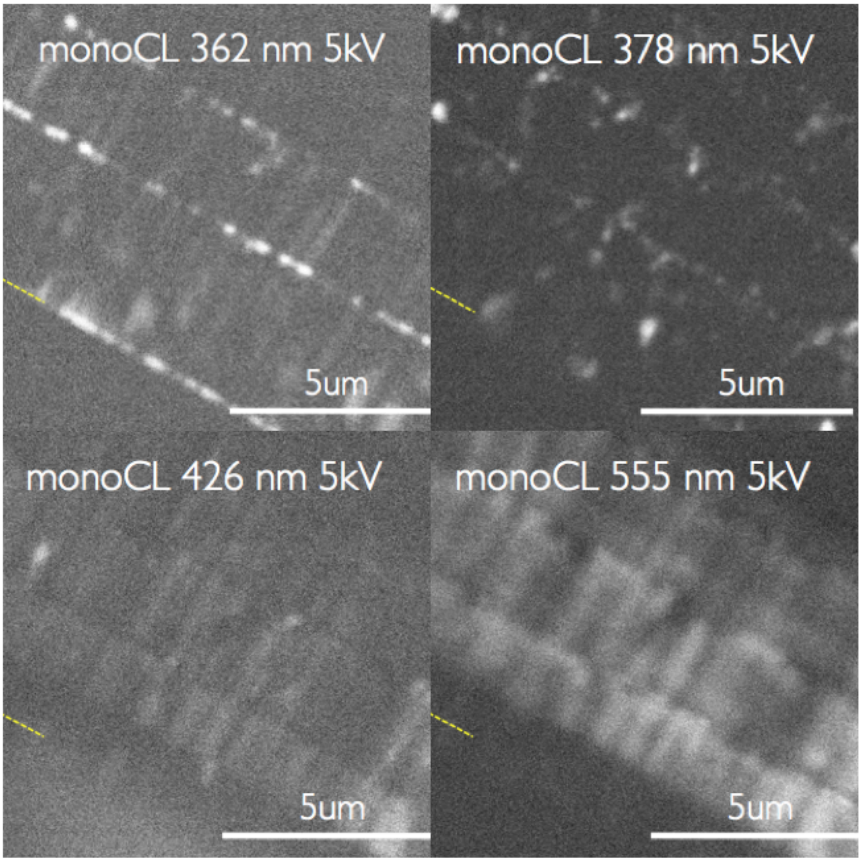

Figure 7.8: CL monochromatic images acquired at 362 nm, 378 nm, 426 nm and 555 nm emission wavelengths. The yellow dashed lines indicated the quantum wells region.

Monochromatic CL images were acquired at each peak wavelength (figure 7.8). The image acquired at 362 nm showed some bright stripes running perpendicular to the sample surface indicating the radiative recombination centres at BSFs. The brighter spotted line running parallel to the sample surface corresponded to the vicinity of SiN interlayers and the origin of higher light emission intensity from these regions could be due to the luminescence from unintentional doping [169] or the 3D islands.

The image acquired at 378 nm showed some luminescence stripes running at a 60° angle perpendicular to the sample surface, which indicated the presence of PSFs and this was also consistent with the previously shown TEM image (figure 7.7) showing some extended PSFs running from the substrate interface to the quantum wells regions unaffected by the interlayer.

Some literature reports [170] have suggested that the luminescence from the images acquired at 426 nm and 555 nm wavelengths originated from point defects. This idea

was supported with their studies on ELOG samples showing that these emission centres were not directly associated with the dislocations as the emissions arise both in the window and wing regions. Also, the reason why no discernable contrast arises at the dislocations in these monochromatic images can be attributed to the long lifetime of these radiative recombination processes, which blurs the image contrast.

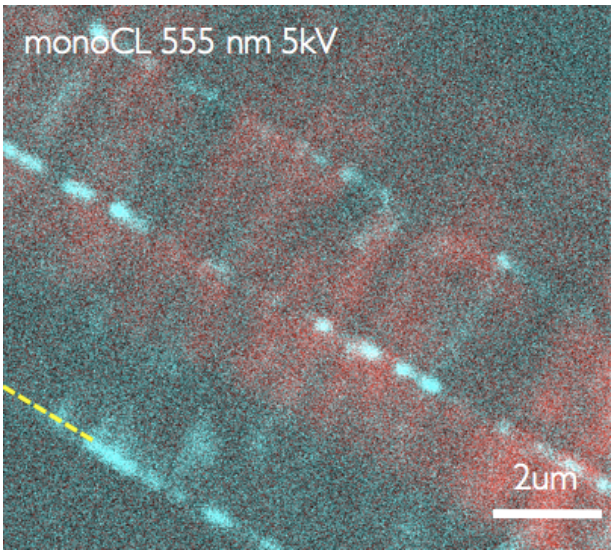

Figure 7.9: A colour coded monochromatic image of the 555 nm emission wavelength (red). 362 nm emission wavelength image (blue) was used as a reference background to increase the contrast of the red colour. The yellow dashed line indicated the quantum wells region.

The monochromatic images acquired at 426 and 555 nm showed an increase in luminescence (indicated by the red colour) toward the sample surface (figure 7.9). Optically active stacking faults could not attributed to this phenomenon, as a decrease in luminescence toward the sample surface would be observed instead. This suggested that there is a correlation between partial dislocations and the point defects, e.g. a decrease in partial dislocations density may lead to an increase in impurities concentration. However, further studies will be required to understand this relationship.

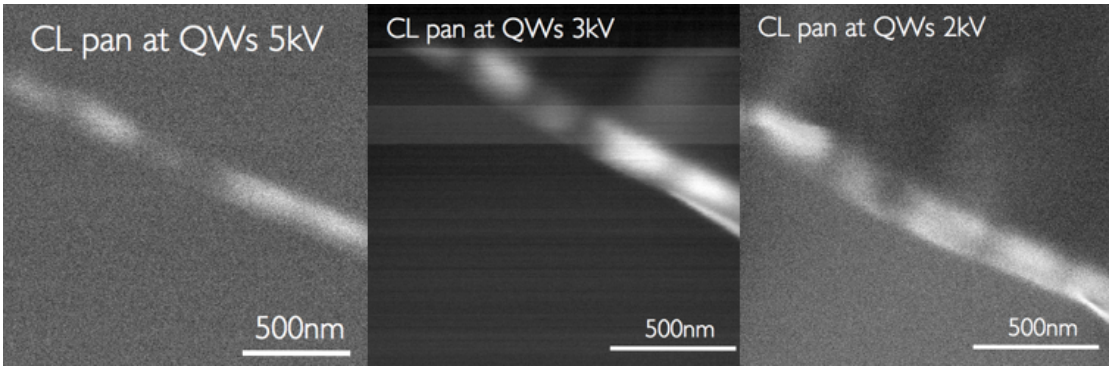

Figure 7.10: High magnification CL panchromatic images acquired at the quantum wells region with 5 keV, 3keV, and 2 keV electron beam energies.

The highest CL resolution was achieved at 2 keV at 7K (<50 nm theoretical spatial resolution) and some weak radiative dark lines were observed perpendicularly intersecting the quantum wells (figure 7.10). These dark lines were separated by a distance of ~200 nm, which is comparable to the TEM image (figure 7.11) showing similar separation distances for the defects (possibly partial dislocations). The observations in both CL and TEM studies suggest that the partial dislocations in nonpolar GaN films are possibly non-radiative centres. However, those dark lines could also be due to the PIPS damage and might not necessary represent the true luminescence property of the defects. Further studies will also be required to confirm this observation.

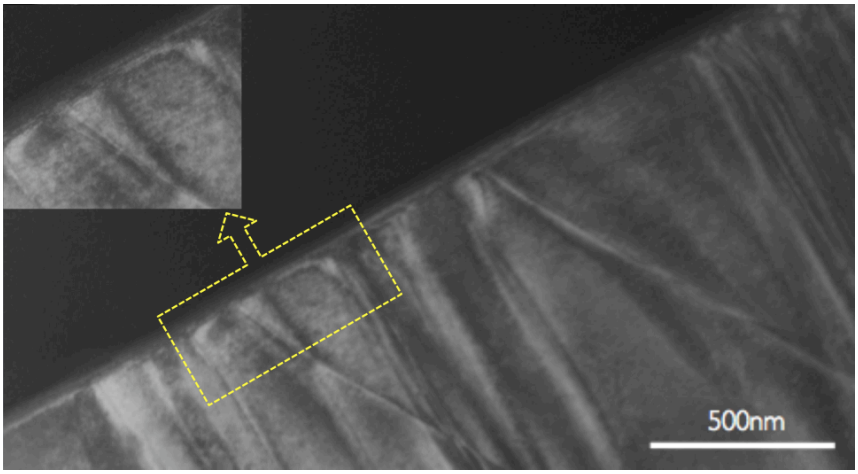

Figure 7.11: Cross-sectional TEM image of the nonpolar sample prepared with the FIB method. The image was magnified to show the quantum wells region (further magnification showing contrast of the MQWs is indicated by the yellow box) and was viewed along [1-100] using g = 10-10.

7.4 Conclusions

Two different sample preparation techniques have been investigated. The sample prepared by the FIB method showed insufficient CL luminescence, but the sample thickness was sufficiently thin for TEM analysis, whilst the sample prepared by the CRHEA method showed the opposite effect. Further optimisation of the sample condition is required to establish a direct correlation between the CL and TEM results using one single TEM sample.

The CL data acquired from the CRHEA sample showed layers of luminescent features that directly corresponded to changes in the growth conditions. Serial CL spectra indicated four distinctive peak wavelengths, each corresponding to a specific type of defect. The origin of luminescence at 362 nm and 378 nm was identified (with both monochromatic CL and TEM images) as BSF- and PSF-related luminescence.
Comparison of selected areas of the serial CL spectra indicated that luminescence is orientation-dependent and could be affected by surface states. Luminescence at 426 nm and 555 nm was only observed outside the active region. Emission from the quantum wells was only observed at 358 nm whereas a PL study on the same wafer showed mostly 362 nm BSF-related emission. It is not yet clear whether this difference is related to a difference in calibration between different instruments or whether it is a genuine effect.

Monochromatic images obtained at 426 nm and 555 nm wavelengths likely corresponded to the point defects, as suggested in the literature. The increase in luminescence intensity after each SiN interlayer suggested that there is an association between partial dislocation density and the impurity concentration. Detectable luminescence could be obtained from the sample prepared by the CRHEA method at 2 keV and close to liquid helium temperatures, which corresponds to a theoretical spatial resolution of less than 50 nm.

8

Conclusions and future work

8.1 Conclusions

This thesis has covered the structural and optical characterisation of the defects and their impact on device performance in the nitride semiconductor materials emitting at near- and deep-UV region. A range of UV structures was investigated, including *c*-plane (polar) AlGaN epilayers grown on an AlN template, and nonpolar GaN/AlGaN MQWs grown on an *a*-plane GaN template. In-depth summaries of each experimental chapter have been given previously so this section will emphasise the main observations and highlight some conclusions.

Chapters 3 and 4 are the two experimental chapters based on the study of the same series of c-plane deep-UV emitting structures: AlGaN epilayers with different aluminium contents grown on thick high quality AlN templates. Several types of defect were found in the AlGaN materials. Stress relaxation in these films occurred by the combined processes of interfacial misfit dislocations and bent threading dislocations. In-situ wafer curvature measurement in conjunction with other characterisation techniques has demonstrated that interfacial misfit dislocations dominate the strain relaxation processes while bent threading dislocations also relieve a fraction of the strain due to their inclined projection to the basal plane, equivalent to interfacial misfits. The strain associated with other types of defects, such as Frank-Read sources, was very small compared to the previous two types. In addition, we have found that these bent threading dislocations occurred in all the different AlGaN compositions studied ranging from 22% to 87% aluminium content. This suggests

that their projected misfit segments were unrelated to the critical thicknesses of the layer and therefore the density of bent threading dislocations was probably inconsequential to the formation of the misfit dislocations.

The inclined dislocation arrays observed in the AlGaN epilayers were found to be lower in aluminium content and were possibly generated during AlGaN growth on the inclined facets at the step edges due to differences in the relative incorporation rates of Al and Ga on different facets. The inclined dislocation arrays distorted the quantum well, the barrier heights and the composition leading to a shift in emission wavelength. Additional misfit dislocations could probably be generated due to the lattice mismatch with the surrounding AlGaN materials. We suggest that reducing the step density of the AlN film may directly reduce the density of inclined dislocation arrays and result in an improved AlGaN film.

As suggested by the previous two chapters, an atomically smooth surface of the template is essential and has a direct impact on the quality of the succeeding epilayer and MQW growth. This leads to the investigation of *c*-plane AlN template growth optimisation in Chapter 5, based on the TMA pre-dose on sapphire method to enhance the quality and the surface morphology of the template even further. The initial growth conditions were shown to be critical for the final AlN film morphology. A higher TMA pre-dose was shown to enable a better Al coverage leading to a fully coalesced AlN film at 1 μm thickness. An atomically smooth surface was achieved over a large 10 x 10 μm AFM scale. The XRD ω scan peak width of this new 1 μm thick AlN template was comparable to the older 2 μm thick reference sample. It is expected that using this approach, a 4 μm AlN film could achieve an even better ω scan result that would be comparable to a typical LDD GaN film.

Chapters 6 and 7 investigate UV emitters based on nonpolar crystal orientations. A series of different GaN multiple quantum well thicknesses and AlGaN barrier compositions were grown on a nonpolar *a*-plane GaN template of low dislocation density using a SiN interlayer. The SiN interlayer was able to reduce the defect density but was also found to generate additional voids with longer SiN growth time. Although the 900 s SiN interlayer significantly reduced the defect density in the *a*-

GaN template, high amounts of voids lead to generation of additional linear defects and cause fluctuations in MQW thicknesses due to inversion domains and v-defects, which is detrimental for their optical properties. Therefore a 600 s SiN interlayer might be a better choice for reduced voids density. This suggests that there is a compromise between obtaining a low defect density film using a SiN interlayer and good quality MQWs.

8.2 Future work

1. **In-situ wafer curvature measurement: real-time stress analysis**

   Strain engineering using wafer curvature measurement has been successfully employed and reported in the literature for various nitride heterostructure growths. This technique has been employed in this work to extract the information of real-time stress evolution in the AlGaN/AlN structures and thus a detailed quantitative stress analysis on the defects could be demonstrated.

   However, as mentioned in chapter 3, the wafer curvature analysis can sometimes lead to misinterpretation of the stress measurement due to the periodic oscillation artefacts, caused by the interaction between the laser and the wafer. This is because real films are not uniformly thick, and unintended thickness gradients produce optical diffraction effects that steer the laser away from the ideal condition, this is particularly severe for transparent films such as the AlN films studied in this work. As a result, the deflection of the laser is actually sensitive to both the film stress and the film-thickness gradient.

   In order to improve the accuracy of wafer curvature measurement (i.e. to differentiate and define these combined effects), an optical diffraction model has been proposed by Breiland *et. al.* [136] that can be used to isolate the oscillating artefacts caused by the film-thickness gradient. This model is fairly complicated and a detailed simulation would be required to correct the results in this work, however a full integration of this model would provide us with a highly accurate wafer curvature measurement that can be beneficial not only for stress analysis purposes but also for the crystal grower to evaluate the

strain management procedures being used more quickly and more accurately in real-time.

2. Further optimisation of AlN template growth

An initial improvement of the AlN template quality has been achieved in this work. However, there is room for further improvement, including: (i) a complete elimination of the randomly oriented AlN polycrystalline compounds, and (ii) an improvement in reproducibility.

The large polycrystalline compounds possibly originate from nanoparticles as suggested in chapter 5. A further detailed EDX analysis on the surface blobs just before the start of AlN growth would be required to understand the role of the nanoparticles formed in the gas-phase, and ultimately to control and eliminate these compounds to achieve an atomically smooth surface over a large surface area. Reproducibility has always been a concern for AlN growth, mainly due to the reactor memory effects, where NH_3 as a molecule can be trapped in the reactor and only outgases when the susceptor is operating at high temperature. A long period of H_2 baking before growth does not remove all the impurities. Future work, including alternative baking recipes and further optimisation of growth parameters, is necessary to achieve high quality AlN templates.

References

[1] *Building Energy Databook 2006* (Energy Efficiency and Renewable Energy U.S. Department of Energy, Washington, DC, 2006; http://buildingsdatabook.eren.doe.gove) (accessed January 2008)

[2] C J. Humphreys, *MRS Bulletin* **33**, 459 (2008)

[3] J.A. Simmons, *Solid State Lighting*. APS Energy Research Workshop (2008)

[4] N. Holonyak, Jr. and S.F. Bevacqua, *Appl. Phys. Lett.* **1**, 82 (1962)

[5] H.P. Maruska, *Mat. Res. Bull*. **7**, 777 (1972)

[6] G.P. Agrawal, *Semiconductor Lasers*. American Institute of Physics, Woodbury, New York. (1994)

[7] S. Nakamura, *The Blue Laser Diode*. Springer-Verlag, Heidelberg (1997)

[8] T. Ikegami, F. Hasegawa, and Y. Takeda (International Symposium on Gallium Arsenide and Related Compounds, Karuizawa, Japan, 1992)

[9] S. Nakamura, M. Senoh and T. Mukai, *Jpn. J. Appl. Phys*. **32**, 8 (1993)

[10] A. Khan, K. Balakrishnan, and T. Katona, *Nature Photonics* **2**, 77 (2008)

[11] F.A. Ponce, and D.P. Bour, *Nature* **386**, 351 (1997)

[12] M. Moram, and M. Vickers, *Rep. Prog. Phys*. **72**, 036502 (2008)

[13] O. Ambacher, J. Smart, J.R. Shealy, N.G. Weimann, K. Chu, M. Murphy, W.J. Schaff, L.F. Eastman, R. Dimitrov, L. Wittmer, M. Stutzmann, W. Rieger, and J. Hilsenbeck, *J. Appl. Phys*. **85**, 3222 (1999)

[14] C. Hums, J. Blasing, A. Dadgar, A. Diez, T. Hempel, J. Christen, A. Krost, K. Lorenz, and E. Alves, *Appl. Phys. Lett*. **90**, 022105 (2007)

[15] Z. Ren, Q. Sun, S.Y. Kwon, J. Han, K. Davitt, Y.K. Song, A.V. Nurmikko, W. Liu, J. Smart, and L. Schowalter, *Phys. Stat. Sol. C.* **4**, 2482 (2007)

[16] X. Hu, J. Deng, N. Pala. R. Gaska, M.S. Shur, C.Q. Chen, J. Yang, G. Simin, M.A. Khan, J.C. Rojo, and L.J. Schowalter, *Appl. Phys. Lett*. **82**, 1299 (2003)

[17] T. Nishida, T. Makimoto, H. Saito, and T. Ban, *Appl. Phys. Lett.* **84**, 1002 (2004)

[18] Compoundsemiconductor.net market report (Yole Development, 2009; http://compoundsemiconductor.net/cws/article/news/37731) (accessed June 2009)

[19] D. Zhu, C. McAleese, K.K. McLaughlin, M. Haberlen, C.O. Salcianu, E.J. Thrush, M.J. Kappers, W.A. Philips, P. Lane, D.J. Wallis, T. Martin, M. Astles, S. Thomas, A. Pakes, M. Heuken and C.J. Humphreys, *Proc. of SPIE* **7231**, 723118 (2009)

[20] C. Berger, A. Dadgar, F. Reiher, G. Strassburger, J. Blasing, and A. Krost, *Curvature measurements during GaN growth on Si*. International Conference on Nitride Semiconductors (2011)

[21] F. Brunner, A. Knauer, T. Schenk, M. Weyers and J.T. Zettler, *Journal of Crystal Growth*, **310**, 2432 (2008)

[22] R.A. Oliver, M.J. Kappers, C. McAleese, R. Datta, J. Sumner and C.J. Humphreys, *Journal of Materials Science: Materials and Electronics*, **19**, S208 (2008)

[23] F.A. Ponce, D. Chern, W.T. Young, and J.W. Steeds, *Appl. Phys. Lett*. **69**, 770 (1996)

[24] P.D. Cherns, *A Transmission Electron Microscopy Study of AlGaN/GaN heterostructures*, PhD Thesis, University of Cambridge (2007)

[25] X.J. Ning, F.R. Chien, P. Pirouz, J.W. Yang, and M.A. Khan, *J. Mater. Res*. **11**, 580 (1996)

[26] X.H. Wu, P. Fini, E.J. Tarsa, B. Heying, S. Keller, U.K. Mishra, S.P. DenBaars and J.S. Speck, *Journal of Crystal Growth*, **189**, 231 (1998)

[27] V. Narayanan, K. Lorenz, W. Kim, and S. Mahajan, *Appl. Phys. Lett*. **78**, 1544 (2001)

[28] R.A. Oliver, M.J. Kappers, and C.J. Humphreys, *Apply. Phys. Lett*. **89**, 011914 (2006)

[29] R.A. Oliver, M.J. Kappers, J. Sumner, R. Datta, and C.J. Humphreys, *Jounral of Crystal Growth*, **289**, 506 (2006)

[30] V. Narayanan, K. Lorenz, W. Kim, and S. Mahajan, *Philosophical Magazine A*, **82**, 885 (2002)

[31] J.W. Matthews, and A.E. Blakeslee, *Jounral of Crystal Growth*, **27**, 118 (1974)

[32] J.H. van der Merwe, *J. Appl. Phys*. **34**, 117 (1963)

[33] D. Holec, *Multi-scale modelling of III-nitrides: from dislocations to the electronic structure*, PhD Thesis, University of Cambridge (2008)

[34] D. Holec, P.M.F.J. Costa, M.J. Kappers, and C.J. Humphreys, *Journal of Crystal Growth*, **303**, 314 (2007)

[35] D. Holec, and C.J. Humphreys, *Mater. Sci. Forum*, **567**, 209 (2007)

[36] D. Holec, Y. Zhang, D.V.S. Rao, M.J. Kappers, C. McAleese, and C.J. Humphreys, *J. Appl. Phys*. **104**, 123514 (2008)

[37] D. Hull, and D.J. Bacon, *Introduction of dislocations*, 4th ed. Butterworth-Heinemann (2001)

[38] C. Johnston, *Characterization of (11-20) nonpolar and (11-22) semipolar GaN epitaxial films*, PhD Thesis, University of Cambridge (2009)

[39] P. Vennegeus, F. Mathal, and Z. Bougrioua, *Phys. Stat. Sol. C*. **3**, 1658 (2006)

[40] Y.T. Rebane, Y.G. Shreter, and M. Albrecht, *Phys. Stat. Sol. A*. **164**, 141 (1997)

[41] W.A. Brantley, O.G. Lorimor, P.D. Dapkus, S.E. Haszko, and R.H. Saul, *J. Appl. Phys.* **46**, 2629 (1975)

[42] S.J. Rosner, G. Girolami, H. Marchand, P. Fini, J.P. Ibbetson, L. Zhao, S. Keller, U. Mishra, S.P. DenBaars, and J.S. Speck, *Appl. Phys. Lett*. **74**, 2035 (1999)

[43] T. Sugahara, H. Sato, M. Hao, Y. Naoi, S. Kurai, S. Tottori, K. Yamashita, K. Nishino, L.T. Romano, and S. Sakai, *Jpn. J. Appl. Phys*. **37**, 398 (1998)

[44] T.M. Katona, M.D. Craven, J.S. Speck, and S.P. DenBaars, *Appl. Phys. Lett*. **85**, 1350 (2004)

[45] S.D. Lester, F.A. Ponce, M.G. Craford, and D.A. Steigerwald, *Appl. Phys. Lett.* **66**, 1249 (1995)

[46] T.M. Smeeton, M.J. Kappers, J.S. Barnard, M.E. Vickers, and C.J. Humphreys, *Appl. Phys. Lett.* **83**, 5419 (2003)

[47] S. Keller, B.P. Keller, Y.F. Wu, B. Heying, D. Kapolnek, J.S. Speck, U.K. Mishra, and S.P. DenBaars, *Appl. Phys. Lett*. **68**, 1525 (1996)

[48] I. Akasaki. H. Amano, Y. Koide, K. Hiramatsu, and N. Sawaki, *Journal of Crystal Growth*, **98**, 209 (1989)

[49] M.J. Kappers, R. Datta, R.A. Oliver, F.D.G. Rayment, M.E. Vickers, and C.J. Humphreys, *Journal of Crystal Growth*, **300**, 70 (2007)

[50] P. Gibart, *Reports on Progress in Physics*, **67**, 667 (2004)

[51] S. E. Bennett, *Nitride Semiconductors by Atom Probe Tomography and Correlative Techniques*, PhD Thesis, University of Cambridge (2010)

[52] K. Hiramatsu, K. Nishiyama, A. Motogaito, H. Miyake, Y. Iyechika, and T. Maeda, *Phys. Stat. Sol. A*. **176**, 535 (1999)

[53] S. Nakamura, M. Senoh, S. Nagahama, N. Iwasa, T. Yamada, T. Matsushita, Y. Sugimoto, and H. Kiyoku, *Jpn. J. Appl. Phys*. **36**, 1059 (1997)

[54] D.A.B. Miller, D.S. Chemla, T.C. Damen, A.C. Gossard, W. Wiegmann, T.H. Wood, and C.A. Burrus, *Phys. Rev. Lett*. **53**, 2173 (1984)

[55] F. Bermardini, and V. Fiorentini, *Phys. Stat. Sol. B*. **216**, 391 (1999)

[56] D. Cherns, J. Barnard, and F.A. Ponce, *Sol. Stat. Com.* **111**, 281 (1999)

[57] X. Guo, and E.F. Schubert, *Appl. Phys. Lett*. **78**, 3337 (2001)

[58] V. Adivarahan, S. Wu, W.H. Sun, V. Mandavilli, M.S. Shatalov, G. Simin, J.W. Yang, H.P. Maruska, M.A. Khan, *Appl. Phys. Lett*. **85**, 1838 (2004)

[59] M. Razeghi, and M. Henini, *Optoelectronic devices: III-nitrides*. Elsevier, Oxford (2004)

[60] F. Bircher, UV-LED curing in industrial printing. 13th SSOM Engelberg (March 2009; http://www.swisslaser.net/libraries.files/UV-LEDcuringindustrialprinting2009-03-18.pdf) (accessed June 2009)

[61] A. Sandhu, *Nature Photonics*, **1**, 38 (2006)

[62] T. Nishida, and N. Kobayashi, *Phys. Stat. Sol. A*. **176**, 45 (1999)

[63] N. Otsuka, A. Tsujimura, Y. Hasegawa, G. Sugahara, M. Kume, and Y. Ban, *Jpn. J. Appl. Phys*. **39**, L445 (2000)

[64] Y. Narukawa, Y. Kawakami, M. Funato. S. Fujita, and S. Nakamura, *Appl. Phys. Lett*. **70**, 981 (1997)

[65] H.K. Cho, J.Y. Lee, N. Sharma, C.J. Humphreys, G.M. Yang, C.S. Kim, J.H. Song, and P.W. Yu, *Appl. Phys. Lett*. **79**, 2594 (2001)

[66] I.C. Ho, and G.B. Stringfellow, *Appl. Phys. Lett*. **69**, 2701 (1996)

[67] C.J. Humphreys, *Philos. Mag*. **87**, 1971 (2007)

[68] M.J. Galtrey, R.A. Oliver, M.J. Kappers, C.J. Humphreys, D.J. Stokes, P.H. Clifton, and A. Cerezo, *Appl. Phys. Lett*. **90**, 061903 (2007)

[69] K. Motoki, T. Okahisa, N. Matsumoto, M. Matsushima, H. Kimura, H. Kasai, K. Takemoto, K. Uematsu, T. Hirano, M. Nakayama, S. Nakahata, M. Ueno,

D. Hara, Y. Kumagai, A. Koukitu, and H. Seki, *Jpn. J. Appl. Phys*. **40**, L140 (2001)

[70] J. Edmond, A. Abare, M. Bergman, J. Bharathan, K.L. Bunker, D. Emerson, K. Haberern, J. Ibbetson, M. Leung, P. Russel, and D. Slater*, Jounral of Crystal Growth,* **272**, 242 (2004)

[71] M.A. Khan, J.N. Kuzina, D.T. Olson, T. George, and W.T. Pike, *Appl. Phys. Lett*. **63**, 3470 (1993)

[72] K. Balakrishnan, A. Bandoh, M. Iwaya, S. Kamiyama, H. Amano, and I. Akasaki, *Jpn. J. Appl. Phys*. **46**, L307 (2007)

[73] J.P. Zhang, H.M. Wang, M.E. Gaevski, C.Q. Chen, Q. Fareed, J.W. Yang, G. Simin, and M.A. Khan, *Appl. Phys. Lett*. **80**, 3542 (2002)

[74] T. Nishida, and N. Kobayashi, *Phys. Stat. Sol. A*. **176**, 45 (1999)

[75] P. Waltereit, O. Brandt, A. Trampert, H.T. Grahn, J. Menniger, M. Ramsteiner, M. Reiche, and K.H. Ploog, *Nature*, **406**, 865 (2000)

[76] A. Chakraborty, B. Haskell, S. Keller, J.S. Speck, S.P. DenBaars, S. Nakamura, and U. Mishra, *Appl. Phys. Lett*. **85**, 5143 (2004)

[77] M.D. Craven, S.H. Lim, F. Wu, J.S. Speck, and S.P. DenBaars, *Appl. Phys. Lett.* **81**, 469 (2002)

[78] B.A. Haskell, F. Wu, S, Matsuda, M.D. Craven, P.T. Fini, S.P. DenBaars, J.S. Speck, and S. Nakamura, *Appl. Phys. Lett*. **83**, 1554 (2003)

[79] A.E. Romanov, T.J. Baker, S. Nakamura, and J.S. Speck, *J. Appl. Phys*. **100**, 023522 (2006)

[80] J.F. Kaeding, M. Iza, H. Sato, S.P. DenBaars, J.S. Speck, and S. Nakamura, *Jpn. J. Appl. Phys*. **45**, L536 (2006)

[81] T.J. Baker, B.A. Haskell, F. Wu, P.T. Fini, J.S. Speck, and S. Nakamura, *Jpn. J. Appl. Phys.* **44**, L920 (2005)

[82] K. Nishizuka, M. Funato, Y. Kawakami, S. Fujita, Y. Narukawa, and T. Mukai, *Appl. Phys. Lett*. **85**, 3122 (2004)

[83] P.P. Paskov, R. Schifano, B. Monemar, T. Paskova, S. Figge, and D. Hommel, *J. Appl. Phys*. **98**, 093519 (2005)

[84] T.J. Badcock, P. Dawson, M.J. Kappers, C. McAleese, J.L. Hollander, C.F. Johnston, D.V.S. Rao, A.M. Sanchez, and C.J. Humphreys, *Appl. Phys. Lett*. **93**, 101901 (2008)

[85] H. Amano, S. Takanami, M. Iwaya, S. Kamiyama, and I. Akasaki, *Phys. Stat. Sol. A*. **195**, 491 (2003)

[86] S. Kamiyama, K. Lida, T. Kawashima, H. Kasugai, S. Mishima, A. Honshio, Y. Miyake, M. Iwaya, H. Amano, and I. Akasaki, *IEEE J. Sel. Top. Quant*. **11**, 1069 (2005)

[87] G. Binnig, and H. Rohrer, *Surface Science*, **126**, 236 (1983)

[88] E.T. Yu, *Mater. Sci. Eng*. **17**, 147 (1996)

[89] E. Meyer, H.J. Hug, and R. Bennewitz, *Scanning Probe Microscopy: The Lab on a Tip*. Springer (2003)

[90] R.A. Oliver, *Rep. Prog. Phys*. **71**, 076501 (2008)

[91] D.K. Bowen, and B.K. Tanner, *High resolution X-ray diffractometry and topography*. Taylor and Francis, London (1998)

[92] P.F. Fewster, *X-ray scattering from semiconductors*. Imperial College Press, London (2000)

[93] T.M. Smeeton, *The nanostructure of InGaN Quantum Wells*. PhD Thesis, University of Cambridge (2005)

[94] V. Holy, *High-resolution X-ray scattering from thin films and multilayers*, Springer, Berlin (1999)

[95] T.A. Lafford, B.K. Tanner, and P.J. Parbrook, *J. Phys. D: Appl. Phys*. **36**, A245 (2003)

[96] A.D. Kurtz, S.A. Kulin, and B.L. Averbach, *Phys. Rev*. **101**, 1285 (1956)

[97] B.G. Yacobi, and D.B. Holt, *Cathodoluminescence microscopy of inorganic solids*. Springer (1990)

[98] *Gatan MonoCL4*, User's Guide

[99] H.A. Zarem, P.C. Sercel, J.A. Lebens, L.E. Eng, A. Yariv, and K.J. Vahala, *Appl. Phys. Lett*. **55**, 1647 (1989)

[100] C.M. Parish, and P.E. Russell, *Advances in Imaging and Electron Physics*, **147** (2007)

[101] R.W. Martin, P.R. Edwards, K.P. O'Donnell, M.D. Dawson, C.W. Jeon, C. Liu, G.R. Rice, and I.M. Watson. *Phys. Stat. Sol. C.* **201**, 665 (2004)

[102] M.A. Reshchikov, and H. Morkoc, *J. Appl. Phys*. **97**, 061301 (2005)

[103] C. Donolato, *Optik*, **52**, 19 (1978)

[104] R. Gauvin, CASINO Monte-Carlo Program. Université de Sherbrooke, Québec, Canada (http://www.gel.usherbrooke.ca/casino/index.html) (accessed June 2009)

[105] L.A. Giannuzzi, and F.A. Stevie, *Micron*, **30**, 197 (1999)

[106] J.P. McCaffrey, M.W. Phaneuf, and L.D. Madsen, *Ultramicroscopy*, **87**, 97 (2001)

[107] D.B. Williams, and C.B. Carter, *Transmission Electron Microscopy*. Kluwer Academic, Dordrecht (1996)

[108] Diagram outlining the internal components of a basic TEM system. (Wikipedia, 2011; http://en.wikipedia.org/wiki/Transmission_electron_microscopy) (accessed June 2011)

[109] D.J.H. Cockayne, I.L.F. Ray, and M.J. Whelan, *Philos. Mag.* **20**, 1265 (1969)

[110] P.B. Hirsch, A. Howie, R.B. Nicholson, D.W. Pashley, and M.J. Whelan, *Electron microscopy of thin crystals*. Krieger Publishing Company (1977)

[111] Y.C. Zhang, *Characterisation of GaN using Transmission Electron Microscopy*. PhD Thesis, University of Cambridge (2008)

[112] J.C.H. Spence, and J.M. Zuo, *Electron microdiffraction*. Plenum Press, New York (1992)

[113] A.M. Sanchez, P. Ruterana, S.I. Molina, F.J. Pacheco, and R. Garcia, *Phys. Stat. Sol. B*. **234**, 935 (2002)

[114] F.A. Ponce, D.P. Bour, W.T. Young, M. Saunders, and J.W. Steeds, *Appl. Phys. Lett.* **69**, 337 (1996)

[115] N. Sharma, D.M. Tricker, and C.J. Humphreys, *Obtaining the correct polarity of GaN using CBED*. EUREM 12, Brno, Czech Republic (2000)

[116] D.A. Porter, and K.E. Easterling, *Phase transformations in Metals and Alloys*. Chapan L Hall, London (1981)

[117] J. Bai, T. Wang, P.J. Parbrook, K.B. Lee, Q. Wang, and A.G. Cullis, *Surface Science*, **602**, 2643 (2008)

[118] V.I. Vdovin, *Phys. Stat. Sol. (a)* **171**, 239 (1999)

[119] J.A. Floro, D.M. Follstaedt, P. Provencio, S.J. Hearne, and S.R. Lee, *J. Appl. Phys.* **96**, 7087 (2004)

[120] P. Cantu, F. Wu, P. Waltereit, S. Keller, A.E. Romanov, U.K. Mishra, S.P. DenBaars, and J.S. Speck, *Appl. Phys. Lett*. **83**, 674 (2003)

[121] A.E. Romanov, and J.S. Speck, *Appl. Phys. Lett*. **83**, 2569 (2003)

[122] R. Beanland, *J. Appl. Phys*. **72**, 4031 (1992)

[123] S.C. Jain, A.H. Harker, and R.A. Cowley, *Philos. Mag. A*. **75**, 1461 (1997)

[124] H. Hirayama, *Appl. Phys. Lett*. **91**, 071901 (2007)

[125] C. McAleese, M.J. Kappers, R.A. Oliver, R. Datta, E.J. Thrush, and C.J. Humphreys, *Influence of initial conditions on MOVPE growth of AlN on c-plane sapphire.* Proceedings of the 11th European Workshop on Metalorganic Vapour Phase Epitaxy, Lausanne, Switzerland, 399-401 (2005)

[126] W.Y. Fu, M.J. Kappers, Y.C. Zhang, C.J. Humphreys, and M.A. Moram, *Appl. Phys. Express*, **4**, 065503 (2011)

[127] M. Albrecht, S. Christiansen, J. Michler, W. Dorsch, and H.P. Strunk, *Appl. Phys. Lett*. **67**, 1232 (1995)

[128] J.P. Hirth, and J. Lothe, *Theory of Dislocations*, 2nd ed. John Wiley and Sons (1982)

[129] W.K. Burton, N. Cabrera, and F.C. Frank, *Philos. Trans. R. Soc. London, Ser. A* **243**, 299 (1951)

[130] B. Heying, E.J. Tarsa, C.R. Elsass, P. Fini, S.P. DenBaars, and J.S. Speck, *J. Appl. Phys*. **85**, 6470 (1999)

[131] V. Merlin, T. Duc, G. Younes, Y. Montiel, V. Souliere, and P. Regreny, *J. Appl. Phys*. **78**, 5048 (1995)

[132] S.R. Lee, D.D. Koleske, K.C. Cross, J.A. Floro, K.E. Waldrip, A.T. Wise, and S. Mahajan, *Appl. Phys. Lett*. **85**, 6164 (2004)

[133] A. Krost, A. Dadgar, G. Strassburger, and R. Clos, *Phys. Stat. Sol. (a)* **200**, 26 (2003)

[134] M. Ohring, *Materials Science of Thin Films; Deposition and Structure*, 2nd Ed. Academic, New York (2002)

[135] A.F. Wright, *J. Appl. Phys*. **82**, 2833 (1997)

[136] W.G. Breiland, S.R. Lee, and D.D. Koleske, *J. Appl. Phys*. **95**, 3453 (2004)

[137] D.M. Follstaedt, S.R. Lee, A.A. Allerman, and J.A. Floro, *J. Appl. Phys*. **105**, 083507 (2009)

[138] K. Hiramatsu, K. Nishiyama, A. Motogaito, H. Miyake, Y. Iyechika, and T. Maeda, *Phys. Stat. Sol. (a)* **176**, 535 (1999)

[139] X.Q. Shen, and H. Okumura, *Appl. Phys. Lett*. **87**, 101910 (2005)

[140] T. Wang, K. Lee, J. Bai, P. Parbrook, R. Airey, Q. Wang, G. Hill, F. Ranalli, and A. Cullis, *Appl. Phys. Lett*. **89**, 081126 (2006)

[141] R. Liu, A. Bell, F. Ponce, C. Chen, J. Yang, and M. Khan, *Appl. Phys. Lett*. **86**, 021908 (2005)

[142] A. Ishibashi, Y. Kawaguchi, G. Sugahara, T. Shimamoto, T. Yokogawa, Y. Yamada, Y. Ueki, K. Nakamura, and T. Taguchi, *Phys. Stat. Sol. (b)* **241**, 2730 (2004)

[143] T. Narita, Y. Honda, M. Yamaguchi, and N. Sawaki, *Phys. Stat. Sol. (c)* **4**, 2506 (2007)

[144] H. Hirayama, and Y. Aoyagi, *The Review of Laser Engineering*, **30**, 308 (2002)

[145] Y. Wu, W. Walukiewicz, K.M. Yu, W. Shan, J.W. Ager, E.E. Haller, H. Lu, W.J. Schaff, W.K. Metzger, S. Kurtz, *J. Appl. Phys*. **94**, 6477 (2004)

[146] A. Kakanakova-Georgieva, R.R. Ciechonski, U. Forsberg, A. Lundskog, and E. Janze, *Cryst. Growth Des*. **9**, 880 (2009)

[147] M. Kneissl, T. Kolbe, C. Chua, V. Kueller, N. Lobo, J. Stellmach, A. Knauer, H. Rodriguez, S. Einfeldt, Z. Yang, N.M. Johnson, and M. Weyers, *Semicond. Sci. Technol.* **26**, 014036 (2011)

[148] V. Kueller, A. Knauer, F. Brunner, U. Zeimer, H. Rodriguez, M Kneissl, and M. Weyers, *Journal of Crystal Growth*, **315**, 200 (2011)

[149] M.A. Khan, R.A. Skogman, J.M. Van Hove, D.T. Olsen, and J.N. Kuznia, *Appl. Phys. Lett*. **60**, 1366 (1992)

[150] C. McAleese, *OMVPE Growth and Characterisation of Nitride Semiconductor Materials*, PhD Thesis, University of Cambridge (2011)

[151] S. Keller, and S.P. DenBaars, *Journal of Crystal Growth*, **248**, 479 (2003)

[152] S. Keller, G. Parish, P.T. Fini, S. Heikman, C.H. Chen, N. Zhang, S.P. DenBaars, U.K. Mishra, and Y.F. Wu, *J. Appl. Phys*. **86**, 5850 (1999)

[153] A. Thon, and T.F. Kuech, *Appl. Phys. Lett*. **69**, 55 (1996)

[154] J. Jasinski, Z. Liliental-Weber, Q.S. Paduano, and D.W. Weyburne, *Appl. Phys. Lett*. **83**, 2811 (2003)

[155] M. Sumiya, and S. Fuke, *MRS Internet J. Nitride Semicond. Res*. **9**, 1 (2004)

[156] H. Hirayama, T. Yatabe, N. Noguchi, T. Ohashi, and N. Kamata, *Appl. Phys. Lett*. **91**, 071901 (2007)

[157] M. David, S.V. Babu, and D.H. Rasmussen, *AlChE Journal*, **36**, 871 (1990)

[158] J.R. Creighton, W.G. Breiland, M.E. Coltrin, and R.P. Pawlowski, *Appl. Phy. Lett*. **81**, 2626 (2002)

[159] E.J. Thrush, private communication

[160] T. Paskova, *Phys. Stat. Sol. (b)* **245**, 1011 (2008)

[161] M.J. Kappers, M.A. Moram, Y. Zhang, M.E. Vickers, Z.H. Barber, and C.J. Humphreys, *Physica B*, **401**, 296 (2007)

[162] C.F. Johnston, M.J. Kappers, M.A. Moram, J.L. Hollander, and C.J. Humphreys, *Journal of Crystal Growth*, **311**, 3295 (2009)

[163] M. Fox, *Optical properties of solids*, Oxford University Press, Oxford (2001)

[164] J.L Hollander, C. McAleese, private communication

[165] L. Zhou, R. Chandrasekaran, T.D. Moustakas, and D.J. Smith, *Journal of Crystal Growth*, **310**, 2981 (2008)

[166] M. Benyoucef, M. Kuball, G. Hill, M. Wisnom, B. Beaumont, and P. Gibart, *Appl. Phys. Lett*. **79**, 4127 (2001)

[167] R. Hao, private communication

[168] M.A. Moram, T.C. Sadler, M. Haberlen, M.J. Kappers, and C.J. Humphreys, *Appl. Phys. Lett*. **97**, 261907 (2010)

[169] T. Zhu, C.F. Johnston, M. Haberlen, M.J. Kappers, and R.A. Oliver, *J. Appl. Phys.* **107**, 023503 (2010)

[170] M. Haberlen, T.J. Badcock, M.A. Moram, J.L. Hollander, M.J. Kappers, P. Dawson, C.J. Humphreys, and R.A. Oliver, *J. Appl. Phys.* **108**, 033523 (2010)

[171] K. Kojima, A.A. Yamaguchi, M. Funato, Y. Kawakami, and S. Noda, *J. Appl. Phys*. **110**, 043115 (2011)

[172] Q. Sun, C.D. Yerino, T.S. Ko, Y.S. Cho, I.H. Lee, J. Han, and M.E. Coltrin, *J. Appl. Phys*. **104**, 093523 (2008)

[173] P.P. Paskov, R. Schifano, B. Monemar, T. Paskova, S. Figge, and D. Hommel, *J. Appl. Phys*. **98**, 093519 (2005)

[174] J.L. Hollander, M.J. Kappers, C. McAleese, C.J. Humphreys, *Appl. Phys. Lett*. **92**, 101104 (2008)

[175] M.A. Moram, C.S. Ghedia, D.V.S. Rao, J.S. Barnard, Y. Zhang, M.J. Kappers, and C.J. Humphreys, *J. Appl. Phys.* **106**, 073513 (2009)

[176] D. Cherns, C.G. Jiao, H.Mokhtari, J.Cai, and F.A. Ponce, *Phys. Status Solidi (b)*, **234**, 924 (2002)

[177] P. Vennegues, B. Beaumont, V. Bousquest, M. Vaille, and P. Gibart, *J. Appl. Phys.* **87**, 4175 (2000)

[178] D. Cherns and A.R. Preston, *Journal of Electron Microscopy Technique.* **13**, 111 (1989)